DOE/ER-0045/13

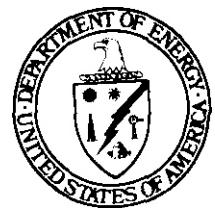

Alloy Development for Irradiation Performance

Semiannual Progress Report
For Period Ending September 30, 1984

U.S. *Department of Energy*
Office of Fusion **Energy**

Printed in the United Stales of America. Available from
National Technical Information Service
U.S. Department of Commerce
5285 Port Royal Road, Springfield, Virginia 22161
NTIS price codes—Printed Copy: A11 Microfiche A01

DOE/ER-0045/13
Distribution
Category
uc-20. 2oc

ALLOY DEVELOPMENT FOR IRRADIATION PERFORMANCE
SEMIANNUAL PROGRESS REPORT FOR PERIOD ENDING SEPTEMBER 30,1984

ARGONNE NATIONAL LABORATORY

GA TECHNOLOGIES, INC.

McDONNELL DOUGLAS ASTRONAUTICS COMPANY

MASSACHUSETTS INSTITUTE OF TECHNOLOGY

NAVAL RESEARCH LABORATORY

OAK RIDGE NATIONAL LABORATORY

SANDIA NATIONAL LABORATORIES

WESTINGHOUSE HANFORD COMPANY

Date Published: March 1985

Prepared by
OAK RIDGE NATIONAL LABORATORY
Oak Ridge, Tennessee 37831
operated by
MARTIN MARIETTA ENERGY SYSTEMS, INC.
for the
U. S. DEPARTMENT OF ENERGY
Under Contract *No.* DE-AC05-840R21400

Reports previously issued in this series are as follows:

DOE/ET-0058/1	Period Ending March 31, 1978
DOE/ET-0058/2	Period Ending June 30, 1978
DOE/ET-0058/3	Period Ending September 30. 197R
DOE/ET-0058/4	Period Ending December 31, 1978
DOE/ET-0058/5	Period Ending March 31, 1979
DOE/ET-0058/6	Period Ending June 30, 1979
DOE/ET-0058/7	Period Ending September 311, 1979
DOE/ER-0045/1	Period Ending December 31, 1979
DOE/ER-0045/2	Period Ending March 31, 1980
DOE/ER-0045/3	Period Ending June 30, 1980
DOE/ER-0045/4	Period Ending September 30, 1980
DOE/ER-0045/5	Period Ending December 31, 1980
DOE/ER-0045/6	Period Ending March 31, 1981
DOE/ER-0045/7	Period Ending September 30. 1981
DOE/ER-0045/8	Period Ending March 31, 1982
DOE/ER-0045/9	Period Endinq September 30, 1982
DOE/ER-0045/10	Period Ending March 31, 1983
DOE/ER-0045/11	Period Ending September 30, 1983
DOE/ER-0045/12	Period Ending March 31, 1984

FOREWORD

This report is the twentieth in a series of Technical Progress Reports on ***"Alloy Development*** for ***Irradiation Performance"*** (ADIP), which is one element of the Fusion Reactor Materials Program, conducted in support of the Magnetic Fusion Energy Program of the U.S. Department of Energy. Other elements of the Materials Program are

- *Damage* ***Analysis and Fundamental Studies*** *(DAFS)*
- ***Plasma-Materials Interaction*** *(PMI)*
- *Special-Purpose* ***Materials*** *(SPM)*
- ***High Heat Flux Components***

The first seven reports in this series are numbered DOE/ET-0058/1 through 7. This report is the thirteenth in a new numbering sequence that begins with DOE/ER-0045/1.

The ADIP program element is a national effort composed of contributions from a number of National Laboratories and other government laboratories, universities, and industrial laboratories. It was organized by the Materials and Radiation Effects Rranch, Office of Fusion Enerqy, DOE, and a Task Group on ***Alloy Development for Irradiation Performance,*** which now operates under the auspices of the Reactor Technologies Branch. The purpose of this series of reports is to provide a working technical record of that effort for the use of the program participants, for the fusion energy program in qent'ral, and for the Department of Energy.

This report is organized along topical lines in parallel to a Program Plan of the same title so that activities and accomplishments may be followed readily relative to that Program Plan. Thus, the work of a given laboratory may appear throughout the report. Chapters 1, 7, 8, and 9 review activities on analysis and evaluation, test methods development, status of irradiation experiments, and corrosion testing and hydrogen permeation studies, respectively. These activities relate to each of the alloy development paths. Chapters 3, 4, 5, 6, and 7 present the ongoing work on each alloy development path. The Table of Contents is annotated for the convenience of the reader.

This report has been compiled and edited under the guidance of the Chairman of the Task Group on *Alloy* ***Development for Irradiation Performance.*** A. F. Rowcliffe, Oak Ridge National Laboratory, and his efforts and those of the supporting staff of ORNL and the many persons who made technical contributions are gratefully acknowledged. T. C. Reuther, Reactor Technoloqies Rranch, is the Department of Energy Counterpart to the Task Group Chairman and has responsibility for the ADIP Proqram within DOE.

G. M. Haas, Chief
Reactor Technologies Rranch
Office of Fusion Fnergy

CONTENTS

1. ANALYSIS AND EVALUATION STUDIES

1.1 MATERIALS HANDBOOK FOR FUSION ENERGY SYSTEMS - J. W. Davis (McDonnell Douglas Astronautics Company - St. Louis Division)

1.1.1 ADIP Task

Task Number I.A.1 - Define material property requirements and make structural life predictions.

1.1.2 Objective

To provide a consistent and authoritative source of material property data for use by the fusion community in concept evaluation, design, safety analysis, and performance/verification studies of various fusion energy systems. A secondary objective is the early identification of areas in the materials data base where insufficient information or voids exist.

1.1.3 *Summary*

During the past six months the handbook effort has been directed towards developing data sheets. For this period the effort has been to maintain a continuous flow of data sheets into the handbook. Progress has been made towards the achievement of this goal by the monitoring of the processing of new data sheets in various stages of preparation.

1.1.4 Progress and Status

Currently there are 128 data pages in various stages of review prior to their incorporation into the handbook. Of these 128 data pages, 26 data sheets on 23 Cr-6Ni-9Mn, HT-9 and 316 steels, lithium and fiberglass epoxy have been approved and are awaiting publication. The 21 Cr-6Ni-9Mn stainless steel data sheets, prepared by N. J. Simon of National Bureau of Standards, provide general and mechanical property information on composition and tensile strength. The HT-9 data sheets, prepared by D. S. Gelles of Westinghouse Hanford Company, provide information on the effect of temperature on Young's Modulus and Shear Modulus, as well as physical property information on thermal diffusivity, thermal emissivity (in vacuum and stably axidized) and thermal conductivity. The 316 stainless steel data sheets, prepared by N. J. Simon of National Bureau of Standards, provide information on impact energy, fatigue life, fatigue crack growth, specific heat, thermal conductivity, thermal expansion, electrical resistivity and fracture toughness at cryogenic temperatures. The fiberglass epoxy data sheets, prepared by C. E. Klabunde of Oak Ridge National Laboratory, are revisions to data sheets currently in the handbook on the effect of irradiation on resistivity and weight loss.

Thirty-nine data sheets on lithium, HT-9, 316 stainless steel have been through the review cycle. Thirty-four were returned to the authors during the previous reporting period to have the reviewers' comments incorporated. The lithium data sheets, prepared by W. F. Brehm of Westinghouse Hanford Company, provide thermal, mechanical, and electrical property information as a function of temperature. The HT-9 data sheets prepared by D. S. Gelles of Westinghouse Hanford Company provide information on irradiation induced stress-free swelling. The 316 stainless steel data sheets, prepared by N. J. Simon of NBS, provide mechanical property information on fracture toughness, ultimate tensile strength, tensile yield, tensile elongation, tensile reduction of area and engineering stress-strain, and thermal property information on specific heat, thermal conductivity and thermal expansion, as well as irradiation induced void swelling (stress-free and stress-affected) and precipitate-related densification. Five data sheets, in revision at MDC, provide electrical, mechanical and thermal property data on lithium. These data sheets are still in the hands of the authors.

Thirty-seven data sheets on lithium compounds (Li_2O and Li_8ZrO_6), 21Cr-6Ni-9Mn, HT-9, 316 stainless steel and MRCOR have been submitted for inclusion into the handbook. The lithium oxide data sheet, prepared at McDonnell Douglas, provides thermal conductivity information. The lithium octazirconate data sheet, prepared by G. W. Hollenberg of Westinghouse Hanford Company, provides information on theoretical density vs ^6Li enrichment. The 21Cr-6Ni-9Mn data sheets, prepared by N. J. Simon of NBS, provide mechanical, thermal and electrical property information at cryogenic temperatures. The 316 stainless steel data sheets, prepared by Bob Simons, M. L. Hamilton, J. S. Pintler, and D. K. Gutierrez of Westinghouse Hanford Company, provide mechanical and thermal property information at elevated temperatures. The MACOR Glass-Ceramic data sheets, prepared by F. W. Clinard of LANL, provide mechanical and thermal property information and effect of irradiation on strength and density.

The HT-9 data sheets, prepared by J. 6. Wattier of GA, provide information on mechanical properties vs temoerature.

Twenty-six data sheets on HT-9 and 316 stainless steel were withdrawn by the authors' organization, Westinghouse Hanford Company. The pages are a part of the Breeder program and were not cleared by the authors.

Data sheets planned will cover structural materials (vanadium alloys and copper alloys), superconducting magnet case materials, ceramic electrical insulators (MACOR, alumina) and neutron multipliers/breeders

(beryllium and lithium lead). In addition, effort is underway to develop data sheets on specific design related issues such as irradiation creep and its treatment in structural design, swelling, and magnetic effects when magnetic materials are used (e.g. ferritic steels).

In our continuing effort to make the handbook more useful to the fusion energy community, we are directing our efforts towards inclusion of materials that are candidates *for* the next generation reactors. Towards that end efforts are currently underway to convert the materials information generated on the TFCX project by ORNL into data pages. This is a cooperative effort between ORNL and MOAC.

1.1.5 Conclusions

There is currently a large backlog of data sheets awaiting publication and efforts will be directed towards relieving this situation. The handbook continues to have the good support of a number of researchers and as a result a number of new data pages are in the process of being prepared or have been received.

1.2 LIFETIME ANALYSIS: THERMALLY DRIVEN FATIGUE CRACK GROWTH IN AN HT-9 FIRST WALL - C. F. Oahms and T. A, Lechtenberg (GA Technologies)

1.2.1 ADIP Task

The Department of Energy, Office of Fusion Energy, has cited the need to investigate ferritic alloys under the ADIP Program Task, Ferritic Steel Development (Path E).

1.2.2 Objective

To develop a fracture management method with which lifetime calculations can be performed to confirm the engineering feasibility of using HT-9 as a first-wall and breeding blanket structural material.

1.2.3 Summary

1.2.4 Progress and Status

1.2.4.1 Introduction

Body-centered cubic (BCC) alloys such as ferritic steels and vanadium base alloys exhibit ductile-to-brittle transition characteristics. In designing with such materials, it is necessary to develop criteria and design procedures to assure that components made from these alloys will not suffer fast or brittle fracture. In order to develop an effective fracture management methodology for fusion first wall/breeding blankets (FW/B), a definition of the critical material's parameters is required in conjunction with a suitable stress analysis of specific configurations. Then, the acceptable beginning-of-life (BOL) flaw sizes and shapes can be calculated for various lifetimes. The results from these studies can guide the manufacturing, quality assurance, inspection, and allowable operating conditions of the component. This contribution reports data on a lifetime analysis code using HT-9 as a structural material and relying on design guidelines and configurations from the Blanket Comparison Selection Study (BCSS).[1]

An important issue involved in using (BCC) materials in a high energy neutron environment is the increase in the ductile-brittle transition temperature (DBTT) that results from irradiation. In order to fully demonstrate the potential of BCC materials such as HT-9, a computer analysis technique based on the University of Wisconsin WISECRACK[2] code has been developed in which crack growth is studied in a FW/B design generated by the BCSS. Mechanical property data, modified for neutron affects (such as changes in strength, DBTT temperature, upper and lower shelf fracture toughness, and fatigue crack growth rates) are incorporated into the code which permits calculations of lifetimes for various load cycle types.

1.2.4.2 Analytical

Design Loadings

Design guidelines are specified in the BCSS for both tokamak and mirror configurations. The main difference between the two configurations from an analysis standpoint is that the tokamak surface wall loading is approximately 20 times greater than that for the mirror. The loadings used for this analysis are for the tokamak design only. Table 1.2.1 describes the loadings which were used to perform the thermal, stress, and fracture analyses of a tokamak first-wall design[1].

Table 1.2.1 Design load guidelines

Neutron Wall Loading = 5 MW/m^2
Surface Wall Loading = 1 MW/m^2
Irradiation Rate = 100 dpa/2 yr life
Wall Erosion Rate = 2 mm/2 yr life
Tokamak Burn Cycle = 1 x 10^4 sec ON, 30 sec OFF

A typical BCSS lobe type configuration was used for this analysis. Other configurations are also being studied in the BCSS and similar results would be anticipated for these configurations.

The plasma side of the wall is smooth and the coolant-breeder side is a finned or ribbed configuration. This is seen in Fig. 1.2.1. The coolant is helium and the breeding material is Li_2O. On the plasma side the wall is allowed to erode 0.1 an per year due to plasma/wall interaction, so at the end of life (EOL), the thickness of the first wall at the minimum section is 0.15 cm. However, a beginning of life (BOL) geometry must also be shown to be adequate because there may be areas of the first-wall/blanket which do not erode, yet will see a very high heat and neutron flux.

Stress Analysis

Earlier calculations show that only flaws with an aspect ratio of a/t = 1/2 propagate to leak-through in less than two years. The BOL shows the fastest crack growth rates in the "relaxed stress state" due to

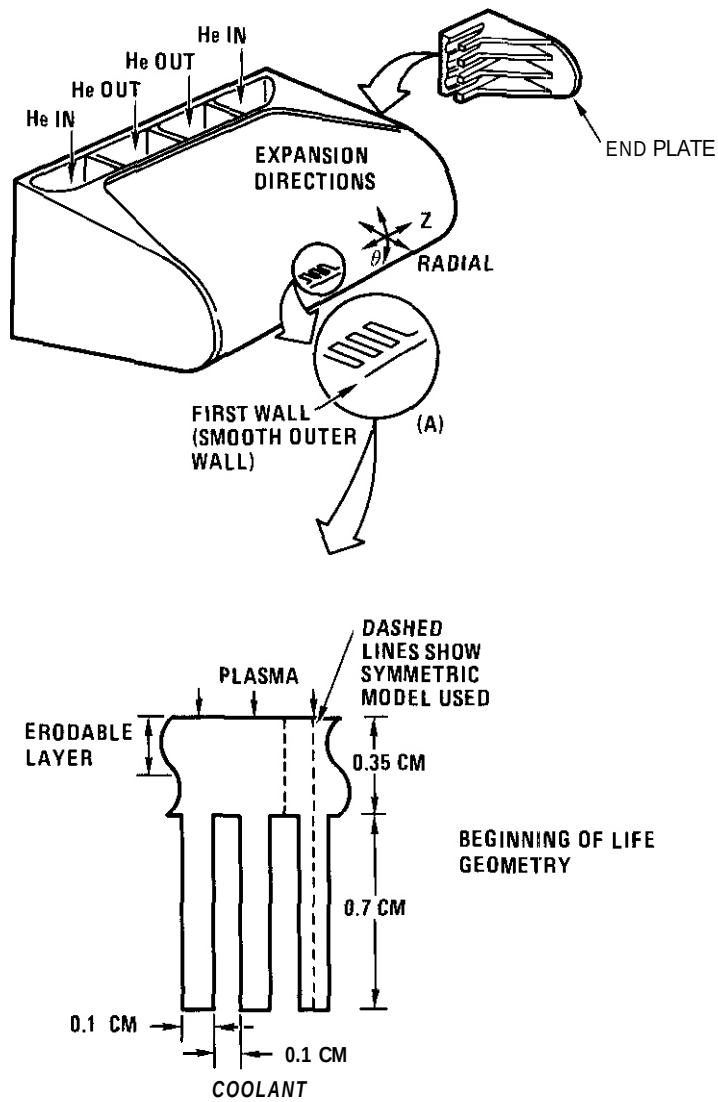

Fig. 1.2.1 Helium cooled blanket module with details

the large AT thermal strains. The "relaxed stress state" is the bounding case for which all thermally induced (secondary stresses) relax to zero. in this case, after a period of time the stresses in the "burn on" part of the cycle will simply change to those caused by the pressure (primary). In order to understand this further, a time-dependent stress analysis was calculated by TEPCS on the BOL geometry to determine how fast creep relaxation would change the stresses to some intermediate stress distribution between the extreme load cases previously analyzed. This would give slower crack growth than the "relaxed stress state", and a larger canponent lifetime estimate.

Figure 1.2.2(a) shows the boundary conditions assumed for the stress analysis models. The first wall is allowed to expand freely in the z-direction by expansion joints between the module end plates and the first wall. In the cross sectional plane (r,θ), normal to the reactor toroidal direction, the lobe is attached to the distribution ducting and is not a true circular cylinder. However, the use of an axisymmetric model has been shown to be conservative in calculating detailed first wall stressed.

The primary pressure stress caused by the 50 atm coolant pressure is superimposed on the secondary thermal stresses resulting in the total elastic theta (θ) stress distribution shown in Fig. 1.2.2(b). The thermal strains are induced only during a "burn on" cycle, but the coolant pressure stays constant during all load conditions. The end plate structure (Fig. 1.2.1) is assumed to support the pressure loads in the Z-direction and therefore, only thermal stresses are experienced by the first-wall in this direction [Fig. 1.2.2(c)].

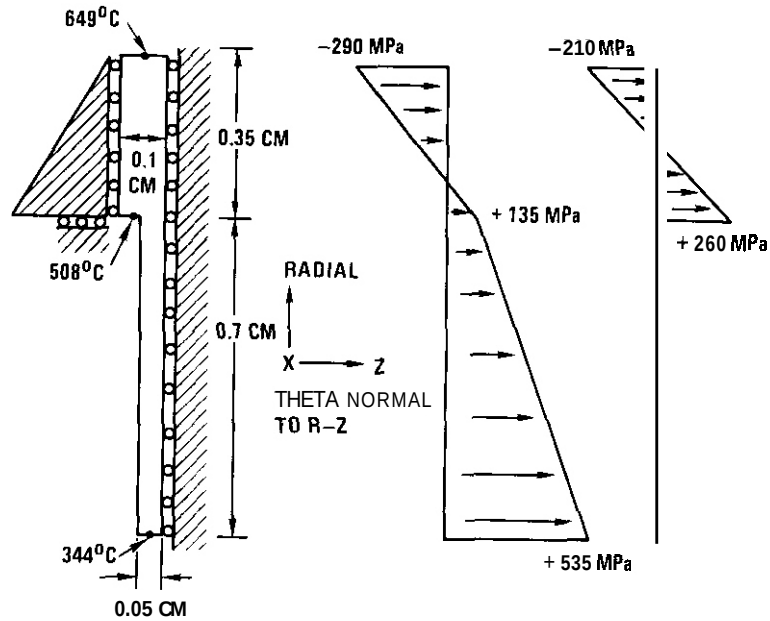

Fig. 1.2.2 Boundary conditions and elastic stress distributions during 'on' load cycle.

Irradiation-induced swelling rate is thought to be a function of temperature, flux and neutron energy. For HT-9, the swelling rate is very low and constant during the incubation period (up to 100 dpa) in the temperature range being considered and then increases to about 0.06%/dpa above 100 dpa. For such a thin structure, the flux and swelling are assumed uniform through the wall thickness. If irradiation-induced swelling varies significantly with temperature, there will be loads induced because of the interaction between different zones of material. very similar to thermal expansion stresses. In the Z-direction, any uniform irradiation induced expansion occuring in the first wall is assumed to b absorbed by the expansion joint. In the r-θ plane, the coolant ducting in the back of the canponent may not swell at the same rate as the first wall. As a result, a bending moment would be induced in the first wall producing tensile loads on the plasma side. The magnitude of these loads depends on the difference between the swelling rate and irradiation/thermal creep rate. The resulting equilibrium state would probably produce slightly larger stresses than calculated in this analysis. This phenomenon clearly warrants further study to determine its impact on fracture managment.

It must be noted that this smooth wall design meets all the design allowable criteria except that the BOL model has a peak temperature of 649°C which exceeds the structural material temperature limit[1] of 550°C by 100°C. More recent designs for the BCSS utilize a "grooved" concept for the first wall in which the material at temperatures above 550°C does not experience thermal stress. The material is grooved to a depth corresponding to the amount of wall that may be eroded during the module life. This technique is used as necessary for all candidate materials. For simplicity, the groove was not included in this analysis.

Irradiation and Thermal Creep

Irradiation creep data is available for some ferritic alloys[5,6], but only at modest fluence levels (<30 dpa). If the creep behavior is assumed the same at higher fluences, then the data suggests an equation of the form:

$$\epsilon_I = B_c \phi \sigma^n$$

where B_c is a constant which is alloy and temperature dependent, ϕ is the flux or dose rate, σ is the equivalent or Von Mises stress, and n is the stress exponent. For HT-9, the following values were used:

$B_c = (686.-1.84T+1.25T^2) \times 10^{-29}$ for $T \geq 737.1$°K
$B_c = 8.67 \times 10^{-29}$ for $T < 737.1$°K
$n = 1.5$
σ in units of MPa
ϵ in units of $\frac{\text{strain}}{\text{hr}}$

and for a tokamak reactor, the assumed flux was:

$$= 1.14 \times 10^{19} \frac{\text{neutrons}}{\text{cm}^2\ \text{hr}}$$

The equation[7] used for thermal creep is:

$$\epsilon_T = \frac{7.38 \times 10^{-3}}{(8.62 \times 10^{-5})T} (\sigma - \sigma_o)^3 \exp\left[\frac{-1.23}{(8.62 \times 10^{-5})T}\right]$$

where T and σ are in units of ^{o}K and ksi respectively. σ_o is considered a friction stress which is temperature-dependent and is defined as:

$$\sigma_o = a\ T + C$$
$$a = -0.218$$
$$C = 198.$$

This formulation for thermal creep is adequate for the temperature range of 500°C-600°C and stress levels ranging from 12.5-50 ksi. Extrapolation to 650°C is questionable and may give a slower creep rate than actually occurs.

The two different types of creep are superimposed to result in total creep. This seems to be a reasonable assumption when compared to the available data. The thermal creep tends to be predominant at higher temperatures and irradiation induced creep can still occur below the thermal creep regime (<500°C).

Fracture Analysis

The canputer code "WISECRACK"[2] was used to perform the fracture analysis of the thin wall section using the stress distributions summarized above. The code utilizes a modified Forman equation, originally proposed by Speidel[8],

$$\frac{da}{dN} = \frac{B\lambda^m[f\Delta K - \Delta K_o]^n}{K_{Ic} - \lambda f \Delta K}$$

where
$\lambda = 1/(1-R)$
$R = K_{min}/K_{MAX}$
$f = E(T_o)/E(T) \quad (\geq 1)$
$K = K_{max} - K_{min}$
K_o = threshhold stress intensity
K_{Ic} = plane-strain fracture toughness

and where
$B = 7.3 \times 10^{-5}$
$m = 1.0$
$n = 1.65$

are constants calculated from test data for HT-9 at 25°C and 600°C[9]. The resulting da/dN behavior is presented in Fig. 1.2.3.

The values of 100 and 9 MPa $\sqrt{m}$ respectively were used for the fracture toughness, K_{Ic}, and the threshold stress intensity factor, K_o. A K_{Ic} of 100 MPa $\sqrt{m}$ is valid for unirradiated material only. It is estimated that irradiation will cause the fracture toughness to decrease to a "lower shelf" value of approximately 60 MPa $\sqrt{m}$. The time required for the toughness to decrease occurs quickly (<1yr) and depends on the neutron fluence and damage. Accordingly it was conservatively assumed that K_{Ic} remained constant at a value of 60 MPa $\sqrt{m}$ from the beginning of life. The effect of a lower K_{Ic} value can be incorporated into the fatigue-crack growth equation either by shifting the whole curve to the left (changing K_{Ic} in the above equation) or simply defining a cutoff point for the unirradiated curve as shown schematically in Figure 1.2.4.

Fatigue crack growth rates of irradiated HT-9 tested at temperatures from 390-600°C in helium show that no apparent change in da/dN vs. ΔK occurs in the lower range of the crack growth rate curve. Some data even indicate that da/dN decreases in this region. It was therefore assumed that the da/dN curves for unirradiated HT-9 at temperatures of interest were valid and probably conservative. The higher growth rates were assumed to be limited by a decrease in toughness and this was estimated to be 60 MPa $\sqrt{m}$.

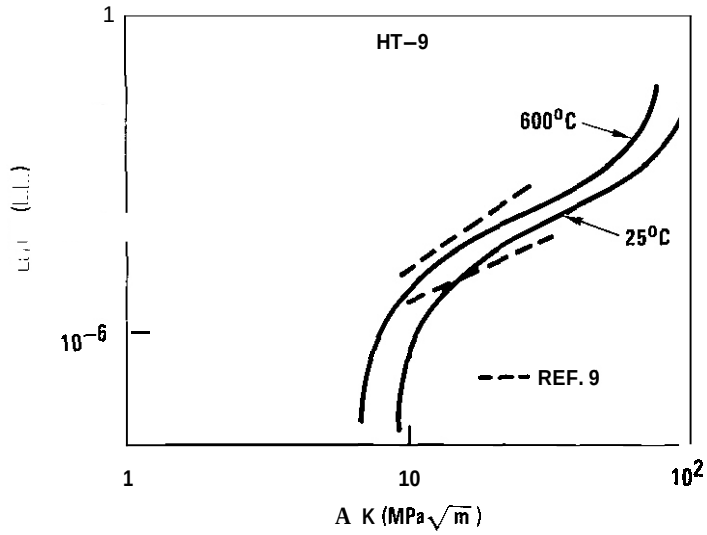

Fig. 1.2.3 Fatlgue crack grath curve for HT-9 plotted fran a modlfled Forman equation using data at 25°C and 600°C (dashed lines) to calculate constants.

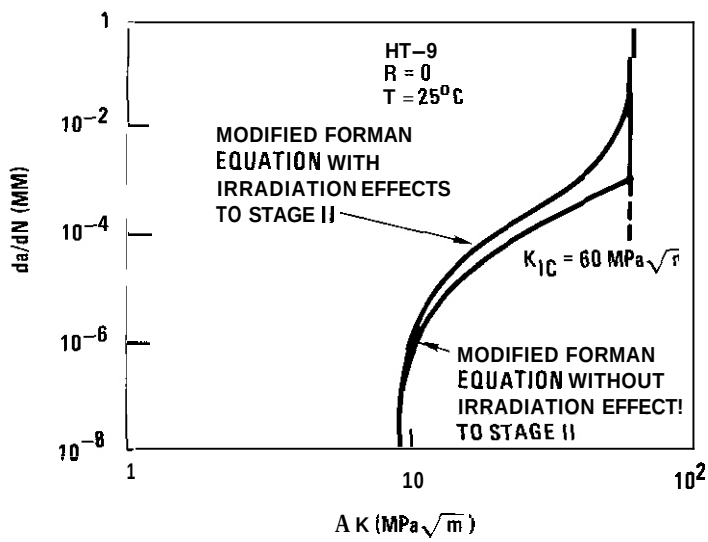

Fig. 1.2.4 Fatigue crack growth rate curve used in thls study Incorporating the lover-shelf K_{Ic} value of 60 MPa $\sqrt{m}$ and irradlation effects on Stage II FCG rate.

1.2.4.3 Results

Stress Results

The steady state stress distrlbutlon experlenced by the first-wall durlng the plasma 'on' state, after stress relaxatlon due to creep is the primary pressure stress. Thls is the condltlon whlch produced the fastest crack growth rates previously analyzed and reported. However, thls stress state is not reached until after a slgnlflcant amount of tlme (calculated to be >0.5 yr). At first, there is an initial shakedown where the outer skin of the first-wall on the plasma slde relaxes very quickly (<25 hrs) due to the thermal creep at 650°C. Then, a steady rate of relaxation occurs, due to Irradlatlon creep taking place throughout the flrst-wall, until the "relaxed stress state" is reached. Thls changing stress condltlon leads to a slower crack growth rate In the flrst few months of llfe because of the Intermedlate stress dlstrlbutlons belng cycled. The stress relaxation occuring In the θ-dlrectlon (most critical) is shan In Fig. 1.2.5. The relaxing distrlbutlons are shown wlth thelr corresponding "off" load values (T = 0) in Flg. 1.2.6.

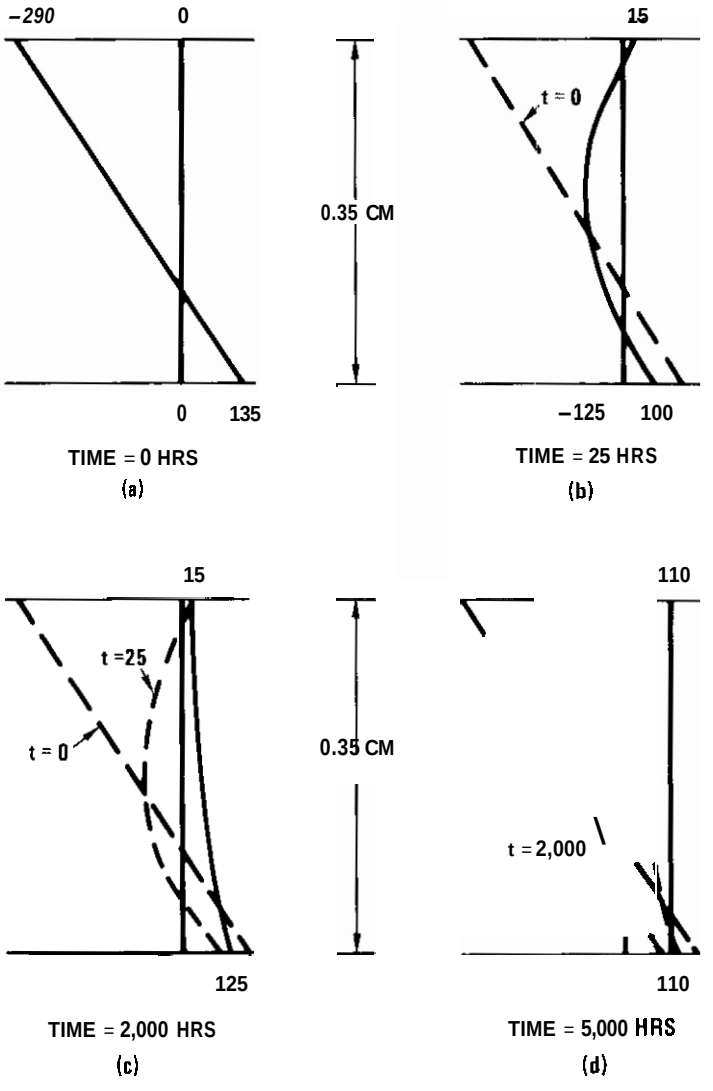

Flg. **1.2.5** 0-stress relaxatlon through the thln sectlon of wall. Stress In unlts of MPa.

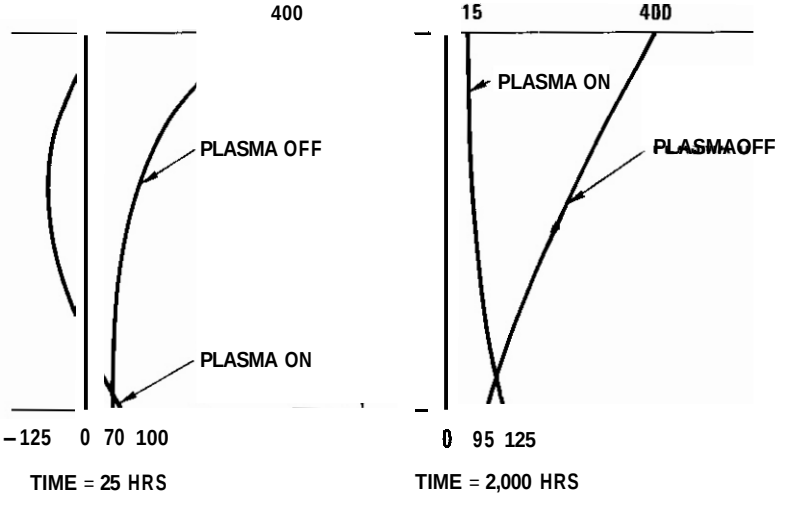

Flg. **1.2.6** 0-stress through the wall at t=25 hrs and t=2000 hrs wlth thelr corresponding off load cycle. Stress In unlts of MPa.

Fracture Results

The fracture analysis for a BOL geanetry has shown that some retardation of the crack grath occurs if the flaw is assumed at the beglnning of life. This is because of the stress relaxatlon occurlng in the first six months of operation producing less severe stress distributions than the completely relaxed case. In addition to the changing stresses, using the da/dN vs ΔK unlrradlated curve wlth a K_{Ic} cutoff of 60 MPa $\sqrt{m}$ ha5 also reduced the predicted crack grath rate. Calculatlons which include the effect of both changing stresses and lower crack grath rates now Indicated that a crack of depth equal to half the wall thlckness (a/t = 1/21 and having a wlde aspect ratio (a/c = 0.2) will propagate to leak-through in about 1.6 years. Thls is a flaw that on the surface would be several mlllimeters long and could be detected by standard NDE techniques. if a less severe flaw is assumed, then leak-through will not occur wlthin the design life of 2 years.

Never in the analysis does K_{max} exceed K_{Ic}. in fact, even a stress distribution equivalent to the yield stress will not glve a K which exceeds K_{Ic} = 60 MPa $\sqrt{m}$. Thls is due to the thin wall geometry which has a constraint condltlon whlch approaches plane-stress. This type of condltlon does not produce extremely high K-values.

1.2.4.4 Conclusions

Crack propagation does not seem a likeiy mode of faliure for a first-wall wlth a two year design life. The only real threat is a surface flaw located on the plasma slde oriented such that it is influenced by the θ-stress. And even then, this large flaw (>5mm on surface) would easily be detected. An eariler calculation showed a much shorter life for the same flaw, but this was due to the bounding load conditions assumed and conservatively uslng the avaliable crack growth behavior data. A more sophisticated tlme-dependent stress analysis shows that the stress dlstributlon during the first six months produces little or no crack growth for any glven flaw. Further revlew of crack growth data suggests that the prior anaiysls was also too conservative for crack growth rates in irradiated material. The analysis presented in this report uses a slightly lower growth rate but maintains a relatlvely low fracture toughness. The greatest K-value calculated In the analysis was 50 MPa $\sqrt{m}$ which is less than (but close to) the assumed K_{Ic} = 60 MPa $\sqrt{m}$. This minimum value for K_{Ic} is conservative and therefore, only faliure due to propagation to leak-through will occur; there will be no catastrophic brittle failure.

Creep crack growth wa5 assumed negilglble since the high temperature reglon, where creep exists, is in the outer half of the wall (plasma side) and only small tensile loads are experienced. Therefore, no crack grath is expected for such low stresses (and small creep zones). Little is known about the influence of irradiation Induced creep on crack growth. But if it behaves slmilarlly to thermal creep, the low stress condltlon would cause no crack growth.

1.2.4.5 Future Work

The effects of changes In materials parameters will be Investlgated. Thls includes changes in toughness and fatlgue crack growth rates. This information will be used to determine quality control requirements for non-destructive evaluation.

1.2.4.6 References

1. M. Abdou, et al, "Blanket Canparison Selection Study", Argonne Natlonai Laboratory report ANL/FPP-83-1, Oct. 1983.

2. R. D. Watson and W. G. Wolfer, "WISECRACK - A Fracture Mechanics Code for Lifetlme Analysis of High Heat Components In Fuslon Reactors", University of Wisconsin Report UWFDM-440 (1981).

3. C. Charman and F. Tzung, "TEPC-2D - A Two-Dlmenslonal Finite Element Computer Program for Thermal-Elastlc-Plastlc-Creep Analysis", GA Technologies, GA-A12753 (1973).

4. Private Discussions with R H. Ryder, GA Technologies, June 1984.

5. D. S. Geiles and R. J. Pulgh, "Evaluation of Ferrltlc Alloy Fe-2-1/4Cr-1Mo after Neutron irradiation-Irradiation Creep and Swelling", Toplcai Conference on Ferritic Alloys for Use in Nuclear Energy Technology. ed. J. Davis and J. Michei, AIME, New York, N.Y. 1984.

6. R. J. Puigh, "In-Reactor Creep of Selected Ferrltlc Alloys", International Conference on Irradlation Effects, ASTM, Williamsburg, VA, June 1984.

7. R. S. Amodeo and N. M Ghoniem, Constltutlve Design Equations for Thermal Creep Deformation for HT-9, Third Topical Meeting on Fusion Reactor Albuquerque, NM, September (1983).

8. M. O. Speldel, "Fatlgue Crack Growth at Hlgh Tempreatures", Proceedings of the Symposium on Hlgh-Temperature Materials In Gas Turbines, ed. P. R. Sahm and M. O. Speldel, Baden, Swltzerland (1973).

9. F. H. Huang. D. A. Mervyn and D. T. Peterson, "Mlcrostructural and Fatlgue Crack Growth Characterlzatlon of til-9". Hanford Englneerlng Development Laboratory, ADlP Semlannual Progress Report DOE-ER0045 17, Dec. 1981.

2.1 NEUTRON SOURCE CHARACTERIZATION FOR MATERIALS EXPERIMENTS - L. R. Greenwood (Argonne National Laboratory)

2.1.1 ADIP/DAFS Tasks

ADIP - Task I.A.2 - Define Test Matrices and Procedures
DAFS - Task II.A.1 - Fission Reactor Dosimetry

2.1.2 Objective

To characterize neutron irradiation facilities in terms of neutron flux, spectra, and damage parameters (dpa, gas production, transmutation) and to measure these exposure parameters during fusion materials irradiations.

2.1.3 *Summary*

Dosimetry measurements and calculations have been completed for the CTR 39-45 and T1 irradiations in HFIR. Neutron flux and damage rates are quite similar to previous results in the PTP position.

2.1.4 Progress and Status

The status of all other experiments is summarized in Table 2.1.1.

Table 2.1.1. Status of Dosimetry Experiments

	Facility/Experiment	Status/Comments
ORR	- MFE 1	Completed 12/79
	- MFE 2	Completed 06/81
	- MFE 4A1	Completed 12/81
	- MFE 4A2	Completed 11/82
	- MFE 4B	Completed 04/84
	- TRC 07	Completed 07/80
	- TRIO-Test	Completed 07/82
	- TRIO-1	Completed 12/83
	- Hf Test	Completed 03/84
	- JP Test	Samples Sent 06/84
HFIR	- CTR 32	Completed 04/82
	- CTR 31, 34, 35	Completed 04/83
	- T2, RB1	Completed 09/83
	- T1, CTR 39	Completed 01/84
	- CTR 40-45	Completed 09/84
	- 30, 36, 46	Samples Received 11/84
	- RB2, T3	Samples Received 11/84
	- CTR 47-52	Irradiations in Progress
	- JP 1-8	Irradiations in Progress
Omega West	- Spectral Analysis	Completed 10/80
	- HEDL1	Completed 05/81
	- HEDL2	Samples Sent 05/83
	- LANL 1	Completed 08/84
EKR II	- X287	Completed 09/81
IPNS	- Spectral Analysis	Completed 01/82
	- LANL1 (Hurley)	Completed 06/82
	- Hurley	Completed 02/83
	- Coltman	Completed 08/83

2.1.4.1 The T1 and CTR 39 Experiments in HFIR

Measurements and calculations have been completed for the T1 and CTR 39 irradiatins in the High Flux isotopes Reactor (HFIR) at Oak Ridge National Laboratory. Both experiments were designed to study ferritic steels and consisted of tensile and fatigue specimens. The irradiation histories are, as follows:

Experiment	Reactor Position	Dates	Exposure, MWD
CTR 39	PTP	6/82 - 10/82	13,004
T I	Target	2/81 - 8/82	32,272

Dosimeters were located at two heights in T I and three heights in the CTR 39 subassembly. The T1 capsules contained Ni, Cu, Co-Al, Mn-Cu, Nb, Ti, Fe, and Zr dosimeter wires while the CTR 39 capsules contained only Fe, Ti, Mn-Cu, and Co-A1 dosimeters.

The measured activation rates are listed in Table 2.1.2. When the present values were compared to previous values[1] measured in similar locations in HFIR, it was apparent that the $^{54}Fe(n,p)^{54}Mn$ and $^{55}Mn(n,2n)^{54}Mn$ reaction rates showed much more scatter (15-20%) than expected. This can be easily explained by the uncertainty in the burnup corrections for ^{54}Mn since the thermal cross section is not well known.

Table 2.1.2. Activity Rates Measured in HFIR-T1, CTR 39
(Values normalized to 100 MW; corrected for burnup)

Reaction	Activity Rate, atom/atom-s		
T1 Experiment:	Height, cm:	7.22	16.95
$^{58}Fe(n,\gamma)^{59}Fe$	(10-9)	2.26	1.82
$^{59}Co(n,\gamma)^{60}Co$	(10-8)	--	*6.03*
$^{54}Fe(n,p)^{54}Mn$	(10-11)	5.58	4.36
$^{46}Ti(n,p)^{46}Sc$	(10-12)	--	6.36
$^{55}Mn(n,2n)^{54}Mn$	(10-13)	1.59	1.35
$^{63}Cu(n,\alpha)^{60}Co$	(10-13)	--	2.99
CTR 39 Exoeriment:		2.00	10.89 19.78
$^{58}Fe(n,\gamma)^{59}Fe$	(10-9)	2.10	1.84 1.30
$^{59}Co(n,\gamma)^{60}Co$	(10-8)	7.54	6.57 4.57
$^{54}Fe(n,p)^{54}Mn$	(10-11)	*7.36*	6.55 4.68
$^{55}Mn(n,2n)^{54}Mn$	(10-13)	2.14	1.95 1.42

ENDF/B-IV[2] listed the ^{54}Mn thermal cross section as <10b. The newly released ENDF/B-V[3] value is ~38b. If we compare reaction rates measured in similar positions over various exposure times (6000 - 30000 MWD), then both reactions show reasonably good agreement (5-10%) using a ^{54}Mn thermal cross section of about 10b. Consequently, we have adopted this value for the present data. Unfortunately, this means that all previous $^{54}Fe(n,p)$ and $^{55}Mn(n,2n)$ rates should be revised: however, the corrections, which scale with the exposure, are less than 10% in all cases. Since these reactions are not the only ones used to determine fluences and damage parameters, these data should have changes of less than 5%. Data from future irradiations in HFIR will help us to further refine our estimate of the ^{54}Mn thermal cross section and all data will be revised as necessary.

The present gradient data is well-described by a quadratic polynomial and the coefficients are listed in Table 2.1.3. Using this function and the midplane values, users can readily determine fluence or damage rates at any point in the subassembly. Of course, helium production in nickel is not so easily determined and the helium and dpa rates are listed separately in Table 2.1.4. A more complete description of helium measurements and calculations was presented at the Albuquerque meeting.4

Table 2.1.3. Neutron Fluence and Damage Parameters for HFIR-T1, CTR 39
Values are listed at midplane; gradients are described
by $f = a(1 + bz + cz^2)$ where b = 1.95 x 10-4, c = -9.75 x 10^{-4}

Neutron Fluence, x 10^{22} n/cm^2	T1	CTR39
Total	14.74	5.92
Thermal (<.5 eV)[a]	1.00	2.47
Fast (>.11 MeV)	3.37	1.54

	T1		CTR 39	
Element	OPA	He, appm	DPA	He, appm
Al	43.85	19.41	20.23	9.86
Ti	27.84	13.37	12.88	6.58
V	31.25	0.67	14.41	0.33
Cr	27.37	4.49	12.71	2.26
Mn[b]	30.80	3.93	14.01	2.00
Fe	24.12	7.89	11.25	4.02
Co[b]	32.42	3.89	14.22	1.98
Ni[c] Fast	26.23	104.68	12.10	53.32
Ni[c] ^{59}Ni	30.82	17476.	8.23	4668.
Ni[c] Total	57.05	17581.	20.33	4721.
Cu	23.67	7.05	10.97	3.58
Nb	23.35	1.44	10.86	0.74
Mo	17.47	--	8.08	--
316 SS[d]	28.94	2291.	12.66	617.

[a] The 2200 m/s thermal flux is equal to 0.866 times the value listed.

[b] Thermal self-shielding must be considered for (n,γ) damage.

[c] See Table 2.1.4 for Ni gradients.

[d] 316 SS: Fe(0.645), Ni(0.13), Cr(0.18), Mn(0.019), Mo(0.026).

Table 2.1.4. Helium and OPA Gradients for Nickel in HFIR-T2, RB1
Helium values include ^{59}Ni and fast reactions
DPA values include extra thermal effect (He/567)
Gradients are very nearly symmetric about midplane

	T1		CTR 39	
Heiaht. cm	He. appm	DPA	He, appm	OPA
0	17,581	57.1	4,721	20.3
3	17,429	56.6	4,666	20.1
6	16,932	55.0	4,487	19.5
9	16.105	52.4	4,192	18.5
12	14,915	48.8	3,781	17.0
15	13,372	44.0	3,268	15.2
18	11,439	38.1	2,660	13.0
21	9,113	31.0	1,984	10.4
24	6,437	22.9	1,284	7.6

2.1.4.2 The CTR 40-45 Experiments in HFIR

Dosimetry measurements and damage calculations have been completed for six irradiations labeled CTR 40-45 in the peripheral target position (PTP) of HFIR. The exposure histories are, as follows:

Experiment	Dates	Exposure, MWD
40	7/18/82 to 12/12/82	13,172
41	8/10/82 to 1/5/83	13,208
42, 43	10/25/82 to 6/18/83	21,604
44, 45	1/30/82 to 5/27/83	10,655

Table 2.1.6. Neutron Fluence and Damage Parameters for HFIR-PTP
Values are listed at midplane; gradients are described by
$f = a(1+bz+cz^2)$ where $b = 1.95 \times 10^{-4}$ and $c = -9.75 \times 10^{-4}$

Energy	CTR40/41	CTR42/43		CTR44/45	
	Neutron Fluence, x 1022 n/cm2:				
Total	5.87	9.45		4.72	
Thermal (<.5 eV)[a]	2.45	3.94		1.98	
0.5 eV - 0.1 MeV	1.89	3.04		1.52	
>.1 MeV	1.53	2.46		1.23	
	DPA	He	DPA	He	DPA	He
Al	20.2	9.86	32.3	15.7	16.1	7.87
Ti	12.8	6.58	20.5	10.5	10.3	5.25
V	14.4	0.33	23.0	0.53	11.5	0.26
Cr	12.7	2.27	20.3	3.61	10.1	1.81
Mn[b]	14.0	2.00	22.4	3.18	11.2	1.59
Fe	11.2	4.02	17.9	6.41	9.0	3.21
Co[b]	14.2	1.98	22.7	3.15	11.3	1.58
Ni[c] Fast	12.1	53.33	19.3	84.9	9.6	42.53
^{59}Ni	8.0	4532	15.5	8789	5.7	3253
Total	20.1	4585	34.8	8874	15.3	3296
cu	10.9	3.58	17.5	5.72	8.7	2.86
Nb	10.8	0.73	17.3	1.17	8.7	0.59
Mo	8.1	--	12.9	--	6.4	--
316 ss[d]	12.6	599.0	20.5	1158.0	10.0	431.0

[a]The thermal fluence is equal to 1.15 times the 2200 m/s value
[b]Thermal self-shielding may lower damage rates
[c]See Table 2.1.7 for nickel gradients
[d]316 ss: Fe(0.645), Ni(0.13), Cr(0.18), Mn(0.019), Mo(0.026)

Table 2.1.7. Nickel Helium and DPA Gradients for HFIR
(He(appm) and DPA include thermal and fast effects)

	CTR40-41		CTR42-43		CTR44-45	
Height, cm	He	DPA	He	DPA	He	OPA
0	4585	20.1	8874	34.8	3296	15.3
3	4532	19.9	8782	34.4	3255	15.1
6	4357	19.3	8483	33.4	3123	14.7
9	4070	18.3	7989	31.8	2908	14.0
12	3669	16.6	7290	29.3	2609	12.8
15	3170	15.0	6402	26.3	2239	11.4
18	2579	12.8	5321	22.6	1806	9.7
21	1921	10.2	4077	18.2	1331	7.8
24	1242	7.5	2731	13.2	850	5.8

2.1.5 Conclusions

The present results are quite similar to those measured previously in HFIR. Dosimeters have been received from the CTR 30, 36, 46, T3, and RB2 experiments and analysis is now in progress. New dosimeters have been prepared and sent to ORNL for further irradiations in HFIR.

2.1.6 References

1. L. R. Greenwood, Neutron Source Characterization for Materials Experiments, Alloy Development for Irradiation Performance, Semi-Annual Progress Report, DOE/ER-0045/11, September 1983.

2. S. F. Mughabghab and D. I. Gerber, Neutron Cross Sections, Resonance Parameters, BNL325, Third Edition, Volume I, Brookhaven National Laboratory, June 1973.

3. S. F. Mughabghab, M. Divadeenam, N. E. Holden, Neutron Cross Sections, Neutron Resonance Parameters and Thermal Cross Sections, Volume I, Part A: Z = 1-60, Academic Press, New York, 1981.

4. L. R. Greenwood, D. W. Kneff, R. P. Skowronski, and F. M. Mann, A Canparison of Measured and Calculated Helium Production in Nickel Using Newley Evaluated Neutron Cross Sections for ^{59}Ni, J. Nucl. Mater. 122, 1002-1010 (1984).

5. L. R. Greenwood, A New Calculation of Thermal Neutron Damage and Helium Production in Nickel, J. Nucl. Mater. 115, 137-142 ***(1983).***

2.1.7 Publications

See references **4** and **5.**

2.2 NEUTRONICS CALCULATIONS IN SUPPORT OF THE ORR-MFE-4A AND -46 SPECTRAL TAILORING EXPERIMENTS – R. A. Lillie (Oak Ridge National Laboratory)

2.2.1 ADIP Task

ADIP Task 1.A.2, Define Test Matrices and Test Procedures.

2.2.2 Objective

The objective of this work is to provide the neutronic design for materials irradiation experiments in the Oak Ridge Research Reactor (ORR). Spectral tailoring to control the fast and thermal fluxes is required to provide the desired displacement and helium production rates in alloys containing nickel.

2.2.3 *Summary*

The calculated fluences from the ongoing three-dimensional neutronics calculations are being scaled to agree with experimental data. As of September 30, 1984. this treatment yields 176.2 at. ppm He (not including 2.0 at. ppm He from ^{10}B) and 11.90 dpa for type 316 stainless steel in ORR-MFE-4A and 133.0 at. ppm He and 9.13 dpa in ORR-MFE-4B.

2.2.4 Progress and Status

The operating and current calculated data based on the fluence scaling factors' are summarized in Table 2.2.1 for the ORR-MFE-4A and -45 experiments.

The real-time projections of the helium-to-displacement ratios based on current calculated data as of September 30, 1984, are presented in Figs. 2.2.1 and 2.2.2 for the ORR-MFE-4A and -48 experiments, respectively. The projected dates were obtained assuming an ORR duty factor of 0.86. As noted, the solid aluminum corepieces were inserted in the ORR-MFE-4A experiment on December 7, 1982, and in the ORR-MFE-45 experiment on August 5, 1983. The 1.0-rnm-thick hafnium corepiece was inserted in the ORR-MFE-4A experiment on May 1, 1984. The target date for insertion in the ORR-MFE-4B experiment is currently projected for December 20, 1984.

The only changes between the current projected helium-to-displacement ratios and those previously reported' occur after the insertion of the 1.0-mm hafnium corepieces.

Table 2.2.1 Operating and calculated data for experiments ORR-MFE-4A and -46 as of September 30, 1984

	ORR-MFE-4A	ORR-MFE-4B
Power (MWh)	709,920	566,640
Equivalent full-power days[a]	986	7a7
Thermal fluence (neutrons/m^2)	1.38×10^{26}	1.15×10^{26}
Total fluence (neutrons/m^2)	4.99×10^{26}	3.85×10^{26}
He (at. ppm)[b]	1.76.2	133.0
dpa[b]	11.90	9.13

'Full power for GRR is 30 MW.

'Helium and dpa values are far type 316 stainless steel.

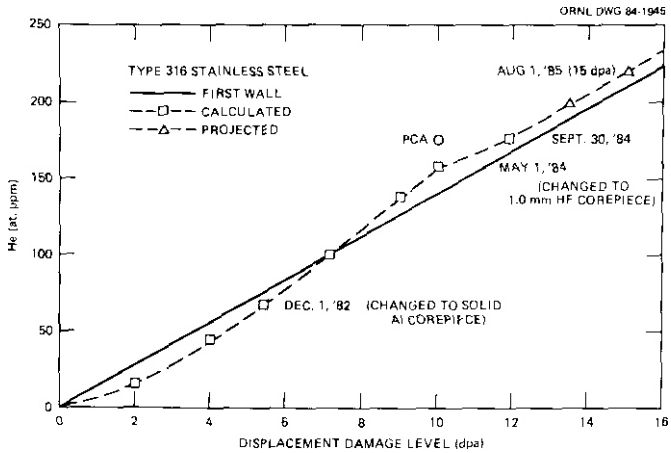

Fig. 2.2.1. Current and projected helium and displacement damage levels in the ORR-MFE-4A experiment.

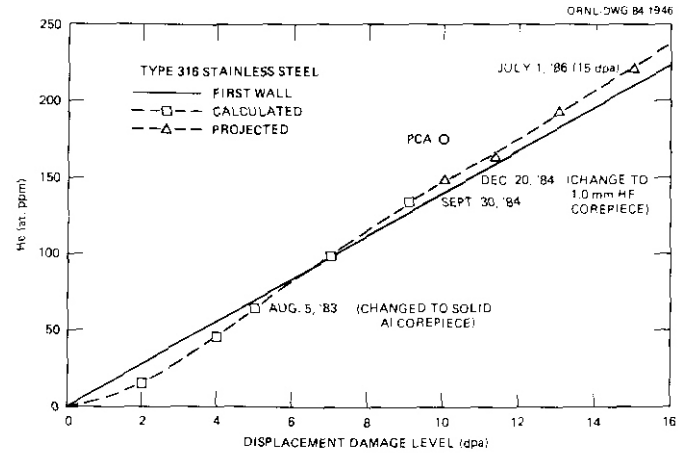

Fig. 2.2.2. Current and projected helium and displacement damage levels in the ORR-MFE-4B experiment.

These changes result because of the difference between the calculated flux changes due to the insertion of the Hf and the measured changes[2] obtained from the dosimetry measurements made during February 1984. For a 1.0-mm-thick hafnium sleeve, neutronics calculations predicted a reduction of 57% in the thermal flux and 28% in the displacements per atom (dpa) and helium production. The dosimetry measurements yielded 40% and 20%, respectively. Thus, the current hafnium corepiece is not performing at the level predicted by the neutronics calculations.

At the present time, i.e., until 15 dpa is reached, the loss of thermal flux reduction and subsequent increased two-step helium production will not greatly affect either experiment. In the MFE-4A specimens, the helium-to-displacement ratio was approximately 9.5% above the first wall ratio when the hafnium corepiece was inserted at 10.4 dpa. At 15 dpa, this ratio will be only 8.3% above the first wall ratio. After 15 dpa, the helium-to-displacement ratio will slowly creep up away from the first wall ratio. In the MFE-4B specimens, a similar effect will take place with the ratio being approximately 6% above the first-wall ratio at 15 dpa. However, at or near 15 dpa, both hafnium sleeves will have to be replaced because of burnup.

The reason that the hafnium corepiece is not performing as well as predicted by the neutronics calculations is most likely due to the size of the hafnium sleeves. In the original plan, hafnium sleeves extending beyond the active fuel region, i.e., greater than 24 in. long, were analyzed using one-dimensional transport methods. Because of hafnium availability and cost, the sleeve employed in the MFE-4A corepiece and the sleeve intended for use in the MFE-48 corepiece are only 12-in. long, i.e., just long enough to shield the experimental region. This length eliminates thermal neutrons entering the specimen region from the side but does nothing to stop thermal neutrons entering from the top or bottom. However, to be certain that the length is the cause of the loss of thermal flux reduction, a two-dimensional transport model which can take into account the finite lengths of the sleeves is being constructed. Data generated using this model for both the original full-length sleeve and the in-use 12-in. sleeve should be available in the next few months. These data should allow the selection of a proper thickness for the shorter sleeves which will be needed at 15 dpa.

2.2.5 Future Work

The three-dimensional neutronics calculations that monitor the radiation environment in the ORR-MFE-4A and -4B experiments will continue with each ORR cycle. The scale factors used to scale the fluences obtained from these calculations will be updated as new experimental data become available.

2.2.6 References

1. R. A. Lillie and T. A. Gabriel, "Neutronics Calculations in Support of the ORR-MFE-4A and -48 Spectral Tailoring Experiments," *ADIP Semiannu. Prog. Rep. Mar. 31, 1984,* DOE/ER-0045/12, pp. 22–23.

2. L. R. Greenwood and R. K. Smither, "Neutron Source Characterization for Materials Experiments," *ADIP Semiannu. Prog. Rep. Mar. 31, 1984*, DOE/ER-0045/12, pp. 13–21.

7.3 OPERATION OF THE ORR SPCCTRAL TAILORING EXPERIMENTS (ORR-MFE-4A AND ORR-MFE-4B) - J. A. Conlin and I. T. Dudley (Oak Ridge National Laboratory)

2.3.1 ADIP Task

ADIP Task I.A.2, Define Test Matrices and Test Procedures.

2.3.2 Objectives

Experiinents ORR-MFE-4A and -4B, which irradiate austenitic stainless Steel, use neutron spectral tailoring to achieve the same helium-to-displacement-per-atom(He/dpa) ratio as predicted for fusion reactor first-wall service. Experiment ORR-MFE-4A contains mainly type 316 stainless steel and Path A Prime Candidate Alloy (PCA) at irradiation temperatures of 330 to 400°C. Experiment ORR-MFE-4E contains similar materials at irradiation temperatures of 500 and 600°C.

2.3.3 *Summary*

The specimens contained in the ORR-MFE-4A experiment have operated for an equivalent of 986 d at 30 MW reactor power, with temperatures of 400 and 330°C. The specimens contained in the ORR-MFE-4B experiment have operated for an equivalent of 787 d at 30 MW reactor power, with temperatures of 500 and 600°C.

2.3.4 Progress and Status

The details of the Oak Ridge Research Reactor (ORR) Spectral Tailoring Experiments have been described previously.[1-8]

The hafnium sleeve for neutron spectral tailoring of the ORR-MFE-4A experiment was installed on April 26, 1984. Displacement damage level of the specimens in the capsule was approximately 10 dpa at that time. The hafnium sleeve was made from a sheet of hafnium 1.04 mm (0.041 in.) thick which was rolled into a cylindrical shape 50.8 mm (2.0 in.) diameter by 311.2 mm (12.25 in.) long and seam welded. The sleeve was fitted into an aluminum corepiece assembly having the external shape of an ORR fuel element. The ORR-MFE-4A experiment was removed from the ORR core position E-3 and the special solid aluminum corepiece was replaced with the corepiece containing the hafnium sleeve. The experiment was then reinstalled.

Measurements reported previously' indicate a reduction of less than 10% in the gamma heat rate could be expected due to the hafnium sleeve installation. Following the hafnium sleeve installation, the range of temperatcre control of the capsule proved to be sufficient to maintain the specified test temperature with the reduced gamma heating. The experiment operation has since been routine.

During this reporting period, there have been no thermocouple failures. Through September 30, 1984, the ORR-MFE-4A experiment specimens have accumulated an equivalent of 986 d at 30 MW reactor power with specimen temperatures of 400 and 330°C.

The ORR-MFE-4B experiment continues to operate. The operation has been routine during this period except for the failure of thermocouple TE-1. Failure of that thermocouple occurred on September 3, 1984 during a reactor startup. We have since used TE-2 as a reference for temperature control purposes.

The specimens contained in this experiment are expected to reach a displacement damage level of 10 dpa near the end of December 1984. At that time a hafnium sleeve similar to the ane used in the ORR-MFE-4A experiment will be installed for neutron spectral tailoring purposes.

Through September 30, 1984, the ORR-MFE-4B experiinent specimens have accumulated an equivalent of 787 d at 30 MW reactor power with temperatures of 500 and 600°C.

7.3.5 References

1. K. R. Thorns and M. L. Grossbeck, "Operation of the ORR Spectral Tailoring Experiment ORR-MFE-4A," pp. 20–24 in *ADIP Quart. Prog. Rep. Sept.* 30, *1980*, DOE/ER-0045/4, U.S. DOE, Office of Fusion Energy.

2. K. R. Thorns, "Operation of the ORR Spectral Tailoring Experiment ORR-MFE-4A," pp. 18–21 in *ADIP Quart. Prog. Rep. Mar. 31, 1981*, DOE/ER-0045/6, U.S. DOE, Office of Fusion Energy.

3. I. T. Dudley, "Operation of the ORR Spectral Tailoring Experiments ORR-MFE-4A and ORR-MFE-4B," pp. 24–79 in *ADIP Semmiannu. Prog. Rep. Sept. 30, 1981*, DOE/ER-0045/7, U.S. DOE, Office of Fusion Energy.

4. I. T. Dudley and J. A Conlin, "Operation of the ORR Spectral Tailoring Experiments ORR-MFE-4A and ORR-MFE-4B," pp. 10–12 in *ADIP Semiannu. bog. Rep. Mar.* 31, *1982*, DOE/ER-0045/8, U.S. DOE, Office of Fusion Energy.

5. J. A. Conlin, I. T. Dudley, and E. M. Lees, "Operation of the ORR Spectral Tailoring Experiments ORR-MFE-4A and ORR-MFE-4B," pp. 17-20 in *ADIP Semiannu. Prog. Rep. Sept. 30, 1982*, DOE/ER-0045/9, U.S. DOE, Office of Fusion Energy.

6. J. A Conlin, I. T. Dudley, and E. M. lees, "Operation of the ORR Spectral Tailoring Experiments ORR-MFE-4A and ORR-MFE-4B," pp. 71-22 in *ADIP Semiannu.* Frog. *Rep. March* 31, 1983, DOE/ER-0045/10, U.S. DOE, Office of Fusion Energy.

7. J. A. Conlin, I. T. Dudley, and E. M Lees, "Operation of the ORR Spectral Tailoring Experiments ORR-MFE-4A and ORR-MFE-40," pp. 40-41 in *ADIP Semiannu. Prog. Rep. Sept. 30, 1983,* DOE/ER-0045/11, U.S. OOE, Office of Fusion Energy.

8. J. A. Conlin, I. T. Dudley, and E. M. lees, "Operation of the ORR Spectral Tailoring Experiments ORR-MFE-4A and ORR-MFE-4B," pp. 24-75 in *ADIP Semiannu. Frog. Rep. Mar.* 31, *1981*, DOE/ER-0045/12, U.S. DOE, Office of Fusion Energy.

2.4 FFTF FUSION IRRADIATIONS - FFTF CYCLES 4-6 - A. M. Ermi (Westinghouse Hanford Company)

2.4.1 ADIP Task

ADIP Task I.A.2, Define Test Matrices and Test Procedures

2.4.2 Objectives

The objective of the FFTF Fusion Irradiations is to provide high fluence data (>100 dpa) at several temperatures for alloys of interest to the ADIP and DAFS programs. The experiment is designed to investigate the effects of radiation on tensile properties, fracture toughness, fatigue crack growth, creep, swelling behavior and microstructure.

2.4.3 Summary

Specimens were prepared and loaded into three in-core canisters of the Materials Open Test Assembly (MOTA) for irradiation during FFTF cycle 4 (January-April 1984). Irradiations were conducted at 407°C (6-11 dpa), 518°C (14-16 dpa) and 595°C (14-16 dpa). Alloys emphasized in this initial irradiation were the Path E ferritic alloys HT-9 and 9Cr-1Mo, and the Path C vanadium alloys.

These specimens were either discharged or reinserted into new MOTA hardware for irradiation during FFTF cycles 5-6 (June 1984-June 1985). New specimens were also included, and additional irradiation volume both in-core and below-core was available for an expanded test matrix. Irradiations are currently underway during cycles 5-6 at 365°C (below-core: 4-7 dpa), at 425, 520 and 600°C (all 25-28 dpa) and 600°C (8-14 dpa). Additional emphasis on low activation alloys was given for this irradiation. Specimens in the peak flux positions during cycles 4-6 will accumulate approximately 45 dpa.

2.4.4 Progress and Status

2.4.4.1 Introduction

The effects of neutron irradiation on the mechanical properties and behavior of fusion reactor candidate alloys need to be characterized over the range of damage levels expected in a fusion reactor environment. In the absences of a device which can simulate that environment, experimenters must rely on existing irradiation facilities to obtain irradiation effects information on fusion reactor alloys. By using clever experiment designs and alloy preparations and taking advantage of inherent facility characteristics, many of the imoortant damage parameters (such as helium level. disolacements oer atom (dpa) and transmutation products) can be investigated.

Until recently, irradiations in support of the ADIP program have been carried out almost exclusively in the two mixed-soectrum reactors at ORNL the High Flux Isotooe Reactor (HFIR) and the Oak Ridge Research Reactor (ORR), and in the fast-spectrum reactor at ANL-West, the Experimental Breeder Reactor II (EBR-II). This report will describe the ongoing irradiations which are currently being conducted at WHC in the Fast Flux Test Facility (FFTF).

2.4.4.2 Description of Test Vehicle and Facility

The FFTF is a 400 MWt, sodium-cooled, low-pressure, high temperature, fast neutron flux reactor which was designed specifically for irradiation testing of fuels and materials for liquid metal fast breeder reactors. The active core is 91.4 cm (36 in.) in length and contains positions for up to eight independently instrumented assemblies. The reactor vessel inlet temperature is 360°C, and the outlet temperature is 525°C. A summary description of the FFTF is given in Reference 1.

The Materials Open Test Assembly (MOTA) is a highly instrumented assembly which has the capability to monitor and control temperatures of specimen canisters during irradiation. The MOTA test train, which occupies the lower portion of the 12.2 m (40 ft.) assembly, contains 30 in-core specimen canisters and one larger below-core canister (equivalent in specimen volume to 7 in-core canisters). Each in-core canister is 29 cm (7.5 in.) long, 3.36 cm (1.325 in.) in diameter and contains approximately 80 cc of specimen volume. The MOTA test train and details of a temperature-controlled canister are illustrated in Figure 2.4.1.

Typically, 80% of the in-core canisters are temperature-controlled, using a mixture of argon and helium to vary the thermal conductivity across an annulus. These canisters are operated at a variety of temperatures, depending on the annulus size, location in the core, and the mass loading. The current range of operation is 485 to 750°C, with a control band of ±5°C.

The belaw-care canister and the remaining 20% of the in-core canisters are "weepers" and operate slightly above the coolant ambient temperature (365°C below-core, and 435°C at the top of the core in MOTA level 5).

The FFTF fuel cycle is nominally 100 full power days with about a 2-month shutdown between cycles. During the shutdown, specimens from MOTA are removed (and measured as is the case for creep tubes) and reinserted into new MOTA hardware with new specimens. This hardware is then placed into a new MOTA assembly for continued irradiation in the next cycle. Although specimens from MOTA were removed after

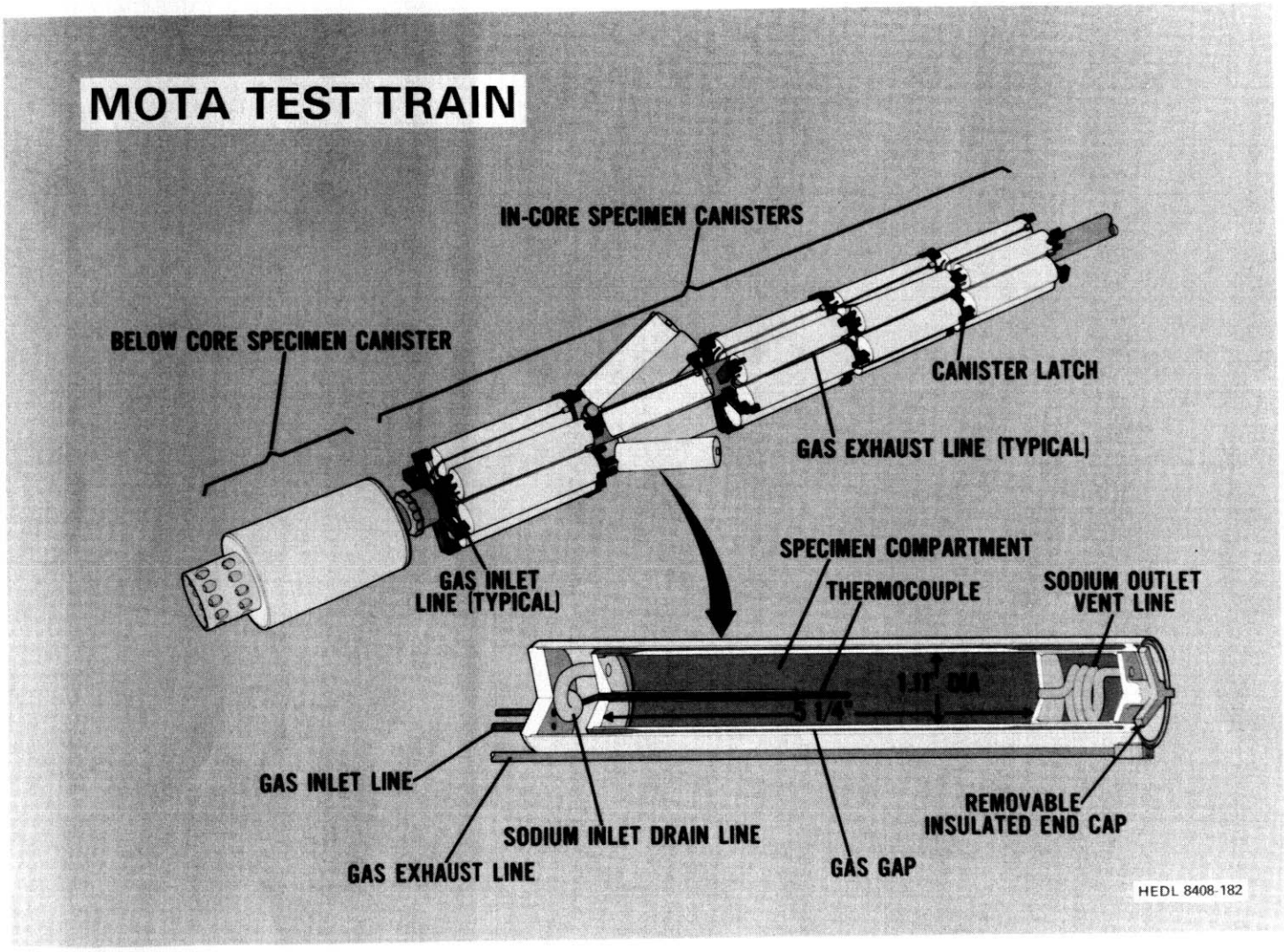

Fig. 2.4.1. MOTA test train and details of a temperature-controlled canister.

FFTF cycle 4 after undergoing irradiation for only one cycle, future plans are to remove MOTA after every two cycles or once per year. The flux and fluence values which can be expected in typical MOTA irradiations are given in Table 2.4.1.

2.4.4.3 Materials Processing and Specimen Preparation

This section describes the materials and final processing treatments used for specimens included in the FFTF cycle 4 and cycles 5-6 irradiations, excluding TEM discs. (The large numbers of discs makes it inappropriate to detail every material-treatment combination in this reports. Individual experimenters supplying TEM discs are responsible for reporting on their own specimens.)

Tables 2.4.2 through 2.4.5 list the chemical compositions of the materials used to fabricate the mechanical properties specimens. The HT-9 and Hi-9 welded plats? were supplied by G. A. Technologies, and the 9Cr-1Mo, 2-1/4Cr-1Mo, vanadium alloys and austenitic alloys were supplied by ORNL. The sources of the low activation and Mn stabilized alloys are included in Table 2.4.4.

A variety of specimen types and geometries were included in the initial irradiations. Table 2.4.6 lists the specimens and principal dimensions along with the institution which supplied that type of specimen.

The final thermal-mechanical-treatments and identification codes for the specimens (excluding TEM discs) are outlined in Tables 2.4.7 through 2.4.10. Final ASTM grain size and DPH hardness values are also included when available.

Specimen preparation for Vanadium alloys

The vanadium alloys portion of the experiment required special preparation during all phases of the experiment. Since it was of interest to investigate the effects of both dpa and helium on the tensile properties and microstructure, a technique was used at ORNL to dope the specimens with helium before irradiating them in the FFTF. Detail of the modified tritium trick used to accomplish this have been previously reported by Braski, et al.[3]

A prime concern when irradiating the vanadium alloys was the possibility of contamination of the specimens by impurities (namely carbon, oxygen and nitrogen) from the surrounding hardware and environment during the irradiation. To minimize this contamination, it: was decided that: (1) the specimens should be separated from the flowing reactor sodium, a source of infinite amounts of oxygen and nitrogen, and (2) the separating medium must not itself be a source of impurities, such as carbon in a stainless steel. Since any subcapsule design would also have to be filled with a liquid metal for thermal bonding, the final constraint was that the subcapsule material had to be compatible with the vanadiumlliquid metal system and also withstand the flowing reactor sodium.

Lithium was selected over sodium as the thermal bonding medium as a result of interest in it as a coolantlbreeder in some fusion device designs, and also because of its higher affinity for oxygen compared to vanadium. TZM was selected as the subcapsule material, being compatible with sodium and lithium, with minimal carbon available for mass transfer to the vanadium.

Enriched 99.99% ^{7}Li had to be used since the 7.5% ^{6}Li present in natural lithium would result in a prohibitive build-up of pressure during irradiation from helium formation and also result in an unacceptable level of activity due to the formation of tritium. The enriched ^{7}Li was supplied by ORNL (two shipments totaling 1500 gms), with final purification done at Westinghouse Hanford Company (WHC) using the following procedure:

(1) Working in an argon atmosphere glove box, melt the dry ingot (200-500 gms) in a stainless steel beaker, and heat to 200°C.

(2) Skim off the 5-10 gms of dross that rises to the top (due to surface tension and non-wetting, not lower density).

(3) Transfer the lithium to a closed 304 SS vessel through a 50 micron filter by vacuum. Keep the lithium temperature at 210 ± 20°C to minimize impurity solubility during the filtration.

(4) Heat the lithium to 750-800°C for 24 hours with titanium foil (2 cm^2 surface/gm of lithium).

(5) Cool to 350°C and withdraw a filtered (5 micron) lithium sample for analysis.

(6) If the nitrogen content is still above the specification (100 ppm), add the amount of aluminum metal required to precipitate the remaining nitrogen as aluminum nitride (AlN).

(7) Hold the temperature at 250°C for several hours, then resarnple and analyze to confirm that the nitrogen is within specification.

(8) Withdraw the purified lithium through a 5 micron filter into 1.9 cm (0.75 in.) O.D. tubes at a temperature as close to the freezing point as practical to further minimize dissolved impurities of all kinds.

The lithium was then extruded through a 0.76 cm (0.300 in.) hole in each of the tubes in preparation for loading the TZM subcapsules with the vanadium specimens and the lithium.

Before specimen loading, the TZM subcapsules were given the pre-weld treatment outlined in Reference 3. The lithium was then cut to length, weighed and inserted into the subcapsule along with the Vanadium SS-3 tensile specimens and TEM discs. After melting the lithium, the subcapsules were loosely capped and transferred (still under argon) to an electron beam welder. Welding was performed under a vacuum of 5×10^{-5} mm. After welding and nondestructive checking for cracks and leaks, the subcapsules were ready to be loaded into the MOTA hardware along with the other fusion alloy specimens.

In addition, Vanadium tensile and TEM specimens for thermal aging studies were also prepared using the same procedures. These thermal aging tests are being conducted at ORNL with the intention of separating the effects of irradiation from other factors which may contribute to changes in material behavior. Some subcapsules were also filled with only lithium to investigate the effects of the encapsulation procedure on lithium purity. The lithium analyses before encapsulation of specimens for the FFTF irradiations and thermal aging studies are given in Table 2.4.11.

2.4.4.4 FFTF Irradiations

Specimens irradiated in the initial two irradiations (MOTA-1B in FFTF cycle 4, and MOTA-1C in cycles 5-6) are detailed in the test matrix appearing as Table 2.4.12. Additional information relevant to the two irradiations follows.

FFTF cycle 4 irradiation

Specimens were loaded into MOTA baskets during the reconstitution of MOTA-1A in November, 1983. The specific basket loading details are beyond the scope of this report but are supplied to the experimenters upon discharge of specimens. The basket assemblies were inserted into three in-core canisters of MOTA-1B: canister 1E (designating MOTA level 1, canister position E), canister 2C and canister 2B.

Canister 1E was a weeper with a nominal operating temperature of 420°C. During cycle 4, the time-averaged temperature calculated from thermocouple data was 407°C. (Specimens from this canister were transferred to MOTA level 2 for subsequent irradiations which should operate closer to 420°C.)

Canisters 2C and 2B were temperature controlled canisters set to operate at 520 and 600°C respectively. During cycle 4, canister 2C operated at 518°C, while canister 2B ran at 595°C. However, due to a brief, inadequate venting of gas from a failed pressurized tube, canister 2B became gas-blanketed and experienced a 220°C temperature excursion to 820°C which lasted for six minutes. Since this over-temperature was severe enough to compromise the results from most of the specimens and place a cloud of uncertainty over the remaining data, all specimens from this canister were removed and replaced.

FFTF cycle 4 commenced in January, 1984, and terminated in April, 1984, achieving 109.5 effective-full-power-days (EFPD). Approximate fluence levels accumulated during cycle 4 can be obtained from the "1 cycle" columns in Table 2.4.1 for the appropriate MOTA level. Specific fluence information for each specimen was supplied to the experimenters upon discharge and delivery of specimens.

FFTF cycles 5-6 irradiation

Specimens irradiated during cycle 4 were either discharged for examination or loaded into new MOTA baskets during the reconstitution of MOTA-1B in May, 1984. (Pressurized tubes were measured and reinserted.) New specimens were also loaded into the baskets at this time. The basket assemblies were inserted into four in-core canisters of MOTA-1C (canisters 2A, 2B, 2C and 5D) and into five of the below-core canister positions (BC-A, B, C, D and D).

Canister 2C is a weeper with a nominal operating temperature of 420°C. Canisters 2A, 2B and 5D are temperature controlled canisters set to operate at 520, 600 and 600°C respectively. The below-core canister is a weeper with a nominal operating temperature of 365°C.

FFTF cycle 5 commenced in June, 1984, and was terminated in November, 1984, after 122.7 EFPD. Specimens remained in MOTA-1C for continued irradiation during cycle 6 which is scheduled to run from December, 1984, to March, 1985. The expected fluence accumulation during cycles 5-6 can be obtained from the "2 cycle" columns in Table 2.4.1 for the appropriate MOTA level.

2.4.5 Future Work

Table 2.4.13 summarizes the past, present and future fusion irradiations in the FFTF.

2.4.6 References

1. C. P. Cabell, "A Summary Description of the Fast Flux Test Facility", HEDL-400, Westinghouse Hanford Company, Richland, WA, December 1980.

2. D. N. Braski and O. W. Ramey, "Helium Doping of a Vanadium Alloys by a Modified Tritium Trick", pp. 72-74 in Alloy Development for Irradiation Performance Semiannual Progress Report March 31, 1984, DOE/ER-0045/12, Oak Ridge National Laboratory, Oak Ridge, TN, July 1984.

3. Metals Handbook, 8th Edition, Vol. 6 - Welding and Brazing, p. 294.

Table 2.4.1. Typical Flux and Fluence Values for FFTF MOTA Irradiations

	MOTA Canister Level	Fast Flux (E > 0.1 MeV) n/cm^2-s	Fast Fluence (E > 0.1 MeV) 1 Cycle (100 days) n/cm^2	dpa	2 Cycles (200 days) n/cm^2	dpa
↑ Active Core ↓	5	1.38×10^{15}	1.19×10^{22}	4-7	2.38×10^{22}	8-14
	4	2.91×10^{15}	2.51×10^{22}	10.5-13	5.03×10^{22}	21-26
	3	3.62×10^{15}	3.13×10^{22}	14.5-15	6.26×10^{22}	29-30
	2	3.19×10^{15}	2.76×10^{22}	12.5-14	5.51×10^{22}	25-28
	1	1.77×10^{15}	1.53×10^{22}	6-9	3.06×10^{22}	12-18
	Below-Core	0.58×10^{15}	0.50×10^{22}	2-3.5	1.00×10^{22}	4-7

NOTES: (1) Flux and fluence (n/cm^2) values for center of MOTA Level.

(2) Fluence (dpa) values indicate ranges within MOTA level, based on 4.8 dpa/($10^{22} n/cm^2$) for HT-9.

(3) Two cycles = 200 full power days; total duration for 2 cycles is approximately 1 year.

Table 2.4.2. Chemical compositions for ferritic alloys irradiated in MOTA during FFTF cycles 4-6 (weight percent)

Element	HT-9 (9607R2)[1]	MTS-4 Weld Wire (27103)[2]	9Cr-1Mo (30176)[3]	2-1/4Cr-1Mo (56447)[4]
C	0.20	0.225	0.092	0.10
Mn	0.57	1.04	0.48	0.40
P	0.016	0.021	0.012	0.009
S	0.003	0.006	0.004	0.006
Si	0.17	0.27	0.15	0.23
Ni	0.51	0.55	0.09	0.14
Cr	12.1	11.1	8.32	2.16
Mo	1.04	1.15	0.86	1.03
V	0.28	---	0.20	0.01
W	0.45	0.34	<0.01	---
Nb	<0.001	---	0.06	---
Ti	0.001	---	0.001	0.01
Co	<0.05	---	0.017	0.01
Cu	0.07	---	0.03	0.03
Al	0.006	---	0.011	---
B	<0.001	---	<0.001	---
As	0.003	---	<0.001	---
Sn	0.004	---	0.002	---
N	0.027	---	0.055	---
O	0.002	---	0.010	---
Pb	<0.0001	---	<0.001	---
Sb	0.0005	---	<0.001	---
Bi	<0.001	---	---	---
Zr	---	---	<0.001	---
Fe	Bal.	Bal.	Bal.	Bal.

[1]International Nickel (ADIP DOE/ER-0045/8, pg. 366).

[2]Thyssen Specialty Steels, Certificate of Composition dated April 16, 1980.

[3]Combustion Engineering (ORNL Report, "Modified 9Cr-1Mo Steel Development Progress Report for Period Ending September 30, 1979").

[4]Cameron Iron Works Inc. Certificate of Composition dated July 21, 1975.

NOTE: Compositions for all TEM Discs not included.

Table 2.4.3. Chemical compositions for Vanadium alloys irradiated in MOTA during FFTF cycles 4-6 (weight percent)

Element	V-15Cr-5Ti (834)[1]	VANSTAR-7 (387)[1]	V-3Ti-1Si (11153)[2]
Ti	15.3	---	3.4
Cr	5.0	9.7	---
Fe	---	3.4	0.04
Zr	---	1.3	---
Si	---	---	1.28
C	0.017	0.064	0.045
O	0.023	0.028	0.091[3]
N	0.052	0.052	0.026
V	Bal.	Bal.	Bal.

[1]R.L. Ammon, "Melting and Processing of Niobium and Vanadium Alloy Sheet and Rod", Report AESD-M-FR-79-004, Westinghouse AESD, Pittsburgh, PA, October 1979.

[2]Compositions supplied by D.N. Braski, ORNL.

[3]Analysis confirmed by neutron activation at ORNL.

Table 2.4.4. Chemical compositions for low activation and Mn stabilized alloys irradiated in MOTA during FFTF cycles 4-6 (weight percent)

nt	Low Activation Alloy[1]										Mn Stabilized[2]	
	V02262	V02263	V02264	V02265	V02266	V02267	V02268	V02269	UC 19	GA 3X	10996	10998
C	0.086	0.093	0.096	0.197	0.097	0.089	0.101	0.097	0.11	0.15	0.10	0.11
Mn	<0.01	<0.01	0.02	1.08	2.68	6.47	2.44	6.47	0.30	----	3.33	6.57
Si	0.08	0.08	0.09	0.09	0.09	0.10	0.10	0.11	0.30	----	0.12	0.10
P	<0.005	<0.005	<0.005	<0.005	<0.005	<0.005	<0.005	<0.005	0.007	----	0.007	0.007
S	0.003	0.002	0.003	0.003	0.003	0.005	0.004	0.005	0.015	----	0.005	0.006
Cr	2.32	2.38	9.13	9.14	9.02	12.19	8.32	11.81	2.46	9.0	11.80	12.00
Ni	0.02	0.01	<0.01	<0.01	<0.01	0.01	<0.01	<0.01	0.05	----	0.01	<0.01
Mo	<0.01	<0.01	<0.01	<0.01	<0.01	<0.01	<0.01	<0.01	0.02	----	0.96	0.96
W	<0.01	<0.01	0.01	0.02	0.01	<0.01	0.39	0.89	----	2.5	<0.01	<0.05
V	0.50	1.01	0.52	1.23	0.51	1.05	0.27	0.28	1.50	0.30	0.21	0.20
N	0.004	0.003	0.003	0.003	0.003	0.003	0.002	0.003	0.015	----	0.003	0.003
Nb	<0.01	<0.01	<0.01	<0.01	<0.01	<0.01	<0.01	<0.01	----	----	0.16	0.15
Cu	<0.002	<0.002	<0.002	<0.002	<0.002	0.002	<0.002	<0.002	0.04	----	0.01	0.012
Sn	<0.001	<0.001	<0.001	<0.001	<0.001	<0.001	<0.001	<0.001	----	----	----	----
Sb	<0.001	<0.001	<0.001	<0.001	<0.001	<0.001	<0.001	<0.001	----	----	----	----
Al	----	----	----	----	----	----	----	----	0.043	----	----	----
Ti	----	----	----	----	----	----	----	----	0.003	----	----	----
Fe	Bal.	Bal.	Bal.	Bal.	Bal.	Bal	Bal.	Bal.	Bal.	Bal.	Bal.	Bal.

[1]Heats V02262-V02265: Carpenter Technology (Analysis Sheet, dated August 9, 1983)
Heats V02266-V02269: Carpenter Technology (Analysis Sheet, dated August 26, 1983)
Heat UC-19: Foote Mineral Company (Letter to N.M. Ghoniem, UCLA, dated July 6, 1982)
Heat GA-3X: Nominal Compositions supplied by G.A. Technologies

[2]Heats 10996, 10998: Carpenter Technology (Certificate of Tests, dated January 13, 1983)

NOTE: Compositions for all TEM discs not included.

Table 2.4.5. Chemical compositions[1] for austenitic alloys irradiated in MOTA during FFTF cycles 5-6 (weight percent)

Element	PCA (K-280)	PCA-13	PCA-19	PCA-20	316 SS (X-15843)	EP-838 (USSR Steel)
C	0.05	0.063	0.076	0.033	0.05	0.02
Mn	1.8	1.9	2.1	2.1	1.7	12-14
P	0.01	0.002	0.030	0.07	0.04	0.4
S	0.003	0.009	0.006	0.007	0.015	0.4
Si	0.4	0.4	0.44	0.42	0.7	0.6
Ni	16.2	15.9	15.9	16.1	12.4	4.4-4.8
Cr	14.0	13.8	13.8	13.8	17.3	11-13
Mo	2.3	2.5	2.44	2.5	2.1	0.3-0.6
V	---	0.5	0.5	0.5	---	---
Nb	---	0.1	0.1	0.1	0.08	---
Ti	0.24	0.3	0.28	0.28	---	---
Co	---	<0.01	0.01	0.01	0.35	---
Cu	---	0.02	0.01	0.01	---	---
Al	---	---	---	---	---	~1.0
B	0.001	<0.001	<0.001	0.001	0.0004	0.0005
N	0.01	0.002	0.002	0.006	---	0.05-0.09
Fe	Bal.	Bal.	Bal.	Bal.	Bal.	Bal.

[1]Compositions supplied by ORNL

NOTE: Compositions for all TEM discs not included.

Table 2.4.6. Specimens irradiated in the FFTF cycles 4-6 fusion irradiations

Specimen Type	Responsible for Fabrication	Nominal Dimensions
SS-1 Tensile	ORNL	44.5 x 4.95 x 0.76 mm; 1.52 mm gauge width (1.75" x 0.195" x 0.030"; 0.060" gauge width)
SS-3 Tensile	WHC, ORNL	25.4 x 4.95 x 0.76 mm; 1.52 mm gauge width (1.00" x 0.195" x 0.30"; 0.060" gauge width)
HFIR Sub-Mini Tensile	ORNL	39.4 x 4.06 mm dia.; gauge: 18.3 x 2.03 mm dia. (1.550" x 0.160" dia.; gauge: 0.720 x 0.080" dia.
1/3 Size Charpy	WHC	23.6 x 3.3 x 3.3 mm (0.930" x 0.131" x 0.131")
1/3 Size Charpy	ORNL	25.4 x 3.3 x 3.3 mm (1.00" x 0.131" x 0.131")
1/2 Size Charpy	WHC	23.6 x 5.0 x 5.0 mm (0.930" x 0.197" x 0.197")
1/2 Size Charpy	ORNL	25.4 x 5.0 x 5.0 mm (1.00" x 0.197" x 0.197")
Compact Tension	WHC	2.54 mm thick x 16.0 mm dia. (0.10" thick x 0.630" dia.)
Pressurized Tube	WHC	22.6 x 4.57 mm dia.; 0.20 mm wall (0.89" x 0.180" dia.; 0.008" wall)
Fatigue Crack Growth	WHC	25.4 x 12.7 x 0.61 mm (1.00" x 0.50" x 0.024")
TEM Disc Packet	WHC, ORNL, UCSB	25.4 x 3.66 mm dia.; 3 mm dia. x 0.25 mm discs (1.00" x 0.144" dia.; 0.118" dia. x 0.010" discs)
TZM Tube*	WHC	38.1 x 9.5 mm dia.; 0.63 mm wall (1.50" x 0.375" dia.; 0.025" wall)

*Used to encapsulate Vanadium SS-3 tensile and TEM specimens in lithium.

Table 2.4.7. Thermal-mechanical-treatments of ferritic specimens* irradiated in MOTA during FFTF cycles 4-6

Alloy	Specimen Type	Spec. I.D. Code	Pre-Fabrication Condition	Post-Fabrication Condition	ASTM Grain Size	Hardness $DPH_{500\ gm}$
HT-9 (9607R2)	SS-3 Tensile (ORNL)	SR	Cold-Rolled to 0.030 in.	1050°C/15 min./AC + 760°C/2.5 hr./AC	-	---
	1/3 Size Charpy (ORNL)	SR	Cold-Rolled to 5/8 in. Plate	1050°C/0.5 hr./AC + 780°C/2.5 hr./AC	-	---
	1/3 Size Charpy (WHC)	AH	45% CW to 0.206 in.; 1050°C/0.5 hr./AC + 760°C/ 2.5 hr./AC	None	6	267
	1/3 Size Charpy (WHC)	TC	25% CW to 3/16 in.; 1050°C/0.5 hr./AC + 760°C/2.0 hr./AC	None	-	---
	1/3 Size Charpy Mod. TMT (WHC)	AE	45% CW to 0.206 in.; 760°C/1.0 hr./AC	1000°C/20 hr./AC + 1100°C/5 min./AC + 700°C/2.0 hr./AC	3	328
	Fracture Toughness (WHC)	KN	As Received: 0.125 in. Annealed Plate; 1050°C/0.5 hr./AC + 760°C/2.5 hr./AC	None	5	246
	CCT Fatigue (WHC)	HE	40% CW to 0.024 in.; 1050°C/0.5 hr./AC + 760°C/2.5 hr./AC	None	6	254
	Pressurized Creep Tube (WHC)	FH	0.188 in. dia. x 0.012 in. wall; 1050°C/0.5 hr./AC + 760°C/2.5 hr./AC	1050°C/5 min./AC + 760°C/2.5 hr./AC	5-6	270
	1/2 Size Charpy (ORNL)	SP	Cold-Rolled to 5/8 in. Plate	1050°C/0.5 hr./AC + 780°C/2.5 hr./AC	-	---
HT-9 Weldment	1/3 Size Charpy (WHC)	AL	0.405 in. HT-9 (ht. 466) & 2.5 mm MTS-4 (ht. 27103) Weld Wire; R.T. Preheat; R.T. Interpass; 760°C/ 2.5 hr./AC PWHT.	None	Base: 5 Weld: 8	239 272

*TEM discs not included.

(continued)

Table 2 4 7 (continued)

Alloy	Specimen Type	I.D. Code	Pre-Fabrication Condition	Post-Fabrication Condition	ASTM Grain Size	Hardness DPH
9Cr-1Mo (30176)	SS-3 Tensile (ORNL)	TK	Cold-Rolled to 0.030 in.	1040°C/0.5 hr. AC + 760°C/1.0 hr./AC		
	1/3 Size Charpy (WHC)	A	40% CW to 0.200 in.; 1038°C/0.5 hr./AC + 760°C/1.0 hr./AC	None	9	220
	Fracture Toughenss (WHC)	N	1038°C/0.5 hr./AC + 760°C/0.5 hr./AC	None	10	22
	CCT Fatigue (WHC)	AZ	40% CW to 0.024 in.; 1038°C/0.5 hr./AC + 760°C/1.0 hr./AC	None	9	213
	Pressurized Creep Tube (WHC)	HN	0.180 in. dia. x 0.0075 in. Wall	1038°C/5 min./AC + 760°C/1.0 hr./AC	10	258
2-1/4Cr-1Mo (56447)	1/3 Size Charpy (ORNL)	TG	Cold-Rolled to 1.0 in Plate	900°C/1.0 hr./AC + 700°C/1.0 hr./AC		

Table 2.4.8. Thermal-mechanical-treatments of Vanadium specimens *irradiated in OTA during FFTF cycles 4-6

Alloy	Specimen Type	Spec. I.D. Code	Pre-Fabrication Condition	Post-Fabrication Condition
V-15Cr-5Ti (CAM 834-3)	SS-3 Tensile (ORNL)	RA, RD	Warm-Rolled From 0.060 in. to 0.034 in. @ 500°C; Pickled	Annealed 1200°C for 1.0 hr.
VANSTAR-7 (CAM 837-7)	SS-3 Tensile (ORNL)	QA	Warm-Rolled From 0.060 in. to 0.032 in. @ 500°C; Pickled	Annealed 1350°C for 1.0 hr.
V-3Ti-1Si (11153)	SS-3 Tensile (ORNL)	RB, RC	Annealed 1050°C for 1.0 hr.	None

*TEM discs not included.

Table 2.4.9. Thermal-mechanical-treatments of low activation and Mn stabilized specimens* irradiated in MOTA during FFTF cycles 4-6

Alloy	Specimen Type	Spec. I.D. Code	Pre-Fabrication Condition	Post-Fabrication Condition
Low Activation (V02262)	SS-3 Tensile (WHC)	TE	2.5" x 0.5" Forged Plate	900°C/20 hr./WQ + 950°C/20 min./WQ + 650°C/2 hr./AC
Low Activation (V02263)	SS-3 Tensile (WHC)	TH	2.5" x 0.5" Forged Plate	900°C/20 hr./WQ + 950°C/20 min./WQ + 650°C/2 hr./AC
Low Activation (V02264)	SS-3 Tensile (WHC)	TM	2.5" x 0.5" Forged Plate	1000°C/20 hr./AC + 1100°C/5 min./AC + 700°C/2 hr./AC
Low Activation (V02265)	SS-3 Tensile (WHC)	TN	2.5" x 0.5" Forged Plate	1000°C/20 hr./AC + 1100°C/10 min./AC + 700°C/2 hr./AC
	1/3 Size Charpy (WHC)	L5	2.5" x 0.5" Forged Plate	1000°C/20 hr./AC + 1100°C/10 min./AC + 700°C/2 hr./AC
Low Activation (V02266)	SS-3 Tensile (WHC)	TP	2.5" x 0.5" Forged Plate	1000°C/20 hr./AC + 1100°C/10 min./AC + 700°C/2 hr./AC
Low Activation (V02267)	1/3 Size Charpy (WHC)	L7	2.5" x 0.5" Forged Plate	1000°C/20 hr./AC + 1100°C/10 min./AC + 700°C/2 hr./AC
Low Activation (V02268)	SS-3 Tensile (WHC)	TR	2.5" x 0.5" Forged Plate	1000°C/20 hr./AC + 1100°C/10 min./AC + 700°/2 hr./AC
	1/3 Size Charpy (WHC)	L8	2.5" x 0.5" Forged Plate	1000°C/20 hr./AC + 1100°C/10 min./AC + 700°C/2 hr./AC

*TEM discs not included.

Table 2.4.9 (continued)

Alloy	Specimen Type	Spec. I.D. Code	Pre-Fabrication Condition	Post-Fabrication Condition
Low Activation (V02269)	SS-3 Tensile (WHC)	TU	2.5" x 0.5" Forged Plate	1000°C/20 hr./AC + 1100°C/10 min./AC + 700°C/2 hr./AC
	1/3 Size Charpy (WHC)	L9	2.5" x 0.5" Forged Plate	1000°C/20 hr./AC + 1100°C/10 min./AC + 700°C/2 hr./AC
Low Activation (UC-19)	SS-3 Tensile (WHC)	TZ	2.0" x 1.0" x 1.0" Plate	900°C/20 hr./WQ + 950°C/20 min./WQ + 650°C/2 hr./AC
	1/3 Size Charpy (WHC)	L3	3" x 4" x 2" As Air Melted	1050°C/10 min./WQ + 650°C/2 hr./AC
Low Activation (GA-3X)	1/3 Size Charpy (WHC)	L0	3.5" x 2.75" x 0.18" Plate; 1000°C/1.0 hr./AC + 700°C/1.0 hr./AC	None
Mn Stabilized (V10996)	1/2 Size Charpy (WHC)	F2	2.5" x 0.5" Forged Plate	1000°C/16 hr./AC + 1100°C/0.5 hr./AC + 700°C/2 hr./AC
Mn Stabilized (V10998)	1.60" Tensile (WHC)	F4	2.5" x 0.5" Forged Plate	1000°C/16 hr./AC + 1100°C/0.5 hr./AC + 700°C/2 hr./AC
	1/2 Size Charpy (WHC)	F4	2.5" x 0.5" Forged Plate	1000°C/16 hr./AC + 1100°C/0.5 hr./AC + 700°C/2 hr./AC

*TEM discs not included.

Table 2.4.10. Thermal-mechanical treatments of austenitic specimens* irradiated in MOTA during FFTF cycles 5-6

Alloy	Specimen Type	Spec. I.D. Code	Pre-Fabrication Condition	Post-Fabrication Condition
Path A PCA (K-280)	SS-1 Tensile (ORNL)	EL	1100°C/0.5 hr./AC + 800°C/8 hr./AC + 25% CW	None
	SS-1 Tensile (ORNL)	EC	1100°C/0.5 hr./AC + 25% CW	None
	HFIR Sub-Mini Tensile (ORNL)	EL	1100°C/0.5 hr./AC + 800°C/8 hr./AC + 25% CW	None
	HFIR Sub-Mini Tensile (ORNL)	EC	1100°C/0.5 hr./AC + 25% CW	None
PCA 13	SS-1 Tensile (ORNL)	HA	1100°C/0.5 hr./AC + 25% CW	None
PCA-19	SS-1 Tensile (ORNL)	HT	1100°C/0.5 hr./AC + 25% CW	None
PLA 20	SS-1 Tensile (ORNL)	HU	1100°C/0.5 hr./AC + 25% CW	None
316 SS Ref. Heat (X-15893)	SS-1 Tensile (ORNL)	AE	1050°C/1.0 hr./AC + 20% CW	None
EP-838 (USSR Steel)	SS-1 Tensile (ORNL)	EP	1050°C/1.0 hr./AC + 20% CW	None

*TEM discs not included.

Table 2.4.11. Lithium-7 analysis after purification (ppm)

Element	FFTF Cycle 4 Capsules, November 22, 1983	Thermal Aging Capsules, February 9, 1984	Cycles 5-6 & Thermal Aging, May 18, 1984
Carbon	0.5	2.0	0.1
Nitrogen	47	6.5	12
Calcium	--	56	9.2
Silicon	--	--	15.0
Sodium	--	480	--
Potassium	--	<0.5	--
Aluminum	--	120	6.3
Chromium	--	5	<1.0
Nickel	--	5	3.3
Magnesium	--	14	7.2
Iron	--	18	1.0

NOTES: (1) Lithium is free of particles larger than 5 microns.

(2) Lithium purified on November 22, 1983, and February 9, 1984, came from the same ingot.

Table 2.4.12. FFTF fusion irradiations - test matrix for cycles 4-6

SPECIMEN TYPE • Alloy Description	Spec Code	January 1984 Cycle 4 MOTA Levels 1 420	2 520	2 600	April 1984 Cycle 4 Specimen Discharge 420	520	600	May 1984 Recon of Irradiated Specimens 420	520	600	May 1984 Insertion of New Specimens 365	420	520	600	600	June 1984 Cycles 5-6 Mota Levels BC 365	2 420	2 520	2 600	5 600
TEM PACKETS																				
• DAFS & ADIP (WHC/HRB)	--	15	9	9	5	3	9	10	6	0	-	10	8	14	-	-	20	14	14	-
• Low Act. & Path E (WHC/DSG)	--	6	3	3	2	1	3	4	2	0	2	2	3	5	-	2	6	5	5	-
• Path A (ORNL/PJM)	--	3	3	3	1	1	3	2	2	0	-	1	3	4	2	-	3	5	4	2
• Path E (ORNL/JMV)	--	2	0	0	1	0	0	1	0	0	-	2	0	0	-	-	3	0	0	-
• Path C (ORNL/DNB)	--	2	2	2	.5	.5	2	1.5	1.5	0	-	0.2	0.2	1	-	-	1.7	1.7	1	-
• DAFS (UCSB/GEL)	--	-	-	-	-	-	-	-	-	-	-	1	1	1	-	-	1	1	1	-
CREEP (0.180")																				
• HT-9 (9607R2)	FH	6	6	6	1	1	6	5	5	0	-	0	0	0	-	-	5	5	0	-
• 9Cr-1Mo (30176)	HN	5	5	6	1	1	6	4	4	0	-	0	0	0	-	-	4	4	0	-
FRACTURE TOUGHNESS																				
• HT-9 (9607R2)	KN	6	6	6	2	6	6	4	0	0	-	0	0	6	-	-	4	0	6	-
• 9Cr-1Mo (30176)	NP	6	6	6	2	6	6	4	0	0	-	0	0	0	-	-	4	0	0	-
CRACK GROWTH																				
• HT-9 (9607R2)	HE	6	0	4	0	0	4	6	0	0	-	0	0	4	-	-	6	0	4	-
• 9Cr-1Mo (30176)	AZ	6	0	0	0	0	0	6	0	0	-	0	0	0	-	-	6	0	0	-
1/3 SIZE CHARPY																				
• HT-9 (9607R2) [WHC]	AH	12	6	6	6	0	6	6	6	0	-	0	0	0	-	-	6	6	0	-
• HT-9 (9607R2);MOD TMT	AE	6	6	0	0	6	0	6	0	0	-	0	0	0	-	-	6	0	0	-
• HT9 Weldment	AL	6	0	0	0	0	0	6	0	0	-	0	0	0	-	-	6	0	0	-
• 9Cr-1Mo (30176)	AP	12	6	0	6	0	0	6	6	0	-	0	0	0	-	-	6	6	0	-
• HT-9 (9607R2) [WHC]	TC	-	-	-	-	-	-	-	-	-	12	-	-	-	-	12	-	-	-	-
• Low Act. (V02265)	L5	-	-	-	-	-	-	-	-	-	12	-	-	-	-	12	-	-	-	-
• Low Act. (V02267)	L7	-	-	-	-	-	-	-	-	-	12	-	-	-	-	12	-	-	-	-
• Low Act. (V02268)	L8	-	-	-	-	-	-	-	-	-	12	-	-	-	-	12	-	-	-	-
• Low Act. (V02269)	L9	-	-	-	-	-	-	-	-	-	12	-	-	-	-	12	-	-	-	-
• Low Act. (UC-19)	L3	-	-	-	-	-	-	-	-	-	12	-	-	-	-	12	-	-	-	-
• Low Act. (GA-3X)	L0	-	-	-	-	-	-	-	-	-	12	-	-	-	-	12	-	-	-	-
• HT-9 (9607R2)[ORNL]	SR	-	-	-	-	-	-	-	-	-	16	-	-	-	-	16	-	-	-	-
• 2-1/4Cr-1Mo (65447)	TG	-	-	-	-	-	-	-	-	-	16	-	-	-	-	16	-	-	-	-

Table 2.4.12 (continued)

SPECIMEN TYPE • Alloy Description	Spec Code	January 1984 Cycle 4 MOTA Levels 1		2		2		April 1984 Cycle 4 Specimen Discharge						May 1984 Recon of Irradiated Specimens						May 1984 Insertion of New Specimens						June 1984 Cycles 5-6 Mota Levels BC	2		2		2		5	
		420		520		600		420		520		600		420		520		600		365		420		520		600		600		365		420		520		600	
1/2 SIZE CHARPY																																			
• Mn Stab. (V10996)	F2	-		-		-		-		-		-		-		-		-		6		-		-		-		-		6		-		-		-	
• Mn Stab. (V10998)	F4	-		-		-		-		-		-		-		-		-		6		-		-		-		-		6		-		-		-	
• HT-9 (9607R2)	SP	-		-		-		-		-		-		-		-		-		16		-		-		-		-		16		-		-		-	
1.60" TENSILE																																			
• Mn Stab. (V10998)	F4	-		-		-		-		-		-		-		-		-		2		-		-		-		-		2		-		-		-	
SS-3 TENSILE																																			
• HT-9 (9607R2)	SR	4		4		4		0		0		4		4		4		0		-		0		0		4		-		-		4		4		4	
• 9Cr-1Mo (30176)	TK	4		4		4		0		0		4		4		4		0		-		0		0		4		-		-		4		4		4	
• V-15Cr-5Ti	RA,RD	20		20		20		4		4		20		16		16		0		-		3		3		15		-		-		19		19		15	
• VANSTAR-7	QA	14		13		14		3		3		14		11		10		0		-		3		3		15		-		-		14		13		15	
• V-3Ti-1Si	RB,RC	10		10		10		2		2		10		8		8		0		-		3		3		15		-		-		11		11		15	
• Low Act. (V02262)	TE	3		-		-		1		-		-		2		-		-		-		0		-		-		-		-		2		-		-	
• Low Act. (V02263)	TH	3		-		-		1		-		-		2		-		-		-		0		-		-		-		-		2		-		-	
• Low Act. (V02264)	TM	3		-		-		1		-		-		2		-		-		-		0		-		-		-		-		2		-		-	
• Low Act. (V02265)	TN	3		-		-		1		-		-		2		-		-		-		0		-		-		-		-		2		-		-	
• Low Act. (V02266)	TP	3		-		-		1		-		-		2		-		-		-		0		-		-		-		-		2		-		-	
• Low Act. (V02268)	TR	3		-		-		1		-		-		2		-		-		-		0		-		-		-		-		2		-		-	
• Low Act. (V02269)	TU	3		-		-		1		-		-		2		-		-		-		0		-		-		-		-		2		-		-	
• Low Act. (UC-19)	TZ	3		-		-		1		-		-		2		-		-		-		0		-		-		-		-		2		-		-	
SS-1 TENSILE																																			
• PCA-B3	EL	-		-		-		-		-		-		-		-		-		-		-		-		-		6		-		-		-		-	6
• PCA-A3	EC	-		-		-		-		-		-		-		-		-		-		-		-		-		8		-		-		-		-	8
• PCA-13	HA	-		-		-		-		-		-		-		-		-		-		-		-		-		2		-		-		-		-	2
• PCA-19	HT	-		-		-		-		-		-		-		-		-		-		-		-		-		2		-		-		-		-	2
• PCA-20	HV	-		-		-		-		-		-		-		-		-		-		-		-		-		2		-		-		-		-	2
• 20% CW MFE Ref. 316	AB	-		-		-		-		-		-		-		-		-		-		-		-		-		4		-		-		-		-	4
• 20% CW Russ. Steel	EP	-		-		-		-		-		-		-		-		-		-		-		-		-		4		-		-		-		-	4
HFIR SUB-MINI TENS.																																			
• PCA-B3	EL	-		-		-		-		-		-		-		-		-		-		-		-		-		2		-		-		-		-	2
• PCA-A3	EC	-		-		-		-		-		-		-		-		-		-		-		-		-		2		-		-		-		-	2

NOTE: Temperatures in ^{o}C.

Table 2.4.13. Schedule for FFTF fusion irradiations

MOTA Designation:	1A[a]	1B	1C[b]	1D[b]
FFTF Cycles (Dates)	2-3 (Jan. 1983-Oct. 1983)	4 (Jan. 1984-Apr. 1984)	5-6 (June 1984-Mar. 1985)	7-8 (May 1985-Feb. 1986)
MOTA Reconstitution	Nov. 1983	May 1984	April 1985	March 1986

[a]Did not contain fusion materials.

[b]Projected dates.

2.5 TEST MATRICES FOR IRRADIATION OF PATH A PRIME CANDIDATE AND DEVELOPMENTAL ALLOYS IN FFTF — P. J. Maziasz (Oak Ridge National Laboratory)

2.5.1 ADIP Tasks

ADIP Task I.A.2, Define Test Matrices and Test Procedures.

2.5.2 Objectives

These irradiations are generally intended to evaluate the void swelling resistance of the Path A Prime Candidate Alloy (PCA) at high fluence (>100 dpa) relative to 20%-cold-worked type 316 after side-by-side irradiation in the Fast Flux Test Facility (FFTF), as well as to evaluate the improvements achieved by additional minor compositional variations of the PCA. Further, these irradiations also serve as a low helium base line against which to gage more accurately the effects of higher helium generation for similar irradiation of exactly the same alloys in the High Flux Isotope Reactor (HFIR).

2.5.3 *Summary*

An initial set of transmission electron microscopy (TEM) disk specimens was assembled for irradiation at approximately 420, 520, and 600°C to fluences of approximately 15, 45, and 75 dpa. Some TEM specimens were discharged at approximately 9.5 to 15.6 dpa at all temperatures, and additional specimens were then reloaded to achieve fluences well beyond 100 dpa. Tensile specimens were also included in the reload for irradiation in an above-core position at approximately 600°C. The general goals of the experiments are outlined and detailed specimen loadings are described.

2.5.4 Progress and Status

2.5.4.1 General Description and Progress

Irradiation space in the Materials Open Test Facility (NOTA) of the FFTF became available to the Fusion Materials Program in about mid-1983.

There were several reasons for taking advantage of this irradiation facility: (1) high fluence could be attained rapidly (approximately 30 dpa/year) with enough irradiation space for many TEM disks to be irradiated side by side, (2) a low helium generation base line was needed to gage the effects of helium for fusion alloys, particularly the PCA, which had been irradiated at the same temperature in HFIR and in the Oak Ridge Research Reactor (ORR). Alloy heat treatment and identification codes are given in Table 2.5.1 and their compositions are listed in Table 2.5.2. The first loading (cycle 4) included three identical tubes of TEM disks at each irradiation temperature of nominally 420, 520, and 600°C for discharges after approximately 15, 45, and 75 dpa. These tubes included all of the PCA thermal-mechanical pretreatment variants to allow comparison with ORR-MFE-4(A and B)[1] and HFIR-CTR-30 through -32 (ref. 2) irradiations. The initial experiment included several heats of type 316 stainless steel (N-lot, IO-heat and heat X15893) to serve as a base line against which to measure improvement in the swelling resistance of the PCA. The Russian, high-manganese steel (heat EP-838) was also included because of its relevance to our program to develop steels with low activation characteristics. Finally, compositional variants of the PCA (alloys 1 through 18 and 00) were also included; these have minor variations and coinbinations of Ti, Nb, V, B, P, and C, intended to vary or improve the stability of the MC phase, which is the basis for the irradiation resistance of this class of alloys for fusion.[3] The distribution of these disks at various temperatures and fluences is included in Table 2.5.3.

Upon completion of cycle 4, several tubes of disks were discharged from the MOTA; tube KE, at 420°C, received 6 to 10.5 dpa, while tubes KK (520°C) and KN, KO, KP (6110°C) received 13.6 to 15.6 dpa (see Table 2.5.3 and ref. 4). The tubes at approximately 600°C all experienced a 6-min excursion to approximately 820°C. Since this probably invalidates the experiment, these tubes were replaced upon reloading.

Additional TEM disk tubes were reloaded into the MOTA for irradiation together with the remaining tubes in levels 1 and 2; these are expected to accumulate 26 to 30 dpa during cycles 5 and 6. Two more TEM disk packets and 30 tensile specimens were also included in a canister at 600°C in level 5, which should accumulate approximately 14 dpa during cycles 5 and 6 (see Table 2.5.3). At levels 1 and 2, new TEM disk tubes KE01 (420°C), KK01-03 (520°C) and KN01–03 (600°C) included a second set of PCA compositional variants (PCAs-19 through -22) and several breeder program 09-type alloys, all 25% cold worked. Tube KN04 (600°C) was a direct replacement for the overheated KO (600°C) tube, which was to accumulate approximately 45 dpa; the new tube also contained several 20%-cold-worked disks of the Path A Fe-Cr-Mn-C alloys [M0, M1, M2, and M6 (see Tables 2.5.1 and 2.5.3)], which are the base alloys for manganese stabilized-low activation austenitic stainless steels being developed at ORNL.[5] At level 5, tubes KN05 and KN06 together replaced the approximately 15 dpa data intended from the overheated KN tube at 600°C (*see* Table 2.5.3). In addition, this tube contained alloys expected to be high swelling (SA type 316s and P7 alloys) in order to provide a three-reactor comparison (FFTF, ORR, and HFIR) to more accurately gage the effect of variable helium generation rate on void swelling and microstructural development. Finally, these tubes contained both solution-annealed and cold-worked samples of the Fe-Cr-Mn-C low activation alloys, to determine the effectiveness of cold working on void swelling resistance in these new alloys.

Table 2.5.1. Alloy chemistries for steels included in FFTF/MOTA (weight percent)

Allay designation	Fe	Cr	Ni	Mo	Mn	51	Ti	Nb	V	C	N	P	Co	Cu	B	S
PCA (K-280)	bal	14.0	16.7	7.3	I.R	0.4	0.24			0.05	0.01	0.01			0.001	0.003
PCA-1	bal	14.0	16.0	2.5	2.1	<0.01	0.13	0.12	<0.01	0.04	0.003	<0.001	<0.01	0.02	<0.001	0.008
PCA-3	bal	14.3	15.8	2.5	2.0	n.4	0.13	0.11	<0.01	0.056	0.005	<0.001	<0.01	0.02	<0.001	0.007
PCA-4	bal	14.0	16.0	2.5	2.1	0.07	<0.01	0.26	<0.01	0.051	0.0003	0.001	<0.01	0.02	<0.001	0.007
PCA-5	bal	14.4	15.9	1.5	2.1	0.1	<0.01	0.26	<0.01	0.048	0.0002	0.001	<0.01	0.02	<0.001	0.007
PCA-7	bal	14.0	16.0	2.6	2.1	n.4	<0.01	<0.01	<0.01	0.057	0.0002	0.001	<0.01	0.02	<0.001	0.007
PCA-6	bal	14.0	16.0	2.4	1.9	0.4	0.23	0.01	<0.01	0.083	0.004	<0.001	<0.01	0.02	<0.001	0.007
PCA-8	bal	13.9	16.0	2.7	2.1	<0.01	0.17	0.14	<0.01	0.081	0.007	<0.001	<0.01	0.02	<0.001	0.008
PCA-9	bal	13.R	Ih.O	2.5	2."	0.4	0.25	<0.01	<0.01	0.073	0.005	0.03	<0.01	0.02	<0.001	0.007
PCA-10	bal	13.R	15.9	2.5	l.v	0.4	0.3	0.1	0.02	0.04	0.002	0.002	<0.01	0.02	<0.001	0.009
PCA-11	bal	13.8	16.0	2.5	1.9	0.4	0.3	0.1	0.5	0.04	0.002	0.002	<0.01	0.03	<0.001	0.008
PCA-12	bal	13.8	15.9	2.4	1.9	0.4	<0.01	0.47	0.01	0.044	0.004	0.002	0.01	0.02	<0.001	0.008
OCA-13	bal	13.8	15.9	2.5	1.9	0.4	0.3	0.1	0.5	0.063	0.002	0.002	<0.01	0.02	<0.001	0.009
PCA-16	bal	15.9	14.1	2.5	1.9	0.4	0.27	<0.01	0.02	0.051	0.002	0.002	<0.01	0.02	<0.001	0.009
PCA-17	bal	15.8	16.0	2.5	1.9	0.4	0.3	<0.01	0.03	0.047	0.002	0.002	<0.01	0.02	<0.001	0.009
PCA-18	bal	17.6	16.1	2.5	1.9	0.4	0.27	<0.01	0.02	0.044	0.002	0.002	<0.01	0.02	<0.001	0.009
PCA-00	bal	14.0	16."	2.46	2.0	0.4	0.24	<0.01	0.02	0.056	0.001	0.002	0.01	0.02	<0.001	0.008
PCA-19	bal	13.8	11.9	2.44	2.1	0.44	0.28	0.1	0.5	0.076	0.002	0.030	0.01	0.01	<0.001	0.006
PCA-20	bal	13.R	16.1	2.5	7.1	0.42	0.28	0.1	0.5	0.083	0.006	0.07	0.01	0.01	0.001	0.007
PCA-21	bal	15.8	15.8	2.44	3.4	0.4	0.27	0.1	0.5	0.077	0.006	0.06	<0.01	0.05	0.001	0.007
PCA-22	bal	13.8	11.9	2.4	7.5	0.4	0.28	0.1	0.5	0.078	0.004	0.03	<0.01	0.05	0.003	0.007
EP-838 (Russian steel)[a]	bal	11–13	4.4–4.8	0.3–0.6	12–14	0.6				0.02	0.05–0.09	0.4			0.0005	0.4
N-lot 316	bal	16.5	13.5	7.5	1.6	0.5				0.05	0.006	0.013			0.0008	0.006
X-15893	bal	17.3	12.4	2.1	1.7	n.7		0.08		0.05		0.04	0.35		0.0094	0.015
DO-316	bal	18.0	13.0	2.6	1.9	0.8	0.05			0.05	0.05	0.01	0.004		0.0005	0.016
P7	bal	17.0	16.7	2.5	0.03	0.1	0.02			0.005			0.03	0.02		
D9-697	bal	14.4	16.2	1.5	1.9	0.5	0.25	<0.01	0.02	0.035	0.009	0.003	0.03	0.02	0.0001	0.002
D9-699	bal	14.2	15.2	2.0	2.1	0.5	0.23	0.01	0.02	0.033	0.004	0.005	0.02	0.02	<0.0001	0.001
D9-A7	bal	13.7	16.3	2.5	2.0	1.42	0.18	0.01	0.023	0.045	0.011	0.075	0.06	0.03	0.0005	0.017
M0	bal	15			15					0.1						
M1	bal	15			15					0.05						
M2	bal	15			20					0.1						
M6	bal	15			20					0.2						

[a]Approximately 1%Al.

Table 2.5.2. Alloy designations, thermal-mechanical treatments, and identification codes for austenitic steel for FFTF/MOTA

Alloy	Thermal-mechanical treatment	Identification number	Alloy	Thermal-mechanical treatment	Identification number
PCA	Solution annealed at 1100°C for 30 min (A1)	ED-#[a]	PCA-5	A1 treatment + 25% CW	FL-#
				A1 treatment	FM-#
	A1 treatment + 10% CW (A2)	EH-#	PCA-6	A1 treatment + 25% Cw	FN-#
	A1 treatment + 25% CW (A3)	EC-#	PCA-7	A1 treatment + 25% CW	FQ-#
	A1 treatment + 8 h at 800°C + 8 h at 900°C (81)	EE-#		A1 treatment	FR-#
			PCA-8	A1 treatment + 25% CW	FS-#
	A1 treatment + 8 h at 800°C + 25% CW + 2 h at 750°C(B2)	EF-#		A1 treatment	FT-#
			PCA-9	A1 treatment + 25% CW	FV-#
				A1 treatment	FW-#
	A1 treatment + 8 h at 800°C + 25% CW (B3)	EL-#	PCA-10	A1 treatment + 25% CW	FH-#
			PCA-11	A1 treatment + 25% CW	FY-#
	A1 treatment + 25% CW + 2 h at 750°C (C)	EG-#	PCA-12	A1 treatment + 25% CW	FZ-#
			PCA-13	A1 treatment + 25% CW	HA-#
	A1 treatment + 10% CW + 2 h at 750°C + 10% CW	D-#	PCA-19	A1 treatment + 25% CW	HT-#
			PCA-20	A1 treatment + 25% CW	HY-#
DO-heat 316	Solution annealed at 1050°C for 1 h(A0)	AJ-#	PCA-21	A1 treatment + 25% CW	HW-#
			PCA-22	A1 treatment + 25% CW	HX-#
	A0 treatment + 20% CW	AL-#	PCA-00	A1 treatment + 25% CW	HH-#
N-lot 316	A0 treatment + 20% CW	AG-#	M0	A0 treatment	MA-#
X-heat 316	A0 treatment + 20% CW	AC-#		A0 treatment + 20% CW	MB-#
EP-838 (Russian steel)	A0 treatment + 20% CW	EP-#	M1	A0 treatment	MC-#
				A0 treatment + 20% CW	MD-#
P7	A0 treatment	AK-#	M2	A0 treatment	ME-#
	A0 treatment + 20% CW	AF-#		A0 treatment + 20% CW	MF-#
			M6	A0 treatment	MG-#
PCA-1	A1 treatment + 25% CW	FC-#		A0 treatment + 20% CW	MH-#
	A1 treatment	FD-#			
PCA-3	A1 treatment + 25% CW	FG-#	D9-699	A1 treatment + 25% CW	GF-#
	A1 treatment	FH-#	D9-697	A1 treatment + 25% CW	GH-#
PCA-4	A1 treatment + 25% CW	FJ-#	D9-A7	A1 treatment + 25% CW	BA-#
	A1 treatment	FK-#			

[a]Numbers from 0 to 99.

Table 2.5.3. Distribution of TEM disk specimens in FFTF/MOTA experiments

Alloy/ pretreatment designations	Number of dies at irradiation conditions (tube identification)																		
	420°C (level 1)				520°C (level 2)						600°C (level 2)							600°C (level 5)	
	[KE][a]	[KF][b]	[KH][b]	[KE01][a]	[KK][d]	[KL][b]	[KM][b]	[KK01][e]	[KK02][a]	[KK03][a]	[KN][e]	[KO][e]	[KP][e]	[KN01][a]	[KN02][a]	[KN03][a]	[KN04][a]	[KN05][f]	[KN06][f]
PCA/A1	3	3	3		3	3	3				3	3	3				2	3	
PCA/A2	2	2	2		2	2	2				2	2	2				2	2	
PCA/A3	3	3	3	2	3	3	3	2	2	2	3	3	3	2	2	2	2	2	
PCA/B1	2	2	2		2	2	2				2	2	2				2	2	
PCA/B2	3	3	3		3	3	2				3	3	3				2	2	
PCA/B3	3	3	3	2	3	3	2	2			3	3	3	2			2	2	
PCA/C	2	2	2		2	2	2				2	2	2				2	2	
PCA/D	2	2	2		2	2	2				2	2	2				2	2	
PCA-1/A1																		1	1
PCA-1/A3	2	2	2		2	2	2				2	2	2	2	2	2		1	1
PCA-3/A1																		1	1
PCA-3/A3	2	2	2		2	2	2		2	2	2	2	2		2	2	2	1	1
PCA-4/A1																		1	1
PCA-4/A3									2	2					2	2		1	1
PCA-5/A1																		1	1
PCA-5/A3									2	2					2	2		2	
PCA-6/A3	2	2	2		2	2	2		2	2	2	2	2		2	2	2	2	
PCA-7/A1															2	2		2	
PCA-7/A3									2	2								2	
PCA-8/A1																		2	
PCA-8/A3	2	2	2	2	2	2	2	2	2	2	2	2	2	2	2	2	2	2	
PCA-9/A1																		2	
PCA-9/A3	2	2	2	2	2	2	2	2	2	2	2	2	2	2	2	2	2	2	
PCA-10/A3	2	2	2		2	2	2				2	2	2						
PCA-11/A3	2	2	2	2	2	2	2	2			2	2	2	2			2		2
PCA-12/A3	2	2	2	2	2	2	2	2			2	2	2	2			2		
PCA-13/A3	2	2	2	2	2	2	2	2	2	2	2	2	2	2	2	2	2		2
PCA-14/A3	2	2	2		2	2	2				2	2	2						
PCA-16/A3	2	2	2		2	2	2				2	2	2						
PCA-17/A3	2	2	2		2	2	2				2	2	2						
PCA-18/A3	2	2	2		2	2	2				2	2	2						
PCA-00/A3				2				2						2	2	2	2		2
PCA-19/A3				2			2	2	2					2	2	2	2		2
PCA-20/A3				2			2	2	2					2	2	2	2		2
PCA-21/A3				2			2	2	2					2	2	2	2		
PCA-22/A3				2			2	2	2					2	2	2	2		
D9-699/A3									2	2					2	2			
D9-697/A3				2										2			2		
D9-A7/A3				1				2						1			1		
N-Lot 316/A0	2	2	2		2	2	2	1			2	2	2						
N-Lot 316/20% CW	2	2	2		2	2	2				2	2	2		2	2	2	2	
X15893 316/ 20% CW	2	2	2		2	2	2		2	2	2	2	2		2	2	2	2	
EP-838/20% CW	3	3	3		3	3	3				3	3	3				2	2	
D0 Heat 316/ A0																	2	2	
D0-Heat 316/ 20% CW	2	2	2		2	2	2		2	2	2	2	2		2	2	2	2	
P7/A0																		2	
P7/20% CW																		2	
M0/A0																			2
M0/20% CW																	2		2
M1/A0																			2
M1/20% CW																	2		2
M2/A0																			2
M2/20% CW																	2		2
M6/A0																			2
M6/20% CW																	2		2

[a]Discharged April 1984, cycle 4; approximately 6 to 10.5 dpa.

[b]Currently being irradiated in cycles 5 and 6 and to higher fluence.

[c]Reloaded June 1984; currently being irradiated in cycles 5 and 6 and to higher fluence.

[d]Discharged April 1984, cycle 4; approximately 13.6 to 15.6 dpa.

[e]Discharged April 1984, cycle 4; approximately 13.6 to 15.6 dpa, with a 6-min temperature excursion to 820°C.

[f]Reloaded June 1984; currently being irradiated and to be discharged after cycles 5 and 6.

The tensile specimens included in level 5 at 600°C are intended to provide a relative comparison of mechanical behavior for several PCA compositional and microstructural variants irradiated in FFTF, as well as fluence-dependent behavior for PCA-A3 and -B3 (Table 2.5.4). In addition, 20%-CW 316 was included to provide a reference base line for the titanium-modified advanced alloys. Furthermore, the type 316 and PCA (K-280) alloys irradiated in FFTF will provide a low helium generation rate base line against which to evaluate the effects of helium embrittlement on similar specimens irradiated at the higher generation rates found in ORR (MFE-4, A and B)[1] and HFIR (CTRs-42 and -43 and JPs-6 through 8).[6,7] The comparison between PCAs-A3 and -B3 in several reactor environments should also help elucidate the mechanism of helium embrittlement resistance that is suggested to hinge upon the development of medium-coarse distributions of grain boundary MC prior to irradiation and its stability during irradiation.[6,8]

Table 2.5.4. Distribution of tensile specimens in the FFTF/MOTA experiments at 600°C (level 5)

Alloy/pretreatment condition	Number of specimens	
	SS-1	Sub-mini
X-15893 316/(20% CW)	4	
EP-838/20% CW	4	
PCA (K-280)/A3	8	2
PCA (K-280)/B3	6	2
PCA-13/A3	2	
PCA-19/A3	2	
PCA-20/A3	2	

Finally, tubes KK02, KK03 (both at 520°C) and KN02, KN03, (both at 600°C) in levels 1 and 2 also contain TEM disks previously irradiated in HFIR. These are part of a unique irradiation experiment to test effects of helium level, distribution, and/or grown-in microstructure from prior HFIR irradiations on void development during subsequent high fluence irradiation in FFTF. These are described in more detail elsewhere.[9]

2.5.5 References

1. M. L. Grossbeck and K. R. Thorns, "ORR-MFE-4: A Spectral Tailoring Experiment to Simulate the He/dpa Ratio of a Fusion Reactor in Austenitic Stainless Steels," pp. 10–23 in *ADIP Quart. Prog. Rep. June 30, 1980*, DOE/ER/0045/3, U.S. DOE, Office of Fusion Energy.
2. M. L. Grossbeck and J. W. Woods, "Experiments HFIR-CTR-30, -31, and -32 for Irradiation of Transmission Electron Microscopy Disk Specimens," pp. 36-44 in *ADIP Quart. Prog. Rep. Sept. 30, 1980*, DOE/ER/0045/4, U.S. DOE, Office of Fusion Energy.
3. P. J. Maziasz, "Swelling and Swelling Resistance Possibilities of Austenitic Stainless Steels in Fusion Reactors," *J. Nucl. Mater.* 122&123, 472–86 (1984).
4. Letter from A. M. Ermi (HEDL) to A. F. Rowcliffe (ORNL) on July 26, 1984.
5. R. L. Klueh and P. J. Maziasz, "The Development of Austenitic Steels for Fast Induced-Radioactivity Decay," pp. 59–60 in *ADIP Semiannu. Prog. Rep. March 31, 1984*, DOE/ER/0045/12, U.S. DOE, Office of Fusion Energy.
6. D. N. Braski and P. J. Maziasz, "The Tensile Properties and Bend Ductility of PCA after Irradiation in HFIR," pp. 61–3 in *ADIP Semiannu. Prog. Rep. March 31, 1984*, DOE/ER/0045/12, U.S. DOE, Office of Fusion Energy.
7. A. F. Rowcliffe, M. L. Grossbeck, S. Jitsukawa, and M. Tanaka, "The U.S./Japan Collaborative Testing Program in HFIR and ORR: Irradiation Matrices for HFIR," Sect. 2.9, this report.
8. P. J. Maziasz and D. N. Braski, "Microstructural Design of PCA Austenitic Stainless Steel for Improved Resistance to Helium Embrittlement under HFIR Irradiation," *J. Nucl. Mater.* 122&123, 305–310 (1984).
9. P. J. Maziasz, "Reirradiation in FFTF of Swelling-Resistant Path A Alloys Previously Irradiated in HFIR," Sect. 2.6, this report.

2.6 REIRRADIATION IN FFTF OF SWELLING-RESISTANT PATH A ALLOYS PREVIOUSLY IRRADIATED IN HFIR — P. J. Maziasz (Oak Ridge National Laboratory)

2.6.1 ADIP Tasks

ADIP Task I.A.2, Define Test Matrices and Test Procedures, I.C.l, Microstructural Stability, and I.C.2, Microstructure and Swelling in Austenitic Stainless Steels.

2.6.2 Objectives

The objective is to test the hypothesis that high concentrations of helium can extend the void swelling resistance of cold-work advanced titanium-modified Path A alloys (like D9 or PCA type alloys) by prolonging the initial low-swelling transient. If the effect exists, it is further our objective to quantify the additional delay of accelerated void swelling and to correlate it with microstructural/microcompositional evolution.

2.6.3 Summary

Disks of PCA (in several pretreatment conditions) and several heats of cold-worked (CW) type 316 and D9 type austenitic stainless steels have been irradiated in HFIR at 300, 500, and 600°C to fluences producing about 10 to 44 dpa and 450 to 3600 at. ppm He. These samples are being reirradiated in the Materials Open Test Assembly (MOTA) in FFTF at 500 and 600°C, together (side by side) with previously unirradiated disks of exactly the same materials, to greater than 100 dpa. These samples, many of which have either very fine helium cluster or helium bubble distributions after HFIR irradiation, are intended to test the possibility and magnitude of a helium-induced extension of the initial low-swelling transient regime relative to the void swelling behavior normally found during FFTF irradiation. Further, these samples will reveal the microstructural stability or evolution differences that correlate with such helium effects.

2.6.4 Progress and Status

2.6.4.1 Introduction

An initially complex sequential HFIR/FFTF irradiation scheme was planned in 1982 to roughly simulate the fusion helium/dpa ratio in large steps by alternately irradiating in one reactor and then the other.' This experiment, however, was postponed. In 1981—84, controversy and two alternative interpretations developed for the effects of helium on swelling for the DO-heat of type 316 irradiated in EBR-II and HFIR; it could not be completely resolved from the limited data available.[2-7] However, the situation was partially resolved when it was suggested that helium effects occurred in the low-swelling transient regime, possibly without affecting the high-swelling rate observed when voids eventually do develop.[8,9] This portion of the experiments involving reirradiation in FFTF/MOTA of specimens previously irradiated in HFIR is concerned with the effects of helium on the low-swelling transient regime.

Both experimental and theoretical studies suggest that helium can either hasten or delay the onset of the accelerated void swelling regime, depending on the degree of increased early bubble nucleation that helium induces, and whether or not this affects development of the other microstructural components.[2,5,9-11] The emphasis of these HFIRIFFTF irradiation experiments is to test for the possibility of helium-delayed void swelling and then to determine the duration of any helium extension of the low-swelling transient regime. Further, it is suggested that the microstructural reasons for an extended low-swelling transient include: (1) helium inducing very high concentrations of fine bubbles early in the irradiation, which then become the dominant point-defect sinks to virtually eliminate the net bias and make the critical radius for conversion of bubbles to voids nearly infinite, and (2) the same concentrated dispersion of fine bubble-sinks causing sufficient dilution of radiation-induced solute segregation to preclude irradiation-induced phases and allow enhanced thermal precipitation instead. Finally, it has been suggested that cold-worked titanium-modified austenitic stainless steels amplify these reinforcing effects relative to type 316; the amplification is due to fine MC precipitates trapping fine bubbles and stabilizing them against the coalescence coarsening which eventually allows voids to form.' Therefore, it is also intended that these HFIR/FFTF experiments test these mechanisms as well.

2.6.4.2 Experimental Test Matrices and Description

Compositions of the alloys included in this experiment are given in Table *2.6.1,* while their thermal-mechanical treatments and specimen identification codes are listed in Table 2.6.2. A listing of the previous HFIR irradiation conditions and their current locations in the FFTF/MOTA is given in Table 2.6.3. Finally, measurements and/or estimates of the microstructural development obtained during HFIR irradiation prior to the FFTF/MOTA irradiations are given in Table 2.6.4. The disks listed for tubes KK02, KK03, KN02, and KN03 were included with a larger number of previously unirradiated disks, as described elsewhere.[12]

The PCA alloy in the solution-annealed (A1) and 25%-cold-worked (A3) conditions, labeled ED and EC, respectively, and the 20%-cold-worked (CW) N-lot 316 samples were irradiated at 300°C to various fluences in HFIR-CTRs-30 through -*32* (ref. 13). The PCA-A3 (EC) specimens irradiated to about 44 dpa at 600°C were also

Table 2.6.1. Alloy chemistries for steels irradiated first in HFIR and then in FFTF/MOTA

Alloy designation	Weight percent															
	Fe	Cr	Ni	no	Mn	Si	Ti	Nb	V	C	N	P	Co	Cu	B	5
PCA (K280)	bal	14.0	16.2	2.3	1.8	0.4	0.24			0.05	0.01	0.01			0.001	0.003
PCA-1	bal	14.0	16.0	2.5	2.1	(0.01	0.13	0.12	<0.01	0.04	0.003	<0.001	<0.01	0.02	<0.001	0.008
PCA-2	bal	14.0	16.0	1.4	2.0	<0.01	0.14	0.11	<0.01	0.053	0.004	0.001	(0.01	0.02	<0.001	0.007
PCA-3	bal	14.3	15.8	25	2.0	0.4	0.13	0.11	<0.01	0.056	0.005	<0.001	(0.01	0.02	<0.001	0.007
PCA-4	bal	14.0	16.0	25	2.1	0.07	<0.01	0.26	<0.01	0.051	0.063	0.001	<0.01	0.02	<0.001	0.007
PCA-5	ba1	14.4	15.9	**1.5**	2.1	0.11	<0.01	0.26	(0.01	0.048	**0.002**	**0.001**	<0.01	0.02	<0.001	0.007
PCA-6	bal	14.0	16.0	2.4	1.9	0.4	0.23	0.01	<0.01	0.083	0.004	<0.001	<0.01	0.02	<0.001	0.007
PCA-7	bal	14.0	16.0	2.4	2.6	0.4	(0.01	<0.01	<0.01	0.057	0.002	**0.001**	<0.01	0.02	<0.001	*0.001*
PCA-8	bal	13.9	16.0	2.7	2.1	<0.01	0.17	**0.14**	(0.01	0.081	*0.001*	<0.001	<0.01	0.02	(0.001	0.008
PCA-9	bal	13.8	16.0	2.5	2.0	**0.4**	0.25	<0.01	<0.01	0.013	0.005	**0.03**	<0.01	0.02	<0.001	0.007
316 (N-lot)	bal	16.5	13.5	2.5	1.6	05				0.05	0.006	0.013			0.0008	0.006
316 (DO-heat)	bal	18.0	13.0	2.6	1.9	08	0.05			0.05	0.05	0.01	0.004		0.0005	0.016
09 A9	bal	16.3	13.1	2.5	2.0	08	0.1	<0.01	<0.01	0.04	0.05	0.036	0.004		0.0005	0.016
09 F	bal	14.3	14.3	2.22	2.1	10	0.3			0.05	0.002					
D9 C1	bal	13.5	**15.5**	1.3	2.0	10	0.2			0.04	0.013					
D9 699-6	bal	14.2	15.2	2.0	2.1	05	0.01	0.02	0.02	0.03	0.004	0.005	0.02	0.02	<0.001	0.001

Table 2.6.2. Alloy designations, thermal-mechanical treatments, and identification codes for austenitic steel irradiated in HFIR and then in FFTF/MOTA

Alloy	Thermal-mechanical treatment	Identification
PCA (K-280)	Solution annealed at 1100°C for 30 min (A1)	ED-#[a]
PCA (K-280)	A1 treatment + 25% CW (A3)	EC-#, EK-#
PCA (K-280)	A1 treatment + 8 h at 800°C + 8 h at 900°C (B3)	EL-#
	Solution annealed at 1050°C for 1 h (A0)	
N-Lot *316*	A0 treatment + 20% CW	AD-#
DO-heat 316	A0 treatment + 20% CW	AL-#
PCA-1	A1 treatment + 25% CW	FC-#
PCA-2	A1 treatment + 25% CW	FE-#
PCA-3	A1 treatment + 25% CW	FG-#
PCA-4	A1 treatment + 25% CW	FJ-#
PCA-5	A1 treatment + 25% CW	FL-#
PCA-6	A1 treatment + 25% CW	FN-#
PCA-7	A1 treatment t 25% CW	FQ-#
PCA-8	A1 treatment t 25% CW	FS-#
PCA-9	A1 treatment + 25% CW	FV-#
D9-A9	A1 treatment t 25% CW	GA-#
D9-C1	A1 treatment + 25% CW	GC-#
D9-F	A1 treatment + 25% CW	GE-#
D9-J699-6	A1 treatment + 25% CW	GG-#

[a]Numbers from 0 to 99.

Table 2.6.3. Distribution of previously irradiated HFIR specimens being reirradiated in FFTFIMOTA

Alloy/ pretreatment	Previous HFIR irradiation conditions			Specimen identification and FFTF/MOTA irradiation conditions (levels 1 and 2)			
	Temperature (°C)	dpa	Helium (at. ppm)	520°C		600°C	
				KK02	KK03	KN02	KN03
PCA (K-280)/A1	300	9.7	450			ED-24	
	300	~22	~1600			ED-16	ED-29
	300	~44	~3600			ED-06	
PCA (K-280)/A3	300	~44	~3600			EC-57	EC-44
	500	~22	~1750	EK-7	EK-8		
	600	~22	~1750			EK-5	
	600	~44	~3600			EC-12	EC-15
316 (N-lot)/	300	~22	~1400			AD-15	AD-39
20% CW	300	~44	~3000			AD-31	AD-43
	500	~22	~1475	AD-52	AD-54		
316 (DO-heat)/	500	~22	~1400	AL-14	AL-11		
20% CW	600	~22	~1400			AL-13	AL-19
PCA (K-280)/B3	500	~22	~1700	EL-5	EL-7		
	600	~22	~1700			EL-4	EL-8
D9-A9/A3	500	~22	~1400	GA-20	GA-19		
	600	~22	~1400			GA-15	GA-14
D9-C1/A3	500	~22	~1500	GC-7	GC-11		
	600	~22	~1500			GC-6	GC-8
D9-F/A3	500	~22	~1600	GE-14	GE-4		
	600	~22	~1600			GE-11	GE-12
D9-699-6/A3	500	~22	~1600	GG-12	GG-3		
PCA-0/A3	500	~22	~1700	FA-1	FA-5		
	600	~22	~1700			FA-4	
PCA-1/A3	500	~22	~1700	FC-5	FC-7		
	600	~22	~1700			FC-1	FC-6
PCA-2/A3	500	~22	~1700	FE-1	FE-9		
	600	~22	~1700			FE-7	FE-0
PCA-3/A3	500	~22	~1700	FG-0	FG-8		
	600	~22	~1700			FG-9	FG-1
PCA-4/A3	500	~22	~1700	FJ-5	FJ-4		
	600	~22	~1700			FJ-2	FJ-8
PCA-5/A3	500	~22	~1700	FL-4	FL-1		
	600	~22	~1700			FL-7	FL-5
PCA-6/A3	500	~22	~1700	FN-18	FN-1		
	600	~22	~1700			FN-12	FN-3
PCA-7/A3	500	~22	~1700	FQ-2	FQ-16		
	600	~22	~1700			FQ-19	
PCA-8/A3	500	~22	~1700	FS-4	FS-8		
	600	~22	~1700			FS-12	FS-2
PCA-9/A3	500	~22	~1700	FV-15	FV-2		
	600	~22	~1700			FV-14	FV-6

Table 2.6.4. Observed[a] or estimated microstructural conditions far HFIR irradiated austenitic stainless steel specimens prior to irradiation in FFTFIMOTA

Alloy/ condition	Specimen	HFIR irradiation conditions			Microstructure					
					Cavities					
		Temperature (°C)	Fluence (dpa)	Helium (at. ppm)	Type	Size (nm)	Concentration (m^{-3})	Total CVF swelling (%)	Dislocation structure	Precipitate microstructures
PCA/A1	ED-R	300			None detected				Tremendous density of small Frank loops plus "black dot" damage; no network	None detected
	ED	300	~22	~1600	Not observed					
	EO-60	300	~44	~3600	Bubbler	<2	>2 × 10^{23}	<0.1	Similar to above plus a little network	None detected
PCA/A3	EC-70	300	~44	~3600	Bubbler	Similar to above			Similar to above, a little more network	None detected
	EC	600	~22	~1750	Bubbles, bimodal	4.3 9	5.3 × 10^{22} 1 × 10^{21}	0.2–0.25	Network plus a feu large Frank loops	Many patches of fine MC particles
	EC	600	~44	~3600	Bubbles, bimodal	4.3 11.7	2.7 × 10^{22} 8.6 × 10^{20}	~0.25	Similar to above	Similar to above
	EC	500	~22	~1150	Not Observed					
316 (N-lot)/ 20% CW	AD	300	~22	~1400	Not observed					
	AD	300	~44	~3000	Bubbles	2.3	1.6 × 20^{23}	0.11	Similar to ED and EC at 300°C	None detected
	AD	500	~22	~1475	Bubbler, voids	4 10	3.7 × 10^{22} 1.7 × 10^{21}	0.25	Many Frank loops (medium-sized) plus network	Some medium-fine MC plus M_6C plus coarser M_6C at faulted bands and in the same matrix
PCA/B3					Expected to be similar to PCA-A3 (EC) irradiated at the same conditions					
PCA-0, -1, -2, -3, -4, -5, -6. -8, and -9 and D9s/ A3					Expected to be somewhat similar to PCA/A3 (EC) at 500 and 600°C					
316 (DO-heat)/ 20% CW[b]		500	~22	~1400	Bubbles	~2–6	0.7–2 × 10^{22}	~0.1–0.3	Lou concentration of network; no loops	Medium-coarse distribution of M_6C, Laves, and $M_{23}C_6$
		600	~22	~1400	Bubbler	~22	>3 × 10^{20}	~0.1–0.3	Lou concentration of networks: no loops	Similar phases but more coarsely distributed
PCA-7/A3					Expected to fall somewhere between the behavior extremes of DO and N-lot heats of type 316 stainless steel					

[a] Determined from TEM examination of an identical disk irradiated side by ride with or at similar conditions to the actual dirt inserted into FFTF/MOTA.

[b] Numbers and observations interpolated from the same steel irradiated in HFIR over the fluence range 7 to 61 dpa from 425 to 650°C, as reported in the following: P. J. Maziasz, pp. 28–56 in *ADIP Quart. Prog. Rep. March 31, 1981*, DOE/ER-0045/6; pp. 54–97 in *ADIP Semiann. Prog. Rep. Sep. 30, 1981*, DOE/ER-0045/7; *J. Nucl. Mater.* 1086109, 359–84 (1982).

obtained from these experiments. All other disks were irradiated at 500 and 600°C to about 22 dpa in HFIR-CTRs-42 and -43 (ref. 14). Microstructural data included in Table 2.6.4 for PCA-A1 and -A3 and for CW N-lot 316 have been generally described,[15-17] but not reported in detail previously. Microstructural development of CW DO-heat 316 after HFIR irradiation at 500 and 600°C to about 22 dpa is estimated, based upon interpolation between data from previous HFIR irradiations of that steel covering a wide range of conditions (see Table 2.6.4 for references). Microstructural development was not measured for the PCA developmental compositional variants (PCAs 0 through 9) or the D9 type alloys, but based on their compositions, they should be roughly similar to the PCA-A3 alloy, consisting of fine distributions of MC particles and helium bubbles.

The primary objective of these experiments is to measure differences in macroscopic void swelling development between samples preconditioned with fine helium cluster and/or bubble distributions via prior HFIR irradiation, and samples irradiated solely in FFTF. This effect should be manifest by PCA-A3 specimens irradiated in both reactors at the same temperatures relative to their control samples irradiated in FFTF at 500 and 600°C. PCA-A1 and -A3 irradiated in HFIR at 300°C to varying fluences contain even finer distributions of helium, equivalent to cold cyclotron pre-injections; these may reveal whether or not longer low-swelling transients continue to correlate with even finer initial helium distributions. The D9 type alloys were included to evaluate the range of heat-to-heat variations to be expected in CW advanced titanium-modified austenitic stainless steels for either the straight FFTF void swelling behavior or the helium extended low-swelling transients. Cold-worked samples of DO and N-lot heats of type 316 were also included (together with PCA-7), with and without HFIR preirradiation, to gage the relative improvement offered by the PCA and D9 type alloys, for either normal or helium-induced void swelling resistance in FFTF. Finally, the compositional variants (modified specifically for improved MC stability) of the PCA are included to evaluate the potential of further improvement in swelling resistance through alloy development.

2.6.4.3 Current Status

All specimens are currently being irradiated in cycles 5 and 6 of FFTF in levels 1 and 2 of the MOTA (500 and 600°C). Current plans are to continue irradiation to at least 60 dpa before beginning alternate discharges of one of the two identical tubes at each temperature, followed by immersion density measurement and then continued FFTF irradiation of those disks which do not show appreciable swelling. Transmission electron microscopy (TEM) is planned only on a select group of specimens, either after significant swelling develops in the 100 to 150 dpa fluence range, or if helium extends the low-swelling transient regime beyond 150 to 200 dpa.

2.6.4.4 References

1. A. M. Ermi and J. M. Vitek, "HFIR/FFTF Irradiation Experiment — Conceptual Plan," pp. 17—24 in *ADIP Quart. Frog. Rep. March 31, 1982,* DOE/ER/0045/8, U.S. DOE, Office of Fusion Energy.

2. G. R. Odette, P. J. Maziasz, and J. A. Spitznagel, "Fission-Fusion Correlations for Swelling and Microstructure in Stainless Steels: Effects of the Helium to Displacement Per Atom Ratio," *J. Nucl. Mater.,* 103&104, 1289-1304 (1981).

3. H. R. Rrager and F. A. Garner, "Comparison of the Swelling and the Microstructural/Microchemical Evolution of AISI 316 Irradiated in EBR-II and HFIR," *J. Nucl. Mater.,* 103&104, 993—98 (1981).

4. H. R. Brager and F. A. Garner, "Influence of Neutron Spectra on the Radiation-Induced Evolution of AISI 316," *J. Nucl. Mater.,* 108&109, 347—58 (1982).

5. P. J. Maziasz, "Some Effects of Increased Helium Content on Void Formation and Solute Segregation in Neutron Irradiated Type 316 Stainless Steel," *J. Nucl. Mater..* 1088,109, 359—84 (1982).

6. H. R. Brager and F. A. Garner, "Microstructural and Microchemical Comparisons of AISI 316 Irradiated in HFIR and EBR-II," *J. Nucl. Mater.,* 117, 159—75 (1983).

7. H. R. Brager and F. A. Garner, "The Microchemical Evolution and Swelling of AISI 316 Irradiated in HFIR and EBR-II," pp. 1-4 in *Proc. Caf. Dimensional Stability and Mechanical Behaviour of Irradiated Metals and Alloys, British Nucl. Energy Soc.,* London, 1984.

8. F. A. Garner, "Recent Insights on the Swelling and Creep of Irradiated Austenitic Alloys," *J. Nucl. Mater.,* 1228123, 459-71 (1984).

9. P. J. Maziasz, "Swelling and Swelling Resistance Possibilities for Austenitic Stainless Steels in Fusion Reactors," *J. Nucl. Mater.* 122&123, 472—86 (1984).

10. R. E. Stoller and G. R. Odette, 'The Effect of Helium on Swelling in Stainless Steel: Influence of Cavity Density and Morphology," pp. 275—94 in Conf. *Proc. Effects of Radiation a Materials: Eleventh Conference,* ASTM-STP-782, eds., H. R. Brager and J. S. Perrin, American Society for Testing and Materials, Philadelphia, 1982.

11. G. R. Odette and R. E. Stoller, "A Theoretical Assessment of the Effect of Microchemical. Microstructural, and Environmental Mechanisms on Swelling Incubation in Austenitic Stainless Steel;," *J. Nucl. Mater.,* 122&123, 514—19 (1984).

12. P. J. Maziasz, "Test Matrices for Irradiation of Path A Prime Candidate Alloy and Developmental Alloys in FFTF," Sect. 2.5., this report.

13. M. L. Grossbeck and J. W. Woods, "Experiments HFIR-CTR-30, -31, and -32 for Irradiation of Transmission Electron Microscopy Disks," pp. 10-23 in *ADIP Quart. Prog. Rep. June 30, 1980,* DOE/ER/0045/3, U.S. DOE, Office of Fusion Energy.

14. D. N. Braski and P. J. Maziasz, "The Tensile Properties and Rend Ductility of PCA after Irradiation in HFIR," pp. 61–3 in *ADIP Semiann. Prog. Rep. March 31, 1984,* DOE/ER-0045/12, U.S. DOE, Office of Fusion Energy.

15. P. J. Maziasz and D. N. Braski, "Swelling and Microstructural Development in Path A PCA and Type 316 Stainless Steel Irradiated in HFIR to About 22 dpa," pp. 44-62 in *ADIP Semiann. Prog. Rep. Sept. 30, 1982,* DOE/ER-0045/9, U.S. DOE, Office of Fusion Energy.

16. P. J. Maziasz and D. N. Braski, "Swelling and Microstructural Development of Path A PCA and Type 316 Stainless Steel Irradiated in HFIR," pp. 28–38 in *ADIP Semiann. Frog. Rep. March 31, 1983,* DOE/ER-0045/10, U.S. DOE, Office of Fusion Energy.

17. P. J. Maziasz and D. N. Braski, "Improved Swelling Resistance for PCA Austenitic Stainless Steel Under HFIR Irradiation Through Microstructural Control," *J. Nucl. Mater.,* 122&123, 305–10 (1984).

2.7 AN ASSESSMENT OF HELIUM EFFECTS ON SWELLING BY REIRRADIATION IN FFTF OF PATH A ALLOYS PREVIOUSLY IRRADIATED IN HFIR — P. J. Maziasz (Oak Ridge National Laboratory), F. A. Garner and H. R. Brager (Westinghouse Hanford Company)

2.7.1 ADIP Tasks

ADIP Task I.A.2, Define Test Matrices and Test Procedures, I.C.1, Microstructural Stability, and I.C.2, Microstructure and Swelling in Austenitic Stainless Steel.

2.7.2 Objectives

The objective of this effort is to determine whether or not large amounts of helium, introduced via prior High Flux Isotope Reactor (HFIR) irradiation, alter the void swelling behavior normally found during Fast Flux Test Facility (FFTF) irradiation.

2.7.3 *Summary*

Specimens of the Path A PCA and of N-lot 316 have been irradiated in HFIP at 400 to 600°C to fluences producing approximately 10 to 44 dpa and 500 to 3600 at. ppm He, in both the solution annealed and 20 to 25% cold-worked conditions. The cavity swelling and total microstructural evolution of most samples have been observed via transmission electron microscopy on identical disks irradiated side by side in HFIR, and immersion densities have also been measured prior to insertion into FFTF/MOTA (Materials Open Test Assembly of the Fast Flux Test Facility). These disks are currently being irradiated in the FFTFIMOTA (cycles 5 and 6), side by side with disks of the same material which were not previously irradiated in HFIR. These specimens have been divided into two subsets for discharges after 30 and 60 dpa.

2.7.4 Progress and Status

2.7.4.1 Introduction

Several interpretations have been advanced for whether or not helium affects void swelling, from a limited but unique set of data on the DO heat of type 316 stainless steel irradiated in EBR-II and in HFIR, as stated elsewhere.[1,2] Aside from these data, there is growing evidence that Fe-Ni-Cr austenitic alloys eventually develop voids and then swell at a typical rate of approximately 1%/dpa in the posttransient regime;[3] however, there is also a growing body of evidence that several effects of helium are most strongly manifest in the transient regime, either accelerating or delaying the onset of void swelling.[4] These data suggest that when helium bubble nucleation is on a sufficiently fine scale, the net bias is lowered and radiation-induced solute segregation is suppressed; under these circumstances void development is retarded.' It is therefore the intent of these experiments to test several questions related to these effects.

2.7.4.2 Experimental Description

Actual specimen identification codes and previous HFIR irradiation conditions for the various transmission electron microscope disks inserted into the FFTF/MOTA experiment are qiven in Table 2.7.1. Also included are the microstructural observations made on duplicate disks irradiated side by side with those in HFIR. The SA N-lot 316 (AGs) samples irradiated in HFIR at 500 and 600°C to 22 dpa and the CW N-lot 316 samples (AD-53, -56) irradiated at 600°C to 22 dpa were obtained from HFIR-CTRs-42 and -43. All other specimens were irradiated in HFIR-CTR-30 through -32.

Several samples were intended to answer the question of whether or not helium has any effect on swelling at 400°C. This question is important because many fusion reactor designs are currently emphasizing lower first wall operating temperatures. This involves continued irradiation in FFTF/MOTA at 400°C of SA and 25% CW PCA and 20% CW N-lot 316 previously irradiated to 10 to 44 dpa at 400°C in HFIR, and their comparison relative to control samples of the same materials irradiated side by side in FFTF without prior HFIR irradiation. Further, if swelling differences arise between the various HFIR preirradiated specimens, these may correlate with bubble or precipitate microstructural differences, as indicated in Table 2.7.1, to suggest responsible mechanisms. Data from specimens irradiated at 400°C are unique to this portion of the overall sequential HFIR/FFTF irradiation experiment.[2]

Two other questions that may be answered by samples irradiated at 500 and 600°C are: (1) Is the void formation and swelling observed in HFIR actually accelerated (shortened low-swelling transient regime) relative to FFTF irradiated material? (2) Once void swelling begins, does it continue unhindered to attain the 1%/dpa rate independent of microstructual differences or helium generation rate? Samples of SA PCA and 20% CW N-lot 316 are included which have either significant levels of void swelling after HFIR irradiation at 500 and 600°C (En-01, ED-72, AD-20, and An-) or microstructures which are approaching the onset of rapid void swelling. In general, such microstructures are characterized by Frank loops plus network and irradiation induced G and γ' phases or irradiation-enhanced M_6C (ED-15, An-19, -34, and -20). Irradiation of these samples is continued at about the same temperatures in FFTF/MOTA, again side by side with control

samples of exactly the same material but without prior HFIR irradiation. These samples should answer several important void swelling behavior and mechanism questions for fusion with regard to helium effects in the transient or posttransient regimes. Further, these samples complement similarly HFIR irradiated specimens of 25%-CW PCA and related alloys designed to test the possibility of helium extended transient regimes in FFTF at 500 and 600°C (ref. 2).

2.7.4.3 Current Status

These specimens have been divided into two groups and are currently being irradiated in cycles 5 and 6 of FFTF. Discharge and examinations are planned after discharges of one group of specimens at 30 dpa and the other group at 60 dpa (ref. 1).

2.7.5 References

1. H. R. Brager, F. A. Garner, and P. J. Maziasz, "Reirradiation of HFIR Specimens in FFTF," to be published in *Damage Analysis and Fundamental Studies Quart. Prog. Rep.*, 1984.

2. P. J. Maziasz, "Reirradiation in FFTF of Swelling-Resistant Path A Alloys Previously Irradiated in HFIR," Sect. 2.6 in this report.

3. F. A. Garner, "Recent Insights on the Swelling and Creep of Irradiated Austenitic Alloys," *J. Nucl. Mater.* 122&123, 459–71 (1984).

4. P. J. Maziasz, "Swelling and Swelling Resistance Possibilities for Austenitic Stainless Steels in Fusion Reactors," *J. Nucl. Mater.* 122&123, 472–86 (1984).

Table 2.7.1. Specimen identification, prior HFIR irradiation history, and microstructural development of specimens subsequently irradiated in FFTF

Alloy, condition	Specimen identification	HFIR irradiation conditions			Microstructural conditions				Dislocation structure[a]	Precipitate microstructure[a]
		Temperature (°C)	dpa	Helium (at. ppm)	Cavity character	Cavity diam (nm)	Concentration (m^{-3})	Total cavity volume fraction swelling (%)		
PCA, SA	(1) ED-09, -98		None			None		None	Solution annealed	Some medium-sized MC particles from fabrication
	(1) B 7	00	~10 5	~20		b	b	b	High concentrations of Frank loops	b
	(1) ED-19	400	~22	~1700	Bimodal	2.5 6.9	1.5×10^{23} 3×10^{21}	0.2	Some network and many Frank loops	Coarser MC, some γ′, and possibly some G phase
	(1) ED-90	400	~44	~3600		5.9	8.2×10^{22}	0.94	Some network and many Frank loops	Coarser MC and some γ′
	(2) ED-15, -18	500	~22	~1700	Bimodal Matrix voids	2.2 10.1	7.8×10^{22} 9.7×10^{21}	0.84	Network and Frank loops	Coarser γ′, a little MC, possibly some G
	(1) ED-01	600	~22	1750	Bubbles Matrix voids Ppt. voids	6.1 21.9 53	1.3×10^{22} 1.3×10^{21} 3×10^{19}	1.7	Network and larger Frank loops	Coarse G phase, some fine MC, and γ′
	(1) ED-72	600	~44	~3600	Bubbles Matrix voids Ppt. voids	4.9 28 41	2.1×10^{22} 1.1×10^{21} 1.13×10^{21}	6.9	Network and some small Frank loops	Coarse G phase, little or no MC and γ′
PCA, 25% CW	(2) EC-99, -68	None			None				Cold-worked network	None
PCA, 25% CW	(1) EC-04	400	~22	~1700		2.3	2.1×10^{23}	0.13	Network plus many Frank loops	Tremendous concentration of fine MC
	(1) EC-92	400	~44	~3600		3.0	2.4×10^{23}	0.37	Network plus many Frank loops	Fine and coarser MC
N-lot 316, 20% CW	(1) AD-04	400	~22	~1475	Bimodal	3.2 5.4	7.4×10^{22} 1.6×10^{21}	0.14	Network plus many Frank loops	Some coarser MC (VC?), very little γ′
	(2) AD-19, -34	500	~22	~1475	Bimodal	4.0 9.8	3.7×10^{22} 1.7×10^{21}	0.25 0.25	Network plus Frank loops	Many medium-sized M_6C particles
	(1) AD-20	500	~44	~3000	Bubbles Matrix voids Ppt. voids	5.8 13.3 60	7.2×10^{22} 9.9×10^{21} 1.7×10^{19}	3.6	Network plus Frank loops	Tremendous density of medium and coarse M_6C
	(2) B 53 5	0	~22	~75	Bubbles Matrix voids	4.5 11.8	2.2×10^{22} 3×10^{21}	0.52	Network plus Frank loops	Some γ′ in matrix, coarse M_6C on faulted bands
	(1) AD-????	600	~44	~3000	Bubbles Matrix voids Ppt. voids	9.3 29.3 86	2.5×10^{21} 2.7×10^{21} 1.86×10^{19}	5.9	Loose network	A tremendous amount of coarse M_6C
N 0 16, SA	(2) AG-3, -6	500	~22	~1475	c	c	c	c	c	c
	(2) AG-5, -9	600	~22	~1475	c	c	c	c	c	c

[a]Transmission electron microscope observations were made on duplicate disks irradiated side by side in HFIR.

[b]Not detectable.

[c]Not measured.

28 MINIATURE TENSILE TEST SPECIMENS FOR FUSION REACTOR IRRADIATION STUOIES — R. L. Klueh (Oak Ridge National Laboratory)

2.8.1 AOIP Tasks

ADIP Task I.A.2, Define test matrices and procedures.

2.8.2 Objectives

Space limitations in nuclear reactors have resulted in the development of several miniature tensile test specimens for use in determining the effect of irradiation on tensile properties. The objective of this study was the comparison of tensile properties obtained from four different commonly used miniature tensile specimens machined from the same heat of material.

2.8.3 Summary

Three miniature sheet-type tensile specimens and a miniature rod-type specimen are being used to determine irradiated tensile properties for alloy development for fusion reactors. The tensile properties of type 316 stainless steel were determined with these different specimens, and the results were compared. Reasonably good agreement was observed. However, there were differences that led to recommendations on which specimens are preferred.

2.8.4 Progress and Status

2.8.4.1 Introduction

Because of space limitations in most nuclear reactors used for irradiating materials for mechanical properties testing, miniature mchanical property test specimens are irradiated. Most of the tensile specimens irradiated in the United States Fusion Reactor Materials Program have been of the SS-1 design, which was developed in the Fast Breeder Reactor Program for irradiations in the Experimental Breeder Reactor-I1 (EBR-II). The SS-1 is a sheet specimen with an overall length of 44.5 mm and a reduced gage section 20.3-mm long by 1.52-mm wide by 0.76-mm thick (Fig. 2.8.1)

A rod-tensile specimen was developed for elevated-temperature irradiations in the High-Flux Isotope Reactor (HFIR) (Fig. 2.8.2). The gage section is 18.3-mm long and 2.03-mm in diameter. The spurs shown on the end of the specimen (Fig. 2.8.2) have two purposes: they are used to secure the specimens in the irradiation capsule and are required to ensure a uniform temperature distribution across the gage and shoulders during irradiation.

To further reduce the space occupied by an individual specimen, an SS-2 sheet specimen was developed (Fig. 2.8.3). This specimen is punched from 0.25-mm-thick sheet and has an overall length of 31.8 mm with a gage section 12.7-mm long by 1.02-mm wide. To date, few data have been reported on this specimen.

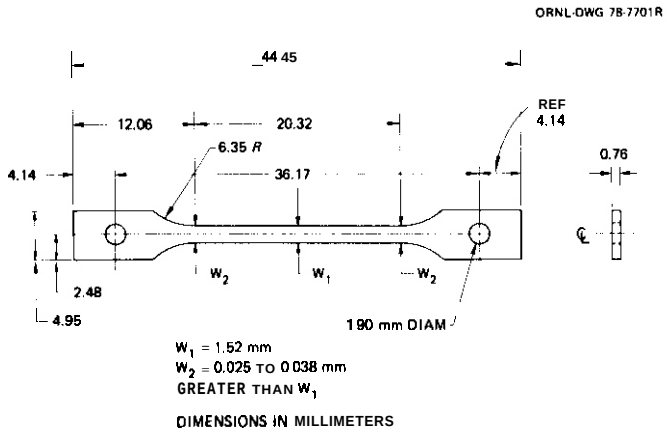

Fig. 2.8.1. The miniature SS-1 sheet tensile specimen.

The Fast Flux Test Facility (FFTF) has recently come into use for materials testing for fusion reactor applications. In the Modular Open Test Assembly (MOTA) in use in FFTF, the maximum utilization of available space requires that the specimen length be restricted to 25.4 mm. Therefore, a 25.4-mm-long variation of the SS-1 sheet specimen was designed. This specimen, designated SS-3, is also machined from 0.76-mm-thick sheet; the reduced section length is 7.02 mm, and the width is 1.52 mm (Fig. 2.8.4).

Still smaller rod specimens have been developed for irradiation in the rotating target neutron source (RTNS-II) and for future use in the fusion materials irradiation test (FMIT) facility.' The gage sections of these specimens were chemically milled from 0.76-mm-diam wire. The reduced section had a minimum diameter of 0.21 to 0.30 mm and a "plastic gage length" of 2.0 to 4.0 mm (ref. 1). When the room-temperature properties of cold-worked type 316 stainless steel, determined using these small specimens, were compared to previous results obtained using larger specimens, reasonable agreement was obtained.' However, no tests were conducted using larger specimens to compare for possible systematic differences between specimens.

Although the various miniature specimens discussed above have been developed and used over the past years, to date no comprehensive experimental comparison using the different specimens on similar material has been made. Such a comparison will be discussed here. Tensile properties have been determined using the four different miniature specimens described above. Tests were made on a single heat of type 316 stainless steel in two different conditions at three test temperatures.

2.8.4.2 Experimental Procedure

The objective of this study was the comparison of the tensile properties obtained from four different tensile specimens machined from the same heat of material. The four specimen types tested were the SS-1 (Fig. 2.8.1), SS-2 (Fig. 2.8.3), SS-3 (Fig. 2.8.4), and the miniature rod-tensile (Fig. 2.8.2).

The type 316 stainless steel test mterial was taken from heat X15893 (magnetic fusion energy reference heat). Tests were made on the steel in the 20%-cold-worked condition and the solution-annealed condition. The SS-1 and SS-3 specimens were machined from 0.76-mm-thick sheet, the SS-2 specimens from 0.25-mm-thick sheet. Prior to the final 20% reduction by rolling, the sheet was annealed 1 h at 1050°C. Miniature rod-tensile specimens were machined from 4.2-mm-diam rod, which was also annealed 1 h at 1050°C prior to the final reduction in area by swaging; the rod used for these tests contained –23% cold work. The solution-annealed specimens were obtained by annealing the cold-worked rod or sheet specimens 1 h at 1050°C.

The grain size of the solution-annealed steels varied somewhat according to the product form from which the specimens were obtained. These ASTM grain size numbers were estimated as follows: grain size No. 4 for the 0.76-mm sheet (SS-1 and SS-3 specimens), grain size No. 3 for the 0.25-mm sheet (SS-2 specimens), and grain sire No. 5 for the 2.03-mm-diam rod (rod-tensile specimens).

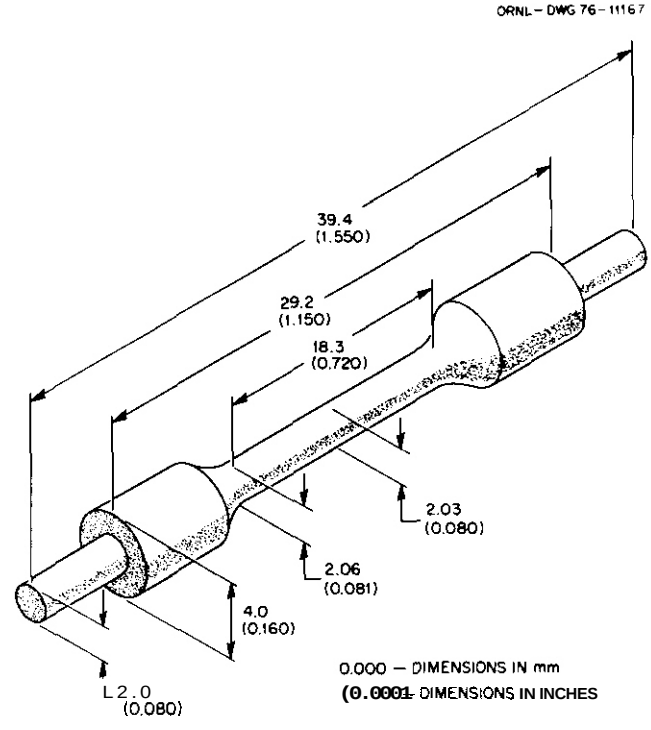

Fig. 2.8.2. The miniature rod-tensile specimen.

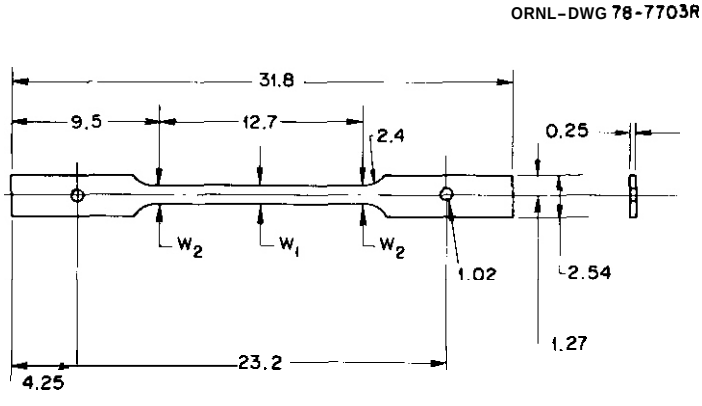

Fig. 2.8.3. The miniature SS-2 sheet-tensile specimen.

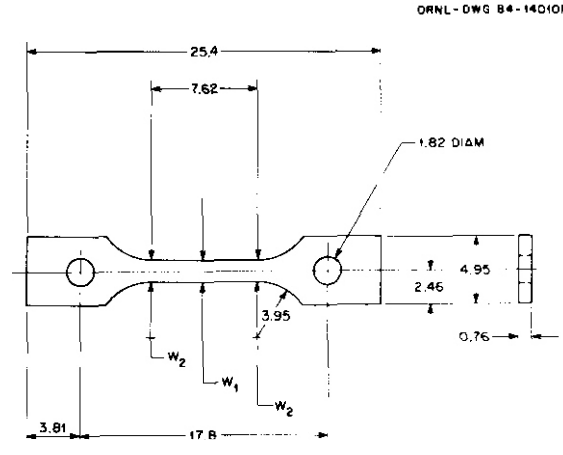

Fig. 2.8.4 The miniature SS-3 sheet-tensile specimen.

All four types of specimens were tested in both the solution-annealed and cold-worked condition. Three of each type of specimen in each condition were tested at room temperature, 300, and 600°C. Tensile tests were conducted in a vacuum chamber on a 120-kV-capacity Instron closed-loop, servohydraulic materials test machine using a crosshead speed of 0.0085 mm/s, which resulted in slightly different nominal strain rates for the different specimens because of the different gage lengths. However, this slight difference in strain rate was not expected to have a significant effect on the tensile properties.

2.8.4.3 Results and Discussion

The tensile results for the various specimens are given in Tables 2.8.1 through 2.8.4. In Figs. 2.8.5 through 2.8.8 the 0.2% yield stress (YS), ultimate tensile strength (UTS), uniform elongation, and total elangation are plotted as a function of temperature. For each set of three tests (on a given type of specimen at a given temperature), the mean value is plotted. Bars that designate plus or minus one standard deviation are also shown for each mean value of the three tensile tests at the given test conditions.

Specimen size or type appears to give rise to several marked differences, and the difference appears to depend on the property being measured. One difference that is not directly attributable to the specimen type is the much higher YS and UTS of the rod-tensile specimens for the cold-worked material. One reason for this difference is that the reduction of area for the rod was −23%. compared to −20% for the sheet

Table 2.8.1. Tensile properties of type 316 stainless steel with SS-1 test specimens

Test temperature (°C)	Strength (MPa)		Elongation (%)	
	Yield	Ultimate	Uniform	Total
Solution annealed				
23	230	590	56	62
23	264	590	53	58
23	215	578	52	57
300	134	479	34	38
300	146	479	33	37
300	134	467	34	37
600	88	441	36	39
600	88	448	35	38
600	96	460	37	39
20%-Cold-worked				
23	135	803	10.1	16
23	748	817	12.0	17
23	733	802	12.4	20
300	646	684	1.6	4.0
300	646	684	2.9	5.3
300	627	684	2.4	4.8
600	536	619	4.6	6.5
600	539	627	4.8	6.9
600	551	634	4.0	6.0

Table 2.8.2. Tensile properties of type 316 stainless steel with SS-2 test specimens

Test temperature (°C)	Strength (MPa)		Elongation (%)	
	Yield	Ultimate	Uniform	Total
Solution annealed				
23	207	577	55	57
23	198	569	48	49
23	224	569	54	56
300	138	465	33	34
300	141	477	34	36
300	152	481	32	34
600	95	440	35	37
600	103	431	27	29
600	86	388	33	35
20%-Cold-worked				
23	733	819	9.8	16.0
23	741	827	6.8	10.0
23	724	827	7.8	10.6
300	655	707	1.0	2.0
300	595	681	1.9	3.2
300	621	638	1.6	2.8
600	534	595	1.6	2.4
600	543	638	2.8	2.9
600	526	603	2.5	3.3

Table 2.8.3. Tensile properties of type 316 stainless steel with SS-3 test specimens

Test temperature (°C)	Strength (MPa)		Elongation (%)	
	Yield	Ultimate	Uniform	Total
Solution annealed				
23	230	605	63	74
23	237	613	67	74
23	222	602	68	80
300	168	505	37	45
300	165	498	41	53
300	167	495	44	54
600	103	464	44	49
600	122	476	44	49
600	103	476	46	51
20%-cold-worked				
23	766	816	14.0	24.3
23	755	816	14.6	23.3
23	761	818	14.6	25.0
300	682	712	4.0	13.0
300	680	706	3.3	11.7
300	669	696	3.0	10.0
600	563	639	5.0	9.7
600	579	640	4.7	9.0
600	585	650	4.7	9.3

Table 2.8.4. Tensile properties of type 316 stainless steel with rod-tensile specimens

Test temperature (°C)	Strength (MPa)		Elongation (%)	
	Yield	Ultimate	Uniform	Total
Solution annealed				
23	239	632	49	56
23	230	621	51	59
23	236	623	50	57
300	165	509	31	38
300	167	512	30	38
300	150	501	30	38
600	111	504	33	40
600	113	506	34	38
600	84	464	31	36
20%-cold-worked				
23	850	882	11.6	20.4
23	849	873	9.8	18.7
23	855	873	8.0	14.8
300	767	774	1.7	7.4
300	762	766	1.0	6.5
300	760	771	1.3	6.4
600	650	712	4.6	9.5
600	647	701	4.0	6.0
600	652	695	3.8	7.4

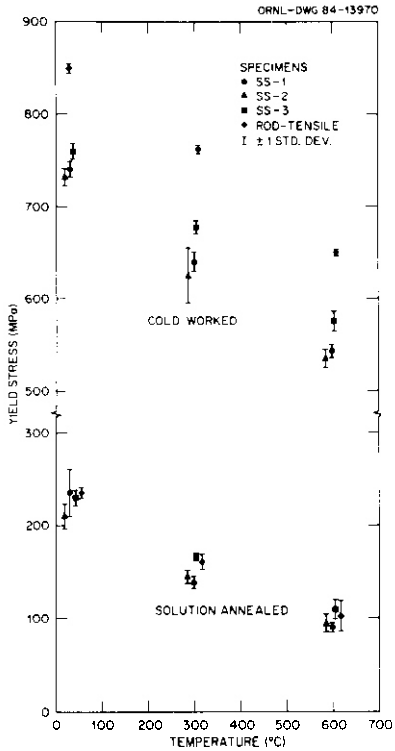

Fig. 2.8.5. The 0.2% yield stress for annealed and cold-worked type 316 stainless steel as a function of temperature for four miniature tensile specimens. The mean value of three tests for each specimen is shown; the error bars indicate ±1 standard deviation.

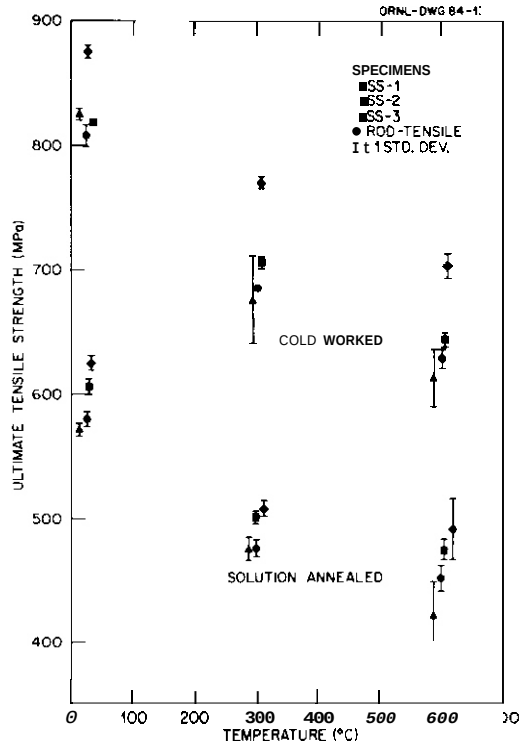

Fig. 2.8.6. The ultimate tensile strength for annealed and cold-worked type 316 stainless steel as a function of temperature for four miniature tensile specimens. The mean value of three tests for each type of specimen is shown; the error bars indicate ±1 standard deviation.

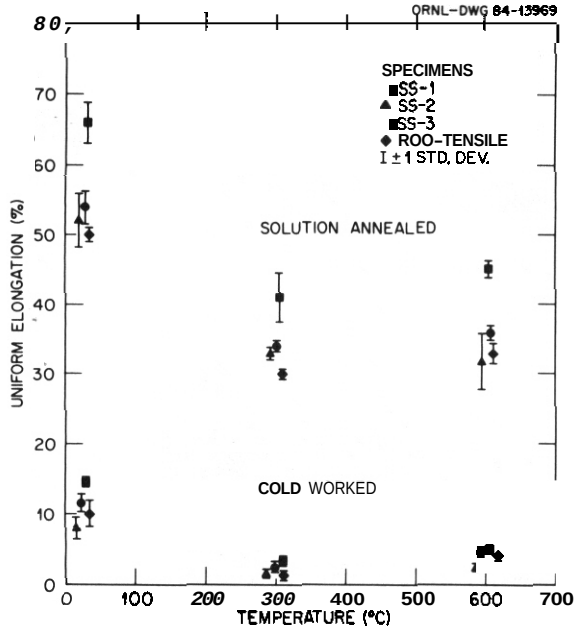

Fig. 2.8.7. The uniform elongation for annealed and cold-worked type 316 stainless steel as a function of temperature for four miniature tensile specimens. The mean value of three tests for each type of specimen is shown; the error bars indicate ±1 standard deviation.

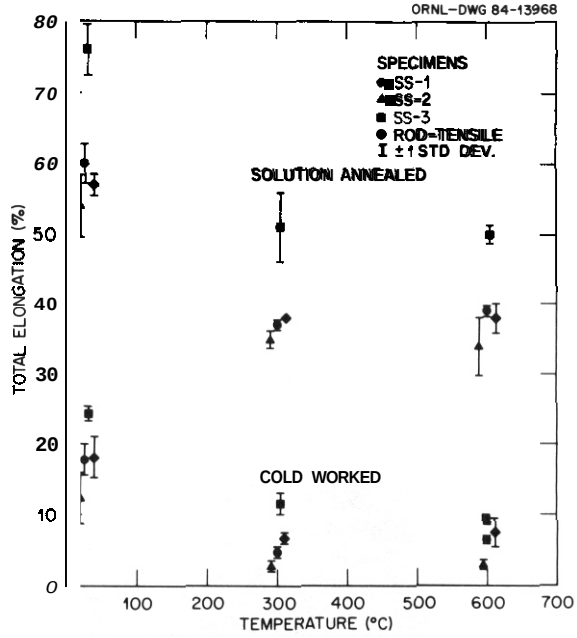

Fig. 2.8.8. The total elongation for annealed and cold-worked type 316 stainless steel as a function of temperature for four miniature tensile specimens. The mean value of three tests for each type of specimen is shown; the error bars indicate ±1 standard deviation.

material. However, part of this large difference in the strength of the rod and sheet may arise because the reductions by rolling and swaging are not directly equivalent, although such equivalence is generally assumed.

In addition to the increased strength of the rod specimens in the cold-worked condition, the UTS of the rod specimens was also somewhat stronger after the solution anneal. The SS-3 specimens generally had the highest YS and UTS of the sheet specimens in both the solution-annealed and cold-worked condition. There was relatively little difference between the strengths of the SS-1 and SS-2 specimens.

Empirical equations have been developed to predict the YS and UTS of solution-annealed austenitic stainless steels.[2] Both YS and UTS were found to depend on chemical composition. The YS was also found to depend on the grain size through the Hall-Petch relationship with strength proportional to $d^{-1/2}$, where d is the grain diameter. No grain size effect was noted for the UTS; instead, it varied with $t^{-1/2}$, where t is the twin spacing. Since only a single composition was tested, the only effect of microstructure on the different specimens should involve grain size and twin spacing.

As stated above, there is little difference in the YS values of the solution-annealed steels. However, if the grain size determines the difference in yield stress, the SS-1 and SS-3 specimens should have similar values, and the rod-tensile specimens should have the highest value. No such systematic difference is observed. Although the UTS values for the solution-annealed rod-tensile specimens is always the largest, the values for the SS-3 are always greater than those of the SS-1 specimens, even though they have the same twin spacing. Although grain size or twin spacing should have no effect on the strenath of the cold-worked material, the results indicate that both the' YS and UTS for the SS-3 specimens are, with one exception, greater than for the SS-1 and SS-2 specimens.

No explanation is available for what appears to be a systematically larger strength obtained using the SS-3 specimen than obtained with the SS-1 specimen for similar test conditions. For all the test conditions used, the greatest difference between the mean values for SS-1 and SS-3 specimens was ~17% for the YS at 300 and 600°C for the solution-annealed material. Differences of <5% were obtained for the YS values of the cold-worked sheet and the UTS values for the solution-annealed and the cold-worked sheet.

Ductility is described by Dieter as "a qualitative, subjective property of a material."[3] Measurements often show considerable variation even for one type of specimen, including large specimens. Surprisingly little difference is noted for the uniform and total elongation of the four types of specimens for the cold-worked condition, although the total elongations for the SS-3 specimens were slightly greater than total elongation values obtained from the other three specimens (Figs. 2.8.7 and 2.R.8). For the solution-annealed material, the uniform and total elongation values of the SS-3 specimens were considerably higher than for the SS-1, SS-2, and rod-tensile specimens, which had similar values. Although the total elongation will depend on the specimen geometry, the uniform elongation should not.[3] Thus, the observation of the

greater uniform elongation of the SS-3 specimens in the solution-annealed condition is unexpected. (The SS-3 specimens also have the highest uniform elongation in the cold-worked condition, but the difference with the other specimens is much less than for the solution-annealed condition.)

When the tested SS-3 specimens were examined, it was found that deformation in the solution-annealed specimens was not confined to the reduced section. Instead, deformation occurred up into the shoulder section [Fig. 2.8.9(*a*)]. This is in contrast to what occurs for the cold-worked SS-3 specimen where essentially all the deformation is confined to the reduced section [Fig. 2.8.9(*b*)]. In effect, therefore, the solution-annealed specimen has a larger gage length than that used to calculate the uniform and total elongation for *SS-3* specimens. A similar observation applies for the SS-1 specimen. However, because the length of the reduced section of the *SS-3* (7.6-mm gage length) is about 38% of the SS-1 (20.3-mm gage length), the effect on the uniform elongation determined with the *SS-3* is considerably affected. (The SS-2 specimens also showed a similar effect.)

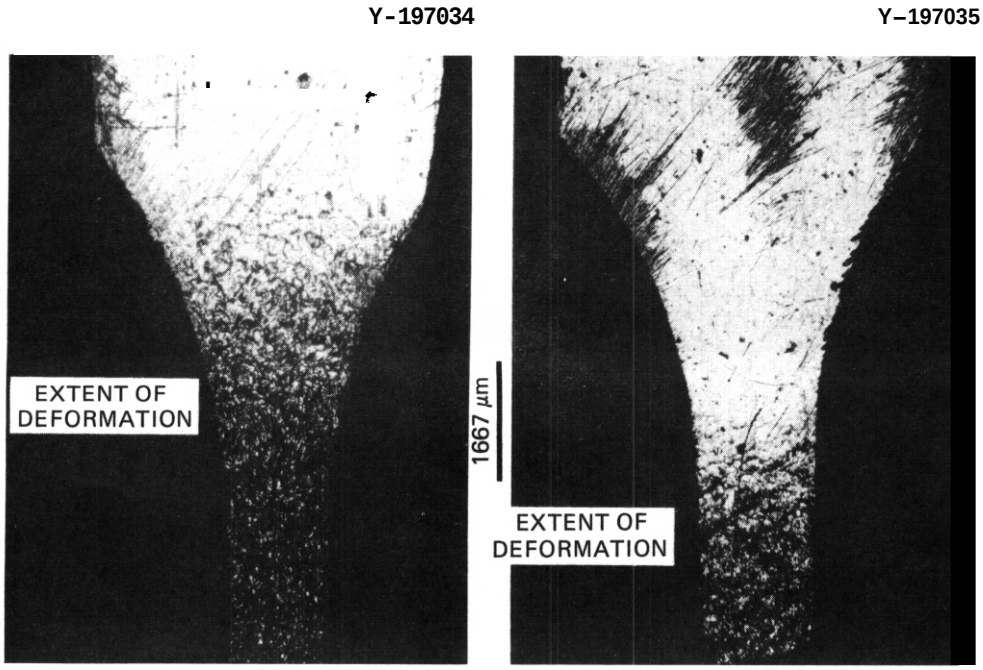

Fig. 2.8.9. A micrograph of *(a)* solution-annealed and *(b)* cold-worked SS-3 tensile specimens tested at room temperature. Note the deformation beyond the reduced section in the solution-annealed specimen.

The reason for the observed behavior involves the deformation behavior of the soft annealed material relative to the stronger cold-worked material. The solution-annealed material in the reduced section work hardens until the strength of this portion of the specimen exceeds the yield stress in the section of the specimen where the reduced section goes into the shoulder section, despite the larger cross-sectional area of the latter portion of the specimen. A similar effect does not occur in the cold-worked specimens because the stainless steel under these conditions does not have the work-hardening capability that it does in the solution-annealed condition. It should be noted, however, that even in the cold-worked condition the *SS-3* specimens have a larger uniform elongation than the 55-1 specimens (Fig. 2.8.7).

Total elongation, e_f can be written as[3]

$$e_f = \frac{L_f - L_o}{L_o} = e_u + \frac{a}{L_o} , \qquad (1)$$

where L_f and L_o are original and final lengths, respectively, e_u is the uniform elongation, and a is the local necking extension. For a fixed cross-sectional area such as for the SS-1 and *SS-3* specimens, the equation indicates that the shorter the gage length, the greater the total elongation.[3] On the other hand, because of the similar cross-sectional areas, Barba's law implies that the total elongations for the SS-1 and SS-3 specimens should be the same if measured over the same center gage length[3] (the largest gage length possible would be 7.2 mm, the length of the SS-3 reduced section). Unfortunately, the measurement of gage marks on irradiated specimens presents considerable difficulty, even if the fractured specimens could be properly fitted together, a process that is extremely difficult with these small cross sections.

Another method to compare ductilities would be the use of reduction of area values. However, for such small specimens this also presents considerable difficulty — even when unirradiated.* Reduction of area measurements were made for the SS-1 and SS-3 specimens tested in this study. Reasonable agreement was obtained, indicating that deformation in the two specimens is similar.

These results indicate that the comparison of total elongations determined on the different types of specimens will prove difficult, although similar values were determined on the SS-1, SS-2, and rod-tensile specimens. The elongations of the three sheet-type specimens will be overestimated because of deformation beyond the reduced section, which has been assumed to be the gage length. The amount of excess deformation will depend on the flow characteristics of the material being tested, and the error introduced into the calculated elongation values will increase as the reduced section is decreased.

The reproducibility of the strength and ductility values for a given type of miniature specimen is indicated by the standard deviation as shown in Figs. 2.8.5 to 2.8.8. No particular specimen always has the largest standard deviation for a given set of test conditions. To further evaluate the reproducibility, a pooled standard deviation was calculated for the solution-annealed and cold-worked material separately and then combined for all specimens of a given type, regardless of the material's condition.

The pooled standard deviation was calculated as follows:

$$S_p = \sqrt{\frac{\sum_{i=1}^{n} (n_i - 1)\, S_i^2}{\sum_{i=1}^{n} n_i - 1}}$$

where n_i is the number of specimens with a standard deviation S_i. For the present calculation, n_i = 3 and S_i is the value shown in Figs. 2.8.5 to 2.8.8; n = 3 (three test temperatures) for the cold-worked or solution-annealed material when treated separately and n = 6 when they are combined. According to Choi,[4] "This quantity is a sort of average standard deviation" of all the S_i values. This calculation of S_p assumes that the standard deviation for a given type of specimen does not depend on temperature. It also assumes that errors introduced by temperature variations during test, by test machine, etc., are the same for each type of specimen. Under these assumptions, the difference in S_p values is indicative of the precision obtained for a given specimen. The S_p was calculated separately for the solution-annealed and cold-worked conditions because of the considerable difference in the magnitude of the properties for these different conditions.

Table 2.8.5 gives the calculated values of S_p for YS and UTS; Table 2.8.6 gives S_p for the uniform and total elongations. If the solution-annealed and cold-worked material is considered separately, it is seen that the SS-2 specimens generally had the largest S_p for all four properties. However, they were not always the largest, and in some cases where this value was the largest, it did not differ substantially from the S_p for the other specimens. For the combined data, the S_p for the SS-2 specimens was largest for all four parameters. Considering the size of the SS-2 specimen (0.25-mm-thick) and the fact that the specimens were punched from sheet material, we would have expected the properties determined from these specimens to be the least reproducible. The small and generally comparable variation for all the specimen types is encouraging.

Table 2.8.5. Pooled standard deviation (MPa) for strength parameters

Yield stress				Ultimate tensile strength			
SS-1	SS-2	SS-3	Rod tensile	SS-1	SS-2	SS-3	Rod tensile
Solution-annealed steel							
15.3	10.0	7.9	11.0	8.1	17.1	6.1	14.7
Cold-worked steel							
9.1	18.8	8.8	3.4	6.5	24.4	7.1	6.4
Combined							
12.6	15.1	8.4	8.1	7.4	21.0	5.9	11.3

Table 2.8.6. Pooled standard deviation (%) ductility parameters

Uniform elongation				Total elongation			
SS-1	SS-2	SS-3	Rod tensile	SS-1	SS-2	SS-3	Rod tensile
Solution-annealed steel							
1.39	3.28	2.64	1.10	1.63	3.58	3.54	1.44
Cold-worked steel							
0.83	0.96	0.39	1.09	1.31	1.96	1.04	2.0
Combined							
1.14	2.42	1.89	1.09	1.48	2.89	2.61	1.74

*Accurate cross-sectional areas are difficult to obtain for noncircular cross sections, even for large specimens, and according to ASTM Spec. E-139 "reduction of area is reported only for specimens of circular cross section."

Although the results of the present tests are encouraging, there are some areas of concern. One such concern is the apparently higher strength values determined with **SS-3** specimens compared with the SS-1 specimens, especially the YS for the cold-worked material and the UTS for the cold-worked and the annealed material. Also of concern are the differences noted for uniform elongation values, which are apparently caused by an undefined gage length over which the elongation values were determined. Differences in total elongation for the different specimen types were expected. However, part of that difference involves the undefined gage length, which thus introduces further uncertainty. These results indicate that caution must be exercised when properties are compared.

For scoping-type studies to determine irradiation effects on tensile behavior, which is presently the basic use of these specimens, any of the specimens appears to be adequate. However, the SS-1 and rod-tensile specimens are preferable, priinarily because of their longer gage lengths. Before any attempts are made to use these specimens to determine design data, studies should be conducted to resolve the discrepancies, especially those between the SS-3 and SS-1 specimens. Studies might be made on specimens with grids etched on the surfaces. Such tests would help determine the nature of the deformation along the specimen as well as help delineate the gage length. For completeness, such tests should be made with materials of different strength and ductility, thus making **it** possible to study the variation of gage length more closely. If, as indicated by the present tests, the gage lengths approach the length of the reduced section as the strength increases, Eq. (1) indicates that for a strong, brittle material, total elongation determined on SS-1 and SS-3 specimens would be the same, and very near the uniform elongation.

2.8.5 Summary and Conclusions

Tensile tests were made to compare the properties obtained with four different miniature tensile specimens that have been developed for testing irradiated materials. Comparisons were made by testing solution-annealed and 20%-cold-worked type 316 stainless steel at room temperature, 300, and 600°C. The types of specimens tested were: Two sheet specimens machined from 0.76-mm-thick sheet, one with a 20.3-mm-long reduced section (SS-1 specimen) and one with a 7.6-mm-long reduced section (SS-3 specimen), both reduced sections 1.52-mm wide. A sheet specimen punched from 0.25-mm-thick sheet with a reduced section 12.7-mm long by 1.02-mm wide (SS-2 specimen), and a rod-tensile specimen with a reduced section of 2.03-mm-diam by 18.3-mm long.

The tensile properties determined with the different specimens were in reasonable agreement when differences in grain size, cold work, and gage length were taken into account. Variation in YS and UTS for a given specimen, as measured by standard deviation, was usually well below 10%. The largest standard deviations were observed for the SS-2 specimen, with little difference for the other three types of specimens. Good reproducibility of uniform and total elongation was also obtained, with the variability of the SS-2 specimen only slightly greater than for the other specimens.

Several problems in the use of the miniature specimens were observed. In particular, the SS-3 specimen gave higher YS and UTS values than the other specimens under certain conditions. This difference was unexpected, especially the difference with the SS-1 specimens, which were machined from the same sheet as the SS-3 specimens and differed only in gage length. Although differences in the total elongation determined with these specimens were expected, the SS-3 specimen also exhibited higher uniform elongations. These discrepancies between specimens indicate that caution needs to be exercised in designing and using miniature specimens. The results indicate that the SS-1 and rod-tensile specimens should be used whenever possible.

2.8.6 References

1. N. F. Panayotou, R. J. Puigh, and E. K. Opperman, "Miniature Specimen Tensile Data for High Energy Neutron Source Experiments," *J. Nucl. Mater.* 103&104, 1523–26 (1981).

2. F. B. Pickering, p. 231 in *Physical Metallurgy and the **Design** of Steels,* Applied Science Publishers Ltd., London, 1978.

3. G. E. Dieter, p. 347 in *Mechanical Metallurgy,* McGraw Hill, Inc., New York, 1976.

4. S. C. Choi, p. 133 in *Introductory Applied Statistics in Science,* Prentice-Hall, Inc., Englewood Cliffs, N.J., 1978.

2.9 THE U.S./JAPAN COLLABORATIVE TESTING PROGRAM IN HFIR AND ORR: SPECIMEN MATRICES FOR HFIR IRRADIATION

A. F. Rowcliffe, M. L. Grossbeck (Oak Ridge National Laboratory), M. Tanaka, and S. Jitsukawa (Japan Atomic Energy Research Institute)

2.9.1 ADIP Tasks

ADIP Task I.A.2, Define Test Matrices and Test Procedures.

2.9.2 Objectives

The objective of this program is to investigate the behavior and measure the properties of Japanese and U.S. structural alloys after irradiation in the mixed-spectrum fission reactors Oak Ridge Research Reactor (ORR) and High Flux Isotope Reactor (HFIR).

2.9.3 *Summary*

The eight capsules which constitute phase I of the U.S./Japan collaboration on HFIR irradiations have been inserted in HFIR on schedule.

2.9.4 Progress and Status

2.9.4.1 Introduction

The U.S./Japan collaborative agreement calls for eight HFIR capsules to be built in FY 1984 with space equally shared between the two participants. The objectives of the experiments and details of the specimen loading in the first few capsules were described in the previous semiannual report.[1] The present report describes the specimen loading in the other four capsules. All eight capsules are currently in-reactor.

2.9.4.2 Specimen Distribution in HFIR Capsules

The general objectives of the HFIR experiments were described in the previous report[1] together with the compositions of the alloys and the distribution of specimens in capsules JP1 through JP4. The distribution of specimens in capsules JP5 through JP8 is shown below in Tables 2.9.1 through 2.9.4. The heat treatment conditions referred to were fully described in the previous report.

Capsules JP1, JP2, and JP7 contain disks supplied by the DAFS program (H. R. Brager, HEDL). For convenience, these are listed separately in Table 2.9.5 and the compositions of these alloys are shown in Table 2.9.6.

2.9.4.3 Current Status

All eight capsules were inserted in HFIR on schedule.

2.9.4.4 Reference

1. A. F. Rowcliffe, M. L. Grossbeck, and S. Jitsukawa, "The U.S./Japan Collaborative Testing Program in HFIR and ORR," pp. 38–43 in *ADIP Semiannu. Prog. Rep. March 31, 1984*, DOE/ER-0045/12, U.S. DOE, Office of Fusion Energy.

Table 2.9.1. Loading list for capsule HFIR-JP-5 (50 dpa)

Level	Specimen type	Temperature (°C)	Alloy	Condition	Identity
1	Tensile	300	PCA	A3	EC34
2	Tensile	400	PCA	A3	EC31
3	Tensile	500	PCA	A3	EC37
4	Fatigue	430	PCA	A3	EC153
5	Fatigue	430	Ref. 316	20% CW	AA27
6	TEM	400	a	a	a
7	Fatigue	430	JPCA	PC2	FE10
8	Fatigue	430	JPCA	PC2	FE11
9	Tensile	500	JPCA	PC2	TE7
10	Tensile	400	JPCA	PC2	TE8
11	Tensile	300	JPCA	PC2	TE9

[a] 100 disks shared between U.S. and Japan. For compositions see previous semiannual report, DOE/ER-0045/12, p. 38.

Table 2.9.2. Loading list for capsule HFIR-JP-6 (30 dpa)

Level	Specimen type	Temperature (°C)	Alloy	Condition	Identity
1	Tensile	600	PCA	83	EL74
2	TEM	500	a	a	a
3	Tensile	500	Ref. 316	70% CW	AA42
4	Fatigue	430	PCA	A3	EC156
5	Fatigue	430	PCA	A3	EC161
6	TEM	600	b	b	b
7	Fatigue	430	JPCA	PC2	FE17
8	Fatigue	430	JPCA	PC2	FE13
9	Tensile	500	JPCA	PC2	TE10
10	Tensile	400	JPCA	PC2	TE11
11	Tensile	300	JPCA	PC2	TE12

[a] 100 disks far U.S. program for subsequent irradiation in, FFTF.

[b] 100 disks shared between U.S. and Japan. For compositions see previous semiannual report, DOE/ER-0045/12, p. 38.

Table 2.9.3. Loading list for capsule HFIR-JP-7 (30 dpa)

Level	Specimen type	Temperature (°C)	Allay	Condition	Identity
1	Tensile	600	PCA	B3	EL26
2	Tensile	600	PCA	B3	EL35
3	Tensile	500	PCA	B3	EL25
4	Fatigue	430	PCA	A3	EC163
5	Fatigue	430	Ref. 316	20% CW	AA53
6	TEM	500	a	a	a
7	Tensile	600	JPCA	PC2	TE21
8	Tensile	500	JPCA	PC2	TE22
9	Tensile	430	JPCA	PS2	TB12
10	Tensile	400	JPCA	PC2	TE23
11	Tensile	300	JPCA	PC2	TE24

[a]100 disks shared between U.S. and Japan. For compositions see previous semiannual report, DOE/ER-0045/12, p 38.

Table 2.9.4. Loading list for capsule HFIR-JP-8 (50 dpa)

Level	Specimen type	Temperature (°C)	Alloy	Condition	Identity
1	Tensile	600	PCA	A3	EC36
2	Tensile	600	PCA	83	EL29
3	Tensile	500	PCA	E3	Et31
4	Fatigue	550	Ref. 316	20% CW	AA54
5	Fatigue	550	PCA	B2	EF5
6	TEM	500	a	a	a
7	Tensile	600	JPCA	PC2	TE16
8	Tensile	600	JPCA	PC2	TE17
9	Tensile	500	JPCA	PC2	TE18
10	Tensile	400	JPCA	PC2	TE19
11	Tensile	300	JPCA	PC2	TE20

[a]100 dirks shared between U.S. and Japan. For compositions see previous semiannual report, DOE/ER-0045/12, p. 38, and Table 2.7.6, this report.

Table 2.9.5. DAFS program TEM disks

Alloy designation	Dirk identity		
	JP1 30 dpa at 300°C	JP2 50 dpa at 300°C	JP7 30 dpa at 500°C
AMCR	H7EU	H7EX	H7EV
AE37	BHEV	BHEU	BHEX
CE37	BFEU	BFEX	BFEY
R77	FREU	FREX	FREI
A5	KPE6	KPE5	KPE4
R111	P9E1	P9EZ	P9E4
A61	LHEZ	LHE5	LHE4
R100	NMEZ	NME5	NME4
R103	PEEZ	PEE5	PEE4
R106	PREZ	PRE5	PRE7
R107	PXEX	PXE5	PXE1
R92	EAEU	EAEX	EAEV
R94	EKEU	EKEX	EKEV
R27	AVEU	AVEX	AVEV
316	EIEU	EIEX	EIEV

Table 2.9.6. Compositions of DAFS program alloys[a]

Alloy designation	Concentration. wt %						
	Fe	Ni	Cr	Mn	C	N	Si
AMCR	Bal	0.5	18.0	18.0	0.1	0.4	0.6
AE37	Bal	35.0	7.5	--	--	--	--
CE37	Bal	35.0	7.5	--	--	--	--
R77	Bal	0.5	2.0	30.0	0.40	0.15	0.4
A5	Bal	14.0	16.0	2.0	0.04	--	1.5
R111	Bal	14.0	10.0	2.0	0.04	--	1.5
A61	Bal	14.0	16.0	2.0	0.04	--	0.8
R100	Bal	18.0	16.0	2.0	0.04	--	1.5
R103	Bal	18.0	10.0	2.0	0.04	--	1.5
R106	Bal	18.0	10.0	2.0	0.04	--	0.8
R107	Bal	18.0	10.0	2.0	0.04	--	1.5
R92	Bal	40.0	7.5	2.0	0.08	--	0.1
R94	Bal	40.0	7.5	2.0	0.02	--	0.1
R27	Bal	40.0	7.5	2.0	0.08	--	0.1
316	Bal	14.0	17.0	1.7	0.05	--	0.6

[a]All materials in 20%-cold-worked condition except AE37 which is solution annealed 1/2 h at 1030°C.

2.10 VANADIUM ALLOY IRRADIATION TEST MATRIX IN FFTF — D. N. Braski (Oak Ridge National Laboratory)

2.10.1 ADIP Tasks

ADIP Task I.B.15, Tensile Properties of Reactive Refractory Alloys.

2.10.2 Objective

The goal of this experiment is to determine the effect of neutron irradiation on the tensile properties and microstructure (including swelling behavior) of vanadium alloys.

2.10.3 *Summary*

Vanadium specimens of V—15Cr—5Ti, VANSTAR-7, V—3Ti—1Si, and V—20Ti are being irradiated in the FFTF-MOTA experiment. Miniature sheet tensile specimens and transmission electron microscopy (TEM) disks were preimplanted with ^{3}He to levels up to 480 at. ppm using the tritium trick and encapsulated in TZM capsules containing ^{7}Li. The specimens will be irradiated to damage levels up to 165 dpa with irradiation temperatures of 420, *520,* and 600°C. All of the capsules at 600°C underwent a temperature excursion during their initial cycle and had to be replaced.

2.10.4 Progress and Status

The ADIP program started irradiation tests in FFTF-MOTA using three vanadium alloys that were already in the program stockpile: V—15Cr—5Ti, VANSTAR-7, and V—20Ti. A fourth alloy, V—3Ti—1Si, was supplied by the Institut für Material und Festkorperforschung II, at Karlsruhe, West Germany. The composition and final annealing treatments for these alloys are listed in Table 2.10.1. Two types of specimens are used in the experiment: SS-3-type sheet tensile specimens (Fig. 2.10.1) and 3-mm-diam by 0.25-mm-thick disks. All of the specimens except those made from V—3Ti—1Si were fabricated prior to the final anneal. The V—3Ti—1Si specimens were fabricated in the annealed condition. Tensile specimens and disks of all the alloys except V—20Ti were preimplanted with ^{3}He using the tritium trick.[1] The specimens were encapsulated in TZM capsules containing ^{7}Li using the technique described in ref. 2. The specimens are being irradiated to several different damage levels at three different temperatures, as shown in Table 2.10.2. A number of additional specimens were encapsulated to provide thermally aged controls and are listed in the same table. During cycle 4 of the FFTF operation, all of the capsules at 600°C underwent a temperature excursion and had to be replaced during the shutdown period following that cycle. At the same time, two capsules (V405 and V505) irradiated at 420 and 520°C, respectively, were removed for testing and evaluation. The specimen distribution in the 600°C replacement capsules was similar to that used to replace V405 and V505, and is listed in Table 2.10.3. The helium level in this replacement series of specimens was ~80 at. ppm. Capsules containing specimens for thermal aging were also prepared for this first reconstitution and their distribution is also shown in Table 2.10.3. The capsules with specimens accruing ~45 dpa are scheduled to be removed from FFTF in the spring of 1985.

Table 2.10.1. Vanadium alloy data

Alloy	Heat number	Composition, wt %								Final heat treatment
		Cr	Ti	Fe	Zr	Si	C	O	N	
V—15Cr—5Ti[a]	CAM-834-3	14.5	6.2				0.032	0.031	0.046	1 h at 1200°C
VANSTAR-7[a]	CAM-837-7	9.7		3.4	1.3		0.064	0.028	0.052	1 h at 1350°C
V—3Ti—1Si[b]	11153		3.4	0.04		1.28	0.045	0.091	0.026	1 h at 1050°C
V—20Ti	CAM-832		20.3				0.020	0.039	0.044	1 h at 1100°C

[a]Source: Westinghouse Electric Corporation.

[b]Source: KFK, Karlsruhe, West Germany (Dr. D. Kaletta).

2.10.5 References

1. D. N. Braski and D. W. Ramey, "Helium Doping of a Vanadium Alloy by a Modified Tritium Trick," pp. 72—74 in *ADIP Semiannu. Frog. Rep. March 31, 1984,* DOE/ER-0045/12, U.S. DOE, Office of Fusion Energy.
2. A. Ermi, Sect. 2.4, this report.

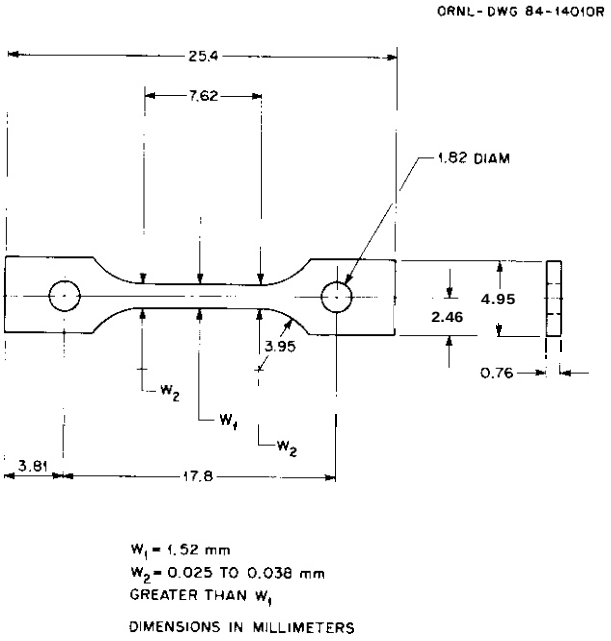

Fig. 2.10.1. The SS-3 sheet tensile specimen.

Table 2.10.2. Vanadium alloy test matrix — FFTF(MOTA)

Alloy	Irradiation/ aging temperature (°C)	Nominal damage level (dpa)	Nominal helium level (at. ppm)	Number 55-3 tensile specimens	Number TEM disks
		MOTA			
V—15Cr—5Ti	420,520,600[a]	15,45,105,165	0	15	74
			14	12	24
			80	18	74
			300	18	24
VANSTAR-7	420,520,600[a]	15,45,105,165	0	12	74
			7	0	24
			40	15	24
			150	15	24
V—3Ti—1Si	420,520,600[a]	15,45,105,165	0	12	24
			75	0	24
			135	15	24
			480	3	24
V—20Ti	420,520,600[a]	15,45,105,165	0	n	60
		AGED CONTROL SPECIMENS			
V—15Cr—5Ti	420,520,600	0	0	18	0
			80	17	0
			300	12	0
VANSTAR-7	470,520,600	0	0	18	0
			40	6	0
			150	6	0
V—3Ti—1Si	420,520,600	0	0	6	0
			135	6	0
			480	6	0
V—20Ti	420,520,600	0	0	0	77

[a]600°C capsules were replaced after cycle 4 — specimen distribution similar to Table 2.10.3.

Table 2.10.3. Vanadium alloy test matrix — FFTF(MOTA) first reconstitution

Alloy	Irradiation/ Aging Temperature (°C)	Nominal Damage Level (dpa)	Nominal Helium Level (at. ppm)	Number ss-3 Tensile Specimens	Number TEM Disks
		MOTA			
V—15Cr—5Ti	420,520,600	30	0 80	3 6	3 6
VANSTAR-7	420,520,600	30	0 80	3 6	3 6
V—3Ti—1Si	420,520,600	30	0 80	3 6	3 6
V—20Ti	420,520,600	30	0	0	6
		AGED CONTROL SPECIMENS			
V—15Cr—5Ti	420,520,600	0	0 80	3 6	3 6
VANSTAR-7	420,520,600			3 6	3 6
V—3Ti—1Si	420,520,600	0	0 80	0 6	6 6
V—20Ti	420,520,600	0	0	0	6

2.11 IRRADIATION EXPERIMENTS FOR THE U.S./JAPAN COLLABORATIVE TESTING PROGRAM IN HFIR AND ORR — J. A Conlin and J. W Woods (Oak Ridge National Laboratory)

2.11.1 ADIP Tasks

ADIP Task I.A.2, Define Test Matrices and Test Procedures.

2.11.2 Objectives

The experiments in the U.S./Japan collaborative testing program for High Flux Isotope Reactor (HFIR) and Oak Ridge Research Reactor (ORR) irradiate austenitic stainless steel candidate alloys for use as first-wall and blanket structural materials in fusion reactors. They will be irradiated with mixed-spectrum neutrons and with spectral tailoring to achieve helium-to-displacement-per-atom (He/dpa) ratios predicted for fusion reactor service.

2.11.3 Summary

The assembly of all eight capsules, HFIR JP-1 through JP-8, has been completed, and they are now being irradiated. The parts fabrication assembly and flow testing of the prototype ORR capsules for 60°C and 200°C MFE6-J were completed and the capsule was inserted in the ORR. Performance was satisfactory in all respects.

2.11.4 Progress and Status

2.11.4.1 Irradiation Experiments for the HFIR

The HFIR-JP experiments consist of eight irradiation capsules designed to evaluate the tensile, fatigue, and microstructural properties of austenitic stainless steels. The capsules occupy peripheral positions in the HFIR target island. Two capsules, JP-1 and JP-2, were completed during the last reporting period. The other six were assembled during the period March through September 1984. Capsules JP-3 through JP-6 were inserted in the HFIR during this reporting period. Capsules JP-7 and JP-8 are scheduled for insertion in the HFIR during the first week of October.

2.11.4.2 Irradiation Experiments for the ORR

The U.S./Japan collaborative irradiation program in the ORR consists of two spectral tailored capsules to irradiate materials specimens at 60, 200, 300 and 400°C. The 300 and 400°C irradiations will be carried out in an irradiation capsule (ORR-MFE-7J) similar in design to that of the ORR-MFE-4A irradiation capsule. The only significant difference is in the length of the specimen test region, which is to be increased to 24 cm (9.5 in.) from 15.2 cm (6 in.) to accommodate the larger specimen complement.

With the exception of the specimen holders, the design modifications were completed in July 1984. Some parts have been fabricated — the remaining parts and the capsule assembly will be completed in the first half of FY 1985, and irradiation will begin in March 1985.

The 60 through 200°C capsule designated ORR MFE6-J was described previously.' A schematic of the 6J capsule is shown in Fig. 2.11.1. A prototype of this new design was recently irradiated to verify the thermal design of this new type of capsule. During the period March through September 1984, the fabrication assembly, flow and checkout tests for the prototype MFE6-J capsule were completed, and the experiment was installed and operated in the ORR. The capsule checkout was completed on September 3, and the capsule was inserted in the ORR on September 5. The reactor was at 30 MW by September 6.

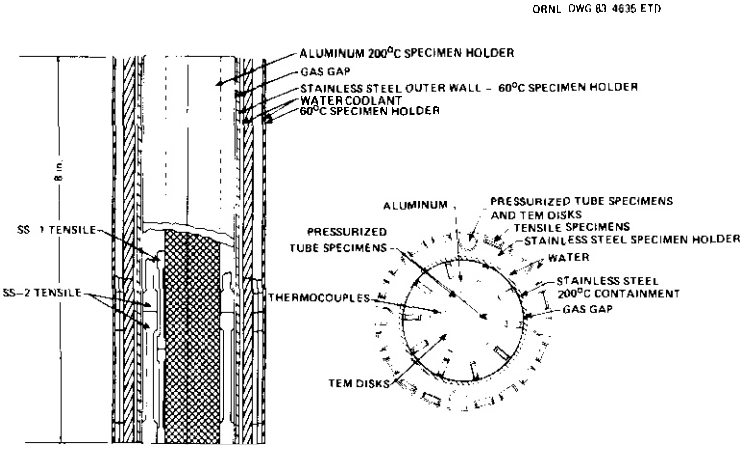

Fig. 2.11.1. Oak Ridge Research Reactor spectral tailoring capsule for irradiation at 60 and 200°C.

The primary purpose of the prototype capsule was to verify the thermal design. The prototype capsule contained a full complement of dummy specimens with thermocouples attached to two of the tensile specimens. During reactor operation, it was possible to maintain specimen temperatures to within ±2°C for extended periods of time. By varying the mixture of gases in the gas gap, temperatures could be controlled at any point between *140* and 305°C. The axial temperature range in the specimen holder also proved to be acceptable. Compared with the midplane, the holder was 10°C lower at the top and 30°C lower at the bottom. These differences will be reduced in the actual irradiation capsule by minor design changes to reduce heat losses at the ends. It *is* concluded that the design performance of the 60/200°C capsule has been satisfactorily confirmed during operation in the ORR.

2.11.5 References

1. J. A Conlin and I. T. Dudley, "Operation of the ORR Spectral Tailoring Experiments ORR-MFE-4A and ORR-MFE-4B," pp. 21-22 in ***ADIP Semiannu. Prog. Rep. Mar. 31, 1984,*** DOE/ER-0045/12, U.S. DOE, Office of Fusion Energy.

3. PATH A ALLOY DEVELOPMENT — AUSTENITIC STAINLESS STEELS

3.1 THE DEVELOPMENT OF AUSTENITIC STEELS FOR FAST INDUCED-RADIOACTIVITY DECAY — R. L. Klueh and P. J. Maziasz (Oak Ridge National Laboratory)

3.1.1 ADIP Tasks

ADIP Tasks I.A.5, Perform Fabrication Analysis, and I.C.I, Microstructural Stability.

3.1.2 Objectives

During the operation of a fusion reactor, the structural material of the first wall and blanket structure will become highly radioactive from activation by the fusion neutrons. Disposal of this material after the service lifetime will be a difficult radioactive waste management problem. One way to minimize the disposal problem is to use structural materials in which radioactive isotopes induced by irradiation decay quickly to levels that allow simplified disposal techniques. We are assessing the feasibility of developing such austenitic stainless steels.

3.1.3 *Summary*

A program was started to develop austenitic steels for fusion reactors in which the induced radioactivity decays to low levels in a reasonable time. Ten small button heats of Fe-Cr-Mn-C alloys were melted, cast, and rolled. After various heat treatments, optical microscopy studies and magnetic measurements were used to assess the microstructural constituents present.

3.1.4 Progress and Status

3.1.4.1 Introduction

During the operation of a fusion reactor, the various elements of the alloys that are proposed for the first wall and blanket structure undergo transmutation reactions when irradiated by high-energy neutrons. After the service lifetime of the reactor, these radioactive components must he properly disposed of. The complexity of this waste disposal procedure depends on the time required for the induced radioactivity to decay to levels that no longer pose a threat to people and the environment. The more rapid the decay, the simpler is the disposal task.

We have proposed an alloy-development program for fast induced-radioactivity decay (FIRD) versions of present first-wall and blanket structural candidate alloys.[1] For the austenitic alloys, manganese was proposed as a replacement for nickel, although it was recognized[1] that this may be difficult, because manganese is not as strong an austenite stabilizer as nickel. Hence, it is not possible to simply replace nickel with equal amounts of manganese. It was proposed that an effort be made to determine stable Fe-Cr-Mn-C compositions that are austenitic and that could then he further alloyed to obtain the strength and irradiation-resistant properties required for a fusion reactor structural material.[1]

As a start in determining a base composition, 600-g button heats with aim compositions given in Table 3.1.1 were produced.[2] These were picked on the basis of available phase diagrams and the Schaeffler diagram (Fig. 3.1.1). For the Schaeffler diagram, the nickel and chromium equivalents were calculated according to:[3]

Table 3.1.1. Aim compositions of button heats melted for fast induced-radiactivity decay (FIRD) alloy-development program

Alloy	Chemical composition, wt %[a]		
	Cr	Mn	C
PCMA-0	15	15	0.1
-1	15	15	0.05
-2	15	20	0.1
-3	10	15	0.1
-4	10	20	0.1
-5	15	15	0.2
-6	15	20	0.2
-7	15	20	0.4
-8	20	20	0.2
-9	20	20	0.4

[a]Balance iron.

$$\text{Ni Equiv} = (\text{Ni}) + (\text{Co}) + 0.5(\text{Mn}) + 0.3(\text{Cu}) + 25(\text{N}) + 30(\text{C}) \quad (1)$$

$$\text{Cr Equiv} = (\text{Cr}) + 2(\text{Si}) + 1.5(\text{Mo}) + 5(\text{V}) + 5.5(\text{Al}) + 1.75\ (\text{Nb}) + 1.5\ (\text{Ti}) + 0.75\ (\text{W}) \quad (2)$$

where the concentration of the respective elements given in parentheses is to be in weight percent. There has been considerable discussion on the value to be assigned to the multiplying factor for manganese for the Schaeffler diagram, and various values besides the 0.5 of Eq. (1) have been proposed.[4-6] The results of the initial microstructural studies should yield information on the effect of manganese as an austenite stabilizer.

3.1.4.2 Experimental Procedure

Ten 600-g button heats were melted and cast with goal cornpositions given in Table 3.1.1. The actual compositions, especially for the manganese, were often different from the aim composition, as seen in Table 3.1.2. Manganese and in some cases carbon were lost during the melting process.

The alloys were cast into a rectangular cross section of 12.7 mm by 25.4 mm by 152 mm. These ingots were cold rolled 30 to 50% and then homogenized 24 h at 1275°C. (Several of the steels were much more difficult to cold work than normal nickel-stabilized stainless steels, such as type 316.) Pieces of each

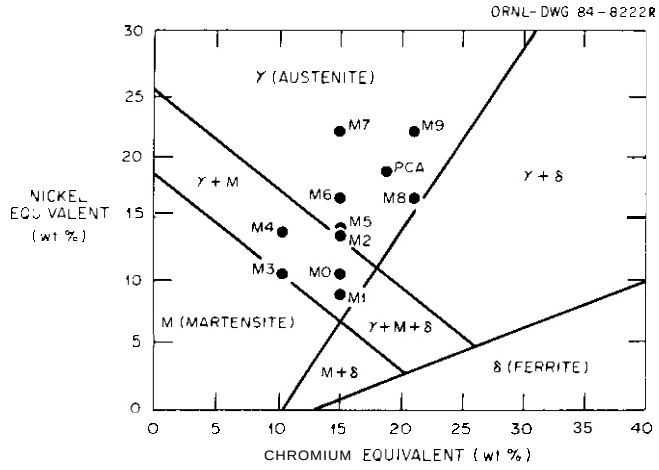

Fig. 3.1.1. Schaeffler diagram with points indicated for experimental Fe-Cr-Mn-C button heats being studied. The M designations refer to the PCMA numbers assigned to the alloys in Table 3.1.1.

heat of the homogenized material were then annealed for 1 h at 1150°C and other pieces annealed for R h at 1050°C. A piece of each cold-worked alloy was annealed 168 h at 800°C. After each of these heat treatments, magnetic measurements were made with a "Ferritescope" to obtain a qualitative measure of the ferromagnetic properties of each alloy. Specimens were also examined by optical microscopy.

All of the heats except PCMA-3 were further rolled (with intermediate homogenization treatments) to 0.76- and 0.25-mm-thick sheet. The PCMA-3 heat cracked extensively when rolled. Oifficulties with rolling were also experienced with PCMA-5. Transmission eletron microscopy (TEM) disks from selected heats were obtained from the 0.25-mm-thick sheet and were inserted in the MOTA for irradiation at 600°C in FFTF cycles 5 and 6. The 0.76-mm sheet is being used for specimens to test comoatibility in lithium and in water. Tensile tests will also be obtained from the 0.76-mm sheet.

3.1.4.3 Results and Discussion

Microstructures were examined by optical microscopy after the homogenization treatment of 24 h at 1275°C, after the solution-anneal treatments of 1 h at 1150°C and 8 h at 1050°C, and after the 168 h aging treatment at 800°C. Based on these observations, the chemical compositions, magnetic measurements, the phase diagrams, and the Schaeffler diagram, the microstructural constituents were tentatively identified (Table 3.1.3). For a complete and accurate identification of phases, a detailed TEM study would be required. Limited TEM studies will he conducted, but for the present evaluations that are concerned with delineating a suitable austenitic base composition, the more qualitative equations described here will suffice.

Table 3.1.2. Chemical compositions of button heats melted for fast induced-radioactivity decay (FIRD) alloy-development program

Alloy	Chemical composition,[a] (wt %)									
	C	Mn	Si	Ni	Cr	Mo	V	Cb	cu	N
PCMA-0	0.069	13.4	0.04	0.01	15.0	0.01	0.01	<0.01	0.03	0.001
-1	0.014	14.2	0.02	0.01	14.8	0.01	0.01	<0.01	0.03	0.001
-2	0.056	17.1	0.04	0.01	15.2	0.01	<0.01	<0.01	0.03	0.001
-3	0.089	13.9	0.02	0.01	10.0	0.01	<0.01	<0.01	0.03	0.002
-4	0.093	18.9	0.02	0.01	9.9	<0.01	<0.01	<0.01	0.02	0.002
-5	0.18	13.9	0.02	0.01	15.3	0.01	<0.01	<0.01	0.04	0.002
-6	0.18	14.3	0.02	0.01	16.0	0.01	<0.01	<0.01	0.03	0.003
-7	0.38	19.1	0.02	0.01	14.8	0.01	<0.01	<0.01	0.05	0.005
-8	0.13	17.7	0.02	<0.01	20.1	0.01	<0.01	<0.01	0.03	0.003
-9	0.26	17.6	0.03	0.01	20.2	0.01	<0.01	<0.01	0.03	0.006

[a]Balance iron.

Table 3.1.3. Tentative identification of microstructural constituents of Fe-Mn-Cr-C steels

Alloy	Phases		
	1275°C/24 h	1150°C/1 h	1050°C/8 h
PCMA-0	γ + δ	γ + δ	γ + δ
-1	γ + δ	γ + δ	γ + δ
-2	γ + δ	γ + δ	γ + δ
-3	γ + M	γ + M	γ + M
-4	γ + M	γ + M	γ + M
-5	γ + δ + P	γ + δ + P	γ + δ + P
-6	γ + δ + P	γ + δ + P	γ + δ + P
-7	γ	γ	γ + P
-8	γ + δ + P	γ + δ + P	γ + δ + P
-9	γ + δ + P	γ + δ + P	γ + δ + P

γ = austenite
δ = δ-ferrite
M = martensite
P = precipitate

As an example of the microstructures obtained, Figs. 3.1.2 through 3.1.6 show the microstructures after the 1 h at 1150°C solution anneal. Except for the relative amount of a given phase or constituent present, the microstructures after 24 h at 1275°C and 8 h at 1050°C were generally similar to those observed after 1 h at 1150°C (Table 3.1.3). Microstructures of the cold-worked steels annealed 168 h at 800°C were considerably different, primarily in the large amount of precipitate that formed at the lower temperature. Because of the complicated precipitate structure of the aged cold-worked steels, no phases are given in Table 3.1.3. However, for the other heat treatments, δ-ferrite (δ), austenite (γ), and martensite (M) are identified as constituents (Table 3.1.3). No precipitate phases are identified in Table 3.1.3 beyond stating that a precipitate (P) was observed, meaning that large amounts of a precipitate phase (or phases) were obvious. Possible precipitate phases include carbides, Laves phase, sigma phase, and chi phase.

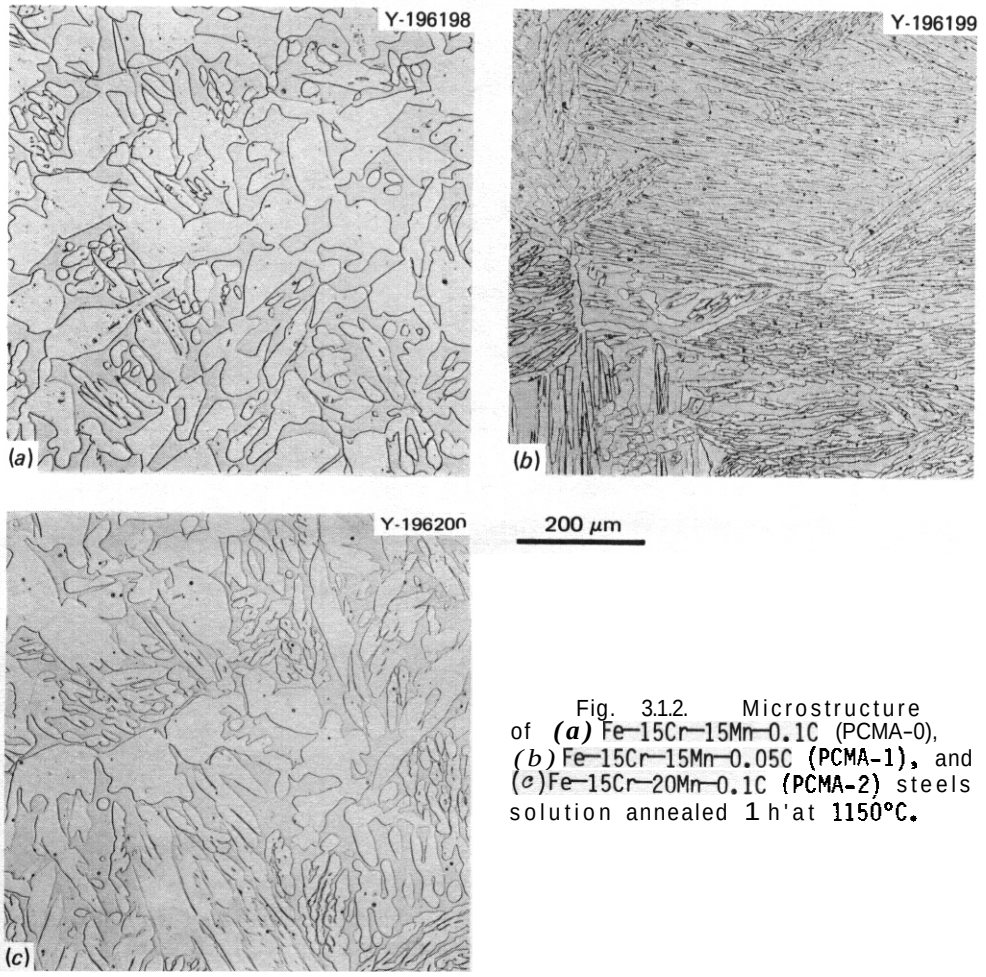

Fig. 3.1.2. Microstructure of (a) Fe-15Cr-15Mn-0.1C (PCMA-0), (b) Fe-15Cr-15Mn-0.05C (PCMA-1), and (c) Fe-15Cr-20Mn-0.1C (PCMA-2) steels solution annealed 1 h at 1150°C.

Fig. 3.1.2. Microstructure of (a) Fe-15Cr-15Mn-0.1C (PCMA-0), (b) Fe-15Cr-15Mn-0.05C (PCMA-1), and (c) Fe-15Cr-20Mn-0.1C (PCMA-2) steels solution annealed 1 h at 1150°C.

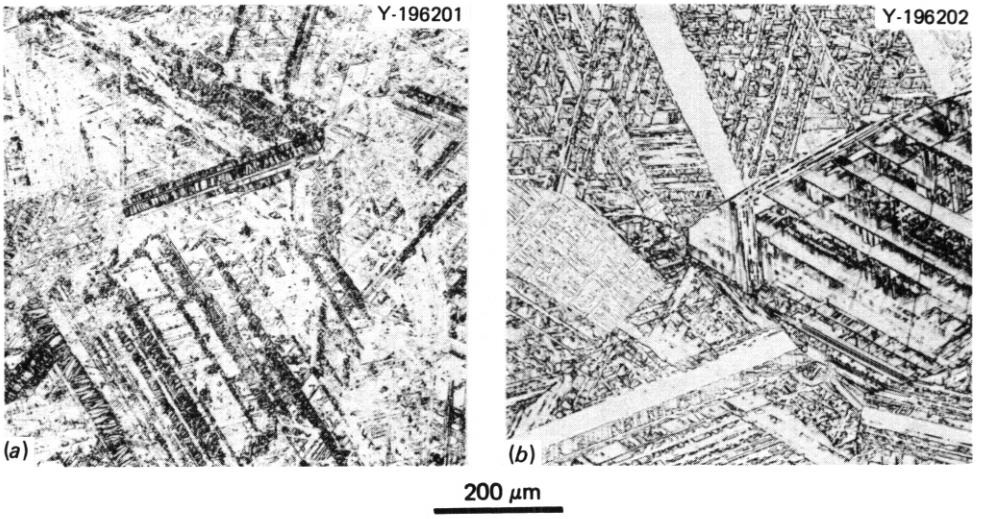

Fig. 3.1.3. Microstructure of *(a)* Fe–10Cr–15Mn–0.1C (PCMA-3) and *(b)* Fe–10Cr–20Mn–0.1C (PCMA-4) steels solution annealed 1 h at 1150°C.

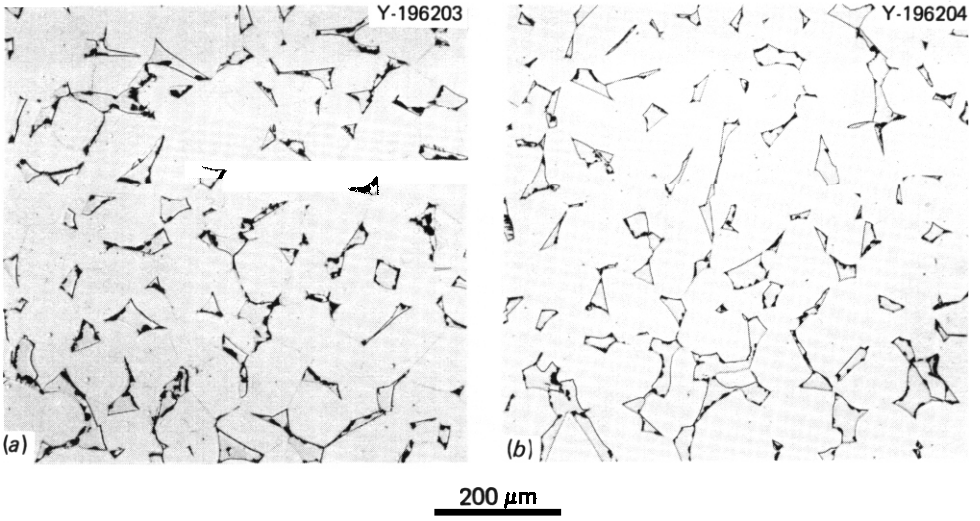

Fig. 3.1.4. Microstructure of *(a)* Fe–15Cr–15Mn–0.2C (PCMA-5) and *(b)* Fe–20Cr–0.2C (PCMA-6) steels solution annealed 1 h at 1150°C.

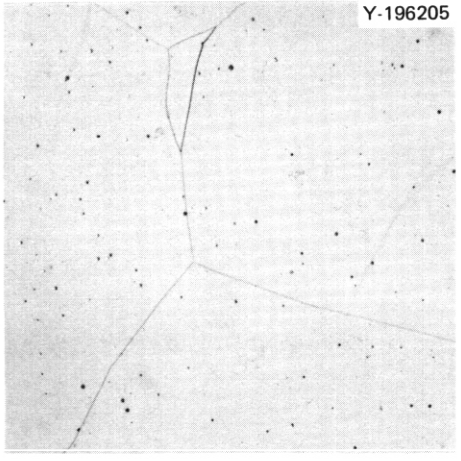

Fig. 3.1.5. Microstructure of Fe–15Cr–20Mn–0.4C (PCMA-7) steel solution annealed 1 h at 1150°C.

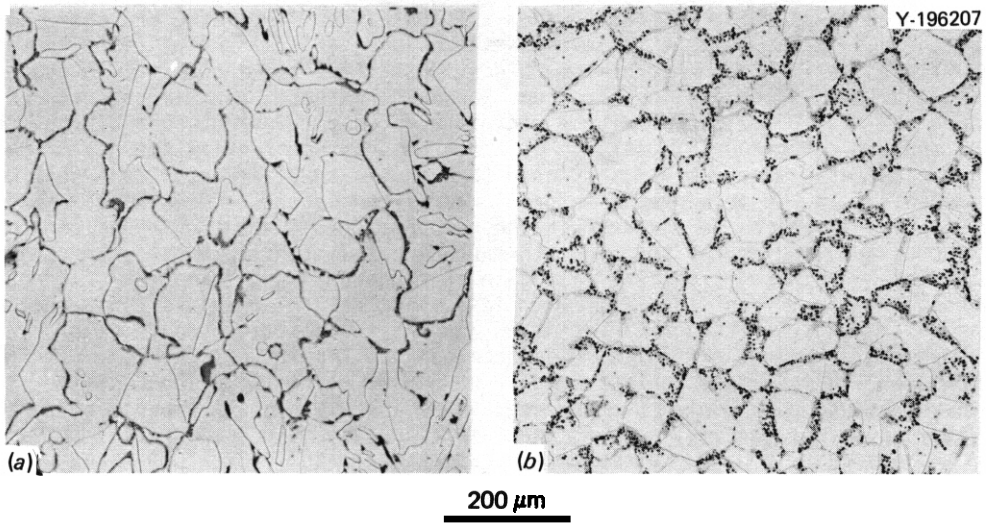

Fig. 3.1.6. Microstructure of (a) Fe–20Cr–20Mn–0.2C (PCMA-8) and (b) Fe–20Cr–20Mn–0.4C (PCMA-9) steels solution annealed 1 h at 1150°C.

The magnetic measurements are qualitative and meant to indicate the presence of magnetic constituents (6-ferrite or α′-martensite) in the microstructure. Results from the Ferritescope measurements are given in Table 3.1.4. The Ferritescope is routinely used to magnetically determine the amount of 6-ferrite present in austenitic stainless steel weld metals where austenite and ferrite are the primary constituents present. A "ferrite number" is determined. This number is approximately equal to the percent of 6-ferrite in the austenitic weld metal for low ferrite contents. A maximum Ferritescope reading of 30 is possible, and a 30' in Table 3.1.4 indicates that the maximum reading was obtained. These ferrite numbers are used here to indicate the amount of magnetic constituent present. Information on the identification of the magnetic constituent will be obtained by metallography.

Table 3.1.4. Ferrite number[a] as a measurement of the extent of ferromagnetism

Alloy	Ferrite number[b]				
	Cold worked	1275°C/24 h	1150°C/1 h	1050°C/8 h	800°C/168 h
PCMA-0	30+	30+	30+	8	0.5
-1	30'	30+	30+	30'	6.8
-2	30+	23.0	30'	30'	0.2
-3	30'	2.8	4.0	3.5	
-4	11.0	0.2	0.2	2.0	0.2
-5	30'	1.5	5.8	3.6	0.5
-6	5.5	0.7	6.3	8.5	0.2
-7	0.5	0	0	0	n.2
-8	30'	30'	30'	30+	0.2
-9	6.0	2.4	19.0	12.0	0

[a] Measurements made with a Ferritescope.

[b] Maximum number measured with a Ferritescope is 30.

The first three alloys (PCMA-0 to -2) which were high-chromium, low-carbon alloys were basically duplex structures of austenite and 6-ferrite (Fig. 3.1.2). The only difference for the homogenized and solution-annealed steels appeared to be a somewhat finer 6-ferrite structure, the lower the heat-treatment temperature. The magnetic measurements on these steels gave a slightly lower reading for the PCMA-2 in the homogenized condition relative to the solution-annealed condition, suggesting that the higher temperature produced less 6-ferrite. High magnetic readings were obtained for all the cold-worked alloys, as might be

expected. Although cold working will not change the amount of δ-ferrite present in the homogenized structure, the rolling can produce magnetic martensite from the austenite. The large decrease in the magnetic reading from PCMA-0 through -2 (as well as the other seven alloys) after 168 h at 800°C was attributed to the transformation of the ferrite to nonmagnetic carbides, austenite, and intermetallic phases.

The PCMA-3 and -4 alloys, which are low-chromium, low-carbon steels, had microstructures indicative of martensite and austenite (Fig. 3.1.3). From these microstructures, it was not possible to estimate the relative amounts of the two constituents, although it appeared that substantial amounts of martensite were present. However, the magnetic measurements indicated that only a small amount of a magnetic constituent was present after annealing, but more magnetic material was present after cold working. This was interpreted to mean that the martensite observed in the homogenized and solution-annealed conditions was nonmagnetic ε-martensite (hcp) which can transform to magnetic a'-martensite (bct) when deformed. The low ferrite number after the 800°C aging treatment was again attributed to the formation of nonmagnetic phases.

The PCMA-0 through -4 steels contained 0.1% C or less. The remaining alloys contained medium (~0.2%) or high (~0.4%) carbon contents. Although carbon is an austenite stabilizer, only one of the higher-carbon alloys (PCMA-7) was essentially 100% austenite in the homogenized condition (Fig. 3.1.5). This alloy contained a high-carbon and high-manganese content. The PCMA-5 and -6 steels, which contained high-chromium and medium-carbon levels, were both duplex structures (Fig. 3.1.4) with small amounts of what appeared to be δ-ferrite and possibly additional precipitates at the δ-ferrite/austenite boundaries. The amount of precipitate appeared to increase as the heat-treatment temperature decreased. The PCMA-8 and -9 steels were both high-chromium, high-manganese alloys, the first with medium carbon, the other with high carbon. Duplex microstructures were observed, with indications that precipitates were present on the δ-ferrite-austenite boundaries (Fig. 3.1.6); the amount of precipitate appeared to increase with increasing carbon content and decreasing annealing temperature. After 168 h at 800°C, the alloys PCMA-5 through -9 contained large amounts of precipitate on grain boundaries and slip bands. Precipitation was generally accompanied by a loss of ferromagnetism (Table 3.1.4).

Because the aim composition for the alloys did not always coincide with the actual composition, the points for the alloys shown in the Schaeffler diagram (Fig. 3.1.1) must be adjusted. This compositional discrepancy involved mainly the austenite stabilizers manganese and carbon, which both fell below goal levels (Table 3.1.2). Thus nickel equivalents must be readjusted, lowering all points for the ten alloys shown in Fig. 3.1.1. This downward translation of the points changes somewhat the microstructures predicted from the diagram. These changes are summarized in Table 3.1.5, where they are compared with the phases that were observed. (Precipitates are not given in Table 3.1.5, since they are not accounted for on the Schaeffer diagram.

Table 3.1.5. Phases and constituents predicted by Schaeffler diagram and those observed

Alloy	Predicted		Observed[1]
	Aim composition	Actual composition	
PCMA-0	γ + δ	γ + δ	γ + δ
-1	γ + M	γ + M	γ + δ
-2	γ	γ + M	γ + δ
-3	γ + M	M	M + γ(?)
-4	γ + M	γ + M	γ + M
-5	γ	γ + M	γ + δ
-6	γ	γ	γ + δ
-7	γ	γ	γ
-8	γ	γ + δ	γ + δ
-9	γ	γ	γ + δ

γ = austenite M = martensite
δ = δ-ferrite P = precipitate

[1]Observed precipitates are not given since they are not given in the Schaeffler diagram.

The most notable differences between the observed and predicted phases involve PCMA-0, -1, -2, -5, -6, and -9, where the major predicted constituents were either γ or γ + M and where the observations indicated that the major phase present were δ and γ. Thus, the Schaeffler diagram boundaries (Fig. 3.1.1) need to be altered for high-manganese alloys. Alternatively, the multiplying factor for manganese needs to be changed. This latter approach has been suggested by several investigators,[4-6] who have also proposed values other than the 0.5 used in Eq. (1). We are investigating which of these alternatives is best.

Regardless of the best approach to explain the discrepancy with the Schaeffler diagram, the investigation of these ten button heats has provided insight into possible austenitic-base compositions. We are obtaining five additional button heats to verify these observations, after which we will determine a final base composition (or compositions) for further alloying. The compositions of the five new heats will vary in chromium between 10 and 16%, manganese between 15 and 20%, and carbon between 0.1 and 0.2%. Observations made on these steels will also help provide a better understanding of the role of manganese as an austenite stabilizer.

3.1.5 References

1. R. L. Klueh and E. E. Bloom, ***Alloy Development for Fast Induced-Radioactivity Decay for Fusion Reactor Applications***, ORNL/TM-8944 (March 1984).

7. R. L. Klueh and P. J. Maziasz, "The Development of Austenitic Steels for Fast Induced-Radioactivity Decay," pp. 59–60 in *ADIP Semiannu. Prog. Rep. March 31, 1984,* DOE/ER/0045/12, U.S. DOE, Office of Fusion Energy.

3. H. Schneider, "Investment Casting of High Hot-Strength 12-Percent Chrome Steel," *Foundry Trade J.*, 108, 563–64 (1960).

4. E. R. Szumachowski and D. J. Kotecki, "Manganese Effect on Stainless Steel Weld Metal Ferrite," *Welding J.,* 63, 156s–61s (1984).

5. F. C. Hull, "Delta Ferrite and Martensite Formation in Stainless Steels," *Welding J.,* 52, 193s–203s (1973).

6. R. H. Espy, "Weldability of Nitrogen-Strengthened Stainless Steels," *Welding J.,* 61, 149s–56s (1982).

3.2 SWELLING BEHAVIOR OF TITANIUM - MODIFIED ALLOYS IN EBR-II - F. A. Garner, H. R. Brager and R. J. Puigh (Hanford Engineering Development Laboratory)

3.2.1 AOIP Tasks

AOIP Task 1.C.2. Microstructure and Swelling of Austenitic Alloys.

3.2.2 Objective

The object of this effort is to determine the impact on swelling of solute modification of AISI 316 alloys.

3.2.3 *Summary*

It appears that titanium additions to stainless steels covering a wide compositional range around the specifications of AISI 316 result only in an increased delay period before neutron-induced void swelling proceeds. Once swelling is initiated the post-transient behavior of both annealed and cold-worked titanium-modified steels is quite consistent with that of AISI 316, approaching a relatively temperature-independent swelling rate of ~1% per dpa.

3.2.4 Progress and Status

3.2.4.1 Introduction

The question is often raised whether the modification of austenitic steels by solute additions can forestall the inevitability of reaching the ~1%/dpa swelling rate exhibited by pure Fe-Ni-Cr ternary alloys and various 300 series stainless steels.[1-3] Although it is known from numerous studies that titanium additions tend to suppress swelling of austenitic alloys, it has not been shown whether the benefit of adding titanium and other elements results in a permanent reduction in the maximum swelling rate or just a delay in the onset of swelling. In a recent design study on the Starfire Tokamak fusion plant it was stated that the assumed swelling of the titanium-modified alloy designated PCA (Prime Candidate Alloy for the fusion Path A alloy series) was one-tenth that of AISI 316.[4] This optimistic assumption implies that solute additions, particularly of titanium, suppress the steady-state swelling rate rather than just extend the incubation period.

The most relevant fission reactor data is that derived from irradiations of PCA and 316+Ti in the high He/dpa environment of HFIR,[5,6] but these data are too sparce to determine whether the inherent post-transient swelling rate of austenitics (~1%/dpa) can be modified by titanium and other elements. If one ignores the possibly synergistic effects of the helium and solutes, however, there are relevant data from the U.S breeder reactor program that can be used to address this question. It has earlier been shown from comparative irradiations of AISI 316 in HFIR and EBR-II that the difference in helium/dpa levels in these two reactors does not substantially affect the swelling behavior of AISI 316.[7,8]

Two sets of EBR-II data will be considered. The first set will be used to establish the relative behavior of Ti-modified 316 and unmodified 316, and also to determine the influence of cold-work on this relationship. Using the insight gained from this analysis a second data set will be analyzed for the effect of more extensive compositional variations.

3.2.4.2 Swelling of LS-1

The alloy LS-1 was developed at Oak Ridge National Laboratory and is one of the earliest titanium-modified alloys irradiated in the U.S. Breeder Program. Conseouently this alloy has one of the highest levels of reactor exposure. Its composition in wt.% is Fe-13Ni-16Cr-1.8Mo-1.0Mn-0.9Si-0.10Ti-0.05C. In addition to the titanium, this alloy has about twice the normal silicon level used in AISI 316 in the U.S. Breeder Program.

Fig. 3.2.1a shows a comparison of the swelling behavior of 20% cold-worked LS-1 with the temperature-independent behavior of 20% cold-worked N-lot AISI 316. N-lot contains very little titanium and does not exhibit the temperature sensitivity of incubation observed in many heats of AISI 316.[1] It is therefore used as a standard "template" curve with which to compare the development of swelling in other alloys. Note that for swelling levels >5% the LS-1 curves tend to parallel the N-lot curve. The transient behavior of LS-1 appears to be quite sensitive to temperature however. This sensitivity has been observed in other heats of AISI 316[1] and is therefore not entirely a consequence of titanium addition.

Fiq. 3.2.1b shows that the annealed condition of LS-1 at 510°C is also swelling at a rate comparable to that of N-lot but with a shorter transient period. Note that the dotted lines drawn in Fig. 3.2.1b indicate that the N-lot steel at comparable voidage levels swells at the same average rate as that determined for LS-1 at 510°C. Fig. 3.2.1c shows that annealed LS-1 at other irradiation temperatures also approaches a steady-state swelling rate comparable to that of the N-lot steel. It therefore appears that the compositional differences between LS-1 and AISI 316 only affect the duration of the transient regime of swelling, which is also sensitive to the starting thermal-mechanical state of the alloy. In addition the post-transient swelling rate of Ti-modified alloys also appears to be relatively insensitive to irradiation temperature over a very broad temperature range.

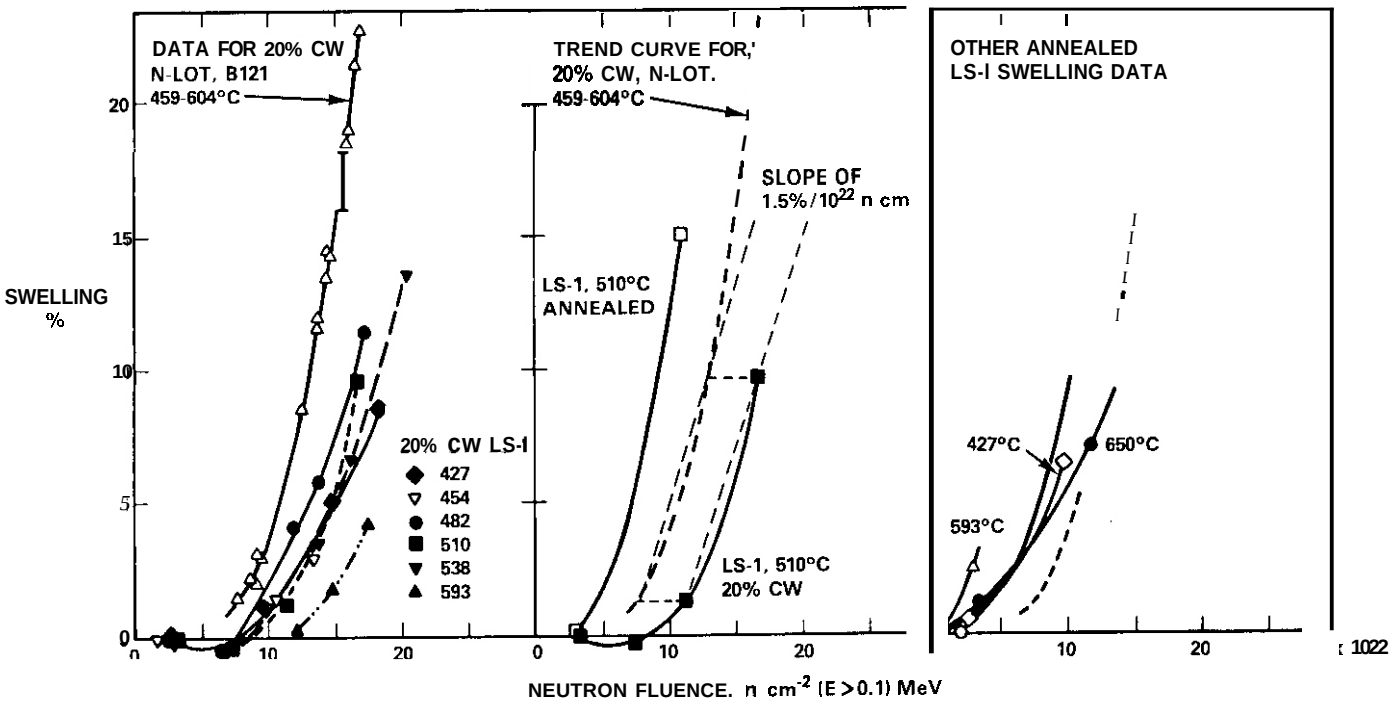

Fig. 3.2.1(a) Comparsion of the swelling behavior in EBR-II of N-Lot AISI 316 and LS-1 at various temperatures. Both alloys are in the 70% cold-worked condition. (b) Comparison of annealed and cold-worked LS-1 swelling behavior at 510°C. Note that linear extrapolation of LS-1 data gives the same result as would be obtained for N-lot at comparable swelling levels. (c) Swelling of annealed LS-1 at other temperatures.

The similarity of post-transient behavior in annealed and cold-worked alloys thus suggests the validity of using data on annealed steels to forecast the influence of solute additions on the swelling of cold-worked alloys. This approach will be used in the following section to study the synergistic effects of titanium and other elements.

3.2.4.3 Swelling of a Series of Titanium-Modified Alloys

In another experiment covered in more depth elsewhere,[',''] the general effect of titanium on swelling can be assessed in synergism with that of other compositional changes. The MV-III experiment involved the irradiation in EBR-II of a large number of compositionally-modified 316-base alloys in both the cold-worked and annealed conditions. Density change data are available for these alloys to exposure levels as large as ~15 x 10^{22} n/cm² (E > 0.1 MeV) or 2.75 dpa.

In general, the predominant effect of titanium additions to both cold-worked and annealed alloys is to extend the duration of the transient regime, but there are occasional exceptions. Fig. 3.2.2 shows density change data at 540°C for nine series of annealed alloys, each with a different base composition and each having variations in titanium. Note that with few exceptions the addition of titanium results only in a shift of the swelling curve to higher fluence. If these data are replotted to show the influence of other solutes a similar conclusion can be drawn, namely that solute additions to AISI 316 affect primarily the duration of the transient regime. Other studies reach the same conclusion for elements such as phosphorous and silicon.[',''] For some combinations of solutes the transient regime is shortened rather than extended, however. As shown in Fig. 3.2.3 the swelling curves continuously accelerate in swelling rate and approach the 1%/dpa rate intrinsic to the austenitic Fe-Ni-Cr system.

Fig. 3.2.4 shows the tendency of the swelling rate in this alloy system to be related only to the current swelling level. Note also in Fig. 3.2.4 that the swelling behavior at 425°C mirrors that at 540°C, even though the transient regime is in general somewhat longer at 425°C for this alloy series, as shown in Fig. 3.2.5. The tendency of the swelling rate in an alloy series to depend only on the swelling level has also been observed in other studies.[']

3.2.5 Discussion

It is important to recognize that the results of this and other studies signal the inevitablity of eventually reaching swelling rates of ~1%/dpa in austenitic alloys, whether modified by cold-working, or by addition of titanium or other elements. Based on comparisons of swelling of AISI 316 in EBR-II and

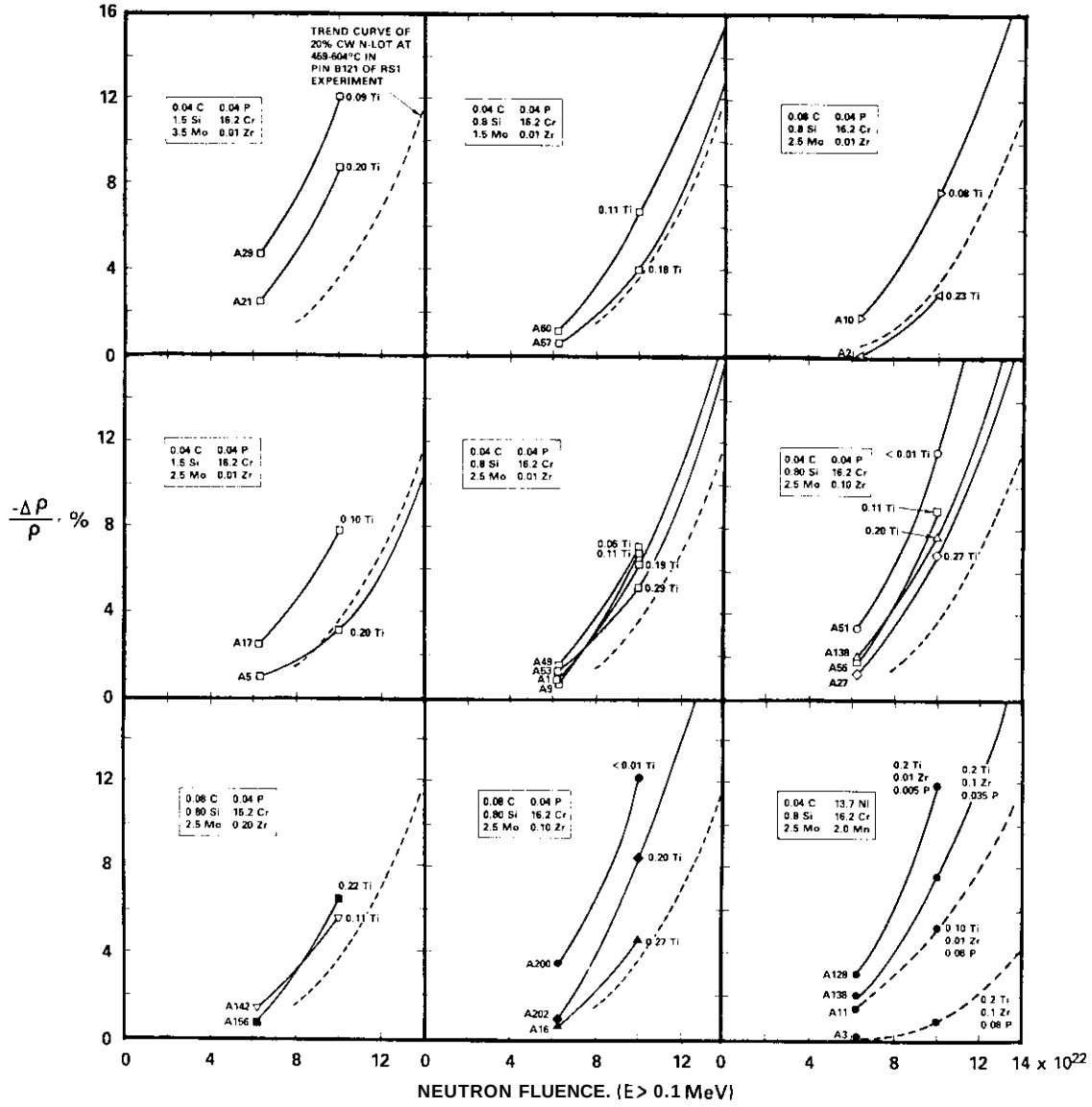

Fig. 3.2.2. Influence of titanium on swelling of various compositionally-modified 316-type alloys in the annealed condition at 540°C. Alloy designations and compositions are shown for each alloy series. Note that percent density change $\Delta\rho/\rho_0$ is plotted in these curves instead of swelling.

HFIR[7,8] there appears to be little chance that such behavior will be modified by large helium levels or other factors relevant to fusion reactors. Alloy development efforts on austenitic alloys for fusion environments therefore should not be directed toward modification of the swelling rate but toward the maximum extension of the transient duration.

3.2.6 Future Work

This effort will continue to identify the synergisms involved in the interactions of various solutes.

3.2.7 References

1. F. A. Garner, J. Nucl. Mater., 122 & 123 (1984) 459-471.
2. F. A. Garner and H. R. Brager, "Swelling of Austenitic Fe-Ni-Cr Ternary Alloys During Fast Neutron Irradiation," Symp. on Effects of Radiation on Materials, ASTM STP R70 (1984), F. A. Garner and J. S. Perrin, Eds., in press.
3. B. J. Makenas, "Swelling of 20% Cold-Worked 316 Stainless Steel Fuel Pin Cladding and Ducts," ibid.
4. "Starfire - A Commerical Tokamak Fusion Power Plant Study", ANLIFPP-80-1, vol. 1, p. 10-41.

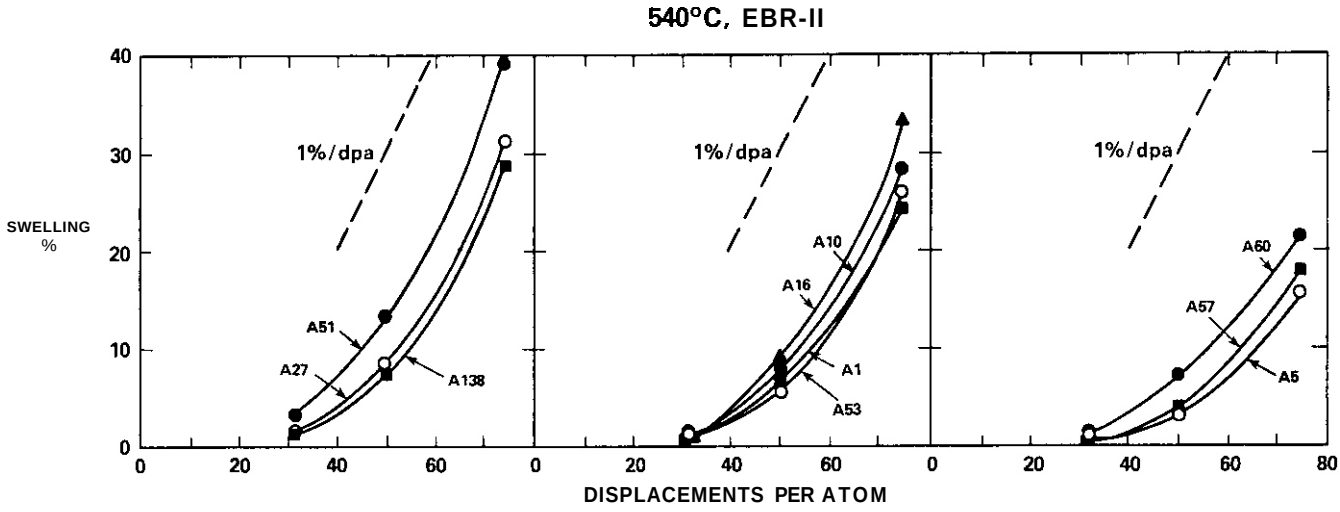

Fig. 3.2.3. Swelling $\Delta V/V_0$ of various annealed titanium-modified 316 alloys at 540°C in EBR-II.

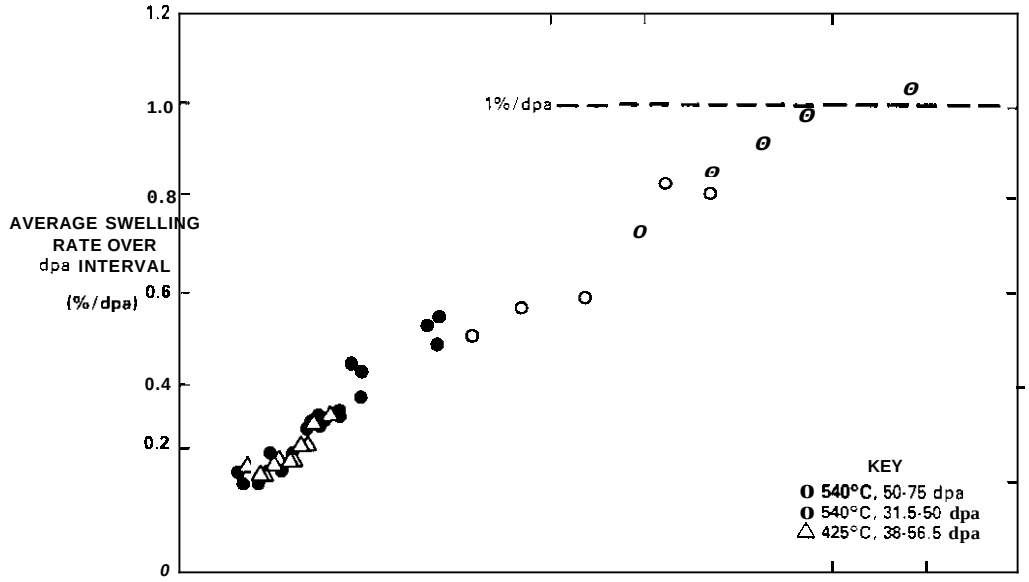

Fig. 3.2.4 Average swelling rate observed in annealed Ti-modified steels at 425 and 540°C, showing similar approach to a swelling rate of 1%/dpa.

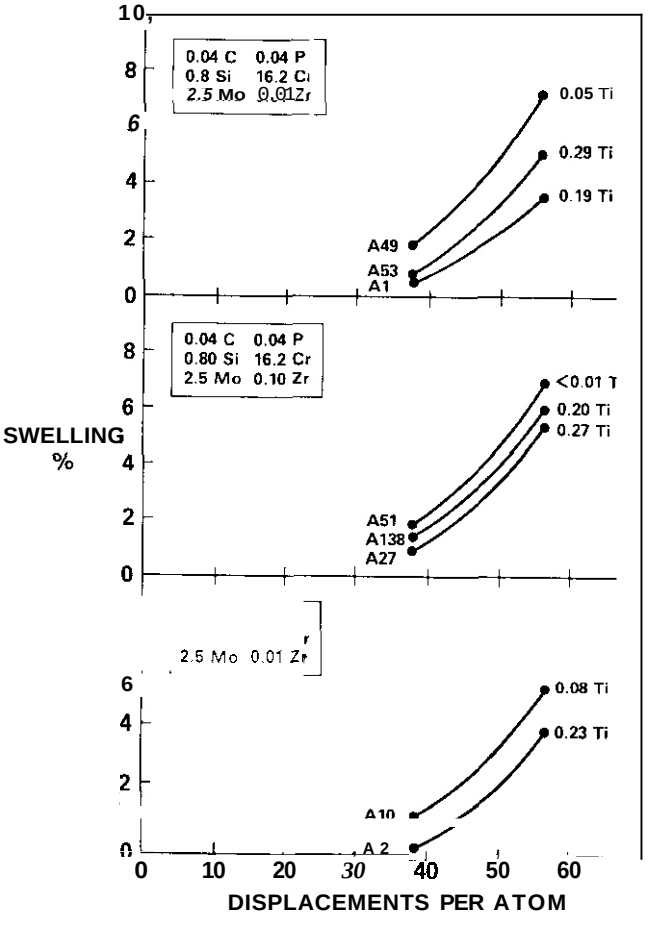

Fig. 3.2.5 Swelling of various titanium-modified AISI 316 steels at 425°C in EBR-II.

5. P. J. Maziasz and E. E. Bloom, "Comparison of Titanium-Modified and Standard Type 316 Stainless Steel Irradiated in HFIR: Swelling and Microstructure," AOIP Quarterly Progress Report, DOE/ET-0058/1, August 1978, p. 40.

6. P. J. Maziasz and D. N. Braski, "Swelling and Microstructural Development in Path A PCA and Type 316 Stainless Steel Irradiated in HFIR to about 22 dpa," ADIP Semiannual Progress Report, DOE/ER-0045/9, September, 1982, p. 44.

7. H. R. Brager and F. A. Garner, J. Nucl. Mater., 117 (1983) 159.

8. H. R. Brager and F. A. Garner, Proceedings BNES Symposium on Dimensional Stability and Mechanical Behavior of Irradiated Metals and Alloys, Brighton, England, Vol. II, p. 1 April 11-14, 1983.

9. F. A. Garner, "Swelling Behavior of Titanium-Modified AISI 316 Alloys", OAFS Quarterly Progress Report DOE/ER-0046/17, May 1984, p. 102-108.

10. F. A. Garner and H. R. Brager, "Influence of Titanium on the Neutron-Induced Swelling of Austenitic Alloys, OAFS Quarterly Progress Report DOE/ER-0046/19, 1984 (in press).

11. F. A. Garner, "A Model Describino the Role of Phosphorus on the Swelling and Creep of Austenitic Alloys," HEOL-SA-3153, to be published in Proc. of First Inter. Conf. on Fusion Reactor Materials, Tokoyo Japan, Dec. 3-6, 1984.

12. F. A. Garner and W. G. Wolfer, J. Nucl. Mater., 122 & 123 (1984) 201-206.

13. B. Esmailzadeh, A. S. Kumar and F. A. Garner, "The Influence of Silicon on Void Nucleation on Irradiated Alloys," in refs. 10 and 11.

14. F. A. Garner, "The Influence of Reactor Spectra and Irradiation Temperature on the Swelling of AISI 316 Stainless Steel," OAF Quarterly Progress Report DOE/ER-0046/12, Feb. 1983, 178-193.

3.3 SWELLING OF Fe-Cr-Mn TERNARY ALLOYS IN FFTF - H. R. Brager and F. A. Garner (Hanford Engineering Development Laboratory)

3.3.1 ADIP Task

AOIP Task 1.C.7 Microstructure and Swelling in Austenitic Alloys.

3.3.2 Objective

The object of this effort is to determine those factors which control the swelling of alloy systems which have the potential for reduced activation.

3.3.2 *Summary*

The swelling of eight simple Fe-Mn binary and Fe-Cr-Mn ternary alloys has been measured hy an immersion density technique after irradiation at ~520°C to 3.2 x 10^{22} n/cm², E > 0.1 MeV, or n15 dpa. The swelling of these alloys decreases with manganese but exhibits a dependence on manganese content that is weaker than that of nickel in Fe-Cr-Ni alloys. The dependence on chromium is even weaker, in sharp contrast to the behavior observed in Fe-Cr-Ni alloys. The addition of other solutes also decreases the swelling.

3.3.4 Progress and Status

3.3.4.1 Introduction

In an earlier report it was noted that a series of austenitic alloys based on manganese substitution for nickel was included in the MOTA-1B experiment for irradiation in FFTF.[1] MOTA-1B has been discharqed from the reactor and the measurement of density changes is in progress. While data will eventually be available for irradiations at 400, 570 and 600°C on manqanese stabilized commercial alloys, developmental alloys and simple binary and ternary alloys, only data on the latter irradiated at 520°C are completely available at this time. The specimens were standard TEM microscopy disks which were irradiated to 3.2 x 10^{22} n/cm² (E > 0.1 MeV) or ~15 dpa.

3.3.4.2 Results

Fig. 3.3.1 shows the density changes measured in the binary and ternary alloys. Fig. 3.3.2 shows a comparison with Fe-Cr-Ni ternary alloys irradiated in the AA-VII experiment in EBR-II.[2] The irradiation conditions depicted in Fig. 3.3.2 for Fe-Cr-Ni alloys bracket the Fe-Cr-Mn data, both in irradiation temperature and neutron exposure level.

Table 3.3.1 lists some limited swelling data on some solute-modified alloys and shows that solute additions to Fe-Cr-Mn alloys lead to substantial decreases in swelling. The neqative swelling values verify that phase changes and/or ordering has occured.

3.3.5 Discussion

While swelling decreases with manganese content, it does *so* at a much lesser rate than would occur if the alloys were stabilized with nickel. Even more importantly, there is very little dependence of swelling on chromium level, in sharp contrast to the behavior of Fe-Cr-Ni alloys. The lesser impact of manganese level on swelling is similar to the reduced effectiveness of manganese relative to nickel in promoting the stability of the austenite phase.

The MOTA irradiation temperature of 520°C lies between the 510 and 538°C irradiation temperatures of the AA-VII experiment in EBR-II. It was in the range 510-538°C that Fe-Cr-Ni alloys with low nickel levels departed from their temperature-independent behavior and began to develop longer transient regimes of swelling. The maximum swellinq of ~5% in the Fe-Cr-Mn alloys at 15 dpa is quite consistent with the swelling behavior developed by the Fe-Cr-Ni alloys below 510°C. These data suggest that the post-transient swelling rate of the Fe-Cr-Mn system is also ~1%/dpa.

3.3.6 Future Work

Density change measurements will continue on the other alloys irradiated at 520°C and on alloys irradiated at ~420 and ~620°C. Electron microscopy examination will also be initiated.

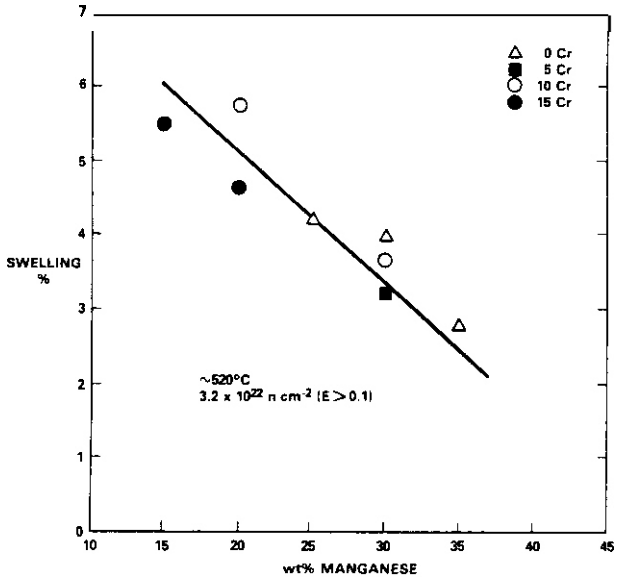

Fig. 3.3.1. Swelling observed in Fe-Cr-Mn alloys irradiated in FFTF to 3.2 x 10^{22} n/cm^2 (E > 0.1 MeV) at ~520°C.

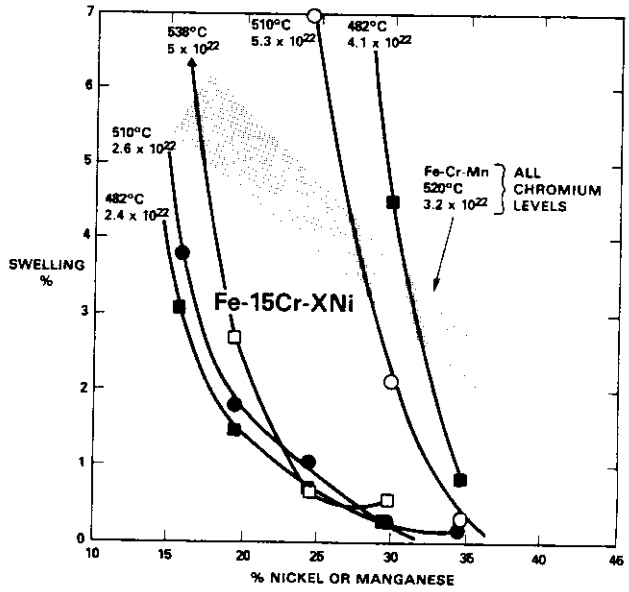

Fig. 3.3.2. Comparison of swelling of Fe-Cr-Ni alloys in EBR-II and Fe-Cr-Mn alloys in FFTF under comparable irradiation conditions.

Table 3.3.1. Composition and swelling of Phase IV solute-modified Fe-Cr-Mn Alloys (%)

	Mn	Cr	C	N	V	P	B	Al	W	Ni	Si	Swelling (%)
R76 (20% CW)	30	2.0	0.60	0.05	-	0.05	0.005	-	-	n.5	0.4	+0.97
R17 (SA)	30	2.0	0.40	0.15	1.0	0.05	0.005	-	1.0	0.5	0.4	-0.14
R77 (SAA)	30	2.0	0.40	0.15	1.0	0.05	0.005	-	1.0	0.5	0.4	-0.12
R83 (SA)	15	5.0	0.60	0.05	-	0.05	0.005	-		0.5	1.0	-0.06

SA = Solution annealed, SAA = SA and aged, CW = cold worked

3.3.7 References

1. H. R. Brager and F. A. Garner, "Fundamental Alloy Studies", DAFS Quarterly Progress Report DOE/ER-0046/17, May 1984, p. 93.

2. F. A. Garner and H. R. Brager, "Swelling of Fe-Ni-Cr Ternary Alloys at High Exposure", DAFS Quarterly Progress Report DOE/ER-0046/16, February 1984, p. 38.

4. PATH B ALLOY DEVELOPMENT — HIGHER STRENGTH Fe-Ni-Cr ALLOYS

5.1. SOLUTE SEGREGATION AND VOID FORMATION IN ION-IRRADIATED VANADIUM-BASE ALLOYS - B. A. Loomis and D. L. Smith (Argonne National Laboratory)

5.1.1 ADIP Task

ADIP Task I.A.l. Define Material Property Requirements and Make Structural Life Predictions.

5.1.2 Objective

The objective of this work is to provide guidance on the applicability of vanadium-base alloys for structural components in a fusion reactor.

5.1.3 Summary

The radiation-induced segregation of solute atoms in the V-15Cr-5Ti alloy was determined after either single- dual-, or helium implantation followed by single-ion irradiation at 725°C to radiation damage levels ranging from 103 to 169 dpa. Also, the effect of irradiation temperature (600-750°C) on the microstructure in the V-15Cr-5Ti alloy was determined after single-ion irradiation to 200 and 300 dpa. The solute segregation results for the single- and dual-ion irradiated alloy showed that the simultaneous production of irradiation damage and deposition of helium resulted in enhanced depletion of Cr solute and enrichment of Ti, C and S solute in the near-surface layers of irradiated specimens. The observations of the irradiation-damaged microstructures in V-15Cr-5Ti specimens showed an absence of voids for irradiations of the alloy at 600-750°C to 200 dpa and at 725°C to 300 dpa. The principle effect on the microstructure of these irradiations was to induce the formation of a high density of disc-like precipitates in the vicinity of grain boundaries and intrinsic precipitates and on the dislocation structure.

5.1.4 Progress and Status

5.1.4.1 Introduction

The V-15Cr-5Ti alloy is considered to be a candidate alloy for structural components in a magnetic fusion reactor (MFR). The simultaneous production of atomic displacement damage and deposition of helium atoms within the alloy during the reactor lifetime can be expected to have a significant influence on the radiation-induced segregation (RIS) and thermal-induced segregation (TIS) of solute atoms in the alloy. The RIS and TIS of the solute atoms will determine the evolution of the microstructure in the irradiated alloy. Therefore, the RIS and TIS of solute atoms will have significant concomitant effects on the dimensional stability (swelling), mchanical properties, and corrosion resistance of the irradiated alloy.

Observations of the microstructure in the V-15Cr-5Ti alloy after neutron or ion irradiation have shown a remarkable absence of voids or helium-filled cavities and the presence of irradiation-induced precipitates which might be attributed to RIS of solute atoms.[1-4] In this report, experimental results are presented on the RIS of solute atoms in the V-15Cr-5Ti alloy after either single- dual-, or helium implantation followed by single-ion irradiation to irradiation damage levels ranging from 103 to 169 dpa. Also, experimental results are presented on the temperature dependence of microstructural changes that occurred in the V-15Cr-5Ti alloy on single-ion irradiation at temperatures ranging from 600°C to 750°C and to radiation damage levels of 200 dpa or 300 dpa.

5.1.4.2 Materials and Procedure

The V-15Cr-5Ti alloy was supplied in the form of 0.81-mm thick sheet (melt number 834-6) from the Fusion Program Research Materials Inventory at Oak Ridge National Laboratory. The chemical analysis of this material is presented in Table 5.1.1. The as-received sheet was reduced in thickness to 0.25 mm and annealed at 1100°C for two hours in a system evacuated to 6.7×10^{-7} Pa.

Table 5.1.1. Chemical analysis of the V-15Cr-5Ti alloy

Element	Concentration (a/o)
Cr	14.1
Ti	6.6
C	0.14
O	0.10
N	0.18
S	4.03

Specimens of the alloy, each with a diameter of 3.05 mm, were mounted in a tungsten holder for either single-ion irradiation with 4.0-MeV $^{58}Ni^{++}$ ions, dual-ion irradiation with 3.0-MeV $^{58}Ni^{++}$ and 0.25-MeV $^{3}He^{+}$

ions or helium implantation using 0.50-MeV $^4He^+$ ions followed by irradiation with 4.0-MeV $^{58}Ni^{++}$ ions. The irradiations of the specimens at 600, 675, 725 and 750°C were conducted in a cryogenically pumped chamber evacuated to 1.3 x 10^{-6} Pa. The chamber was connected by cryogenically pumped, ion-beam transport tubes to the 2-MeV tandem and 0.25-MeV ion accelerators at Argonne National Laboratory. The irradiation temperatures for this study were selected on the basis of the temperature for maximum void swelling in pure V.[3]

Following irradiation, the dependence on depth in the irradiation-damaged layer (~1500-nm thickness) of the RIS and TIS of solute atoms was determined by use of the Auger Electron Spectroscopy (AES) technique in combination with sputter-ion erosion of the specimen surface. AES analyses at room temperature were performed using a primary electron beam at 5 keV with a diameter of ~10 μm to excite the electron transitions. Depth profiling was accomplished by sputter-ion erosion with 1-keV Ar ions in an Ar atmosphere of 6.5 x 10^{-3} Pa. The sputter-ion erosion rate was ~3.0 nm per minute for specimens eroded to a depth of ~100 nm. It should be noted that the AES analyses did not show the presence of Ni atoms which might be attributed to the irradiations with Ni ions. Moreover, profilometry of the irradiated surface on the specimens before the AES analyses showed no evidence for a step-height between the unirradiated and irradiated areas which might be attributed to swelling and/or sputtering during ion irradiation. Following the AES analyses, the specimens were sectioned from the irradiated surface to a depth of 1050 nm in the case of 4.0-MeV $^{58}Ni^{++}$ ion irradiations and 650 nm in the case of the 3.0-MeV $^{58}Ni^{++}$ ion irradiation, then thinned from the backside to perforation in an 80% CH_3OH-20% H_2SO_4 solution at ~5°C.

Deposited energy densities as a function of ion range in the alloy from a computerized TRIM code were converted to displacements per atom (dpa) and helium atom deposition using a threshold energy of 40 eV.[5] The depths in the V-15Cr-5Ti alloy for peak irradiation damage during 3.0-MeV and 4.0-MeV $^{58}Ni^{++}$ ion irradiation were computed to be 900 and 1150 nm, respectively. The depths for peak deposition of helium atoms during 0.25-MeV $^3He^+$ and 0.50-MeV $^4He^+$ ion implantation were computed to be 670 and 1110 nm, respectively. The specimens were irradiated to displacement damage levels of 103 to 300 dpa at a damage rate of ~5 x 10^{-3} dpa/s. In the case of the specimen implanted with helium prior to 4-MeV $^{58}Ni^{++}$ ion irradiation, the helium concentration was 780 appm. In the case of the dual-ion irradiated specimen, the helium implantation rate was 11.6 appm/dpa.

The microstructures of the irradiated alloy specimens were observed by transmission electron microscopy (TEM) in a Philips EM 400T electron microscope operated at 120 kV. The thickness of the specimens for TEM was typically 100 nm.

5.1.4.3 Experimental Results

RIS in the V-15Cr-5Ti alloy

The RIS of the Cr, Ti, C and S solute atoms in single-, dual-, and helium implanted plus single-ion irradiated V-15Cr-5Ti alloy specimens after irradiation at 725°C is shown in Fig. 5.1.1 and Fig. 5.1.2. A comparison of the solute segregation results from the AES analyses for the single- and dual-ion irradiated alloy shows that the simultaneous production of irradiation damage and deposition of helium resulted in enhanced depletion of Cr solute in the near-surface layers (0-10 nm) and enrichment of Ti (0-25 nm), C (0-70 nm), and S (0-30 nm) solute atoms. An increase of the irradiation damage level from 0 dpa to 169 dpa resulted, generally, in an increase of the solute concentration in the near-surface layers of the specimens. In the case of specimens that were pre-injected with helium prior to single-ion irradiation, the Cr and S concentrations in the near-surface layers were increased whereas the Ti and C concentrations were decreased relative to the concentrations for the single-ion irradiated specimens. The concentration and distribution of oxygen and nitrogen solute atoms in the near-surface layers of the irradiated specimens were not significantly altered from the concentration and distribution of these atoms in the unirradiated specimen.

TEM for the irradiated V-15Cr-5Ti alloy

The microstructures for the V-15Cr-5Ti alloy specimens after irradiation at 600, 675, 725 and 750°C to 200 dpa and at 725°C to 300 dpa are shown in Figs. 5.1.3 and 5.1.4, respectively. Voids were not visible in the microstructures of these irradiated specimens. The principle effect on the unirradiated alloy microstructure of these irradiations was the formation of a high density of disc-like precipitates in the vicinity of grain boundaries and intrinsic precipitates and on the dislocation structure. An increase of the irradiation temperature from 600°C to 750°C resulted in an increase of the average diameter of the precipitates from ~1 nm to ~90 nm. In the case of the irradiation at 600°C, the precipitates were uniformly distributed in the matrix with a diameter (~1 nm) near to the resolution limit of the electron microscope (~0.3 nm). An increase of the irradiation temperature from 600°C resulted in the redistribution of these small diameter precipitates and growth of the precipitates in the vicinity of grain boundaries and intrinsic precipitates. Moreover, the microstructures suggested that the precipitates were redistributed primarily by interactions with gliding dislocations. An increase of the radiation damage level from 200 dpa to 300 dpa on irradiation of 725°C resulted in growth of the precipitates from ~1.5 nm to ~40 nm. A comparison of the microstructures for the single-ion irradiated alloy (Figs. 5.1.3 and 5.1.4) with the microstructure for the dual-ion irradiated alloy (Reference 4, Fig. 5.1.7) shows the significant effect of simultaneous radiation-damage production and deposition of helium atoms on precipitate distribution and void (cavity) formation in the V-15Cr-5Ti alloy, i.e., a uniform distribution of precipitates and cavities in the dual-ion irradiated alloy. Additional information on the composition of the precipitates in the irradiated alloy is presented in Reference 4.

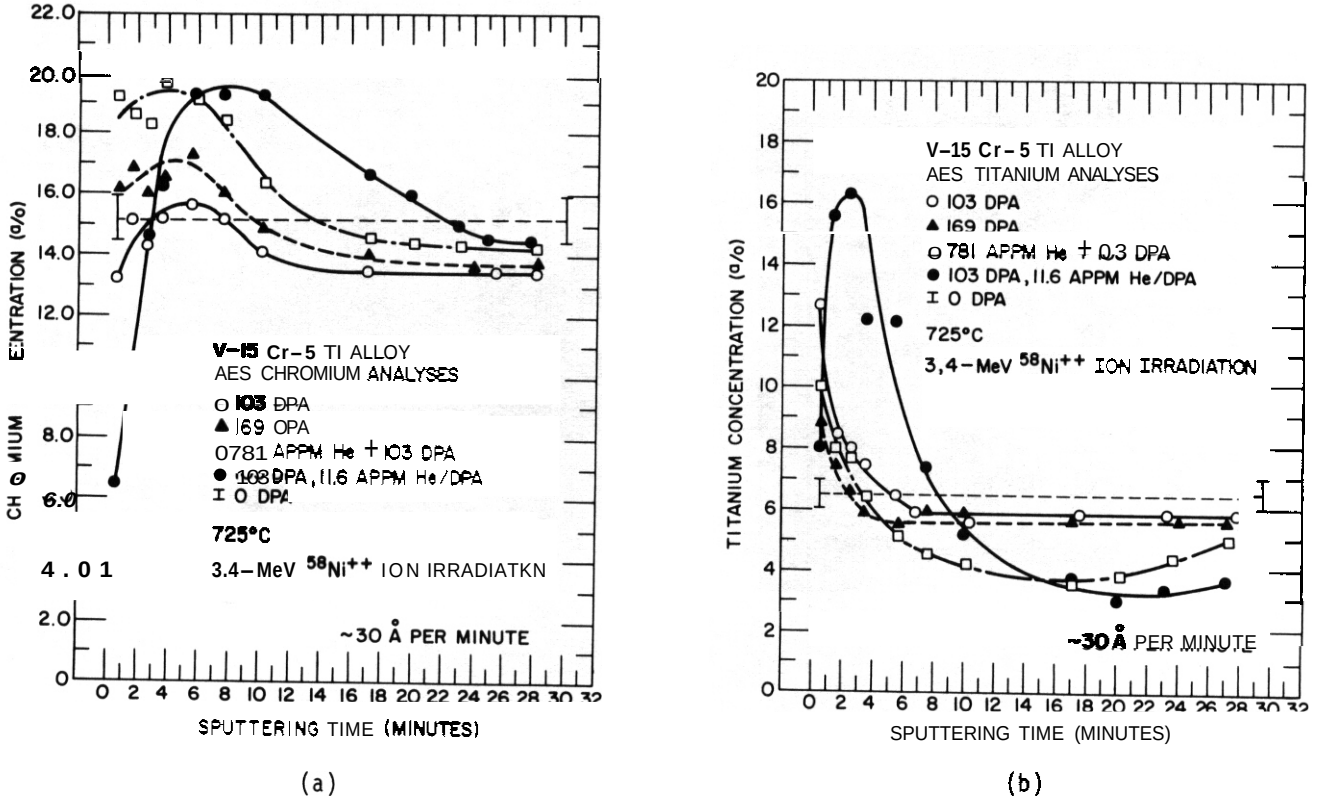

(a) (b)

Fig. 5.1.1 Dependence of Cr (a) and Ti (b) concentration on depth in the irradiation-damage layer for the V-15Cr-5Ti alloy.

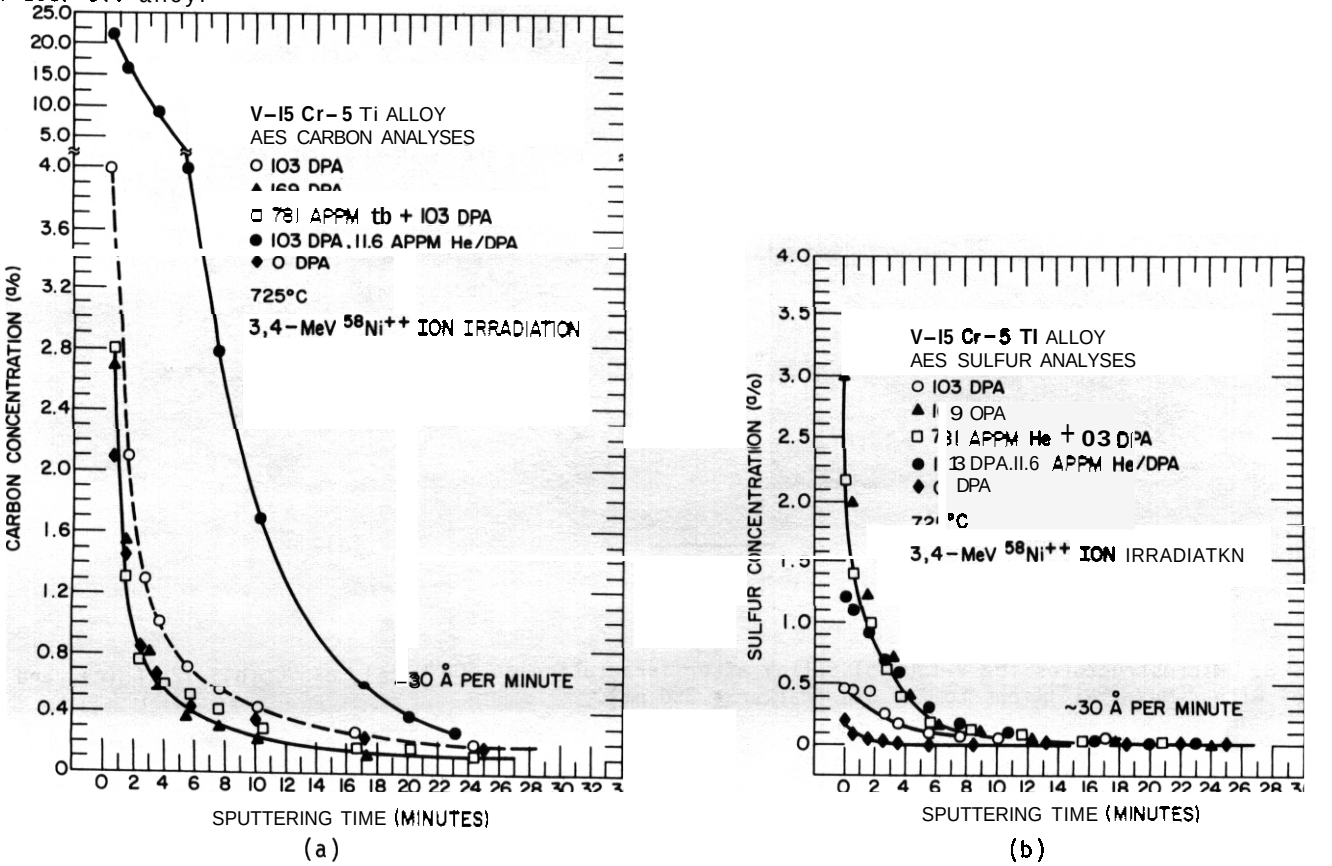

(a) (b)

Fig. 5.1.2 Dependence of C (a) and S (b) concentration on depth in the irradiation-damage layer for the V-15Cr-5Ti alloy.

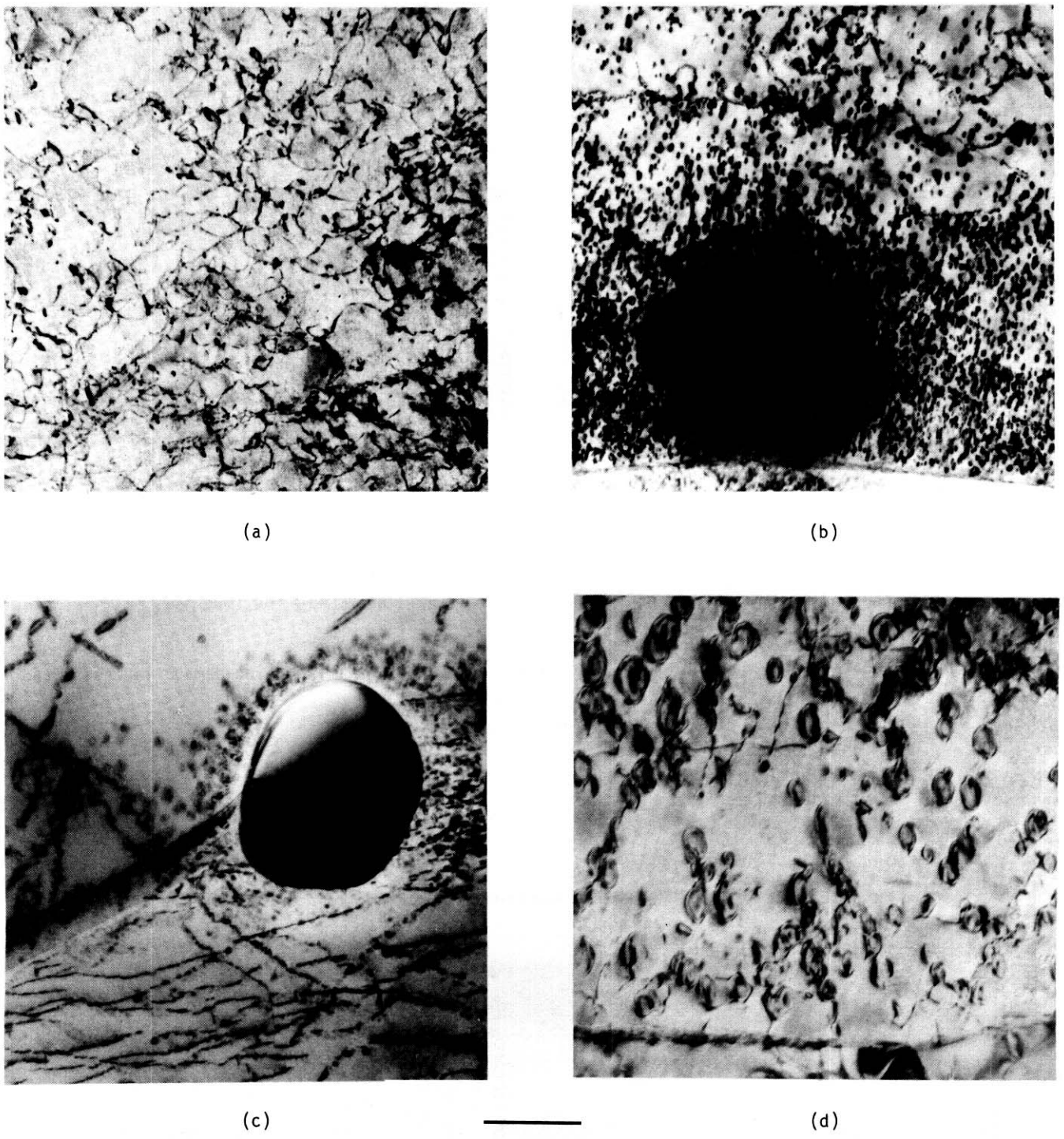

Fig. 5.1.3. Microstructures for V-15Cr-5Ti alloy after irradiation at 600°C (a), 675°C (b), 725°C (c), and 750°C (d) with 4-MeV $^{58}Ni^{++}$ ions to 200 dpa (marker = 350 nm).

Fig. 5.1.4. Microstructure for the V-15Cr-5Ti alloy after irradiation at 725°C to 300 dpa (marker = 350 nm).

5.1.5. Discussion

In this study, we have made the tacit assumption that the enrichment or depletion of solute atoms determined by AES analyses in the near-surface region (< 100-nm depth) of an ion-irradiated specimen provides an accurate assessment of the tendency for segregation of solutes to grain boundaries, intrinsic precipitate interfaces, and irradiation-produced void (cavity) surfaces. This assumption was justified on the basis of results obtained previously for other irradiated metals.[6,7] Moreover, it was expected that the qualitative aspects on the RIS of solutes observed in the present ion-irradiation situation would be applicable to the MFR environment.[6] On this basis, the RIS results suggested that the corrosion resistance of the V-15Cr-5Ti alloy in a MFR environment may be impaired by the Cr depletion in the near-surface layers.[8] Also, the RIS results suggested that the mechanical properties of the V-15Cr-5Ti alloy in a MFR environment may be deteriorated due to the formation of (V, Ti)C and (V, Ti)S compounds in the vicinity of grain boundaries. Future studies that utilize the Electron Energy Loss and Energy Dispersive X-ray techniques in combination with TEM observations of the irradiated specimens will test the validity of the assumption regarding the results from AES analyses.

The results from the TEM observations of the single-ion irradiated V-15Cr-5Ti alloy suggested also that the formation of a high density of disc-like precipitates in the vicinity of grain boundaries may result in deterioration of the mechanical properties for the alloy. The TEM observations showed that the dimensional change of the alloy due to void formation during 4-MeV $^{58}Ni^{++}$ ion irradiation was negligible for irradiation temperatures between 600 and 750°C and damage levels of 200-300 dpa. However, before utilization of these single-ion irradiation results for guidance in the selection of the V-15Cr-5Ti alloy for use in a MFR environment, TEM observations of the alloy should be performed after dual-ion irradiation, e.g. 4-MeV $^{51}V^{++}$ + 500-keV $^{3}He^{++}$ ions, of the alloy at ~700°C to 200-300 dpa.

5.1.6. Conclusions

1. Dual-ion (3.0-MeV $^{58}Ni^{++}$ + 0.25-MeV $^{3}He^{+}$ ions) irradiation in comparison with single-ion (4.0-MeV $^{58}Ni^{++}$ ions) irradiation of the V-15Cr-5Ti alloy results in enhanced depletion of Cr solute and enrichment of Ti, C and S solute at the free surface. The radiation-induced segregation of these solute atoms may result in loss of corrosion resistance and in embrittlement of the alloy in the environment of a MFR.

2. Single-ion irradiation of the V-15Cr-5Ti alloy at 600-750°C to 200 dpa and 725°C to 300 dpa does not result in void formation.

3. The principle effect on the microstructure of the V-15Cr-5Ti alloy on single-ion irradiation at 600-750°C to 200-300 dpa is to induce the formation of a high density of disc-like precipitates in the vicinity of grain boundaries and intrinsic precipitates and on the dislocation structure.

4. The V-15Cr-5Ti alloy should be irradiated with dual ions at ~700°C to 200-300 dpa for TEM observation of the precipitate distribution and cavity formation.

5.1.7 References

1. R. Carlander, S. D. Harkness and A. T. Santhanam, "Effects of Fast-Neutron Irradiation on Tensile Properties and Swelling Behavior of Vanadium Alloys", pp. 399-414 in *Effects of Radiation on Substructure and Mechanical Properties of Metals and Alloys,* ASTM-STP-529, American Society for Testing and Materials, 1973.

2. A. F. Bartlett, J. H. Evans, B. L. Eyre, E. A. Terry and T. M. Williams, "High Temperature Irradiation Damage Structures in Fast Reactor Irradiated Niobium and Vanadium Alloys", pp. 122-129 in *Radiation Effects and Tritium Technology for Fusion Reactors,* Vol. I, J. S. Watson and F. W. Wiffen, Eds., 1976.

3. B. A. Loomis and G. Ayrault, "Cavity Formation in Single- and Dual-Ion Irradiated V-15Cr-5Ti Alloy", pp. 194-205 in *Damage Analysis and Fundamental Studies Quarterly Progress Report, October-December* 1982, DOEIER-0046112, U. S. Department of Energy, Office of Fusion Energy.

4. B. A. Loomis and D. L. Smith, "Swelling of V-15Cr-5Ti Alloy on Single- and Dual-Ion Irradiation", pp. 66-71 in *Alloy Development for Irradiation Performance*, Semiannual Progress Report for Period Ending March 31, 1984, DOE/ER-0045/12, U. S. Department of Energy, Office of Fusion Energy.

5. J. P. Biersack and L. G. Haggmark, "A Monte Carlo Computer Program for the Transport of Energetic Ions in Amorphous Targets", *Nuclear Instruments and Methods*, 174, 257-269 (1980).

6. H. Wiedersich and N. Q. Lam, "Theory of Radiation-induced Segregation", pp. 1-46 in *Phase Transformations During Irradiation*, Frank V. Nolfi, Jr., Ed., Applied Science Publishers, N.Y., 1983.

7. B. A. Loomis, G. Ayrault, S. Gerber and Z. Wang, "Cavity Formation and Solute Segregation in Dual-Ion Irradiated Fe-20Ni-15Cr Alloy", pp. 145-156 in *Damage Analysis and Fundamental Studies Quarterly Progress Report*, April-June 1982, DOE/ER-0046/10, U. S. Department of Energy, Office of Fusion Energy.

8. B. A. Loomis and D. L. Smith, "Corrosion and Oxidation of Vanadium-Base Alloys in Helium Environments", pp. 209-215 in *Alloy Development for Irradiation Performance*, Semiannual Progress Report for Period Ending September 30, 1983, DOE/ER-0045/11, U. S. Department of Energy, Office of Fusion Energy.

5 2 RADIATION EFFECTS IN VANADIUM ALLOYS IN FUSION REACTOR ENVIRONMENTS

- A. Kumar and R. F. Mattas (Argonne National Laboratory, University of Missouri, Rolla)

5.2.1 ADIP Task

ADIP Task I.A.l. Define Material Property Requirements and Make Structural Life Predications.

5.2.2 Objective

The objective of this work is to provide guidance on the applicability of vanadium-base alloys for structural components in a fusion reactor.

5.2.3 Summary

The swelling behavior of neutron irradiated vanadium has been modelled to establish the theoretical limits for swelling. Void and dislocation sink strengths along with the net bias factors for vacancies and interstitials have been calculated. These factors have been combined to predict the maximum steady state swelling rate. The maximum rate is predicted to be about 0.2%/dpa which is close to the value calculated for ferritic steels and about a factor of seven lower than for austenitic stainless steels. This value is also consistent with the limited irradiation data for vanadium.

5.2.4 Progress and Status

5.2.4.1 Introduction

The limited amount of radiation data indicates that vanadium alloys are resistant to swelling and embrittlement. The choice of vanadium alloys for fusion reactor applications suffers, however, from a lack of an adequate data base for neutron-induced swelling at high damage levels ($\gtrsim$ 100 dpa). Much of the available radiation data is taken from ion irradiations, and there are difficulties in translating ion-induced swelling behavior to neutron-induced swelling behavior. Thus, there is a need to model the swelling behavior of vanadium alloys to establish the theoretical limits for swelling and to aid in the analysis of both ion and neutron irradiation experiments. The work presented in this note extends, with some modifications, the earlier work of Sniegowski and Wolfer[1] on ferritic steels to vanadium alloys. All calculations for the maximum swelling rate of vanadium alloys use measured or best estimates of point defect and material properties of vanadium. It is shown that the maximum rate of swelling of the alloys will be governed by the host matrix of vanadium. The calculated maximum swelling rate is then compared with experimental data on swelling of vanadium with various impurity contents and vanadium alloys.

5.2.4.2 Results

The theoretical approach followed here is the same as that of Sniegowski and Wolfer[1] where the void and dislocation sink strengths along with the net bias factors are calculated. These factors are then combined to predict the maximum steady state swelling rate.

Wolfer and Garner[2] have shown that the steady state swelling rate can be expressed as

$$\frac{d}{dt}\left(\frac{\Delta V}{V}\right) = \frac{S_o\, S_d}{(S_o + S_d)^2} \cdot B \cdot F \qquad (1)$$

where S_o and S_d are void and dislocation sink strengths, E is the net bias and F is a function weakly dependent on temperature and the total sink strength-but is strongly dependent on the production rate of point defects, P. P equals the displacement rate, dpa, times the point defect survival fraction in cascades, β. Then the swelling rate per dpa can be expressed as

$$\frac{d(\Delta V/V\%)}{d\,(dpa)} = \frac{S_d}{(S_o + S_d)^2}\, 100\, \beta\, B(F/P) \qquad (2)$$

To obtain the maximum swelling rate, maximum possible values of the F/P ratio and the ratio $(S_o S_d/(S_o+S_d)^2$ need to be substituted in Eq. (2). It has been shown earlier[2] that F/P has a maximum value of 1/2. The ratio $S_o S_d/(S_o + S_d)^2$ has a maximum value of 0.25 when $S_o = S_d$. A reasonable value of β is 0.1[1]. Thus the swelling rate becomes

$$\frac{d(\Delta V/V\%)}{d(dpa)} \leq 1.25\, B \qquad (3)$$

The net bias is given by

$$B = \frac{Z_i^d}{Z_v^d} - \frac{Z_i^o}{Z_v^o} \tag{4}$$

where Z_i^d and Z_v^d are dislocation bias factors for interstitials and vacancies, respectively. Z_i^o and Z_v^o are void bias factors for interstitials and vacancies, respectively. The definition of B in (4) assumes a dislocation dominated regime and that adding a vacancy to the void does not change its surface area significantly.

The void bias factor is given by

$$Z^o(a) \simeq 1 + \left[\frac{\sqrt{1+\eta} - 1}{2\lambda}\right]^{1/3}, \quad a = \text{void radius} \tag{5}$$

where

$$\eta = 4 A \Gamma/[a^3 kT \ell n 2]$$

$$\lambda = \alpha_o - \frac{\Gamma 2 \mu^2 a}{3 \alpha^G \gamma^2}$$

$$\alpha_o = \frac{(7 - 5\nu)}{30}$$

$$\Gamma = \mu v^2 \frac{(1+\nu)^2}{36\pi (1-\nu)}$$

where μ is the shear modulus, v is the relaxation volume, ν is the Poisson's ratio, γ is the surface tension, and α^G is the shear polarizability.

Dislocation bias factors are shown to be

$$Z^d = \text{en}\,(R/c)/(Q_1 - Q_2) \tag{6}$$

where $R \simeq 1000$ x Burgers vector (b), and c is the core radius ($\approx 2b$).

The contributions of the size interaction and the modulus interaction to the bias factor are represented by Q_1 and Q_2, respectively. However, the modulus interaction contribution is found to be very small relative to the size interaction. Therefore,

$$Z^d = \text{en}\,(R/c)/Q_1 \tag{7}$$

where

$$Q = \frac{K_o (r_o/R)}{I_o (r_o/R)} - \frac{K_o (r_o/d)}{I_o (r_o/d)}$$

where K_o and I_o are the modified Bessel functions of the zeroeth order, and,

$$d = b^2 \left|A_o - A_2\right| / \left|B_o\right| \tag{8}$$

where

$$A_o = 0.0136\ \alpha^G$$

$$A_2 = 0.0094\ a^G$$

and $$r_o = B_o/2kT \quad (9)$$

where $$B_o = v\,\frac{\mu b}{3\pi}\left(\frac{1+\nu}{1-\nu}\right)$$

The relaxation volumes needed for the bias calculations are for the saddlepoint configuration. The interstitial relaxation volume in the saddlepoint is believed to be close to its value in the stable configuration. The value of v_i has not been measured for the stable configuration. The value chosen for the bias calculation is based on the pressure derivative of the shear modulus as given in Ref. 1.

The vacancy relaxation volume is calculated from the following equation.

$$v_v = \Delta v_v - \Omega = (Q/T_m)\,(\Delta V_m/\Delta S_m) - \Omega \quad (10)$$

where Ω is the atomic volume, Q is the activation energy of self diffusion, T_m is the melting point, ΔV_m is the volume change upon melting, and ΔS_m is the entropy change upon melting. The dominant value of Q in the temperature regime of interest (~ 700 C) was obtained from the compilation of Peterson[3], and all other parameters were obtained from Turkdogan.[4]

Calculations of the bias factors were done using the parameters given in Table 1. The void bias factors as calculated are 1.018 and 1.010 for interstitials and vacancies, respectively. The dislocation bias factors are 1.160 and 1.009 for interstitials and vacancies, respectively. The calculated net bias is 0.15 which gives the maximum swelling rate of about 0.2% per dpa. This swelling rate is close to the value of ferritic steels and is a factor of seven lower than for austenitic steels.

Table 1. Input Parameters Selected for Calculating Bias

Parameter	Symbol & Value	(Unit)	Ref.
Lattice parameter	a_o = 0.242	nm	*
Surface tension	γ = 1.0	J/m^2	1
Poisson's ratio	ν = 0.3		1
Shear modulus	μ = 46.4	GPa	11
Interstitial shear polarizability	a_i^G = -150.0	eV	1
Vacancy shear polarizability	α_V^G = -15.0	eV	1
Cascade survival fraction	β = 0.1		*
Gas pressure in voids	0		*

* Values assumed or calculated based on CRC handbook data.

The calculated maximum swelling rate of 0.2%/dpa is in agreement with published experimental data. The work of Agarwal et al.[5] shows a maximum of 0.1%/dpa for vanadium with various impurity contents (C, N, O). These samples were irradiated with 3 MeV vanadium ions at various temperatures. Irradiation of vanadium of various carbon contents by fast neutrons to 25 dpa in the work of Takahashi et al.[6] showed a maximum swelling rate of 0.02%/dpa. Vanadium alloys (V-20Ti, V-15Ti-7.5Cr, V-15Cr-5Ti) irradiated to 6 dpa with fast neutrons showed a maximum swelling rate of 0.01%/dpa in the work of Carlander et al.[7] Similar low swelling rates are obtained for vanadium and vanadium base alloys in other published experimental data.[8-10]

5.2.5 Conclusions

The maximum swelling rates predicted for vanadium and vanadium alloys are expected to be significantly below the rates in austenitic stainless steels and similar to the rates in ferritic stainless steels. Future effort in the modeling of swelling in vanadium alloys should focus on the swelling transition period and on correlating the results of fast neutron and ion irradiation experiments. It is felt that ion-simulation experiments can provide swelling data for use in fusion neutron environments provided the data are obtained in a region where damage energy curve is flat to reduce fluxes of point defects to and away from the damage zone. However, the effect of injected interstitials, and differences in survivable fraction of point defects must be taken into account when developing correlations.

5.2.6 References

1. J. J. Sniegowski and W. G. Wolfer, "On the Physical Basis for the Swelling Resistance of Ferritic Steels," University of Wisconsin Report UWFDM-535, August, 1983.

2. W. G. Wolfer and F. A. Garner, "Temperature Dependence of Swelling Rate in Austenitic Steels," OAFS Quarterly Progress Report DOE/ER-0046/12, February, 1983, p. 141.

3. N. L. Peterson, J. Nucl. Matls., 69 & 70, (1978) 3.

4. E. T. Turkdogan, Physical Chemistry of High Temperature Technology, Academic Press, New York, 1980, Tables 1.2 and 3.5.

5. S. C. Agarwal, O. I. Potter, and A. Taylor, Irradiation Effects on the Microstructure and Properties of Metals, ASTM STP 611, 1976, 298-311.

6. H. Takahashi, S. Ohnuki, T. Takeyama, and H. Kayano, J. Nucl. Matls., 96 (1981) 233-242.

7. R. Carlander, S. D. Harkness, and A. T. Santhanam, Effects of Radiation on Substructure and Mechanical Properties of Metals and Alloys, ASTM STP *529,* 1973, 399-414.

8. A. T. Santhanam, A. Taylor, B. J. Kestel, and C. Steves, J. Vac. Sci. Tech., 12, No. 1 (1975) 528

9. J. Bentley and F. W. Wiffen, Nucl. Tech., 30 (1976) *376.*

10. J. Bressers and W. Van Witzenburg, J. Nucl. Matl., 85 & 86 (1979) 757.

11. Metals Handbook, Vol. 2, Properties and Selection: Nonferrous Alloys and Pure Metals, American Society for Metals, Metals Park, Ohio (1979).

5.3 THE EFFECT OF HELIUM ON THE TENSILE PROPERTIES OF SEVERAL VANADIUM ALLOYS — D. N. Braski (Oak Ridge National Laboratory)

5.3.1 ADIP Tasks

ADIP Task I.B.15, Tensile Properties of Reactive and Refractory Alloys.

5.3.2 Objective

The immediate goal of this work is to develop suitable techniques for implanting helium in vanadium alloys; this will provide a better simulation of fusion conditions for specimens irradiated in the Materials Open Test Assembly of the Fast Flux Test Facility (FFTF/MOTA) experiment. The primary goal of this work is to develop vanadium alloys that are resistant to deleterious radiation effects such as helium embrittlement and swelling.

5.3.3 *Summary*

Specimens of three vanadium alloys were implanted with different levels of ^3He using the tritium trick and subsequently tensile tested at elevated temperatures. The V—15Cr—5Ti and V—3Ti—1Si specimens were embrittled by ^3He at a level of 150 at. ppm while the VANSTAR-1 specimens were not. The embrittlement appeared to be caused by extensive ^3He bubble networks and possibly precipitate particles on the grain boundaries; hopefully the bubble distribution can be changed (for better simulation) by altering parameters of the tritium trick. The results of the investigation also show that the embrittlement resistance of vanadium alloys can be improved by adjustment of their composition and/or microstructure.

5.3.4 Progress and Status

5.3.4.1 Introduction

For better simulation of first wall conditions, vanadium alloys have been implanted with 'He, using the tritium trick,' before neutron irradiation tests in FFTF (MOTA). However, after implanting approximately 300 at. ppm ^3He, the V—15Cr—5Ti specimens were already embrittled.' The present report shows the effects of preimplanted ^3He on selected tensile properties of other vanadium alloys under investigation as well as V—15Cr—5Ti, and relevant electron metallography that relate the properties with the associated microstructures. Directions for future alloy development are also pointed out.

5.3.4.2 Experimental

The procedure for implanting ^3He in vanadium alloys using the tritium trick has been described.' Three alloys were included in the experiment: V—15Cr—5Ti, VANSTAR-1, and V—3Ti—1Si. The source, heat number, composition, and final annealing treatment are listed for each alloy in Table 5.3.1. Elevated-temperature tensile tests of "SS-3" type specimens (gage section = 7.6-mm long by 1.5-mm wide by 0.76-mm thick) were conducted under vacuum ($<10^{-4}$ Pa), using a crosshead speed of 0.51 mm/min (0.02 in./min). Transmission electron microscope specimens were prepared by electropolishing in a solution consisting of 1 part H_2SO_4 to 7 parts methanol, by volume. The electrolyte temperature was —25°C and the current density was approximately 1 A/cm^2.

Table 5.3.1. Vanadium alloy data

Alloy	Heat	Composition (wt %)								Final heat treatment
		Cr	Ti	Fe	Zr	Si	C	O	N	
V—15Cr—5Ti[a]	CAM-834-3	14.5	6.2				0.032	0.031	0.046	1 h at 1200°C
VANSTAR-7;	CAM-837-7	*9.1*		3.4	1.3		0.064	0.028	0.052	1 h at 1350°C
V—3Ti—1Si	11153		3.4	0.04		1.28	0.045	0.091	0.026	1 h at 1050°C

[a]Source: Westinghouse Electric Corporation.

[b]Source: KFK, Karlsruhe, West Germany (Dr. D. Kaletta).

5.3.4.3 Results

A listing of the tensile properties for the three vanadium alloys with different amounts of ^3He is given in Table 5.3.2. Test temperatures ranged from room temperature to 600°C for the V—15Cr—5Ti, but only data for 600°C is shown for the other two alloys. Small amounts of implanted 'He were observed to raise the yield strength of an alloy, but concurrent increases in the ultimate strength did not always occur. Larger amounts of ^3He had less effect on the yield strength, but usually caused reductions in the ultimate strength

Table 5.3.2. Tensile properties of vanadium alloys containing different levels of ^3He

Alloy	Helium level[a] (at. ppm)	Test temperature (°C)	Strength (MPa)		Elongation (%)	
			Yield	Ultimate tensile	Uniform	Total
V–15Cr–5Ti	0	25	552	662	14.3	24.3
	0	25	600	714	14.6	25.0
	300	25		540		0
	300	25		352		0
	0	420	370	504	15.2	24.3
	14	420	379	520	13.8	22.8
	80	420	338	470	14.4	23.0
	300	420	366	394		1.0
	0	520	334	513	13.5	23.3
	14	520	419	536	12.8	20.2
	80	520	363	563	14.0	20.7
	300	520	329	443		2.3
	0	600	317	557	12.6	20.5
	14	600	328	517	13.5	21.1
	80	600	349	570	12.0	15.5
	300	600	336	407		1.3
	300	600	407	463		1.2
VANSTAR-7	0	600	277	521	14.5	22.3
	7	600	321	492	12.2	20.0
	42	600	261	494	13.2	20.8
	150	600	268	494	13.6	20.5
V–3Ti–1Si	0	600	320	504	15.5	23.6
	23	600	407	550	9.7	15.5
	135	600	383	555	9.2	14.7
	480	600	378	541		6.3

[a] ^3He analysis performed by Dr. Brian Oliver, Rockwell International, Canga Park, Calif.

and elongation. From the standpoint of helium embrittlement, ductility is the specific property that is most affected. The total elongation of the V–15Cr–5Ti specimens is shown as a function of test temperature in Fig. 5.3.1. With no implanted ^3He, the total elongation dropped only a few percent in the temperature range from 420 to 600°C. The addition of 14 at. ppm ^3He had little effect on the elongation within the normal scatter of tensile measurements. The same was true of specimens containing 80 at. ppm ^3He at 420 and 520°C, but a noticeable loss in elongation was observed at 600°C. The V–15Cr–5Ti specimens containing 300 at. ppm ^3He were severely embrittled at all three elevated temperatures and also at room temperature (see Table 5.3.2). Figure 5.3.2 shows total elongation at 600°C for specimens of all three alloys as a function of ^3He

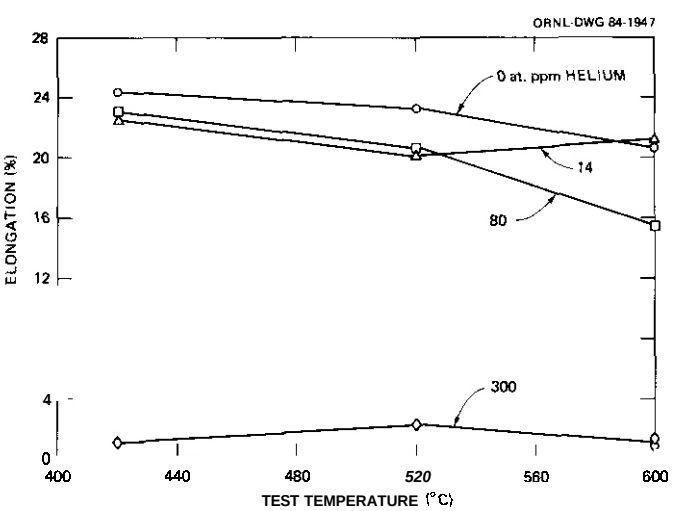

Fig. 5.3.1. Total elongation of V–15Cr–5Ti tensile specimens with different ^3He levels as a function of test temperature.

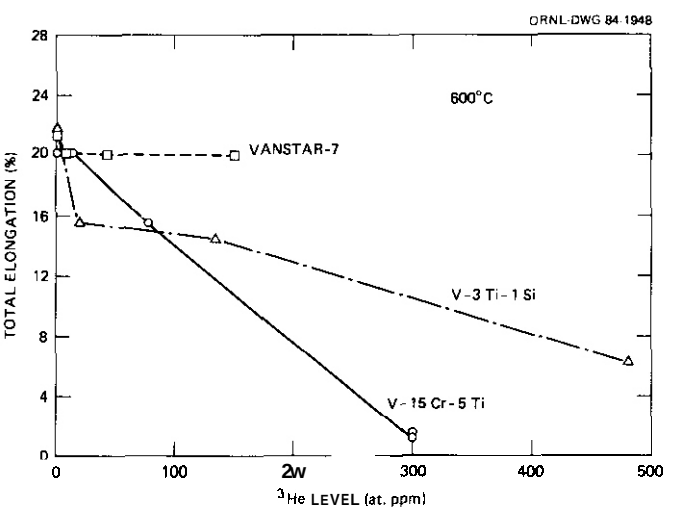

Fig. 5.3.2. Total elongation of different vanadium alloys tested at 600°C as a function of ^3He level.

level in the specimen. The elongation values of V–15Cr–5Ti dropped in a linear fashion to low values with ^{3}He levels of 300 at. ppm. The V–3Ti–1Si demonstrated better resistance to helium embrittlement with over 6% total elongation remaining at 480 at. ppm ^{3}He. The VANSTAR-7 alloy exhibited the best resistance to embrittlement with no ductility losses up to 150 at. ppm ^{3}He which was the maximum level tested. It will be interesting to see if the VANSTAR-7 is able to continue its excellent performance when implanted to the higher levels of ^{3}He, as is planned. These results show a wide variation in susceptibility of the vanadium alloys to helium embrittlement. This forms the basis for the development of embrittlement-resistant alloys through compositional changes.

A TEM examination of one of the V–15Cr–5Ti specimens with 300 at. ppm ^{3}He revealed the presence of an extensive network of helium bubbles as well as precipitate particles in the grain boundaries as shown in Fig. 5.3.3. The last step in the tritium trick process takes place at 700°C and is probably responsible for the precipitation and bubble growth. From the standpoint of simulation, it is hoped that using lower processing temperatures in the tritium trick closer to planned irradiation temperatures will produce more realistic bubble distributions. It will also be necessary to develop suitable alloy microstructures, especially at the grain boundaries.

With bubble distributions similar to those in Fig. 5.3.3, it was not too surprising to find that the fracture surfaces of the implanted V–15Cr–5Ti specimens tested at 600°C (300 at. ppm) were entirely intergranular as shown in Fig. 5.3.4(*d*). However, the fact that fracture at this ^{3}He level was intergranular at room temperature [Fig. 5.4.3(*b*)] indicates that the problem is more extensive than classical helium embrittlement. Classical helium embrittlement usually occurs only at elevated temperatures. A fracture surface of an unimplanted specimen tested at room temperature is also shown for comparison [Fig. 5.3.4(*a*)]. The dimpled appearance of the fracture surface is characteristic of a ductile failure mode. With intermediate ^{3}He contents the V–15Cr–5Ti specimen exhibited a fracture surface with both intergranular and ductile dimpled areas as shown in Fig. 5.3.4(*c*).

In conclusion. the tritium trick orocedure has been used to successfully implant ^{3}He in vanadium but the conditions were obviously too severe for some simulation purposes. Nevertheless, the results are very encouraging in that one alloy performed well even under these very adverse conditions. Even if the vanadium alloys are sensitive to helium, it appears that the door is open to the development of embrittlement-resistant alloys.

5.3.4.4 Reference

1. D. N. Braski and D. W. Ramey, "Helium Doping of a Vanadium Alloy by a Modified Tritium Trick," pp. 72–74 in *ADIP Semiannu. Prog. Rep. March 31, 1984*, DOE/ER-0045/12, U.S. DOE, Office of Fusion Energy.

ORNL PHOTO 3701-84

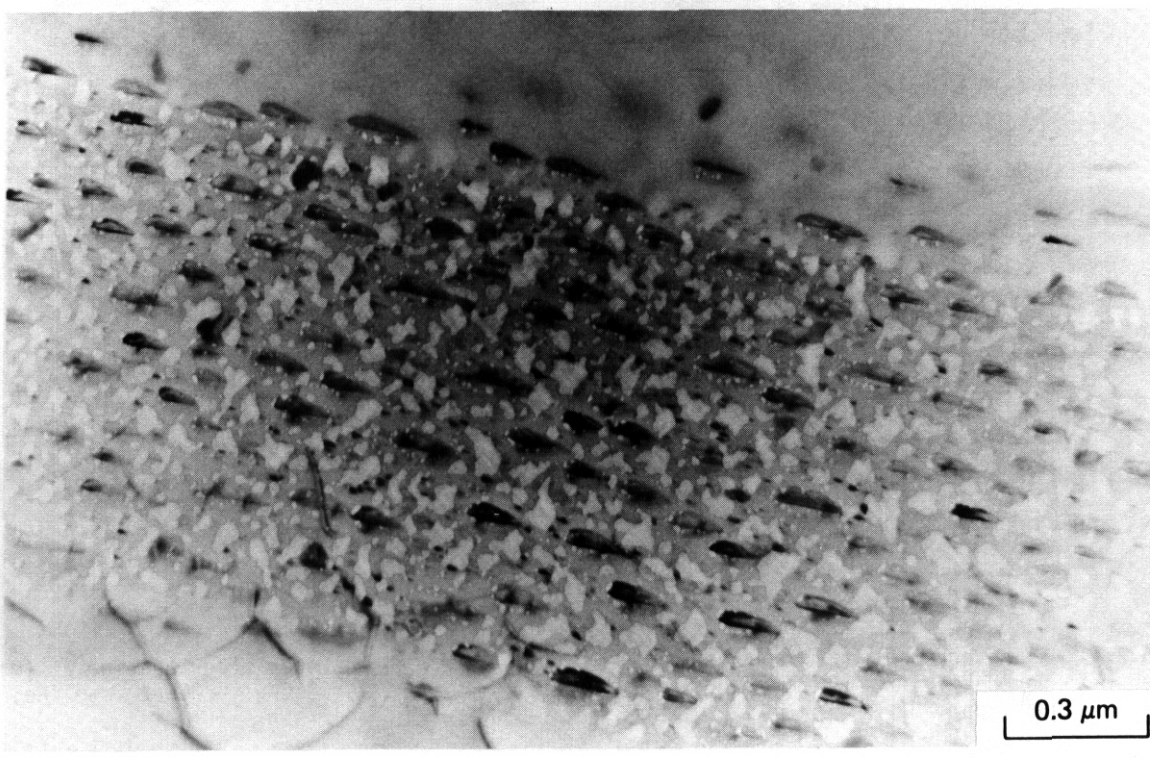

Fig. 5.3.3. Bubbles of ^{3}He in grain boundary of V–15Cr–5Ti after implantation of 300 at. ppm ^{3}He by the tritium trick.

ORNL PHOTO 7699-84

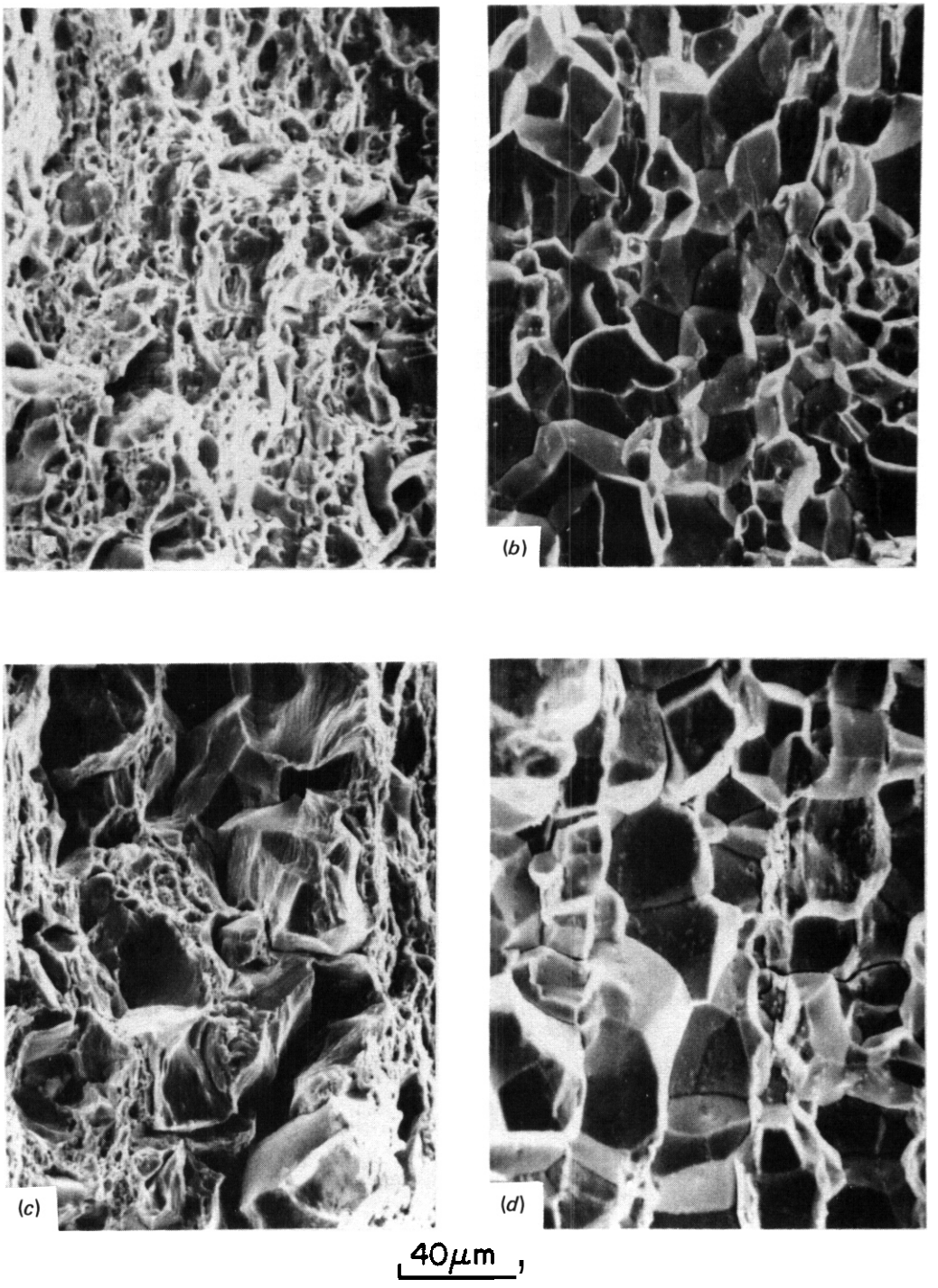

Fig. 5.3.4. Scanning electron micrographs of V–15Cr–5Ti fracture surfaces after testing at *(a)* room temperature with no ^3He, *(b)* room temperature with 300 at. ppm ^3He, *(c)* 600°C with 80 at. ppm ^3He, and *(d)* 600°C with 300 at. ppm ^3He.

5.4 TENSILE PROPERTIES OF HELIUM-INJECTED V-15Cr-5Ti AFTER IRRADIATION IN EBR-II — M. L. Grossbeck and J. A. Horak (Oak Ridge National Laboratory)

5.4.1 ADIP Tasks

AOIP Task I.B.15, Tensile Properties of Reactive/Refractory Alloys.

5.4.2 Objective

This experiment will investigate the effect of cyclotron-injected helium and neutron irradiation on the tensile properties of V—15Cr—5Ti.

5.4.3 *Summary*

Miniature specimens of V—15Cr—5Ti were prepared in the annealed condition and with 10, 20, and 30% cold work. The annealed specimens were cyclotron injected with helium and irradiated in sodium in EBR-II. The cold-worked specimens were irradiated in EBR-II but not helium injected. The specimens were irradiated at 400, 525, 625, and 700°C and received a fluence of 4.1 to 5.5 $\times 10^{26}$ neutrons/m^2 ($E > 0.1$ MeV). Tensile testing revealed very significant embrittlement as a result of the neutron irradiation but a much smaller change, mostly at 400°C, resulting from helium injection.

5.4.4 Progress and Status

5.4.4.1 Introduction

Exposed to a fusion reactor neutron spectrum, vanadium alloys such as V—15Cr—5Ti are expected to form about 5 at. ppm He per dpa,' about half of the amount found in stainless steel but nonetheless a very significant amount for expected fusion reactor first wall lifetimes. Unlike stainless steels which form transmutation helium from thermal neutron absorption in ^{58}Ni and ^{59}Ni, neither vanadium, chromium, nor titanium undergo (n,α) reactions in fission reactor spectra. Therefore, unlike stainless steels which may be irradiated in mixed spectrum reactors, such as the HFIR, to achieve simultaneous displacement damage and helium formation, vanadium alloys cannot be irradiated in fission reactors to form a significant amount of helium. Other techniques must be resorted to such as tritium trick doping[2] or ion implantation. It is the latter technique that was used in this investigation. In this investigation specimens were helium implanted with 52 MeV a-particles and then neutron irradiated in the EBR-II.

5.4.4.2 Experimental Procedure

The chemical composition of V-15Cr-5Ti is given in Table 5.4.1. Sheets 0.25-mm thick were given a recrystallization anneal at 900°C for 0.5 h in a vacuum environment of 0.5 to 2 $\times 10^{-7}$ torr (<2.7 $\times 10^{-5}$?a) pressure. The average grain diameter was about 30 μm after this heat treatment. The 0.25-mm-thick V—15Cr—5Ti sheet formed the front face of the irradiation chamber through which 18 to 20°C water flowed at a rate of 9.5 $\times 10^{-4}$ m^3/s. Helium was injected into these sheets using a 52 MeV a-particle beam from the Oak Ridge Isochronous Cyclotron (ORIC). A rotating energy degrader was used to produce a uniform helium deposition over the entire thickness of the sheet. The a-particle beam was collimated to provide essentially uniform helium deposition over the gage length of the samples. The chamber was oscillated horizontally in front of the beam to irradiate the sheet. A measured average helium concentration of 80 at. ppm was achieved. Tensile specimens were subsequently stamped from this sheet with a precision die. Final dimensions were 31.8 mm long, 12.7 mm gage length, 1.02 mm wide, and 0.25 mm thick (Fig. 5.4.1). Cold-worked material was prepared to allow optimization of the microstructure of the alloy and to permit a valid

Table 5.4.1. Chemical composition of V—15Cr—5Ti

Element	(wt %)	Element	(wt %)
Cr	15.00	Ni	0.002
cu	0.02	P	0.0002
Fe	0.08	S	0.001
Mn	0.001	Ti	4.8
Mo	0.02	Zr	0.01
Nb	0.02	V	ba1

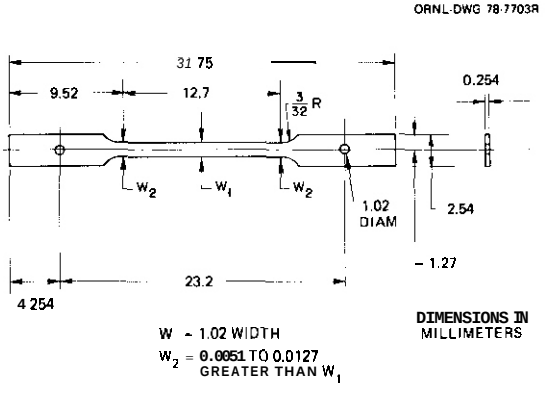

Fig. 5.4.1. Miniature sheet tensile specimen.

comparison with other alloys for which data are available for the cold-worked state. The cold-worked material was prepared by annealing sheets at 900°C in thicknesses that resulted in 10, 20, and 30% reduction in area upon one pass of a rolling operation following the anneal to provide 0.25-mm-thick sheet for specimen stamping.

The specimens were neutron irradiated in a sodium environment with zirconium foil introduced as a getter material in row 7 of the EBR-II. The specimens received a neutron fluence of 4.1 to 5.5 × 10^{26} neutrons/m^2 ($E > 0.1$ MeV) producing 24 to 32 dpa. Irradiation temperatures were controlled by direct thermal contact with reactor coolant (400°C), helium gas gaps (525°C), and heat pipes (625 and 700°C).

Tensile tests were conducted on an Instron Universal testing machine equipped with a high vacuum furnace. Pressures below 9 × 10^{-5} Pa (7 × 10^{-7} torr) were maintained during the test, and the time at elevated temperatures was minimized in order to prevent significant oxygen contamination. A strain rate of 6.7 × 10^{-4} s^{-1} was used for the tests, and all specimens were tested at the irradiation temperatures.

5.4.3.3 Results

Only for annealed material are results available for all four conditions: unirradiated, helium injected, neutron irradiated, and helium injected plus neutron irradiated. The 10, 20, and 30% cold-worked material was not implanted with helium. The results of the tensile tests on all specimens appear in Table 5.4.2.

Table 5.4.2. Tensile data for V–15Cr–5Ti

Specimen	Condition	Test temperature (°C)	Strength (MPa)		Elongation (%)	
			Yield	Ultimate tensile	Uniform	Total
			Controls			
100C	Annealed	400	491	610	7.4	8.9
101C	Annealed	625	417	621	8.9	10.3
103C	Annealed	625	405	621	9.3	11.1
102C	Annealed	700	403	574	9.2	15.2
3c	10% CW	400	672	769	1.1	2.6
15c	10% CW	525	655	774	0.86	1.9
14c	10% CW	700	517	683	2.4	6.9
4c	20% CW	400	724	827	1.1	2.1
13C	20% CW	525	603	796	1.0	1.8
2C	20% CW	700	543	707	2.1	5.6
14C	20% CW	700	517	698	2.3	5.3
2C	30% CW	400	724	827	1.1	2.7
8C	30% CW	525	603	814	1.1	2.3
6C	30% CW	700	483	698	2.3	6.1
			Helium implanted			
3-64	Annealed	400	503	574	4.4	5.9
1-8	Annealed	400	512	590	2.1	3.5
3-57	Annealed	700	336	531	10.0	12.3
1-58	Annealed	700	365	548	12.1	15.3
			Neutron irradiated			
7	Annealed	625	776	853	0.38	0.50
8	Annealed	700	738	943	0.94	0.94
9	10% CW	400	1140	1260	1.1	1.2
6	10% CW	525	819	972	4.2	4.9
16	10% CW	700	608	883	1.9	6.6
11	20% CW	400	1130	1220	1.3	1.4
12	20% CW	400	1100	1200	0.94	1.0
7	20% CW	525	710	853	1.0	1.0
19	20% CW	700	612	1000	1.8	1.8
15	30% CW	400	1130	1210	0.92	1.2
11	30% CW	525	664	910	3.3	3.6
17	30% CW	700	434	533	2.3	4.4
			Helium implanted plus neutron irradiated			
1-80	Annealed	400	991	1170	0.76	0.76
1-72	healed	700	741	822	2.0	3.0

The strength and ductility values for annealed V-15Cr-5Ti appear in Figs. 5.4.2 and 5.4.3. It is observed from Fig. 5.4.2 that injection of 80 at. ppm He alone has little effect on the strength of the material. However, neutron irradiation and, as expected, neutron irradiation plus helium injection increase the yield and ultimate strengths by about a factor of 2. Helium injection reduced tensile elongation of V-15Cr-5Ti at 400°C but not at 700°C. Neutron irradiation, however, reduced elongation to below 1%. Following helium injection plus neutron irradiation ductilities were below *1%* at 400°C and above 2% at 700°C.

The tensile test results for cold-worked V-15Cr-5Ti are plotted in Figs. 5.4.4 through 5.4.9. Slight strengthening is observed in the unirradiated cold-worked material, an effect which appears to saturate at

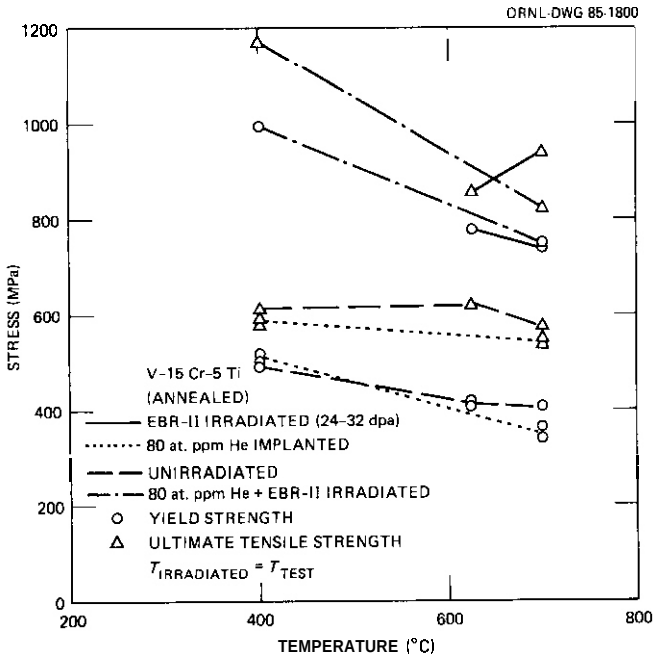

Fig. 5.4.2. Stress as a function of test temperature for annealed V-15Cr-5Ti.

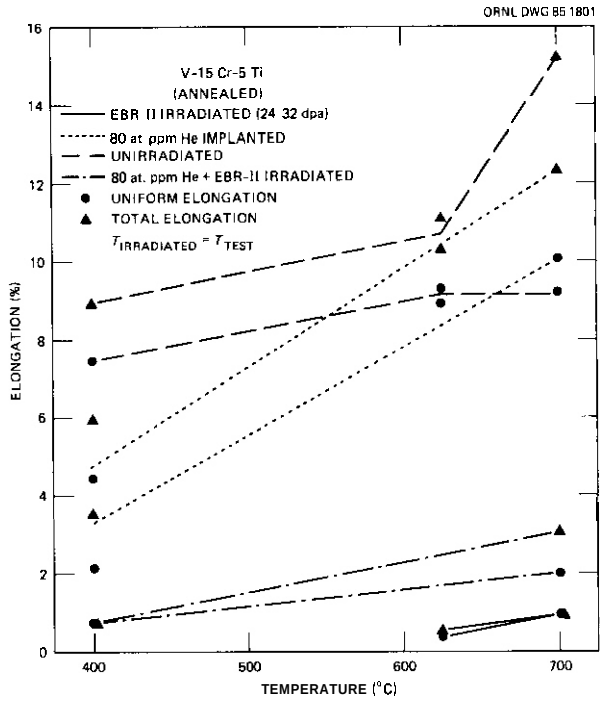

Fig. 5.4.3. Tensile elongation as a function of test temperature for annealed V-15Cr-5Ti.

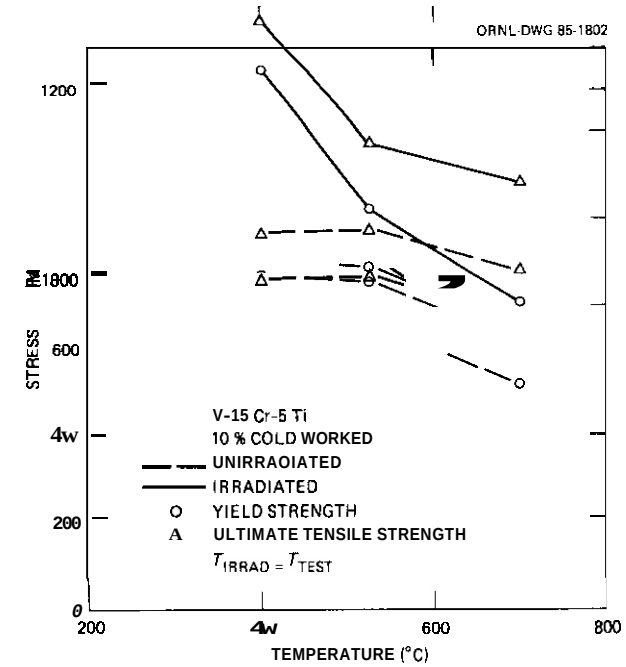

Fig. 5.4.4. Stress as a function of test temperature for 10% cold-worked V-15Cr-5Ti.

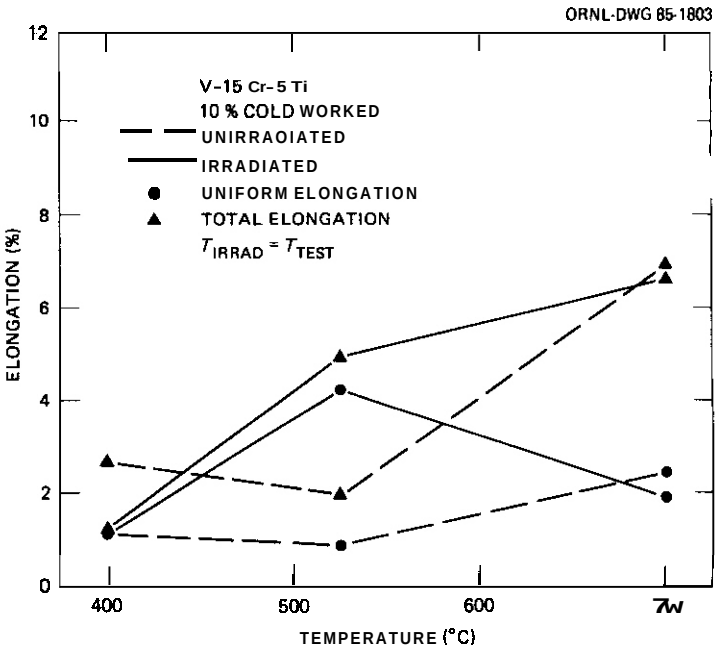

Fig. 5.4.5. Tensile elongation as a function of test temperature for 10%-cold-worked V-15Cr-5Ti.

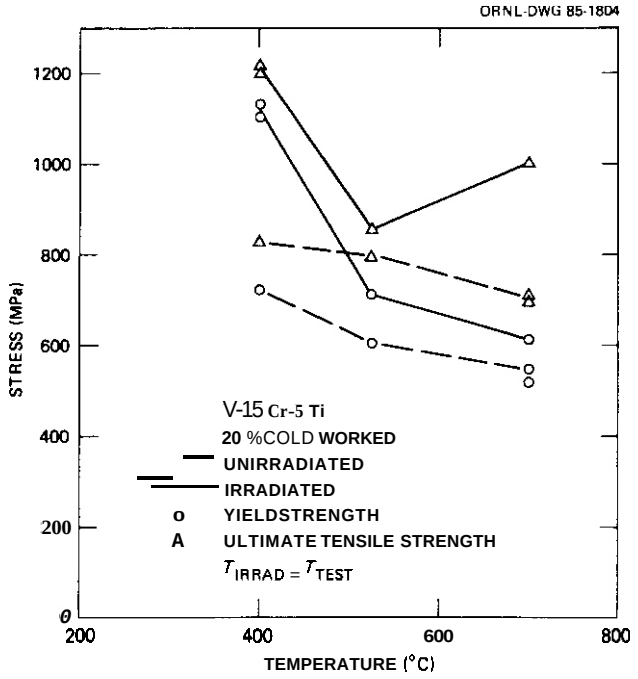

Fig. 5.4.6. Stress as a function of test temperature for 20%-cold-worked V-15Cr-5Ti.

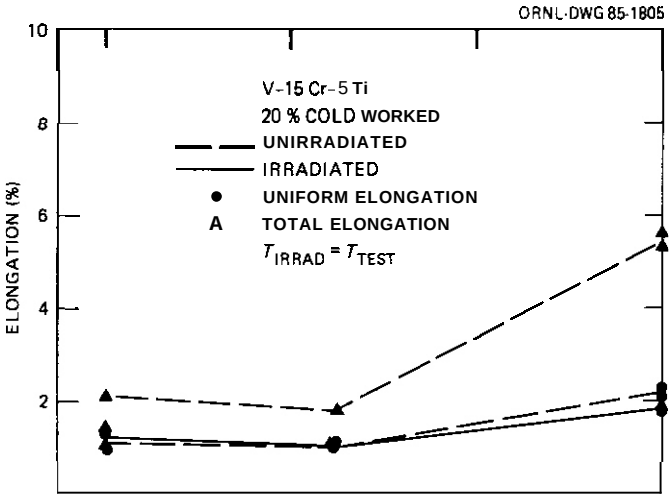

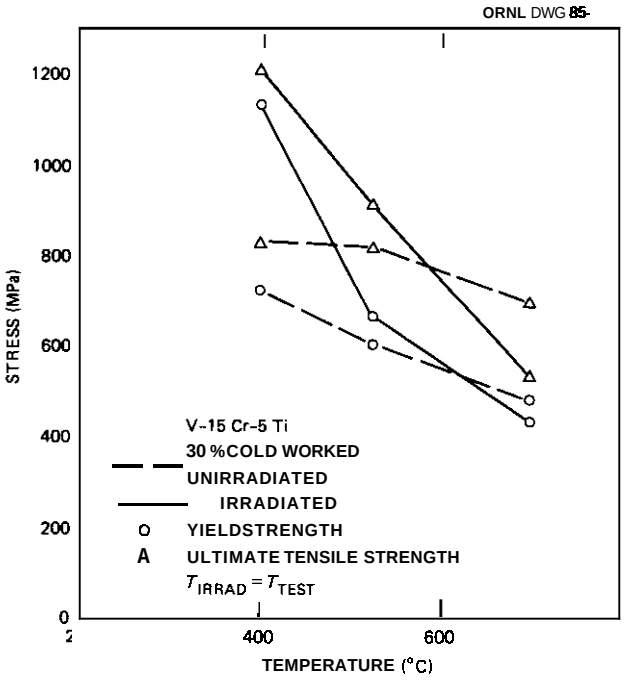

Fig. 5.4.8. Stress as a function of test temperature for 30%-cold-worked V-15Cr-5Ti.

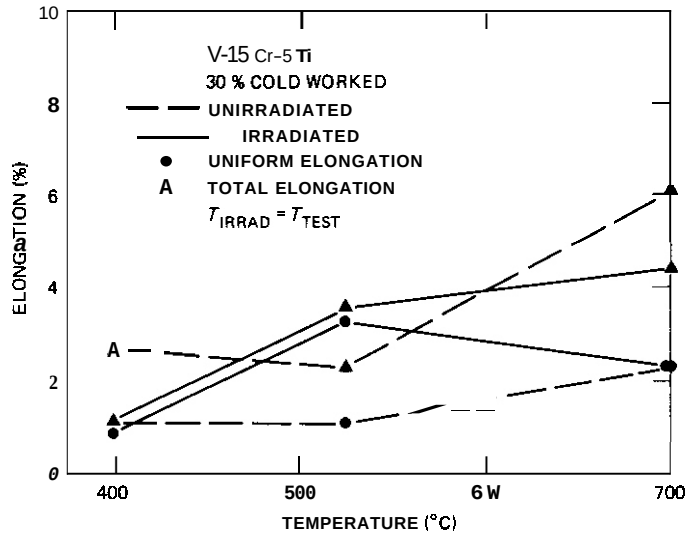

Fig. 5.4.9. Tensile elongation as a function of test temperature for 30%-cold-worked V-15Cr-5Ti.

about 20% cold work. Neutron irradiation strengthens the cold-worked material to about the same level as the annealed material. The strengthening decreases rapidly with temperature with yield strength returning to nearly the unirradiated value at 700°C for 10 and 20% cold-worked material. For 30% cold-worked material, recovery appears to have been sufficient at 700°C for yield and ultimate strengths to return to essentially the unirradiated values. The tensile elongations for cold-worked material are about 25% of those for annealed material in the unirradiated condition with evidence of recovery of cold work at 700°C.

Irradiation results in little change in the uniform elongation at 400°C, but the total elongation is significantly lower indicating a reduced ability to work harden. For 10 and 30% cold-worked material, ductility is higher than the unirradiated material at 525°C and about as ductile as the unirradiated material at 700°C.

5.4.4.4 Discussion

It is of importance that the implanted helium had no significant effect on strength and ductility at 700°C and below. Similar behavior was not observed by Tanaka et al. in V-20Ti irradiated in the same capsules in EBR-II.[3] They observed a reduction in ductility attributable to helium at 625°C and above. However, our results are consistent with those of Santhanan et al. who observed no reduction in ductility at temperatures below 700°C in V-15Cr-5Ti with 25 at. ppm He implanted.[4] Transmission electron microscopy remains to be done on the specimens from the present investigation, but it is proposed that helium is more strongly bound to traps in V-15Cr-5Ti than in V-20Ti, thus preventing migration to grain boundaries below 700°C.

Neutron irradiation alone was observed to have a major embrittling effect in annealed V-15Cr-5Ti. A likely explanation for refractory metal alloys is contamination by interstitials from exposure to the environment of sodium in contact with other materials during irradiation. However, the fact that the strength is essentially the same for annealed irradiated and unirradiated material is strong evidence that the zirconium foil getter was adequate to prevent specimen contamination. The cold-worked material provides further evidence for this since the strengthening from cold work appears to at least partially recover at 700°C for 10 and 20% cold-worked material and perhaps fully recover for the 30% cold-worked material.

Cold work results in stronger but less ductile material, especially at 400°C. However, for all three levels of cold work, recovery of the original strength levels is observed at 700°C. Ductility for unirradiated material is never fully restored to the annealed value, probably because of the short test period. The elongations of the irradiated specimens are usually lower than for the corresponding unirradiated material since ductility is a sensitive measure of irradiation ernbrittlement. An exception occurs at 525°C possibly because of an increased irradiation temperature. However, a thermal expansion detector indicated a maximum temperature of only 550°C. Also characteristic of irradiated bcc metals, the necking strain is very low making the uniform and total elongations nearly equal in most cases. This is often the result of channel fracture in such materials.[5] Further investigation of this possibility has been initiated.

Since cold work has a small effect on mechanical properties, it is important to determine its effect on swelling resistance. If cold work results in swelling resistance as is observed in stainless steels, it might be a satisfactory aid to swelling resistance in vanadium alloys since it does not have a detrimental effect on mechanical properties.

5.4.4.5 Conclusions

1. Cyclotron injection of 80 at. ppm He has little effect on mechanical properties of V-15Cr-5Ti at 700°C and 625°C and causes a factor of about 2 reduction in elongation at 400°C.
2. Neutron irradiation to 24 to 32 dpa increases the strenqth of annealed material by a factor of about 2 and decreases ductility by a factor of about 10.
3. Althouqh cold work strengthens slightly and reduces ductility by a factor of about 4, the level of cold work has little effect between 10 and 30%.

5.4.4.6 References

1. T. A Gabriel, B. L. Bishop, and F. W Wiffen, ***Calculated Irradiation Response of Materials*** *Using* ***a Fusion-Reactor First-Wall Neutron Spectrum,*** p. 5, ORNL/TM-5956, June 1977, Oak Ridge National Laboratory.
2. J. F. Remark, A B. Johnson, Jr., Harry Farrar IV, and D. G. Atteridge, "Helium Charging of Metals by Tritium Decay," ***Nucl. Technot.*** 29, 369 (1976).
3. M P. Tanaka, E E. Bloom, and J. A. Horak, "Tensile Properties and Microstructure of Helium Injected and Reactor Irradiated V-20Ti," ***J. Nucl. Mater.*** 103&104, 895 (1981).
4. A. T. Santhanan, A Taylor, and S D. Harkness, "Charged-Particle Simulation Studies of Vanadium and Vanadium Alloys," in *Proc.* ***of International Conference a Defects and Defect Clusters in B.C.C. Metals and Their Alloys, August 14-16, 1973,*** National Bureau of Standards, Washington, D.C., pp. 302–320.
5. F. W. Wiffen, "Effects of Irradiation on Properties of Refractory Alloys with Emphasis on Space Power Reactor Applications," in *Proc.* ***of Symposium a Refractory*** *Alloy* ***Technology for Space Nuclear Power Applications, Oak Ridge, TN, August*** *10–11,* ***1983,*** pp. 252-77.

ins

7.1 CHARPY IMPACT TEST RESULTS OF FERRITIC ALLOYS AT A FLUENCE OF 6 x 10^{22} N/CM^2 - W.L. Hu (Westinghouse Hanford Company)

7.1.1 AUIP Task

The Office of Fusion Energy/Department of Energy, has established the need to determine the fracture toughness of candidate fusion program ferritic alloys (path E).

7.1.2 Objective

The objective of this work is to evaluate the shift of the ductile to brittle transition temperature (DBTT) and the reduction of the upper shelf fracture energy (USE) due to the neutron irradiation on the candidate ferrtic alloys.

7.1.3 *Summary*

Charpy impact tests on specimens in the AD-2 reconstitution experiment were completed. One hundred and ten specimens made of HT-9 base metal, 9Cr-1Mo base metal and 9Cr-1Mo weldment at various heat treatment. conditions were tested in temperature range from -73°C to 260°C. The specimens were irradiated from 390°C to 550°C and the fluence of the specimens reached 6 x 10^{22}n/cm^2. This is the first time that the transition behavior of ferritic alloys at high fluence was obtained. This is also the first time that comprehensive results on the irradiated 9Cr-1Mo weldment are available.

The test results show a small additional shift in transition temperature for HT-9 base metal irradiated at 390°C and 450°C as the fluence was raised to 6 x 10^{22}nicm2. At higher irradiation temperatures, however, the shift in transition temperature is less conclusive. Further reduction in USE was observed at higher fluence for all the irradiation temperatures. There is no apparent fluence effect for 9Cr-1Mo base metal at all the irradiation temperatures studied.

Contrary to the previous finding on HT-9 base metal and weldrnent, the 9Cr-1Mo weldment shows a higher transition temperature (+60°C) and a higher USE (+100%) as compared to the 9Cr-1Mo hare metal for the same irradiation conditions.

Significant improvement of both DBTT and USE on Hl-9 base metal specimens fabricated from normalized and tempered plate stock was observed over the Hi-9 base metal specimens fabricated from mill-annealed bar stock.

Overal1, the highest DBTT encounted for HT-9 alloys is 141 °C for specimens irradiated at 390°C. The effect on transition temperature due to additional neutron exposure appears to be saturated at 6 x 10^{22}n/cm^2. The highest DBTT encounted for 9Cr-1Mo alloys, on the other hand, is 91°C for the weldment and 45°C far base metal both irradiated at 390°C.

7.1.4 Progress and Status

7.1.4.1 Introduction

It is well known that the temperature at which ferritic alloys undergo a transition in fracture mode from ductile to brittle shifts toward higher temperatures with increasing neutron exposure. Accordingly, the change in the DBTT with fluence as well as irradiation temperature is an important factor in the selection of alloys for fusion reactor applications.

This document reports the Charpy inmpact test results of specimens discharged from the AD-2 reconstitution experiment. Test results were compared with the transition behavior obtained from the specimens discharged in the first AD-2 experiment.

7.1.4.2 Specimen Preparation

Miniature Charpy impact specimens were prepared for the study of the effect of irradiation on the transition of fracture mode in ferritic alloys. The specimen has an overall dimension of 5mm x 5mm x 23.6mm and has a notch depth of 0.76mm. Specimens were precracked to an a/W approximately equal to 0.5 where a is the notch depth plus the precrack length and the W=5mm is the specimen heiqht.

Mdterial stocks involved in the AD-2 reconsitution experiment for Charpy impact test include:

1. HT-9 base matal in mill annealed condition (TT series). The bar stock was hot worked after soaking at 1149°C for a minimum of one hour, then tempered at 750°C for one hour and air cooled.

2. HT-9 base metal in plate stock (KT series), with heat treatment of 1038°C/10 min/AC + 760°C/30 min/AC.

3. 9Cr-1Mo base metal from heat 30182 (TV series). The heat treatment was 1038°C/1 hr/AC + 760°C/1 hr/AC.

4. 9Cr-1Mo base metal from heat 30176 (AF series]. The heat treatment is essentially identical to the TV series, i.e., 1038°C/30 min/AC + 760°C/30 min/AC.

5. 9Cr-1Mo weldment (NL series), with post weld treatment of one hour at 780°C followed by air cool.

Specimens of KT, AF, and TV series were fabricated from plate stock with the crack plane oriented in the T-L direction. Specimens of TT series were fabricated from bar stock and having a crack plane orientation of C-R. In the case of 9Cr-1Mo weldment (NL series), the orientation was assumed to be irrelevant.

Specimens of both TT and TV series were irradiated from the beginning of the AD-2 experiment and received a peak fluence of approximately 6 x 1022nlcm.2 (-26 dpa). The rest of the specimens, KT, AF and NL series, were inserted as part of the AD-2 reconstitution test matrix and hence only experienced a peak fluence of 3 x 10^{22}n/cm^2 1-13 dpa). The irradiaton temperatures ranae from 390°C to 5500C. Details of the alloy compositions, specimen' preparation, heat treatments, test matrix and capsule loading have been previous1y reported.[1,2]

Charpy impact test results for TT and TV series at fluence level of 3 x 10^{22}n/cm^2 (-13 dpa) were documented previously.[3,4] These test results were incorporated in this report for comparision.

7.1.4.3 Experimental Procedures

The tests were conducted on a drop tower installed in the hot cell. The heating andlor cooling, transport and test were automated to handle the irradiated specimen. Load traces were digitized and stored in both magnetic tape and disk. A computer program was developed to integrate the load data and calculate the fracture energy. The detail of the test system were described in reference 4.

Prior to the test, the specimen temperature, as indicated by the spring loaded contact thermocouple, was calibrated versus a thermocouple spot welded on a dummy specimen. During the test period, the load cell and the impact velocity were checked daily. The load cell calibration was conducted dynamically by comparing the maximum load obtained during an impact test of a calibrated 112 size CVN specimen with the predetermined maximum load from a three point bending test. The calibration specimens were made of loading rate insensitive 6061 Aluminum allov in the T651 heat treated condition. The imoact velocitv was calculated from the time interval obtained when a flag with a known gap width on the crosshead passe; through an stationary infrared sensor during a free fall.

The total energy absorbed in the impact test can be calculated from the area under the load time record and the initial impact velocity following Newton's second law.

$$E = E_a (1-E_a/4E_0)$$

where $E_a = V_0 \int Pdt$ is the apparent energy absorbed by the specimen during the impact, V_0 is the initial impact velocity, P is the load and t is the time. $E_0 = mV_0^2$ 12 is the total available energy at the impact where m is the mass of the crosshead.

7.1.4.4 Results and Discussion

The Charpy impact energies for each material were plotted as a function of temperature in Fig. 7.1.1 to 7.1.5. The energy was normalized by multipling a factor of $L/B(W-a)^2$ where B = 5 mm is the specimen width, W = 5 mm is the specimen height, a is the notch depth plus the precrack length, and L = 4W is the span. Although in a preliminary stage, it is speculated that such normalization could extend the data base to cover other specimen sizes. Test results were tabulated in Tables 7.1.1 - 7.1.5. The tables also included the maximum load during the impact and the energy absorbed by the specimens up to the maximum load. This information is related to the failure initiation and requires more detailed examination. It is documented here for the relevant interest.

A Gausian integral curve was fitted through each searies of test results. The curve fitting technique was described in detail in a previous report.[4] The DBTT, which is defined as the deflection point on the curve, was tabulated in Table 7.1.6 together with the shift in the DBTT as compared with the test results of unirradiated control specimens. Due to the limited specimens available for each irradiation conditions, the USEs are not well defined. Nevertheless, the reduction of the USE can still be detected in most cases. The estimated USEs in each case are listed in Table 7.1.6 as well. USEs, DBTTs, and shift in DBTTs for other relevant ferritic alloys tested in the past[4] are tabulated in Table 7.1.7 for comparison.

Table 7.1.1 Test results on HT-9 base metal irradiated to 26 dpa (TT Series)

Irradiation Temperature (°C)	Test Temperature (°C)	Maximum Load (Newton)	Energy to Max. Load (Joule)	Fracture Energy (Joule)	Normalized Energy (Joule/cm^2)
390	260	1.4262	0.2516	2.7980	85.053
	188	1.4545	0.2640	2.6361	80.440
	132	1.4827	0.1739	1.0244	31.783
	88	1.5275	0.1517	0.7173	21.270
450	260	0.9777	0.1813	2.7314	88.725
	160	1.0824	0.2030	2.7351	83.380
	93	1.1858	0.2213	2.3468	70.217
	29	1.1182	0.1186	0.7218	22.742
500	177	1.1837	0.2112	2.9166	87.265
	93	1.1196	0.2442	2.4859	76.078
	29	1.3863	0.1747	1.3391	41.102
	-18	1.5020	0.1392	0.2848	8.723
550	149	0.9880	0.4592	2.5686	81.173
	93	1.1768	0.2225	2.7174	84.606
	29	1.1858	0.1277	1.1147	33.982
	-23	1.3401	0.0894	0.6221	7.573

Table 7.1.2 Test results on HT-9 base metal irradiated to 13 dpa (KT Series)

Irradiation Temperature (°C)	Test Temperature (°C)	Maximum Load (Newton)	Energy to Max. Load (Joule)	Fracture Energy (Joule)	Normalized Energy (Joule/cm^2)
390	143	2.6168	0.4131	4.3046	117.972
	116	2.5307	0.4007	4.3036	116.876
	104	2.4411	0.2507	1.8431	50.273
	93	2.6196	0.4159	1.4512	39.744
	77	2.3908	0.2447	0.7720	21.148
	54	2.0332	0.1649	0.3480	9.382
	29	1.7721	0.1084	0.3297	8.965
450	77	2.1228	1.7834	5.8877	158.124
	54	2.1697	1.0535	5.1522	154.551
	29	2.2372	1.2237	5.5202	147.939
	10	2.2420	1.0806	5.9092	160.137
	4	2.1648	1.0436	4.3066	116.008
	-18	2.4818	0.4086	2.6062	69.996
	-46	2.2096	0.1929	0.3735	10.331
550	104	2.1049	0.3605	6.1669	167.771
	54	2.1015	0.9609	4.8832	131.590
	29	2.1786	1.0538	4.7679	128.711
	10	2.1517	0.9872	3.3006	89.792
	-7	2.1173	0.2545	1.9166	52.390
	-29	1.8658	0.1608	0.6274	16.885
	-57	1.3539	0.1031	0.2357	6.408

Table 7.1.3 Test results on 9Cr-1Mo base metal irradiated to 26 dpa (TV Series)

Irradiation Temperature (°C)	Test Temperature (°C)	Maximum Load (Newton)	Energy to Max. Load (Joule)	Fracture Energy (Joule]	Normalized Energy (Joule/cm^2)
390	49	1.7535	0.2060	5.3551	163.888
	29	1.8010	0.2462	2.7852	85.405
	-18	1.1265	0.1552	0.6597	20.258
500	29	1.3752	1.3306	7.4042	230.979
	-7	1.6267	0.2745	6.1353	184.625
	-34	1.1375	0.1149	1.9695	61.777
	-57	1.0624	0.0744	1.1352	34.260

Table 7.1.4 Test results on 9Cr-1Mo base metal irradiated to 13 dpa (AF Series)

Irradiation Temperature (°C)	Test Temperature (°C)	Maximum Load (Newton]	Energy to Max. Load (Joule)	Fracture Energy (Joule)	Normalized Energy (Joule/cm^2)
390	77	2.1622	0.2867	6.3771	175.615
	66	2.1231	0.3079	6.6816	183.359
	49	2.3469	0.3928	2.9583	79.758
	38	2.2633	0.2836	2.6233	70.334
	29	2.1642	0.2660	1.8006	48.549
	10	2.1001	0.1799	0.3769	10.226
	-18	1.4703	0.1090	0.6906	18.658
450	88	1.9285	1.5212	7.8665	214.750
	71	1.9720	1.5797	8.1090	218.529
	49	1.8985	1.4603	7.6781	209.698
	29	1.8864	1.5360	6.2338	170.253
	10	2.0691	1.6962	6.1101	165.440
	-18	2.1531	0.3804	2.2212	59.961
	-46	1.6894	0.1113	1.4608	39.637
	-73	1.0619	0.0567	0.1845	4.983
500	54	2.0415	1.9005	8.5074	230.847
	29	1.9120	1.5720	7.0931	194.481
	4	2.0388	0.2474	4.6196	127.105
	-18	2.1400	0.2860	2.4084	65.606
	-62	1.6564	0.1036	0.2487	6.816
550	66	1.9643	1.5410	7.7772	209.498
	49	1.8210	1.4259	7.1011	194.109
	29	1.9747	1.5225	R.2997	221.768
	16	2.0298	1.5962	7.3705	197.781
	-1	2.1697	1.7129	6.2799	169.672
	-18	2.0043	0.3103	3.3333	91.753
	-40	2.0153	0.1856	1.0483	28.348

Table 7.1.5 Test results on 9Cr-1Mo weldment irradiated to 13 dpa (NL Series)

Irradiation Temperature (°C)	Test Temperature (°C)	Maximum Load (Newton)	Energy to Max. Load (Joule)	Fracture Energy (Joule)	Normalized Energy (Joule/cm^2)
390	104	2.3076	0.3922	13.4756	358.547
	82	7.4703	0.3070	4.0681	107.512
	60	2.5413	0.3370	2.6314	69.515
	43	7.0175	0.1871	2.0421	54.658
	29	2.2410	0.1822	1.0472	28.440
450	99	2.1669	3.1093	14.1705	379.443
	71	2.2225	3.2512	17.8790	340.943
	54	2.1703	7.9617	13.5778	357.339
	43	7.1544	1.6721	8.5986	733.623
	29	2.5067	0.3084	2.1041	55.122
	10	2.2785	0.3719	1.8921	51.054
	-18	1.6736	0.1090	1.3883	38.281
500	88	2.1591	3.1046	14.4736	384.617
	66	2.0570	2.8745	14.4847	389.333
	43	7.1939	3.1473	11.9625	374.180
	29	2.6376	1.6203	3.7674	99.400
	-1	1.5854	0.1493	2.6386	71.629
	-18	1.3436	0.1052	1.1106	29.414
	-34	1.3401	0.0859	0.7818	7.476
550	99	1.8899	1.5779	10.9099	290.651
	77	2.1949	3.1631	12.5143	323.934
	43	7.7790	3.2988	13.6713	359.648
	35	2.0747	7.9711	11.7788	316.883
	10	1.9891	0.7924	8.8880	241.382
	-1	1.6219	0.1802	4.0465	107.893
	-18	1.6756	0.1196	1.2410	32.771

The shift in DBTT due to neutron exposure for both HT-9 and 9Cr-1Mo base metal was plotted in Fig. 6 as a function of irradiation temperature and fluence. The additional shifts in DBTTs from 3 x 10^{22}n/cm^2 to 6 x 10^{22}n/cm^2 for HT-9 are 20, 37, 10 and -6°C for specimens irradiated at 390, 450, 500, and 550°C, respectively. The reduction of USEs at 6 x 10^{21}n/cm^2 is 53% for all the irradiation temperatures. The small increases in DBTT suggest that the fluence effect is approaching saturation. The 9Cr-1Mo base metal, on the other hand, does not show any additional change in both DBTTs and USEs as the result of extra neutron exposure.

Test results on 9Cr-1Mo weldment, as shown in Fig. 5, exhibit a high USE in the range of 400 Joules/cm^2. The USE for preirradiated 9Cr-1Mo base metal is only 370 Joules/cm^2. This is attributed to the high energy associated with the failure propagation. A typical load and the fracture energy for a weldment specimen tested at an upper shelf temperature is shown in Fig. 7. It is clear that a sizable amount of energy is required to carry on the fracture process beyond the failure initiation. The transition temperature of 9Cr-1Mo weldment is approximately 60°C higher than the base metal under the same irradiation conditions. This is in conflict with the transition behavior of HT-9 alloy studied earlier where the DBTTs of weldment as well as HAZ are lower than the base metal.[4] The DBTT of 9Cr-1Mo weldm t irradiated in HFIR at 55°C was also found to be 25°C higher than the similarly irradiated base metal? The 9Cr-1Mo weldment also shows a less well defined upper and lower shelf. In particular, specimens irradiated at 550°C show a decreasing USE when temperature increases. On the other hand, the lower shelf energies increase with the temperature for all the weldment specimens tested.

Table 7.1.6 Use, DBTT and shift in DBTT of ferritic alloys in the AD-2 reconstitution experiment

Material	Fluence X 10^{22} (n/cm^2)	Irradiation Temperature (^oC)	USE (Joule/cm^2)	DBTT (^oC)	Reduction in USE (%)	DBTT (^oC)
HT-9	6	390	89	149	53	144
Base Metal	6	450	89	63	53	59
TT Series	6	500	89	48	53	43
	6	550	89	46	53	41
HT-9	3	390	120	94	36	89
Base Metal	3	450	165	-8	12	-13
KT Series	3	550	165	14	12	9
9Cr-1Mo	6	390	200	27	37	52
TV Series	6	500	240	-22	25	3
9Cr-1Mo	3	390	200	45	37	70
Base Metal	3	450	220	-1	31	24
AF Series	3	500	230	0	28	25
	3	550	220	-11	31	14
9Cr-1Mo	3	390	360	91	--	--
Weldment	3	450	360	39	--	--
NL Series	3	500	390	29	--	--
	3	550	350	13	--	--

Table 7.1.7 Previous impact test results on ferritic alloys (Reference 4)

Material	Fluence X 10^{22} (n/cm^2)	Irradiation Temperature (^oC)	USE (Joule/cm^2)	DBTT (^oC)	Reduction in USE (%)	DBTT (^oC)
TT Series						
HT-9	3	390	96	129	49	124
Base Metal	3	450	122	31	35	21
TT Series	3	500	120	37	36	33
	3	550	108	61	43	57
9Cr-1Mo Control AF Series	0	---	320	-25	0	0
9Cr-1Mo	3	390	188	29	41	54
Base Metal	3	450	240	-23	25	2
TV Series	3	500	212	-27	34	-2
	3	550	208	-33	35	-8

It has been shown[9] that the toughness for HT-9 alloy irradiated at 390°C is attributed to irradiation hardening due to G phase formation. At higher irradiation temperature, irradiation enhanced prepicitation along the delta ferrite stringers induced a reduction in USE and a concurrent shift in OBTT. This premise is further illustrated by the test results of the KT series. The specimens of KT series were fabricated from a plate stock with the crack plane oriented in T-L direction. As a consequence, the delta ferrite stringers in the specimens of KT series are perpendicular to the crack front and parallel to the fracture direction whereas the delta ferrite stringers in the specimens of the TT series are parallel to the crack front. Neutron irradiation enhanced carbide prepicitation on delta ferrite stringer surfaces which is expected to cause carbide cracking at lower levels of stress. Owing to the particular orientation of the crack plane, this degradation mechanism should be less effective in the case of KT series. The reduction in USE for the KT series was merely 12% for the specimens irradiated above 450°C. On the other hand, the USE for the TT series under same irradiation condition was reduced to approximately 40% of the preirradiated specimens. Specimens irradiated at 390°C show greater reduction in USE and larger OBTT due to the G phase formation.

7.1.4.5 Conclusions

Charpy impact tests on specimens in the AD-2 reconstitution experiment were completed. It is concluded that:

1. The effect of Neutron irradiation on \$he DBTT appears to be approaching saturation for HT-9 base metal specimens irradiated to 6 x 10^{22} nlcm at 390°C. The DBTT increased 20°C as the fluence was rasied from 3 x 10^{22} n/cm^2 to 6 x 10^{22} n/cm^2.

2. No apparent effect on both DBTT and USE was detected for 9Cr-1Mo base metal due to the additional neutron exposure.

3. 9Cr-1Mo weldment irradiated to 3 x 10^{22} n/cm^2 exhibited a maximum of 62°C higher DBTT than the base metal under the same irradiation conditions.

4. Significant improvement in both DBTT and USE on HT-9 base metal were observed due to the different crack plane orientation.

7.1.5 References

1. R. J. Puigh and N. F. Panayotou, "Specimen Preparation and Loading for the AD-2 Ferritic Experiment", ADIP Quarterly Progress Roport, June 30, 1981. DOE/ER-0045/3, pp 261-293.

2. A. M. Ermi, "Reconstitution of the AD-2 Ferritic Experiment", ADIP Quarterly Progress Report, March 31, 1982. DOE/ER-0045/8, pp 431-441.

3. W. L. Hu and N. F. Panayotou, "Miniature Charpy Specimen Test Device for the Ferritic Alloy HT-9", AOIP Quarter1y Progress Report, Sept. 30, 1981. DOE/ER-0045/7, pp 235-251.

4. W. L. Hu, "Miniature Charpy Impact Test Results for Irradiated Ferritic Alloys", ADIP Quarterly Progress Report, Sept. 30, 1982. DOE/ER-0045/9, pp 255-272.

5. D. S. Gelles, W. L. Hu, F. H. Huang, G. D. Johnson, "Effects of HFIR Irradiation at 55 C on Microstructure and Toughness of HT-9", ADIP Quarterly Progress Report, Sept. 30, 1983. DOE/ER-0045-11, pp 115-127.

6. W. L. Hu and O. S. Gelles, "Miniature Charpy Impact Test Results for the Irradiated Ferritic Alloys HT-9 and Modified 9Cr-1Mo", Proceedings of Topical Conference on Ferritic Alloys for Use in Nuclear Energy Technologies, Snowbird, Utah, June 19-23, 1983. pp 631-646.

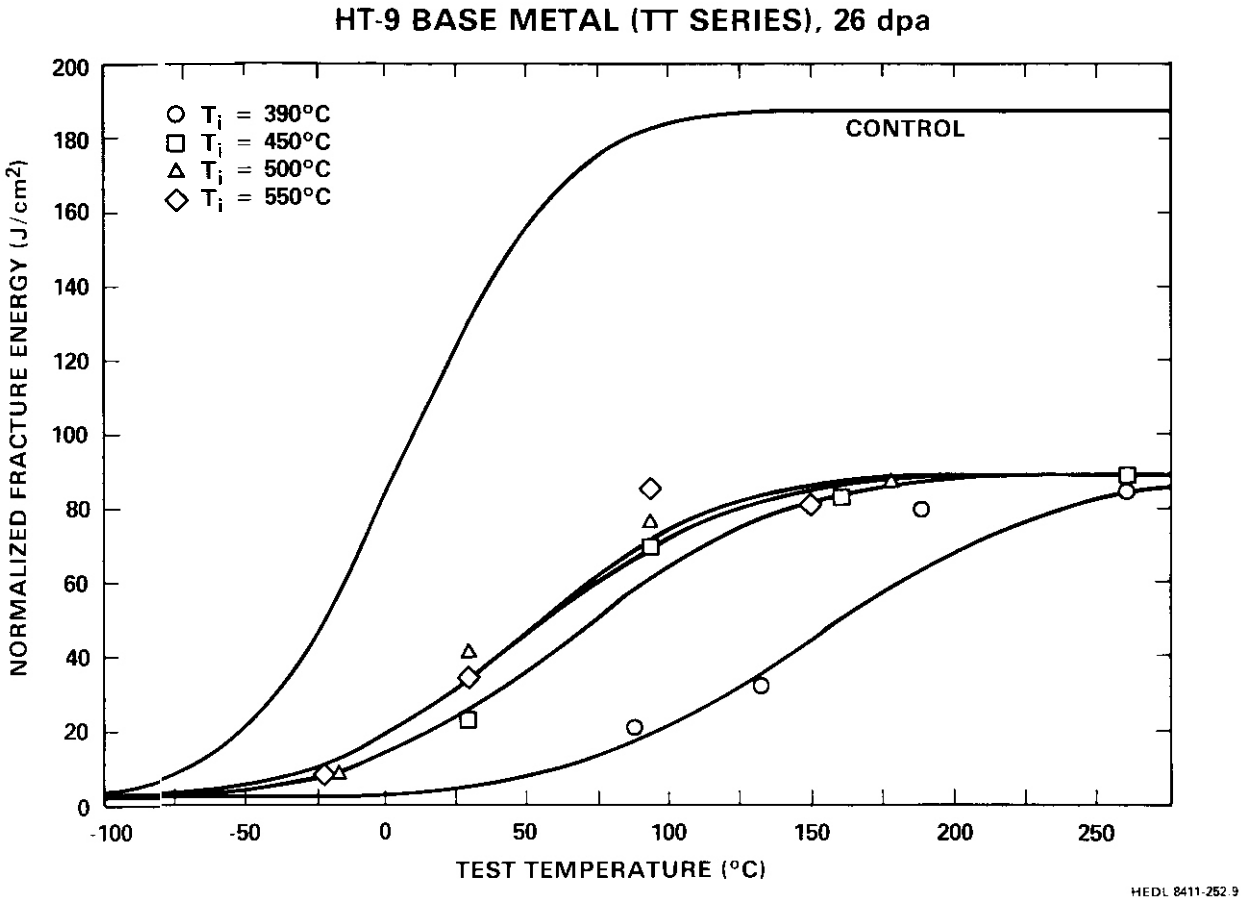

Fig. 7.1.1. Charpy impact test results on HT-9 base metal irradiated to 6 x 10^{22} n/cm² (TT Series)

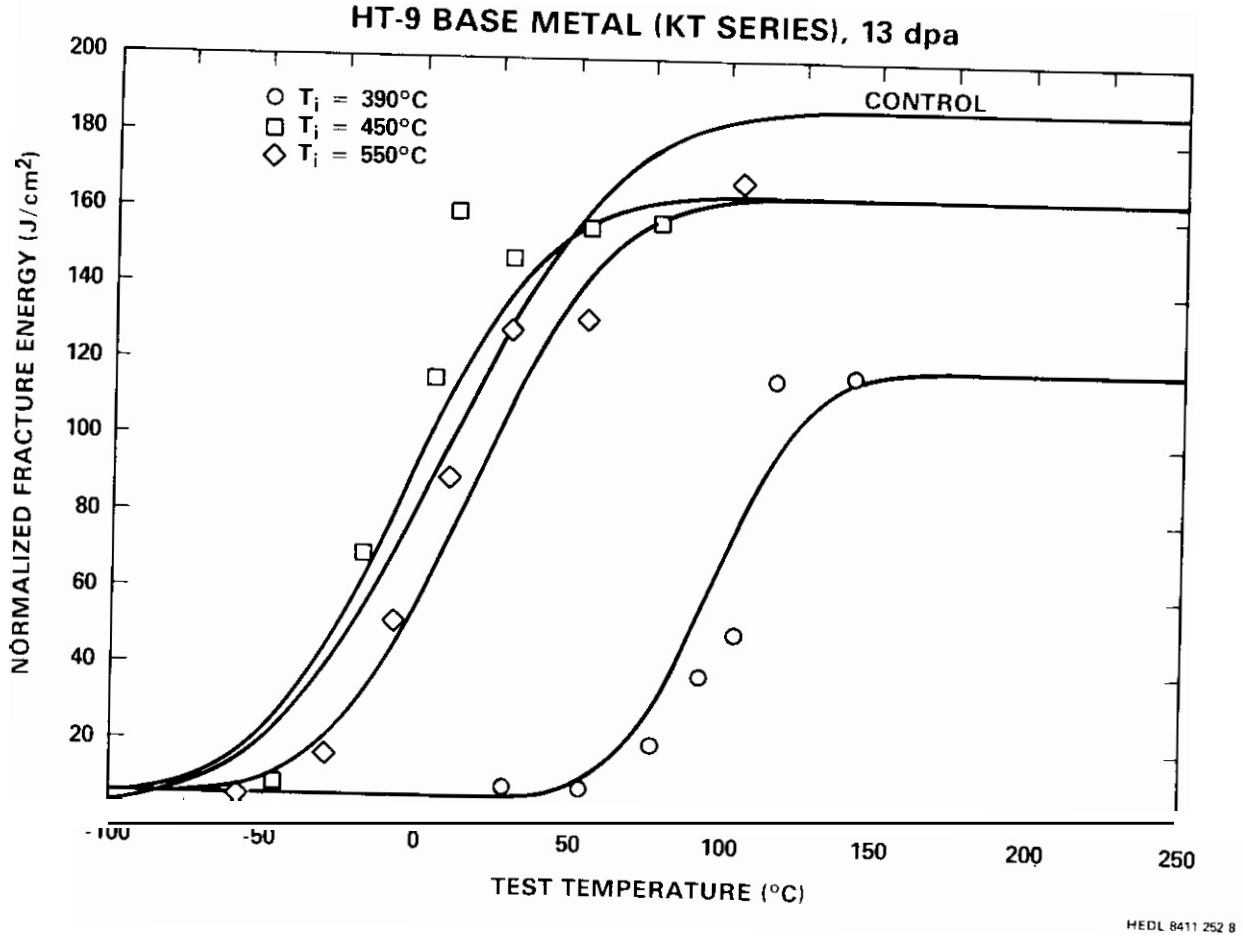

Fig. 7.1.2. test on HT-9 base metal irradiated to 3 x (KT Series)

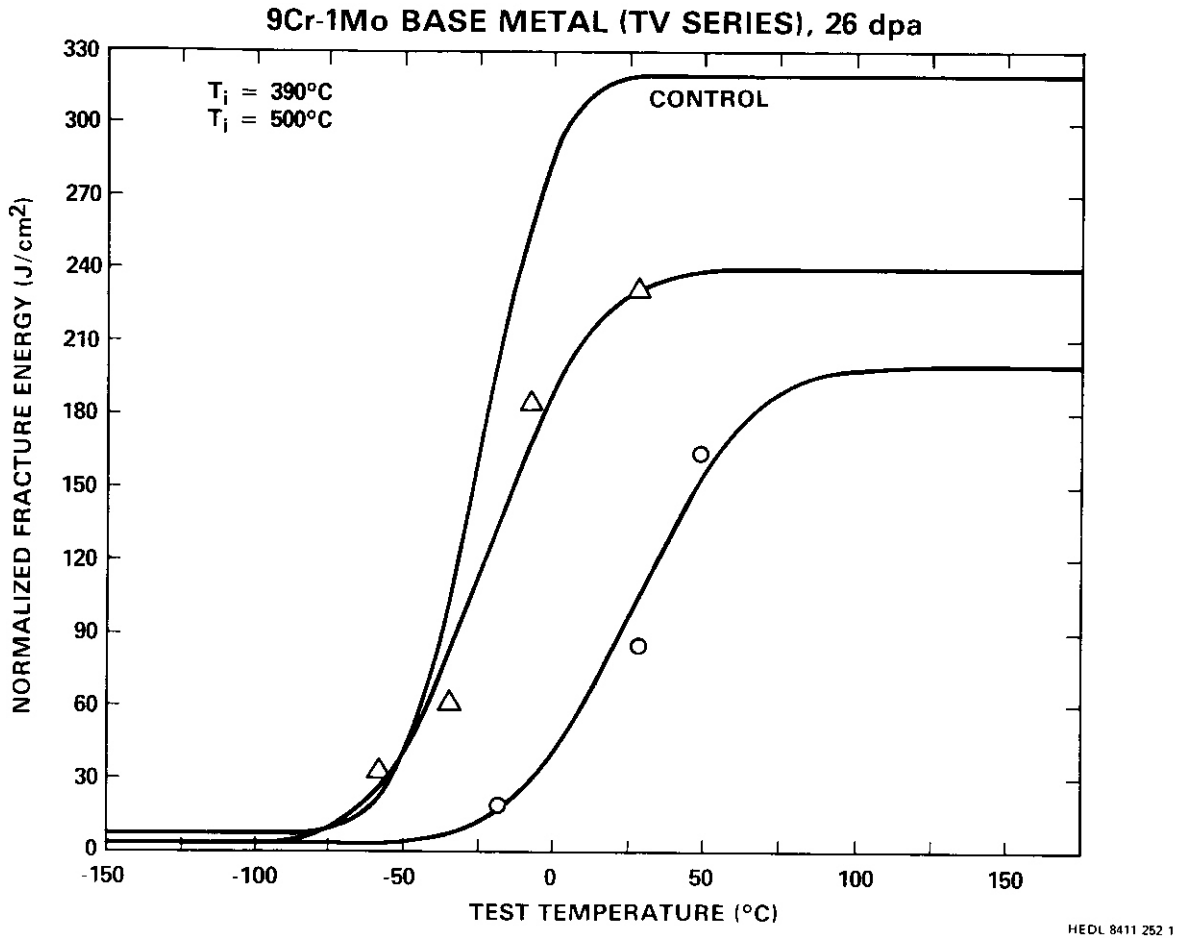

7.1.3. Charpy impact test results on 9Cr-1Mo base metal to 6 x (TV Series)

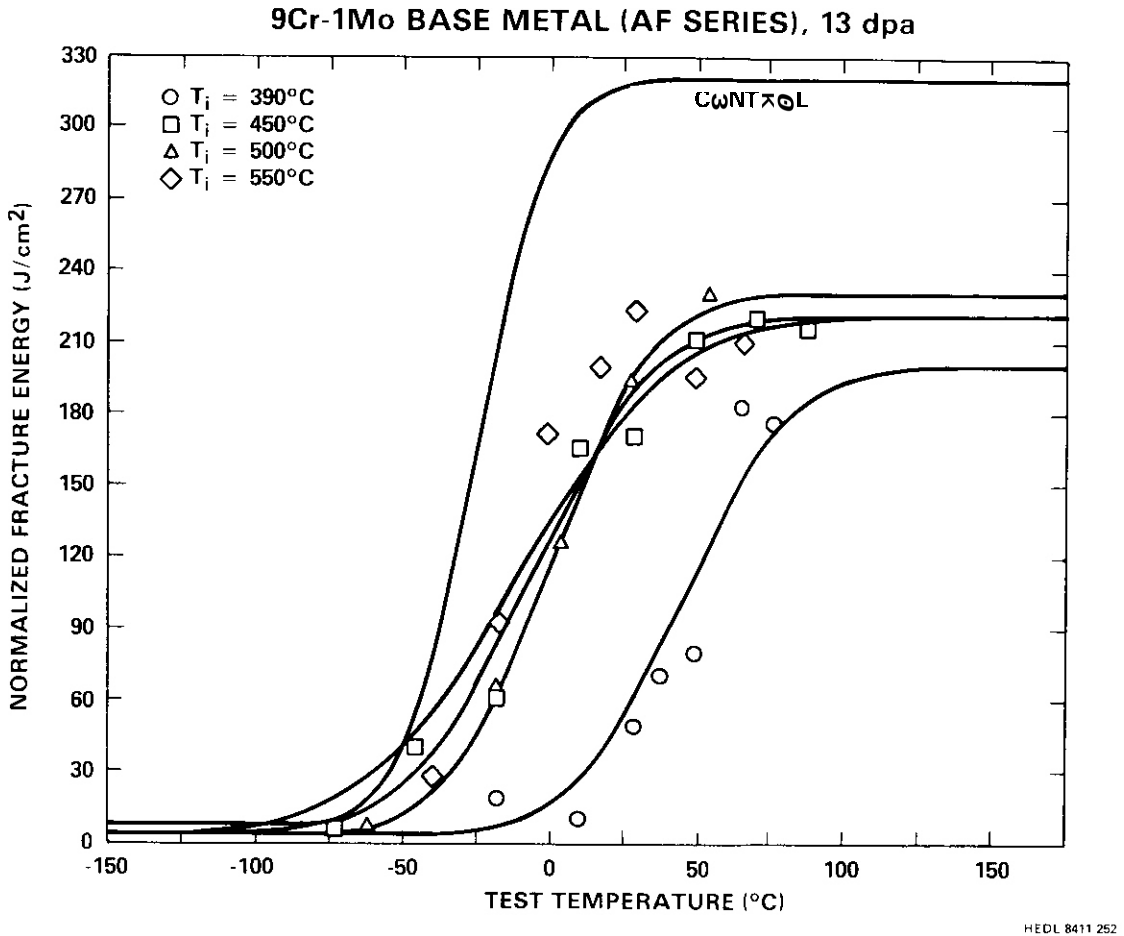

Fig. 7.1.4. test results on 9Cr-1Mo base metal ir to 3 x (AF Series)

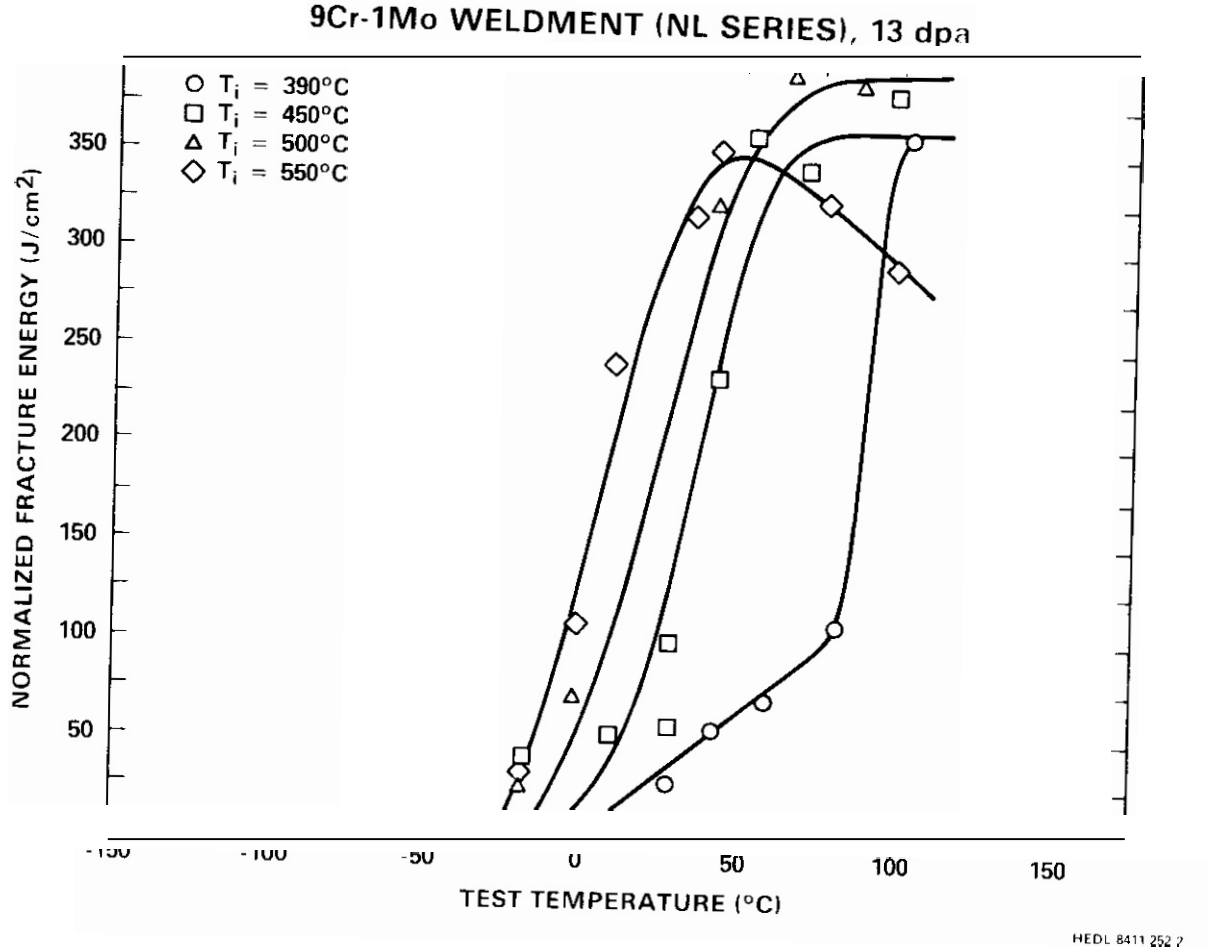

7.1.5. Charpy r on 9Cr 1Mo to 3 x (NC Ser

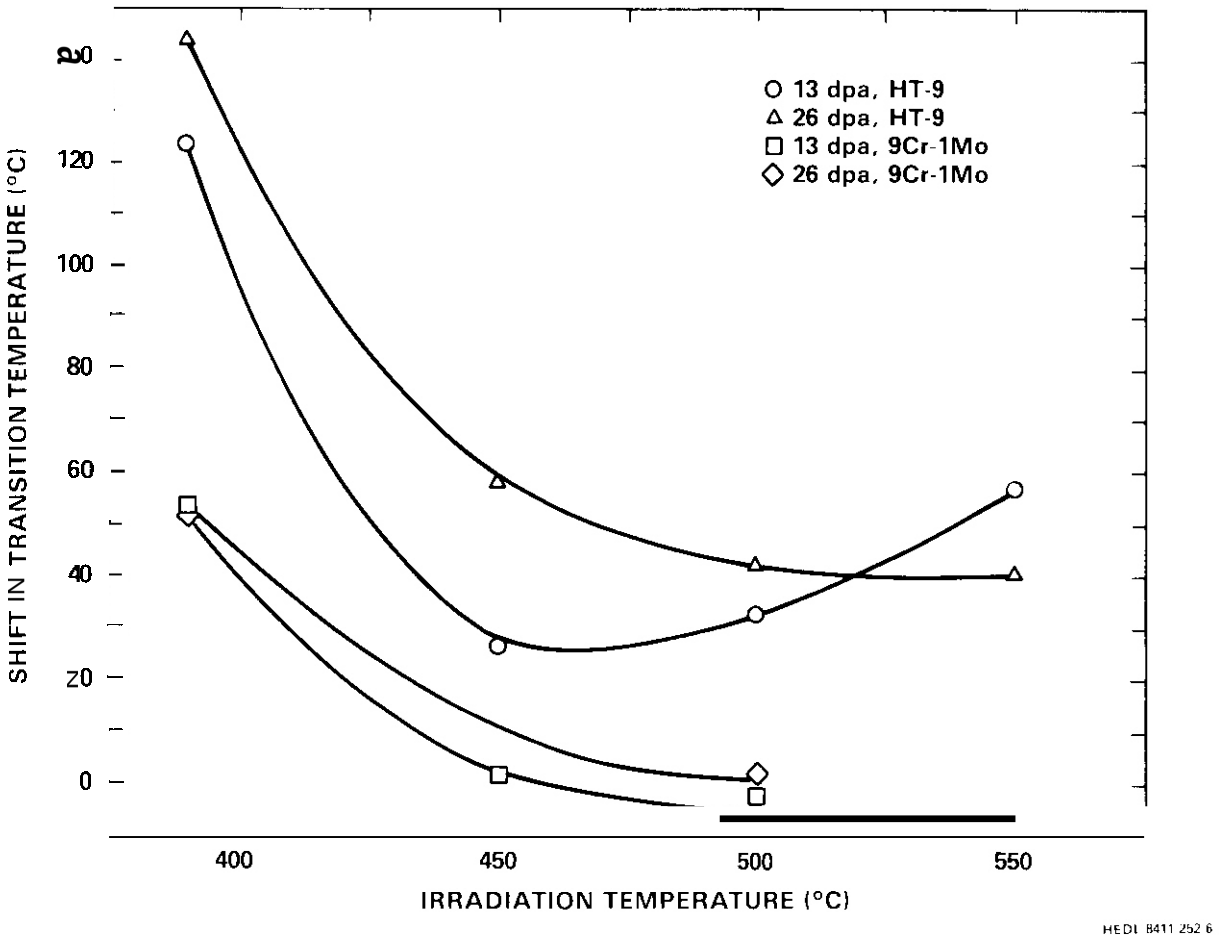

Fig. 7.0.2. Irradiation and f on the shift of ductile-to-brittle transition temperature for ferritic alloys

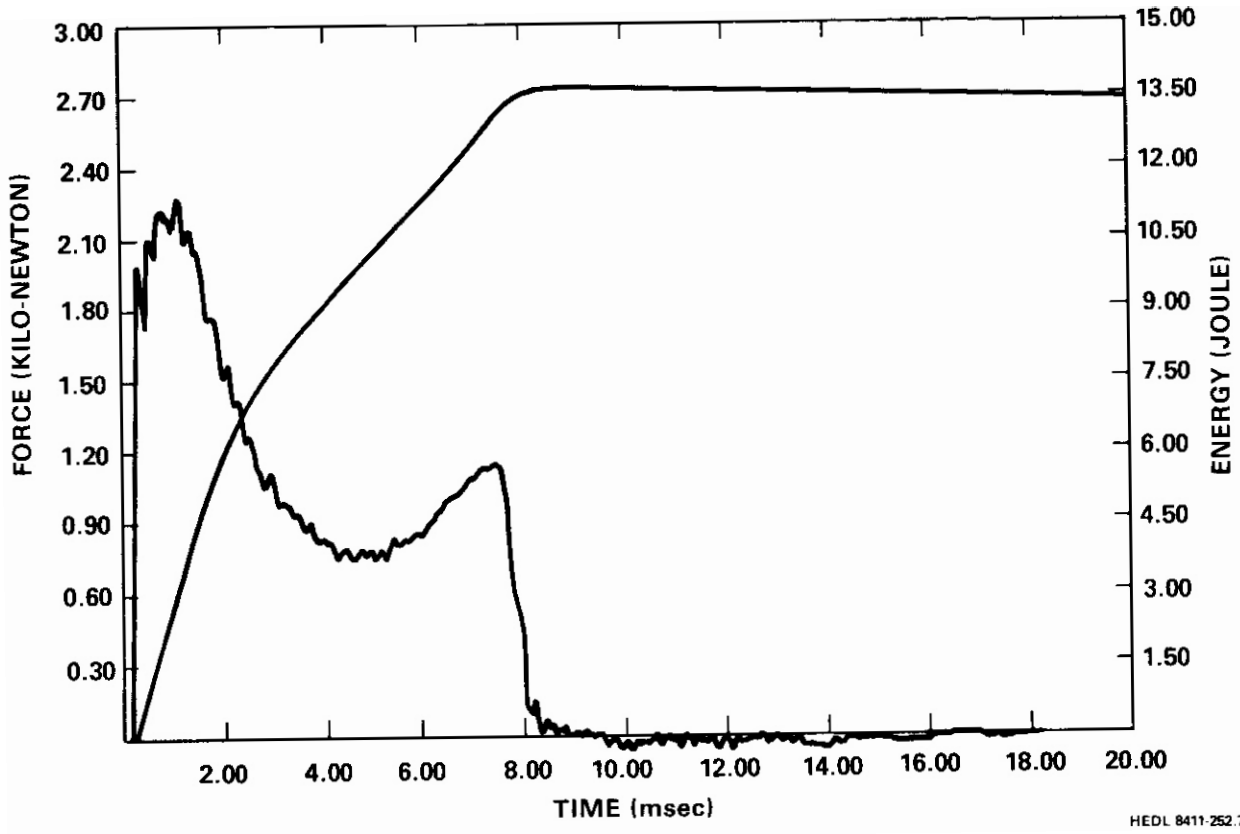

Fig. 7.1.7. Typical load and energy traces for a 9Cr-1Mo weldment specimen tested at upper shelf temperature

7.2 EFFECT OF NICKEL CONTENT ON THE AGING AND IRRADIATION RESPONSE OF IMPACT PROPERTIES OF 9 Cr-1 MoVNb AND 12 Cr-1 MoVW IN THE ABSENCE OF INTERNAL HELIUM EFFECTS — W. R. Corwin, J. M. Vitek, and R. L. Klueh (Oak Ridge National Laboratory)

7.2.1 AOIP Task

AOIP tasks are not defined for Path E, ferritic steels in the 1978 Program Plan.

7.2.2 Objective

The objectives of this study are to provide information on the radiation-induced degradation of impact properties of high chromium ferritic steels at moderate irradiation doses. It will concurrently examine the viability of simulating helium effects in these engineering alloys by adding nickel and irradiating in a mixed spectrum reactor.

7.2.3 Summary

Impact testing was completed on aged and EBR-II irradiated 9 Cr-1 MoVNb and 12 Cr-1 MoVW steels, each with and without small additions of nickel. Only limited property changes resulted from aging or irradiating to 12 dpa in the temperature range of 450°C to 550°C. Irradiation of the 12 Cr-1 MoVW at 390°C with and without nickel produced severe degradation of impact properties. Nickel additions affected the unirradiated material properties, but subsequent radiation-induced changes were similar regardless of nickel content.

7.2.4 Progress and Status

7.2.4.1 Introduction

The simultaneous effect of displacement damage and transmutation helium on ferritic candidate materials for the first wall of magnetic fusion reactors can be examined by doping the materials with small amounts of nickel and irradiating in a mixed-spectrum fission reactor.[1] In such reactors, the fast neutrons produce displacement damage, while helium is produced by a two-step reaction of ^{58}Ni with thermal neutrons. Such irradiations are being conducted in HFIR for the 9 Cr-1 MoVNb and 12 Cr-1 MoVW steels. However, to assess the metallurgical effects of adding Ni, irradiations were carried out in EBR-II where very little helium is produced in either doped or undoped alloys. In this report, the results of the impact tests on the 9 and 12 chromium alloys with and without nickel additions of up to 2% are presented for materials in the unirradiated, aged, and EBR-II irradiated conditions.

7.2.4.2 Experimental

Electroslag-remelted heats of 9 Cr-1 MoVNb and 12 Cr-1 MoVW steels with and without nickel additions were prepared by Combustion Engineering, Inc., Chattanooga, Tennessee. The heats included 9 Cr-1 MoVNb (XA3590), 9 Cr-1 MoVNb-2 Ni (XA3591), 12 Cr-1 MoVW (XA3587), 12 Cr-1 MoVW-1 Ni (XA3588), and 12 Cr-1 MoVW-2 Ni (XA3589); the chemical compositions are given in Table 7.2.1. Specimens were obtained from 5.3-mm-thick plate, which was normalized and tempered prior to machining; details on the heat treatments are given in Table 7.2.2. Information on the microstructures and tensile properties of the normalized-and-tempered steels were previously presented.

The details on the subsize Charpy V-notch specimens and the procedures developed for testing them were previously presented.[2] The specimens were 5 mm square and 25.4 mm long and contained a 0.76-mm-deep 30° V-notch with a 0.05 to 0.08-mm-root radius. Each individual Charpy data set was fitted to a hyperbolic tangent function for purposes of analysis.

The shift in the ductile to brittle transition temperature (OBTT) was the major concern in this

Table 7.2.1. Composition of 9 Cr-1 MoVNb and 12 Cr-1 MoVW heats of steel

Element	Concentration[a] (wt %)				
	9 Cr-1 MoVNb		12 Cr-1 MoVW		
	0%[b] Ni	2% Ni	0%[b] Ni	1%Ni	2% Ni
C	0.09	0.064	0.21	0.20	0.20
Mn	0.36	0.36	0.50	0.47	0.49
P	0.008	0.008	0.011	0.010	0.011
S	0.004	0.004	0.004	0.004	0.004
Si	0.08	0.08	0.18	0.13	0.14
Ni	0.11	2.17	0.43	1.14	2.27
Cr	8.62	8.57	11.99	11.97	11.71
Mo	0.98	0.98	0.93	1.04	1.02
V	0.209	0.222	0.27	0.31	0.31
Nb	0.063	0.066	0.018	0.015	0.015
Ti	0.002	0.002	0.003	0.003	0.003
Co	0.013	0.015	0.017	0.015	0.021
Cu	0.03	0.04	0.05	0.05	0.05
Al	0.013	0.015	0.030	0.017	0.028
B	<0.001	<0.001	(0.001	(0.001	(0.001
W	0.01	0.01	0.54	0.53	0.54
As	<0.001	(0.001	(0.001	0.002	<0.002
Sn	0.003	0.003	0.002	0.001	0.002
Zr	<0.001	(0.001	(0.001	(0.001	(0.001
N	0.050	0.053	0.020	0.016	0.017
O	0.007	0.006	0.005	0.007	0.007

[a] Balance iron.

[b] Standard alloy composition.

study. Because of space limitations in the irradiation capsules, only a limited number of irradiated specimens were available. These specimens were tested primarily to determine the DBTT, and consequently, the upper shelf energy (USE) can only be estimated in some cases. The DBTT is calculated at two fixed energy levels (5.5 and 9.2 J) in addition to the energy corresponding to one half the USE.

While the temperature at 1/2 USE is a useful measure of the DBTT, particularly when comparing specimens of varying sizes,[2] it has two drawbacks. It is inherently sensitive to the level of USE: the greater the USE the higher the DBTT, even if the data up to the lower of the two upper shelves are identical. Also, and of greater concern in this case, accurate values of the DBTT cannot be obtained without accurate levels of USE. The transition energy values of 5.5 and 9.2 J correspond to the common indexing values of 41 and 68 J, respectively, used for analysis of full-size Charpy specimens after volumetric scaling.[3]

Table 7.2.2. Normalizing and tempering conditions 9 Cr-1 MoVNb and 12 Cr-1 MoVW heats of steel[a]

Alloy	Heat treatment conditions[b]
9 Cr-1 MoVNb	0.5 h 1040°C, AC; 1 h 760°C, AC
9 Cr-1 MoVNb-2 Ni	0.5 h 1040°C, AC; 5 h 700°C, AC
12 Cr-1 MoVW	0.5 h 1050°C, AC; 2.5 h 780°C, AC
12 Cr-1 MoVW-1 Ni	0.5 h 1050°C, AC; 2.5 h 780°C, AC
12 Cr-1 MoVW-2 Ni	0.5 h 1050°C, AC; 5 h 700°C, AC

[a]Heat treatment was on 5.3-mm-thick plates.

[b]AC = air cool.

Specimens were irradiated in EBR-II in the AD-2 (reconstitution) experiment in capsules designed to maintain temperatures of 390, 450, 500, and 550°C. The 9 Cr-1 MoVNb and 9 Cr-1 MoVNb-2 Ni specimens were irradiated at 450 and 550°C, the 12 Cr-1 MoVW and 12 Cr-1 MoVW-2 Ni were irradiated at 390°C, and the 12 Cr-1 MoV-1 Ni and 12 Cr-1 MoVW-2 Ni were irradiated 500°C. Irradiation was in row 4, level 7 of EBR-II. The capsules were exposed to approximately 2.5×10^{26} neutrons/m^2 (>0.1 MeV), which produced a displacement damage of about 12 dpa and resulted in helium levels for all materials of less than 1 ppm. The uncertainty in fluence has been estimated as ±10% and the temperature uncertainties as 390 ±10°C, 450 ±15°C, 500 ±20°C, and 550 ±30°C.

To separate thermal aging and irradiation effects, groups of specimens were aged at 300, 400, and 500°C for times up to 5000 hours which corresponded to the irradiation time.

7.2.4.3 Results and Discussion

An examination of the effects of the 2% nickel addition on the Charpy impact properties of the 9 Cr-1 MoVNb steel (Fig. 7.2.1) reveals that the USE remains virtually unchanged and that the DBTT of the alloy is notably lower after the addition of nickel (Table 7.2.3). This behavior compares well with the effect of nickel in pearlitic steels[4] where nickel typically reduces the DBTT. Of the three criteria listed in Table 7.2.3 for measuring the DBTT, the temperature corresponding to 9.2 J appears to be the most useful as it is typically at or below mid-transition, yet above the beginning of the lower knee of the curve. Moreover, it is unaffected by changes or uncertainties in the upper shelf and hence will be the primary criterion used in comparing shifts in the DBTT. Using this criterion, the reduction in the DBTT (9.2 J) due to the nickel addition is 50.5°C. This reduction in the DBTT in the 9 Cr-1 MoVNb-2 Ni will need to be accounted for in judging radiation and/or helium effects.

The effects of aging the undoped 9 Cr-1 MoVNb steel are small for the conditions examined (Fig. 7.2.2). Aging for 2500 h at either 300° or 400°C caused a steepening of the ductile-to-brittle transition about its center. As 9.2 J is lower than the center of the transition, this resulted in a measured increase of 10 to 13°C in the DBTT. Estimates of the USE for both aged conditions indicated only small, unsystematic changes from the unaged condition. Aging the 9 Cr-1 MoVNb-2 Ni steel had a slightly larger effect (Fig. 7.2.3) as the DBTT shift was about +15°C for the aged condition.

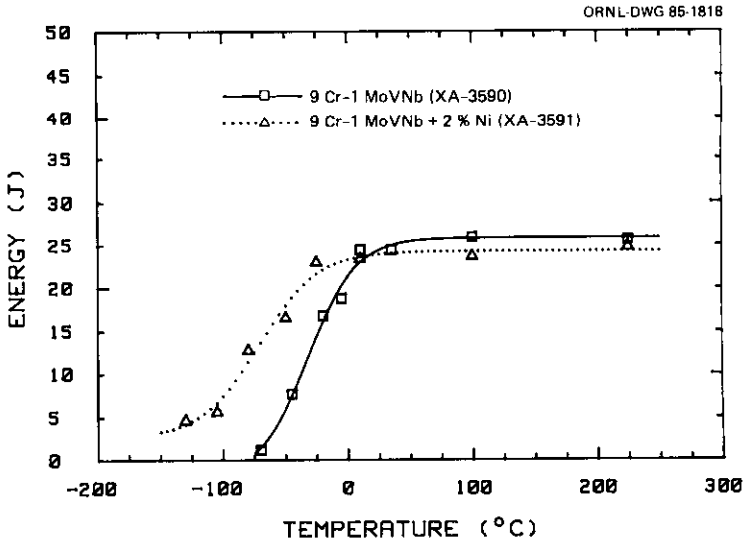

Fig. 7.2.1. The addition of 2% nickel reduces the DBTT in unirradiated, unaged 9 Cr-1 MoVNb.

Table 7.2.3. Effects of nickel content, aging and irradiation on the ductile to brittle transition temperature and upper shelf energy of 9 Cr-1 MoVNb steel

Heat	Nickel content (%)	Condition	Transition temperature (°C)			Upper shelf energy (J)
			1/2 USE	5.5J	9.2J	
XA-3590	0.11	Unirradiated	−29.2	−51.5	−39.8	25.8
		Aged, 300°C, 2500 h	−19.4	−41.2	−29.4	27.8[a]
		Aged, 400°C, 2500 h	−25.6	−29.8	−26.5	20.6[a]
		Irradiated, 450°C, 12 dpa	−14.5	−44.8	−29.4	28.9
		Irradiated, 550°C, 12 dpa	−40.7	−62.0	−52.8	32.3
XA-3591	2.17	Unirradiated	−76.6	−114.7	−90.3	24.3
		Aged, 400°C, 2500 h	−42.1	−104.4	−74.1	28.9[a]
		Irradiated, 450°C, 12 dpa	−91.3	−121.7	−104.2	25.1[a]
		Irradiated, 550°C, 12 dpa	−61.1	−111.2	−87.8	29.7[a]

[a]Estimated.

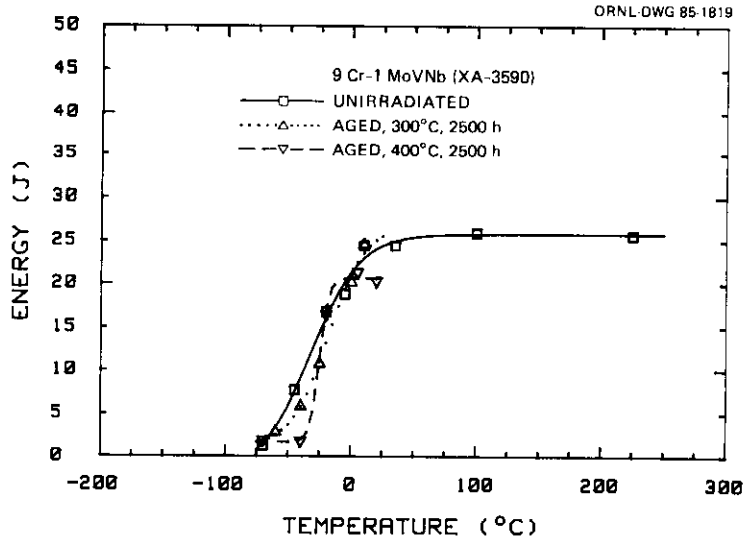

Fig. 7.2.2. Aging steepens the impact transition region in undoped 9 Cr-1 MoVNb.

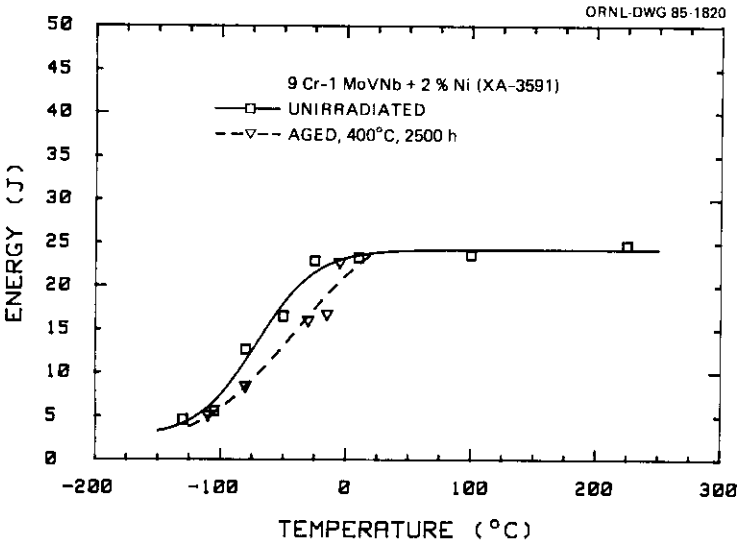

Fig. 7.2.3. Aging slightly increases the DBTT in 9 Cr-1 MoVNb-2 Ni.

Irradiation of the undoped 9 Cr-1 MoVNb steel to 12 dpa at 450° or 550°C had little effect on the impact properties (Fig. 7.2.4). In fact, the USE increased slightly for both irradiation conditions and the DBTT decreased slightly for the 550°C irradiation. At 450°C the DBTT increased only 10°C, approximately that which was caused by thermal aging alone.

The increase in the USE of the 9 Cr-1 MoVNb is consistent with the observations[5] of a slight increase in tensile strength but similar tensile ductility when irradiated under conditions similar to those examined here. If the strength of a Charpy specimen is increased while maintaining its ductility, it follows that it will generally absorb more energy in breaking. This seems to be the case here for specimens on the upper shelf.

The effect of irradiation on the 9 Cr-1 MoVNb doped with 2% nickel was similar to that on the undoped material (Fig. 7.2.5). Irradiation at 450°C decreased the DBTT slightly (14°C) and at 550°C increased it very slightly (3°C). In both cases the estimated USE went up slightly after irradiation. Compared with the fact that aging at 400°C had increased the DBTT about 15°C, the irradiation can be seen to be quite benign.

Summarizing the effects of nickel on the unirradiated, aged, and irradiated impact properties of 9 Cr-1 MoVNb and 9 Cr-1 MoVNb-2 Ni it can be seen (Table 7.2.3) that the only substantial effect is the general reduction of the DBTT in all cases where the nickel was present. At this relatively low irradiation dose and high irradiation temperature, very little degradation of impact properties is observed with or without nickel. For the aged material, a slight increase in the DBTT was uniformly observed.

The effect of 1 and 2% nickel additions on the impact behavior of the unirradiated, unaged 12 Cr-1 MoVW steel is somewhat different from that for 9 Cr-1 MoVNb (Fig. 7.2.6). While the upper shelf is noticeably reduced by the addition of nickel, the DBTT can be observed to increase or decrease, depending upon the method of measurement used. If the temperature of 1/2 USE is used to measure the DBTT, then the DBTT appears to decrease with increasing nickel content, agreeing with previous studies on these heats.[3] If, however, the 9.2 J index of DBTT is used, then a slight (10°C) increase is seen when 2% Ni is added to the 12 Cr-1 MoVW steel. For the 5.5 J index, virtually no change is observed (Table 7.2.4). For consistency in comparing sets of data, we will use the 9.2 J index.

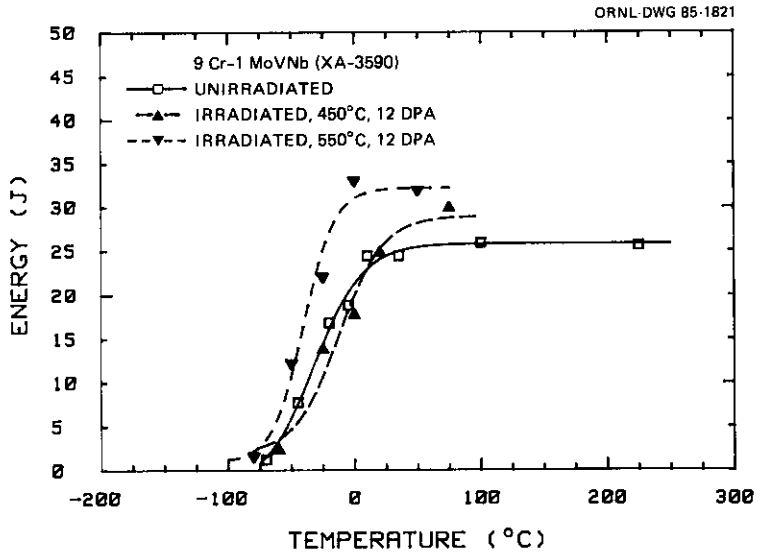

Fig. 7.2.4. High temperature irradiation of the 9 Cr-1 MoVNb steel does not degrade its impact properties.

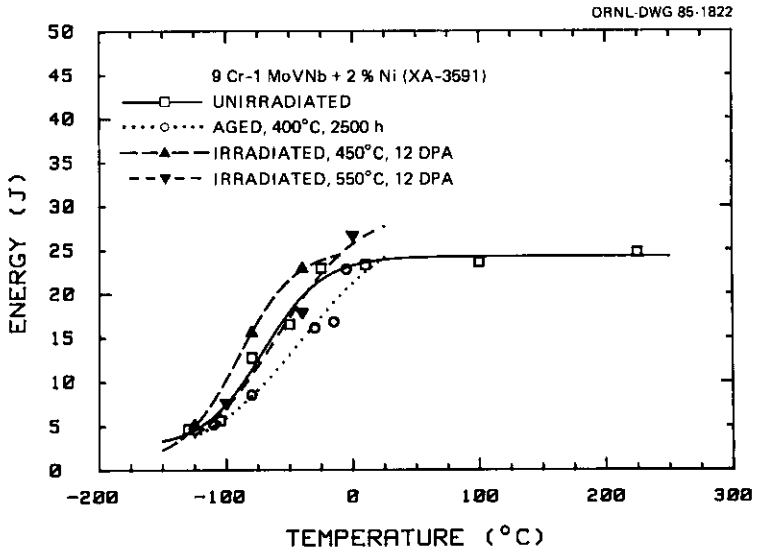

Fig. 7.2.5. High temperature irradiation of the nickel doped 9 Cr-1 MoVNb slightly improves its impact properties compared to aging under similar conditions.

The decrease in the USE corresponds well to the lower tensile ductility observed for the same heats of the nickel doped 12 Cr-1 MoVW[1] as compared to undoped heats. Aging the undoped 12 Cr-1 MoVW produced minor effects similar to those in the 9 Cr-1 MoVNb (Fig. 7.2.7). The transition steepened, resulting in an increase of 14 to 19°C in the DBTT measured at the 9.2 J level. Aging the 12 Cr-1 MoVW-1 Ni at 500°C and the 12 Cr-1 MoVW-2 Ni at 400°C also increased the DBTT and lowered the USE. The 12 Cr-1 MoVW-2 Ni (Fig. 7.2.8) exhibited only a modest 6°C increase, whereas the 12 Cr-1 MoVW-1 Ni (Fig. 7.2.9) underwent a 34°C shift in the DBTT. Whether this varying shift is due to the difference in alloy chemistry or the tempering or aging treatment is not known.

It is necessary to examine separately the effects of irradiation temperature and nickel content on the response of the 12 Cr-1 MoVW steels to irradiation. The results demonstrate quite clearly that the lower (390°C) irradiation temperature was far more damaging than the higher temperatures investigated. In the undoped 12 Cr-1 MoVW irradiation at 390° produced a large drop in USE (Fig. 7.2.10) and an increase in the DBTT of 166°C, as compared to only 14°C for equivalent thermal aging. This observation agrees with the large increase in tensile strength and decrease in ductility in the same alloy when similarly irradiated.[6]

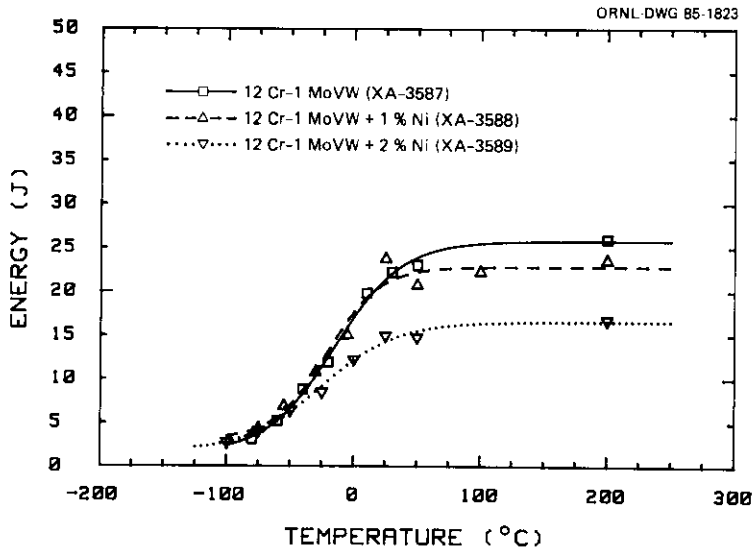

Fig. 7.2.6. Addition of nickel to 12 Cr-1 MoVW steel reduces its upper shelf energy.

Table 7.2.4. Effects of nickel content, aging and irradiation on the ductile to brittle transition temperature and upper shelf energy of 12 Cr-1 MoVW steel

Heat	Nickel content (%)	Condition	Transition temperature (°C)			Upper shelf energy (J)
			1/2 USE	5.5J	9.2J	
XA-3587	0.43	Unirradiated	−18.1	−57.6	−35.2	25.8
		Aged, 300°C, 2500 h	−13.9	−32.5	−18.3	23.1[a]
		Aged, 400°C, 2500 h	−16.6	−33.5	−20.1	22.3[a]
		Aged, 400°C, 5000 h	−19.8	−32.0	−21.7	21.2[a]
		Irradiated, 390°C, 12 dpa	103.9	92.3	131.3	13.2
XA-3588	1.14	Unirradiated	−27.4	−61.4	−37.4	22.8
		Aged, 500°C, 5000 h	−28.4	−55.1	−31.1	19.4[a]
		Irradiated, 500°C, 12 dpa	−16.9	−43.4	−15.9	18.1[a]
XA-3589	2.27	Unirradiated	−31.8	−56.6	−24.6	16.6
		Aged, 400°C, 2500 h	−10.7	−17.7	9.1	12.7[a]
		Irradiated, 390°C, 12 dpa	58.3	55.6	99.1	11.5[a]
		Irradiated, 500°C, 12 dpa	−18.6	−55.0	−18.3	18.3[a]

[a]Estimated.

Irradiation of the 12 Cr-1 MoVW-1 Ni at 500°C showed only a modest increase in DBTT (~20°C), compared to that of either the normalized-and-tempered or aged conditions (Fig. 7.2.11). This agrees well with tensile data available on undoped 12 Cr-1 MoVW irradiated under similar conditions at 500°C which showed only modest hardening.[6]

The only 12 Cr-1 MoVW alloy for which both low and high temperature irradiation data are available is the 12 Cr-1 MoVW-2 Ni. The data conform to the effects seen in the 12 Cr-1 MoVW and 12 Cr-1 MoVW-1 Ni alloys. The 12 Cr-1 MoVW-2 Ni when irradiated at 390°C underwent a 124°C upward shift in the DBTT which was much larger than thermal aging alone had produced; this is similar to, but not quite as severe as that experienced in the undoped alloy. Its USE was also reduced substantially. However, when the same alloy was irradiated at 500°C, it exhibited almost no change in the DBTT (~ 6°C), very much like the 12 Cr-1 MoVW-1 Ni alloy (Fig. 7.2.12).

In general the nickel doping of the 12 Cr-1 MoVW alloy seemed to produce no systematic changes in either the DBTT of the normalized-and-tempered material or in its thermal aging response. A noticeable decrease in the USE with increasing nickel content was observed for all conditions where adequate data were available. While a complete matrix of nickel and irradiation temperature effects does not exist, it can be concluded that the nickel additions do not qualitatively affect the irradiated behavior of the 12 Cr-1 MoVW alloys in the absence of helium production. At 390°C, severe upward shifts in the DBTT are experienced with or without nickel additions, although with the nickel they are not quite as extreme. At 500°C, very little irradiation induced degradation was observed in any case.

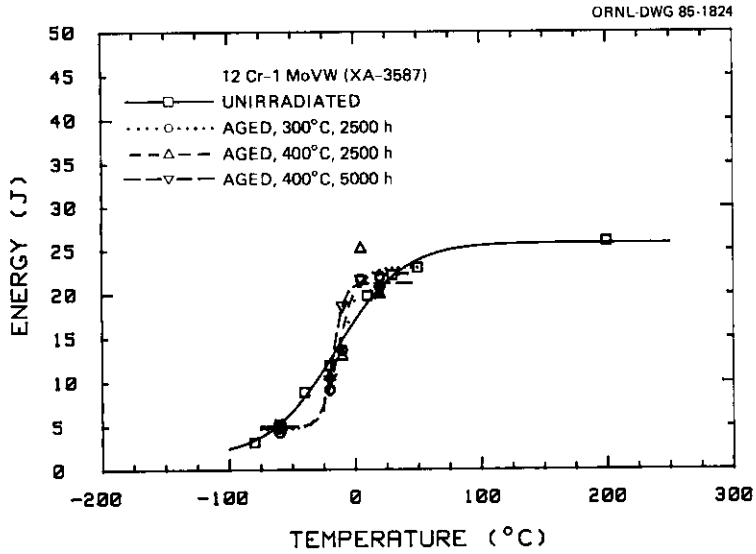

Fig. 7.2.7. Aging steepens the impact transition in undoped 12 Cr-1 MoVNb.

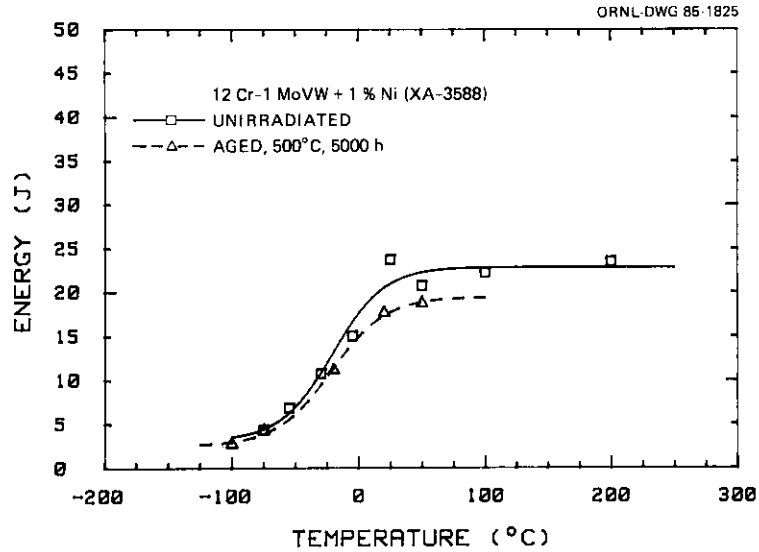

Fig. 7.2.8. Aging the 12 Cr-1 MoVW-1 Ni steel degrades its impact properties very slightly.

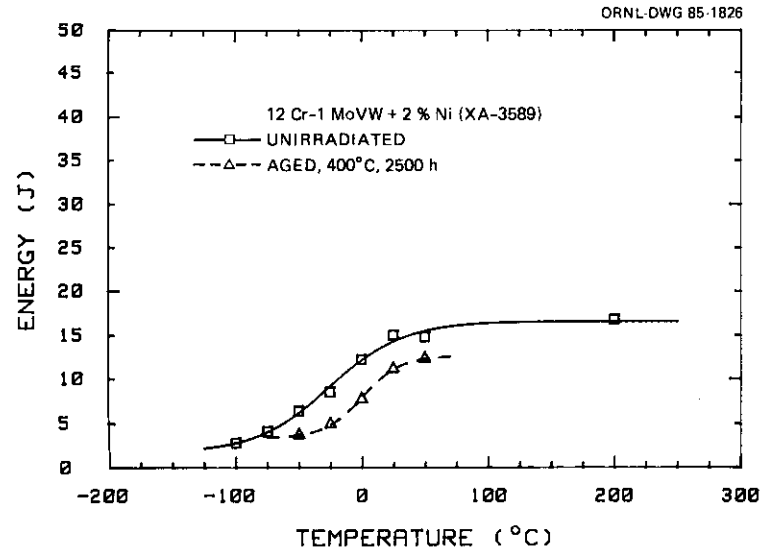

Fig. 7.2.9. Aging of 12 Cr-1 MoVW-2 Ni shifts the DBTT upward about 35°C.

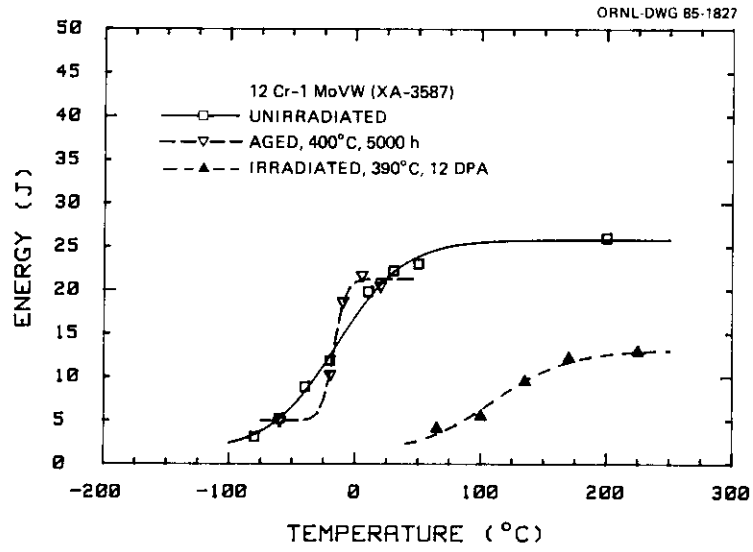

Fig. 7.2.10. Relatively low temperature irradiation of the undoped 12 Cr-1 MoVNb causes a large increase in the DBTT and large decrease in the upper shelf energy compared to thermal aging which produces no substantive change.

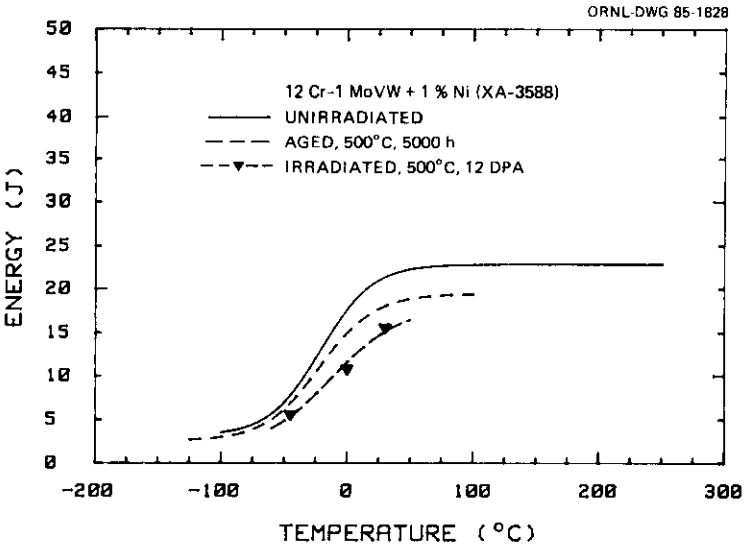

Fig. 7.2.11. High temperature irradiation of 12 Cr-1 MoVNb-1 Ni degrades its impact properties slightly more than similar thermal aging.

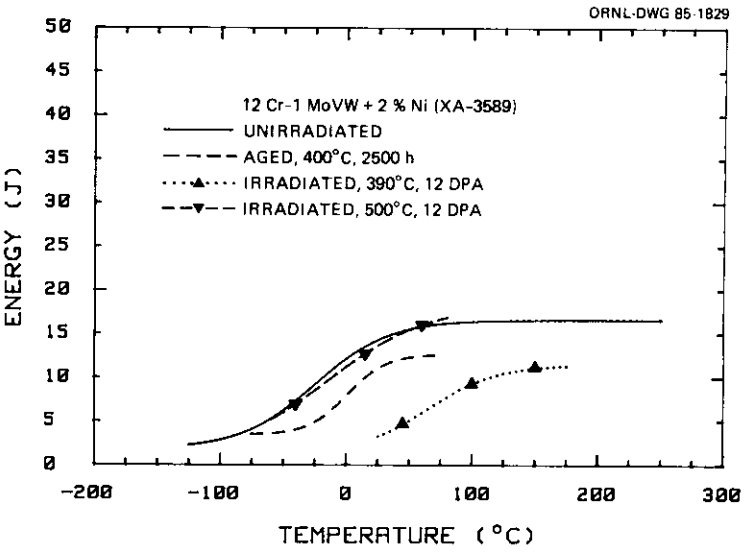

Fig. 7.2.12. A 2% addition of nickel to the 12 Cr-1 MoVNb steel does not appreciably change its response to low or high temperature irradiation.

The results of this study indicate that the addition of nickel to 9 Cr-1 MoVNb and 12 Cr-1 MoVW ferritic steels has not resulted in mechanical behavior substantially different from the undoped steels, either before or after irradiation. In TEM studies by Gelles and Thomas[7] on 12 Cr-1 MoVW steel irradiated in EBR-II at 390°C, the nickel-rich G-phase was detected. They expressed the concern that the addition of nickel, over the ~0.5% present in the commercial steel, could lead to larger quantities of G-phase and exacerbate any irradiation embrittlement.[7] The present studies do not indicate such a problem, as the 12 Cr-1 MoVW-2 Ni steel showed a smaller shift in DBTT than the undoped steel. This result agrees with tensile studies on the nickel-doped steels irradiated at ~50°C in HFIR. In those studies 9 Cr-1 MoVNb and 12 Cr-1 MoVW steels with and without nickel showed similar relative hardening effects.[7] Also, the low irradiation temperature of those tests was felt to preclude the formation of large amounts of G-phase. We thus continue to look favorably on the irradiation of nickel-doped ferritic steels in a mixed-spectrum reactor to simultaneously produce displacement damage and transmutation helium as a viable method to simulate the irradiation effects in a fusion reactor first wall.

7.2.5 Conclusions

Two heats of 9 Cr-1 MoVNb and three heats of 12 Cr-1 MoVW steel were tested to examine the effects of aging, irradiation, and nickel doping on the impact behavior. Only minimal effects were observed on any materials when thermally aged for times and temperatures similar to those experienced during the companion irradiation experiments. The greatest factor in the irradiation experiment was the irradiation temperature. The only radiation damage that occurred was produced at 390°C, the lowest irradiation temperature investigated, where large upward shifts in the DBTT and drops in the USE were observed in the 12 Cr-1 MoVW and 12 Cr-1 MoVW-2 Ni steels. No 9 Cr-1 MoVNb steels were irradiated at 390°C. At 450" and 550°C, irradiation temperatures for the 9 Cr-1 MoVNb alloys, and at 500°C, the other irradiation temperature for 12 Cr-1 MoVW alloys, virtually no degradation in the impact properties was observed, with or without nickel additions.

The effects of the nickel additions can be divided into the effect of nickel on the baseline alloys themselves and those effects on the response of the doped alloys versus the undoped ones to aging and irradiation. The effects the addition of 1 to 2% nickel had on the baseline impact properties of the materials varied by alloy. The addition of nickel to the 9 Cr-1 MoVNb reduced the DBTT (~50°C) but did not appreciably affect the USE. In the 12 Cr-1 MoVNb the effect was reversed. The DBTT was largely unaffected but the USE experienced an appreciable drop.

However, once the new baseline properties were established for the doped alloys, their response to aging and irradiation were similar to the undoped alloys. Aging and high temperature irradiation had only limited effect on the impact properties with or without nickel additions; irradiations at 390°C substantially degraded the impact properties, with or without nickel. Hence, at least for the conditions examined here, it appears that nickel additions can be used to investigate helium effects in the high-chromium ferritics. They can provide qualitatively similar material response to irradiation exposure of undoped alloys. By varying the irradiation to which they are exposed, they can be used to examine radiation damage in either the presence or absence of internal helium.

7.2.6 Future work

The alloys investigated here have been irradiated under similar conditions in HFIR where substantial helium production occurs in nickel doped alloys. The HFIR-irradiated steels will be evaluated to assess the effects of internal helium with all other irradiation factors held nominally constant.

7.2.7 References

1. R. L. Klueh, J. M. Vitek, and M. L. Grossbeck, "Nickel-Doped Ferritic (Martensitic) Steels for Fusion Reactor Irradiation Studies: Tempering Behavior and Unirradiated and Irradiated Tensile Properties," in *Effects of Radiation on Materials: Eleventh Conference*, eds. H. R. Brager and J. S. Perrin, ASTM STP 762 (American Society for Testing and Materials, 1982) pp. 548–664.

2. W. R. Corwin, A. M. Hougland, "Effect of Specimen Size and Material Condition on the Charpy-Impact Properties of 9 Cr-1 MoVNb Steel," *Proc. of Conference on the Use of Subsize Specimens for Irradiated Testing, Albuquerque, Sept. 1983*, to be published by American Society for Testing and Materials (in preparation).

3. W. R. Corwin, R. L. Klueh, and J. M. Vitek, "Effect of Specimen Size and Nickel Content on the Impact Properties of 12 Cr-1 MoVW Ferritic Steel." *J. of Nuclear Materials*, 122–123, 1984 pp. 343348.

4. J. A. Rinebolt and W. J. Harris, Jr., Trans. *Am. Soc.* Met. 43 (1951) 1175–1214.

5. R. L. Klueh and J. M. Vitek, "Elevated Temperature Tensile Properties of 9 Cr-1 MoVNb Steel Irradiated in the EBR-II AD-2 Experiment," pp. 100–103, in *ADIP Semiannual Progress Report for Period Ending March 31, 1984*, DOE/ER-0045/12.

6. R. L. Klueh and J. M. Vitek, "Elevated-Temperature Tensile Properties of 12 Cr-1 MoVW Steel Irradiated in the EBR-II, AD-2 Experiment," pp. 104–106, in *ADIP Semiannual Progress Report for Period Ending March 31. 1983*, DOE/ER-0045/10, U. S. DOE, Office of Fusion Energy.

7. D. E. Gelles and L. E. Thomas, "Microstructural Examination of HT-9 and 9 Cr-1 Mo Contained in the AD-2 Experiment," pp. 343–362, in *ADIP Semiannual Progress Report for Period Ending March 31, 1982*, DOE/ER-0045/8, U.S. DOE, Office of Fusion Energy.

7.3 EFFECTS OF IRRADIATION ON LOW ACTIVATION FERRITIC ALLOYS - D. S. Gelles and M. L. Hamilton (Hanford Engineering Development Laboratory)

7.3.1 ADIP Task

The Department of Energy (DOE) Office of Fusion Energy (OFE) has cited the need to investigate ferritic alloys under the ADIP Program task, Ferritic Steels Development (Path E). The tasks involved are akin to task number 1.8.13., Tensile Properties of Austenitic Alloys, l.C.l, Microstructural Stability and 1.C.2., Microstructures and Swelling in Austenitic Alloys.

7.3.2 Objective

The objective of this work is to provide guidance on the applicability of low activation bainitic and martensitic steels for fusion reactor structural components.

7.3.3 *Summary*

A series of low activation ferritic alloys has been designed, fabricated, irradiated in MOTA 1B, and tested and examined following irradiation. The series consists of alloys similar to 2-1/4Cr-1Mo with vanadium substituted for molybdenum, alloys similar to 9Cr-1Mo with tungsten and/or vanadium substituted for molybdenum and alloys similar to HT-9 with tungsten and/or vanadium substituted for molybdenum. The results demonstrate that low activation alloys can be successfully produced in the ferritic alloy class. The 2-1/4Cr-V alloys develop excessive irradiation hardening due to precipitation following irradiation at 420°C and the 2-1/4Cr-V and 9Cr-V/W alloys developed excessive softening due to precipitate coarsening and dislocation recovery following irradiation at 585°C. In comparison, the 12Cr-W-V alloy appears to have excellent properties; α' precipitation at 420°C in-reactor did not significantly increase strength and reasonable strength was maintained after irradiation at 585°C propbably in part due to intermetallic precipitate development.

7.3.4 Progress and Status

7.3.4.1 Introduction. A significant advantage can be gained by limiting alloy compositions of fusion reactor structural materials in order to control activation levels following irradiation and storage.[1] Within the limitations for reduced activation after storage defined by NRC regulation 10CFR61 class C, low activation steels appear possible provided the alloying additions of Nb, Mo, Cu, N and Ni are controlled.[2-4] For example, after irradiation in Starfire to 10 MW·yr/m² and 3 x 10⁷ days (8.2 yrs) storage, the following restrictions would apply: Nb<2.9 ppm, Mo<30 ppm, Cu<0.12%, N<0.33% and Ni<0.91% such that if any of these elements reach this concentration limit, none of the other elements should be present.[1]

For a low activation ferritic alloy class, such a compositional specification requires that niobium be excluded, that substitutes be found for molybdenum and nickel and that nitride and copper precipitation not be used for hardening. Possible substitutes for molybdenum are tungsten, vanadium and tantalum. Manganese can be substituted for nickel. Within these restrictions, it appears possible to obtain both bainitic alloys (similar to 2-1/4Cr-1Mo) and martensitic alloys (similar to 9Cr-1Mo and HT-9).

This report is intended to describe work at Westinghouse Hanford Company to develop bainitic and martensitic low activation alloys. Initial alloy design was done during a visit to Hanford by Professor N. Ghoniem of UCLA. He described his interest in a low activation alloy in the 2-1/4Cr-1.5V composition range and it became apparent that other alloys were possible which might have as good or better properties. A number of alloys have since been defined, melted, fabricated, irradiated and examined following irradiation. Similar efforts are underway to Oak Ridge National Laboratory (ORNL,)[5] Sandia Livermore (SL) and GA Technologies (GA). The present effort is intended to provide input along with input from the ORNL, SL and GA alloys so that the potential of the ferritic alloy class can be evaluated with respect to the low activation issues.

7.3.4.2 Basis for the Alloy Class. In order to develop low activation ferritic alloys with properties similar to commercial heat resistant ferritic alloys, a substitute for molybdenum is the major requirement. Molybdenum is universally added to improve hardenability. Adjacent elements in the periodic table are V, Cr, Mn, Nb, Ta, W, Tc and Re with V, Ta and W appearinq to be the prime prospects. Most is known about effects of vanadium. For example, Fig. 7.3.1 provides a pseudo-carbide phase diagram for the Fe-Cr-V-C system at 700°C.[6,7] Phase fields for V_4C_3, M_7C_3 and $M_{23}C_6$ are shown for 0.12C (solid lines) and for 0.2C (dashed lines). The boundaries defining the limits of delta ferrite formation at 0.1C (solid line) and 0.2C (dashed line) are also shown. From Fig. 7.3.1 it can be shown that for carbon contents on the order of 0.1%C, a bainitic alloy will contain only V_4C_3 above 0.5%V whereas for 0.2%C greater than 1%V is required. Also, for chromium contents of 9% or greater, if vanadium contents are kept at 1% or below, only $M_{23}C_6$ is present as the stable phase.

Based on Fig. 7.3.1, several low activation steels can be envisioned. Bainitic allovs strenuthened bv V_4C_3 with carbon levels of 0.1% should be possible for vanadium levels above 0.5%. Martensitic alloys in the 9Cr range strengthened entirely by $M_{23}C_6$ should be possible for alloys with vanadium contents below 1% with 0.1C. However, in order to get V_4C_3 strengthening as well, higher carbon and/or vanadium contents are required. In the 12Cr range, careful alloy design is needed to avoid significant delta ferrite contents. Either carbon must be increased or other austenite formers such as manganese must be added.

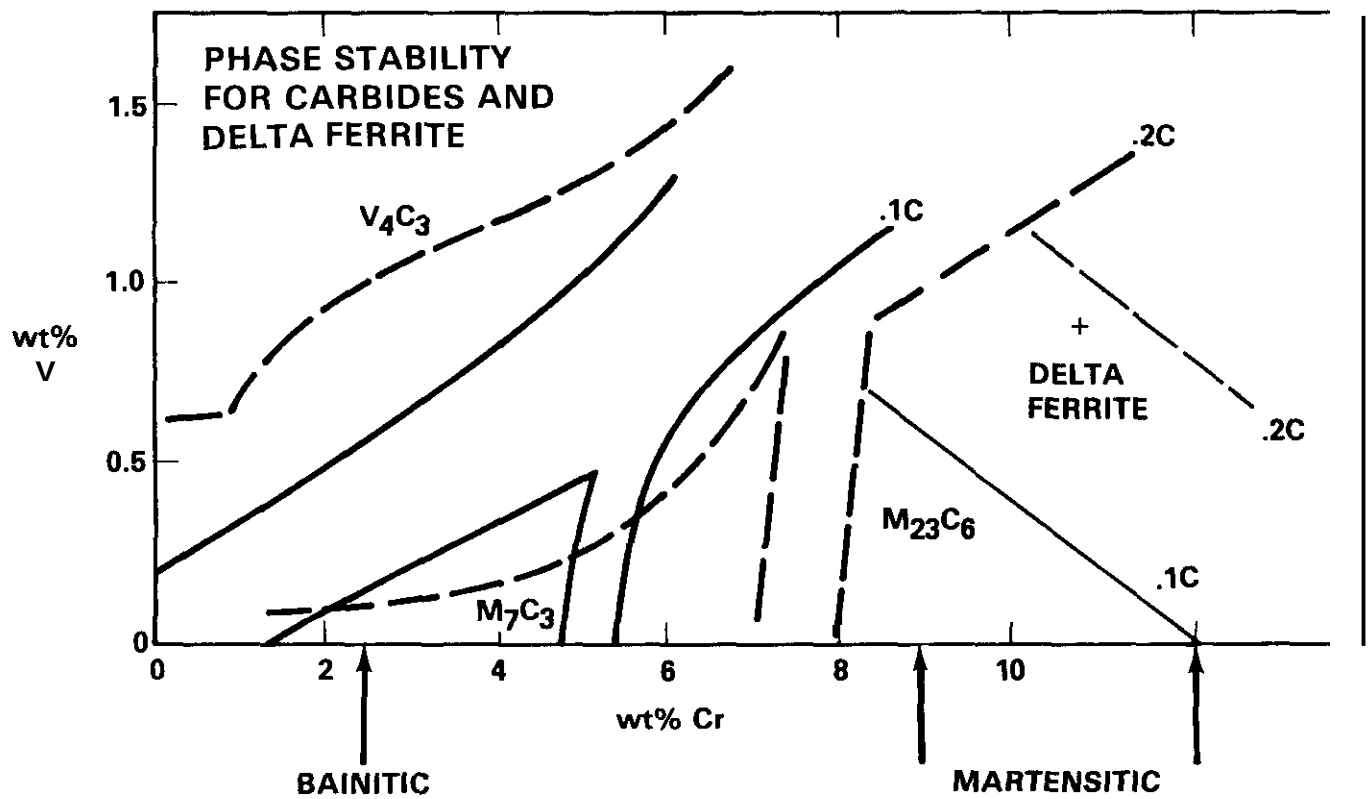

Fig. 7.3.1. Carbide phase stability in the Fe-Cr-V system

Based on these observations, the series of bainitic and martensitic alloys given in Table 7.3.1 were defined. Alloys 1 to 3 are similar to 2-1/4Cr-1Mo but vanadium has been substituted for molybdenum. Comparisons between these alloys should indicate the optimum vanadium level required. Alloys 4 to 7 are similar to 9Cr-1Mo but additions of vanadium, tungsten and manganese have been substituted for molybdenum. Note that alloy 4 includes virtually no manganese and therefore based on Fig. 7.3.1, additions of vanadium must be kept below 0.5% in order to eliminate delta ferrite. Alloy 6 increases the vanadium level with a compensating increase in the carbon level and alloy 5 examines increased manganese content response. Alloy 7 is intended to investigate effects of tungsten additions. Alloys 8 and 9 are similar to HT-9 except that molybdenum has been excluded and carbon levels have been reduced. In order to compensate for the lower carbon levels, the manganese content has been increased significantly. Alloy 8 contains no tungsten whereas alloy 9 contains more tungsten than vanadium.

This report documents results of tensile testing and microstructural examinations both before and after irradiation in FFTF at 420, 520°C and 585°C to fluences as high as 14.5 dpa. The work demonstrates that development of a low activation ferritic alloy is practical and possible.

7.3.4.3 Experimental Procedure. Alloys 1, 2 and 4 through 9 were manufactured by Carpenter Technology Corporation in Reading, PA as 18 lb billets. The alloys were vacuum induction melted into ingots approximately 5 cm square by 20 cm in height and then hot forged from 1150°C into bar 1.25 cm x 7 cm in cross section by ~1 m in length. Chemical analysis was provided by the vendor. Alloy 3 was manufactured by Foote Mineral Company in Exton, PA as a 68 lb ingot. The alloy was air melted into an ingot approximately 75 cm x 10 cm x 5 cm. The chemical analysis was supplied by the vendor. A block of the as-melted material approximately 2 cm x 2 cm x 2 cm was provided for this study by Professor N. Ghoniem of the University of California at Los Angeles.

Table 7.3.1. Low activation ferritic alloy compositions as supplied by the vendor with heat treatment and commercial alloy counterparts provided for comparison

Alloy No.	Heat No.	Composition (w/o) Cr	C	V	W	Mn	Si	N	P	S		Heat Treatment
1	VO2262	2.32	0.086	0.50	<0.01	<0.01	0.08	0.004	<0.005	0.003		A
2	VO2263	2.38	0.093	1.01	<0.01	<0.01	0.08	0.003	<0.005	0.002		A
3	uc-19	2.46	0.11	1.50	---	0.30	0.30	0.015	0.007	0.015	Ti = 0.003 Cu = 0.04	A
	2-1/4Cr-1Mo*	2.25	0.09	<0.03	---	0.45	0.20	---	<0.015	<0.015	Mo = 1.0 Cu <0.35	
4	VO2264	9.13	0.096	0.52	0.01	0.02	0.09	0.003	<0.005	0.003		B
5	VO2266	9.02	0.097	0.51	0.01	2.68	0.09	0.003	<0.005	0.003		
6	VO2265	9.14	0.197	1.23	0.02	1.08	0.09	0.003	<0.005	0.003		C
7	VO2268	8.82	0.101	0.27	0.89	2.44	0.10	0.002	<0.005	0.004		C
	9Cr-1Mo*	8.75	0.10	0.2	---	0.45	0.35	0.05	≤.02	≤0.01	Ni <0.40 Nb = 0.08 Mo = 0.90	
8	VO2267	12.19	0.089	1.05	<0.01	6.47	0.10	0.003	<0.005	0.005		C
9	VO2269	11.81	0.097	0.28	0.89	6.47	0.11	0.003	<0.005	0.005		C
	HT-9*	12	0.20	0.3	0.5	0.6	0.4		≤0.03	≤0.02	Ni = 0.5 Mo = 1.0	

*Nominal Commercial Alloy Compositions.
A = 900°C/20 hr/WQ to RT + 950/20 min/WQ to RT + 650/2 hr/AC.
B = 1000°C/20 hr/AC to RT + 1100/5 min/AC + RT + 700/2 hr/AC.
C = 1000°C/20 hr/AC to RT + 1100/10 min/AC +RT + 700/2 hr/AC.

Specimens for examination and irradiation were prepared as follows. Specimens for tensile testing were of the SS-3 sheet type geometry, 0.075 cm thick by 2.5 cm in length. The sheet direction was oriented normal to the rolling direction. Specimens for microstructural examination were 3 mm diameter disks 0.020 mm in thickness. The sheet direction was normal to the rolling direction. Heat treatment schedules were selected for the 9-12Cr alloys based on a study to minimize the amount of delta ferrite after treatment and for the 2-1/4Cr alloys based on a recommendation by Professor Ghoniem which was checked using optical metallography. The heat treatments used are included in Table 7.3.1. Alloy 8 was found to contain 10 percent delta ferrite after heat treatment optimization. As this was expected to be detrimental to mechanical properties, no tensile specimens were fabricated from alloy 8.

Specimens of the low activation ferritic alloys were put into the Materials Open Test Assembly (MOTA) of the Fast Flux Test Facility (FFTF) at the beginning of cycle 4. Three identically loaded disk packets containing five disks of each alloy condition were placed in each of the three fusion canisters designed to operate at 420, 520 and 600°C. Three tensile specimens of each alloy excluding alloy 8 were also irradiated in the 420°C canister but due to space limitations at 520 and 600°C, another canister (2D) was used to provide a higher irradiation temperature, 585°C.

During cycle 4, the canister designed to operate at 600°C experienced a brief 220°C overtemperature transient. The other canisters were generally maintained within +5° of their respective design temperatures. At the completion of cycle 4, one TEM disk packet and one-tensile specimen were removed for each irradiation condition except for the 600°C overtemperature transient case where all packets were removed. All specimens remaining in MOTA will be irradiated through cycles 5 and 6. Also three new packets have been fabricated and are being irradiated in the 600°C fusion canister through cycles 5 and 6.

Postirradiation tests and examinations were performed using standard procedures. A hydraulically actuated modular testing machine with a 1000 pound Schaevitt load cell was used to test both unirradiated and irradiated specimens. Metallographic examinations were performed on specimens etched with Vilella's etch. Microstructural examinations were performed on a JEM 1200EX scanning transmission electron microscope operating at 120 kV and outfitted with a Tracor Northern EDX detector and TN5500 computer and with a Gatan Electron energy loss spectrometer. Determination of precipitate compositions from extraction replicas involved computer analysis of EDX spectra which included analysis for tungsten.

7.3.4.4. Results

Optical metallography

The microstructures of the as-heat-treated low activation ferritic alloys were found to be typical of bainitic and martensitic steels, as shown by optical metallography. However, differences between the alloys

could be found and in one case, alloy 8, the amount of delta ferrite present was excessive. Fig. 7.3.2 provides examples of the as-heat-treated alloys at 400x. Alloys 1 to 3, in the 2-1/4Cr range show structures typical of tempered bainite whereas structures typical of tempered martensite are found in alloys 4 through 9. Careful examination of alloy 8 across the thickness of the billet had revealed that there was more delta ferrite at the edge of the billet than at the center. Therefore, some composition gradient is indicated but the exact nature of the gradient has not been determined. From Fig. 7.3.2h, the delta ferrite content in alloy 8 is estimated to be 5%. Therefore, it is apparent that the compositional specification for alloy 8 requires more austenite stability. For example, carbon content could be increased by 0.025%, manganese content could be increased by 0.75%, or chromium content could be decreased by 0.35%.[8]

Tensile properties

The tensile properties of the as-heat-treated low activation alloys were in most cases comparable to their comnercial alloy counterparts. Exceptions were found for the bainitic alloys and the 12Cr alloy. The low vanadium bainitic alloy (alloy 1) was considerably stronger than 2-1/4Cr-1Mo (by 65%) but the other bainitic alloys were weaker having much lower yield strengths, slightly lower ultimate tensile strengths and much higher elongations. The 12Cr martensitic alloy had significantly higher strength properties with comparable elongation response in comparison with HT-9. This may be due in part to differences in heat treatment. The properties for the commercial alloys are taken from Reference 9.

However, following irradiation at 420°C to between 6 and 10 dpa, the response could be divided into two types. The bainitic alloys all showed large increases in strength and decreases in elongation. 2-1/4Cr-1Mo also showed increases in strength and decreases in elongation[10] but alloys 1 and 2 were considerably stronger than 2-1/4Cr-1Mo after irradiation at 420°C. In comparison, the 9Cr and 12Cr martensitic alloys showed only moderate if any increase in strength. This is quite different from the behavior of 9Cr-1Mo and HT-9 where significant hardening occurs following irradiation at 400°C.[11] However, in all cases, elongation values for the low activation alloys remain acceptably high.

Irradiation at 585°C to between 13.7 and 14.8 dpa resulted in considerable softening in all alloys. However, the smallest decrease occurred in alloy 9. In comparison, commercial alloys show a maximum of about 10% decrease in strength following irradiation at ~585°C.[11] Therefore, the high temperature properties of the low activation alloys do not appear to be as good as those of their commercial counterparts.

The results given in Table 7.3.2 have been represented graphically in Fig. 7.3.3. Figs. 7.3.3a-b provide comparison of yield strength response as a function of irradiation temperature. For the bainitic alloys (Fig. 7.3.3a), the yield strength is increased 200 MPa following irradiation at 420°C but following irradiation at 585°C, strength is greatly reduced. Hardening at 420°C is much smaller in the martensitic alloys (Fig. 7.3.3b) and reductions in strength for the 9Cr alloys after irradiation at 585°C are not as large as those for the bainitic alloys. However. the strength remains high for the 12Cr alloys after irradiation at 585°C. Fig. 7.3.3c demonstrates that elongation is reduced more substantially in the bainitic alloys following irradiation at 420°C but the lower elongation levels are still satisfactory.

Electron microsopy

As-heat-treated: The as-heat-treated structures of the low activation ferritic alloys were characteristic of bainitic and martensitic steels. However, the bainitic alloys were found to be much more heterogeneous than the martensitic alloys with regard to carbide distributions. Also, recovery was more complete in the 9Cr martensitic alloys compared to the 12Cr alloys. Examples of these structures at low magnification are provided in Fig. 7.3.4. Fig. 7.3.4a-c show the bainitic alloys. Coarse V_4C_3 carbides, can be seen distributed non-uniformly. Of particular note is the cellular V_4C_3 seen in the grain on the right hand side in Fig. 7.3.4b. Several examples of regions containing aligned rod shaped particles were found whereas not all regions contained them. Figs. 7.3.4d-g show the 9Cr alloy structures. Dislocation structures have relaxed to form well defined cell walls and carbide particles are on the order of 130 nm. The 12Cr alloys shown in Figs. 7.3.3h-i are similar except that the dislocation structures which had formed during the martensitic transformation recovered less during tempering.

420°C irradiated: Effects typical of irradiation at 420°C to 7.7 dpa were found in all alloys. Most alloys developed perfect dislocation loops, in two cases voids were found, in the bainitic alloys heavy precipitation was found and in the 12Cr alloys, evidence for α' precipitation was observed. Examples of microstructures found in the bainitic alloys are provided in Fig. 7.3.5. Figures 7.3.5a and b give examples of dislocation and precipitate structures in alloy 1. Figure 7.3.5a shows a region in light strain contrast, g = 110 near (001). The structure is found to contain predominately a<100> dislocation loops but several examples of a/2 <111> dislocations can be seen. Also, a number of examples of small rod-shaped precipitate particles can be seen which are imaged in dark field contrast in Figure 7.3.5b. The imaging condition used in Figure 7.3.5b is such that this micrograph could show at most 1/6 of the rod-shaped particles. Therefore, these particles should be responsible for the high irradiation hardening observed in tensile tests. The remainder of Figure 7.3.5 gives examples of precipitate and dislocation structures in alloy 3. Figures 5c and d compare bright field and precipitate dark field images under similiar conditions to those used for Figure 7.3.5b. The same precipitate development is found. Precipitate identification has not yet been established; it may be M_7C_3. Figures 7.3.5e-f provide comparison of the dislocation structure. under 110 and 200 imaging conditions near an (001) orientation. Comparison of these images provides demonstration that both a<100> and a/2 <111> loops are present. Arrows mark examples of voids found in

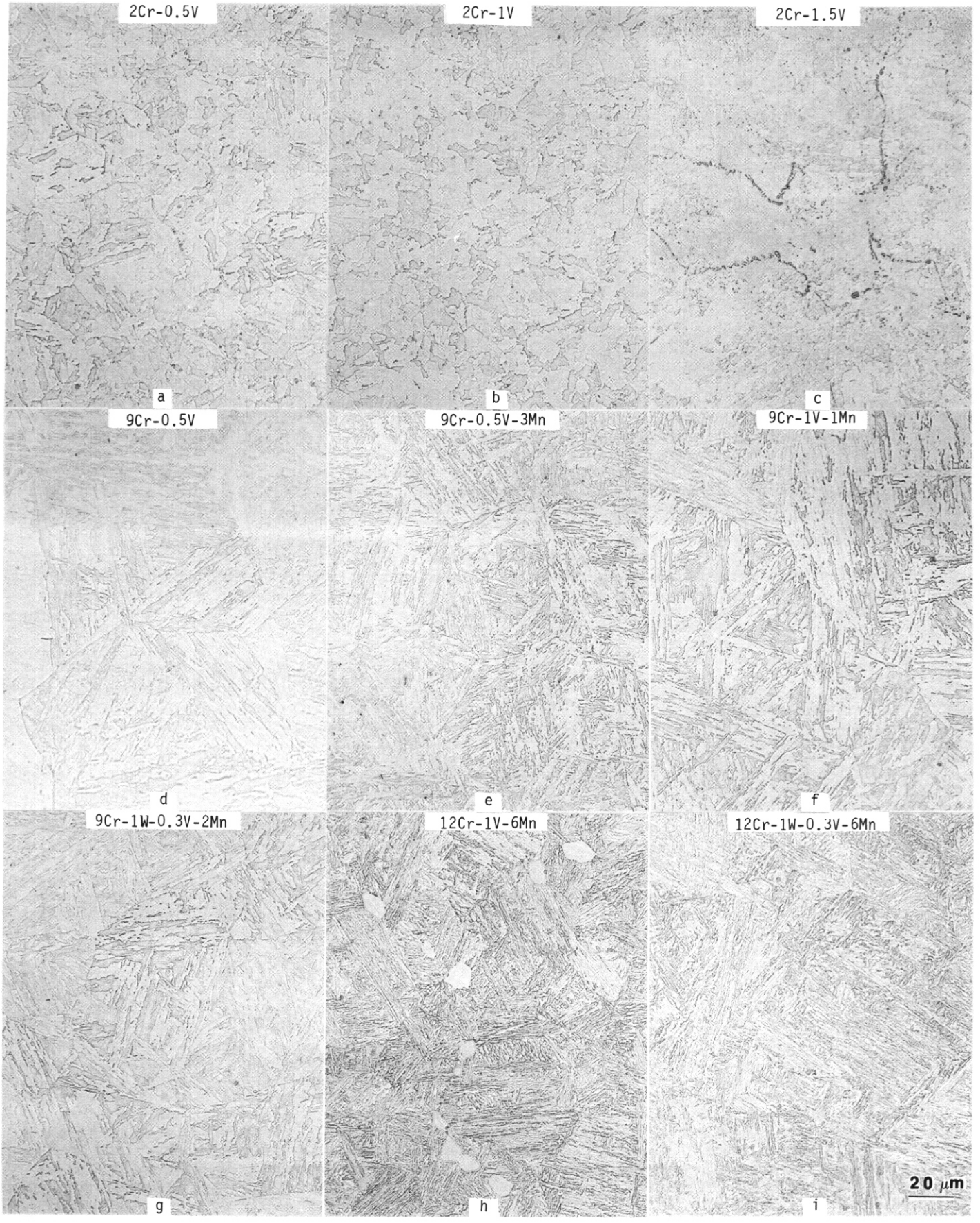

Fig. 7.3.2. Optical metallography of low activation ferritic alloys.

Table 7.3.2. Results of tensile tests at room temperature for low activation ferritic alloys with commercial alloy results given for comparison.[9,10] $\dot{\varepsilon} = 4 \times 10^{-4}$/sec

Alloy	Specimen ID	Dose (dpa)	Irrad Temp (°C)	Yield Strength (MPa)	Ultimate Strength (MPa)	Uniform Elongation (%)	Total Elongation (%)
2-1/4Cr-1MO*	---	---	---	~480	x.575	---	~15
2-1/4Cr-1MO*		12	400	815	830	1.7	4.1
2-1/4Cr-1MO*		12	550	460	530	18.5	21.2
1	TE 07	---	---	778	900	5.3	13.9
	08	---	---	792	902	6.1	13.9
	01	6.0	420	1248	1279	0.8	8.3
2	TH 07	---	---	288	566	16.6	28.5
	08	---	---	335	544	13.4	24.9
	03	9.5	420	1055	1086	1.0	8.1
	04	13.7	585	146	351	23.9	38.9
3	TZ 08	---	---	297	477	12.3	24.4
	01	6.0	420	706	755	1.7	6.1
	04	14.3	585	180	367	16.9	25.7
9Cr-1Mo	---	---	---	575	690	---	~10
4	TM 07	---	---	565	666	4.6	16.6
	08	---	---	567	664	4.0	14.9
	01	9.5	420	660	698	2.2	12.0
	04	14.3	583	310	460	12.8	22.7
5	TP 07	---	---	565	673	5.7	14.8
	08	---	---	600	677	6.5	16.9
	01	7.7	420	599	670	5.9	15.8
	04	13.7	585	343	419	17.8	33.5
6	TN 07	---	---	553	712	6.4	>10.5
	08	---	---	578	731	6.8	17.6
	01	9.5	420	622	730	5.5	15.9
	04	13.7	585	367	562	18.3	30.2
7	TR 07	---	---	587	716	5.6	15.8
	01	7.7	420	608	714	5.8	15.8
HT-9	---	---	---	610	760	---	~12
9	TU 08	---	---	822	1002	2.3	10.1
	01	6.0	420	848	942	6.0	14.7
	04	14.3	585	531	749	9.3	19.4

*Tested at 205°C.

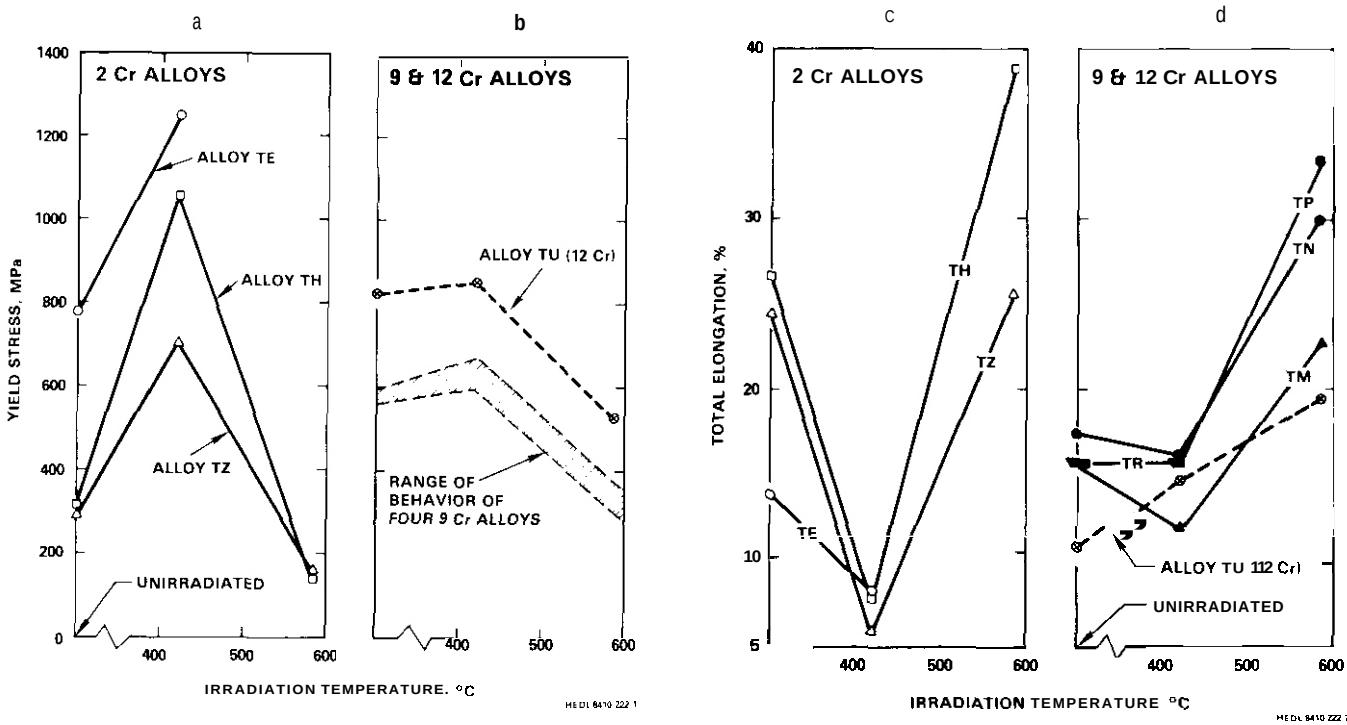

Fig. 7.3.3. Uniaxial tensile test results for low activation ferritic alloys showing yield strength and total elongation response as a function of irradiation temperature. Testing was at room temperature.

alloy 3 following irradiation at 420°C. These examples of voids are not unusual; a moderate density of 7 nm voids was found throughout this material but the accumulated swelling after 7.7 dpa at 420°C is expected to be less than 0.1%.

The 9Cr and 12Cr alloys are shown following irradiation at 420°C to 7.7 dpa in Fig. 7.3.6. The micrographs were selected to show dislocation, void and precipitate structure. Fig. 7.3.6a shows dislocation loops in alloy 4, the loops are uniformly distributed but at lower density than in the bainitic alloys. Fig. 7.3.6b provides an example of the dislocation structure in alloy 5. A subgrain boundary appears at the left and both loops and dislocation tangles can be identified. Figs. 7.3.6c and d are of alloy 6. Fig. 7.3.6c shows dislocation loops and tangles with a subgrain boundary at the lower right. Fig. 7.3.6d provides several examples of voids found in this condition. The voids were non-uniformly distributed and the accumulated swelling was very low. The dislocation structure in alloy 7 is shown in Fig. 7.3.6e; it consists of dislocation tangles and a few individual dislocation loops between subgrain boundaries. Therefore, in summary the 9Cr alloys are found to be altered by irradiation at 420°C primarily by the formation of dislocation structure; very little change in precipitate structure could be identified and only alloy 6 was found to contain voids. These observations are compatible with very moderate increases in strength found for these conditions. The 12Cr alloys were found to have developed less dislocation structure but more precipitation. Fig. 7.3.6f shows a few examples of small dislocation loops in alloy 8. The loop structure should be differentiated from the α' precipitate structure in this figure. Fig. 69, also of alloy 8, shows another area in better contrast for a' observation. It can be noted that the α' precipitate density varies greatly from one subgrain to another. This observation was a general one and it is not yet understood what causes the non-uniformity; it may be an imaging effect but is more likely to be due to area-to-area variations. As shown in Fig. 7.3.6h, alloy 9 behaved similarly to alloy 8 except that no loops were found. The lack of loops may have been a result of the narrow martensitic lath structure obtained in this alloy. The small amount of hardening found in this condition suggests that the α' which formed in this alloy does not cause significant hardening, at least for a 420°C irradiation temperature.

520°C irradiated: Following irradiation at 520°C to 14.5 dpa, the alloys were found to be relatively unaffected by irradiation. No void swelling was observed and only a few examples of irradiation induced dislocation loops were found. In general, the precipitate structure was similar to the preirradiation structure. However, compositional analysis of extracted particles revealed that different phases than expected had developed. Examples of the microstructures are shown in Fig. 7.3.7. They have been selected to provide easy comparison with the preirradiation structure shown in Fig. 7.3.4. The bainitic alloys are shown in Figs. 7.3.7a-b. Of particular note is the retention of V_4C_3 cellular precipitate and a few examples of rod shaped precipitate in alloy 1 shown in Fig. 7.3.7a. Also an example of dislocation loop develoement in alloy 6 can be found in the center of Fig. 7.3.7e. Comparison of Figs. 7.3.4 and 7.3.7 demonstrate that the dislocation and subgrain structures have relaxed and that precipitate coarsening has occurred. These changes are

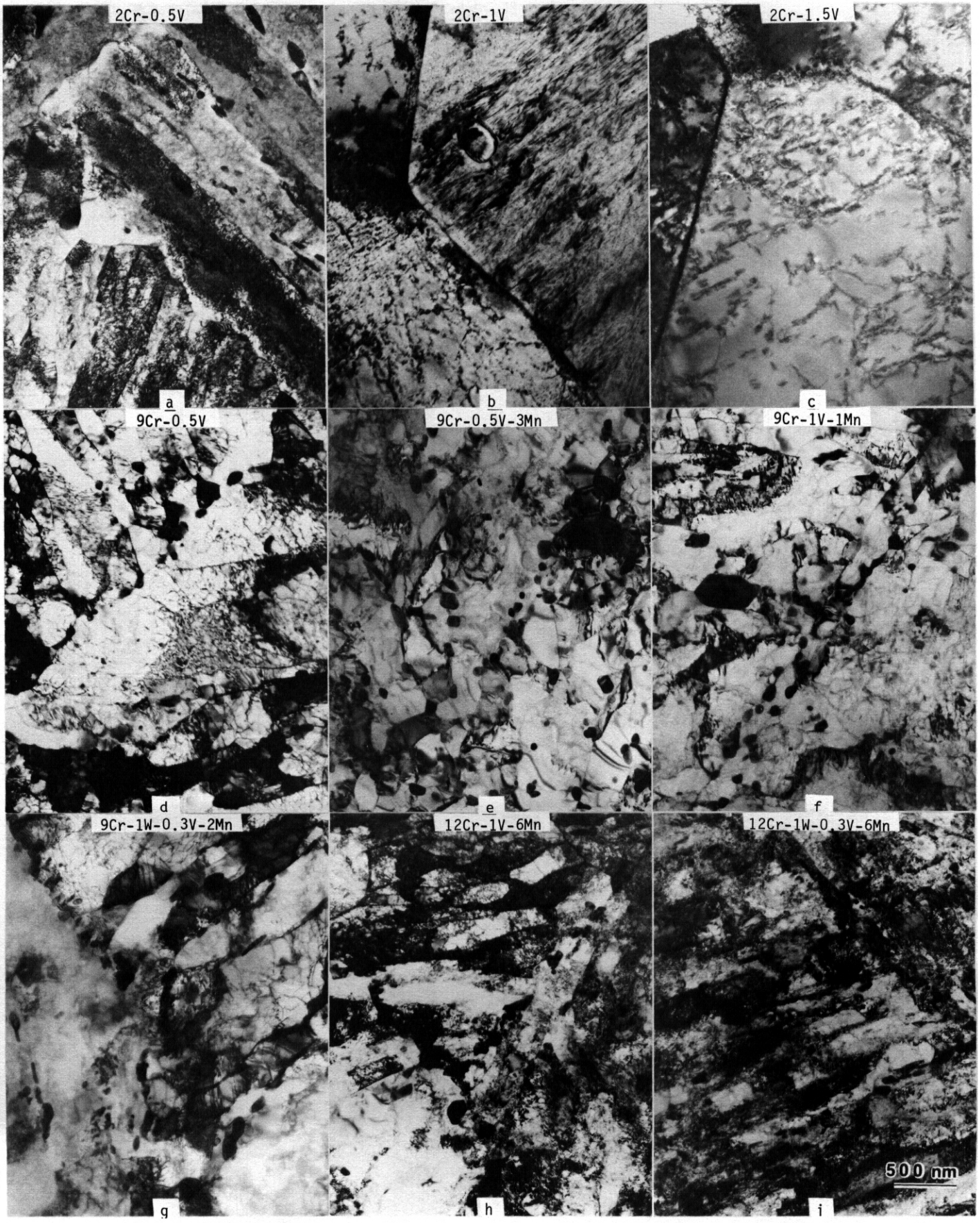

Fig. 7.3.4. Microstructures of the low activation **ferritic alloys following heat** treatment

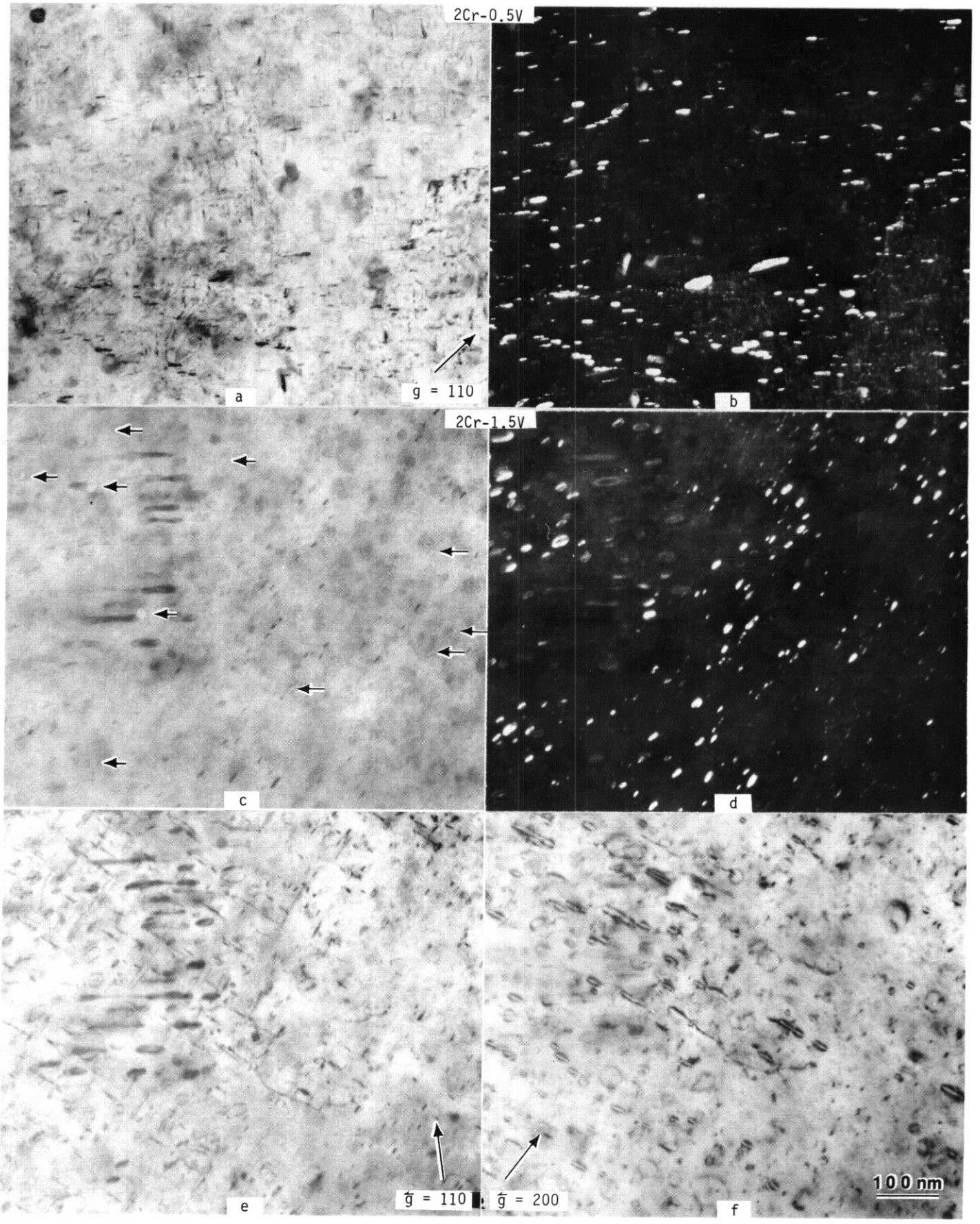

Fig. 7.3.5. Microstructures of the low activation bainitic alloys following irradiation at 420°C to 7.7 dpa.

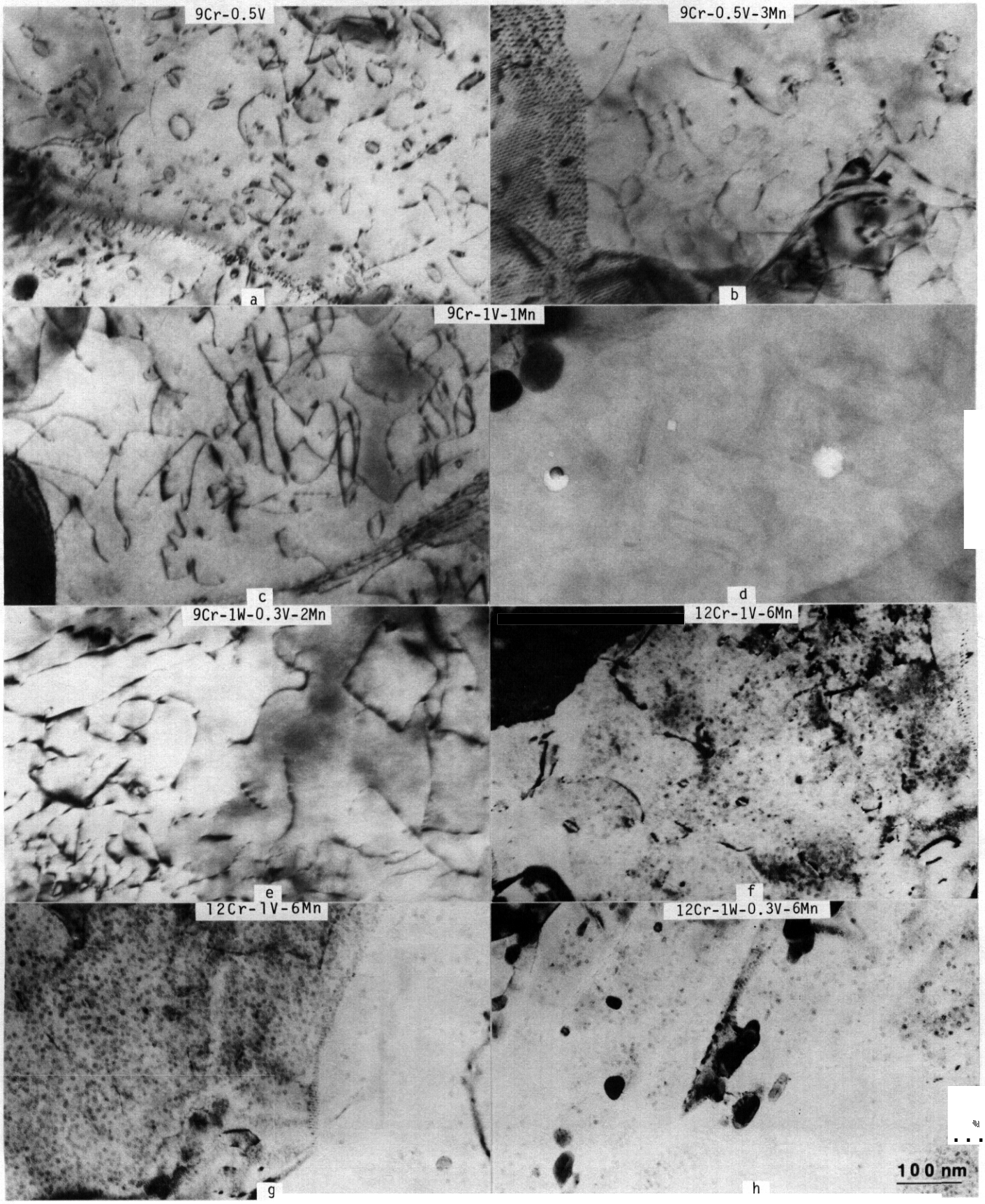

Fig. 7.3.6. Microstructures of the low activation martensitic alloys following irradiation at 420°C to 7.7 dpa.

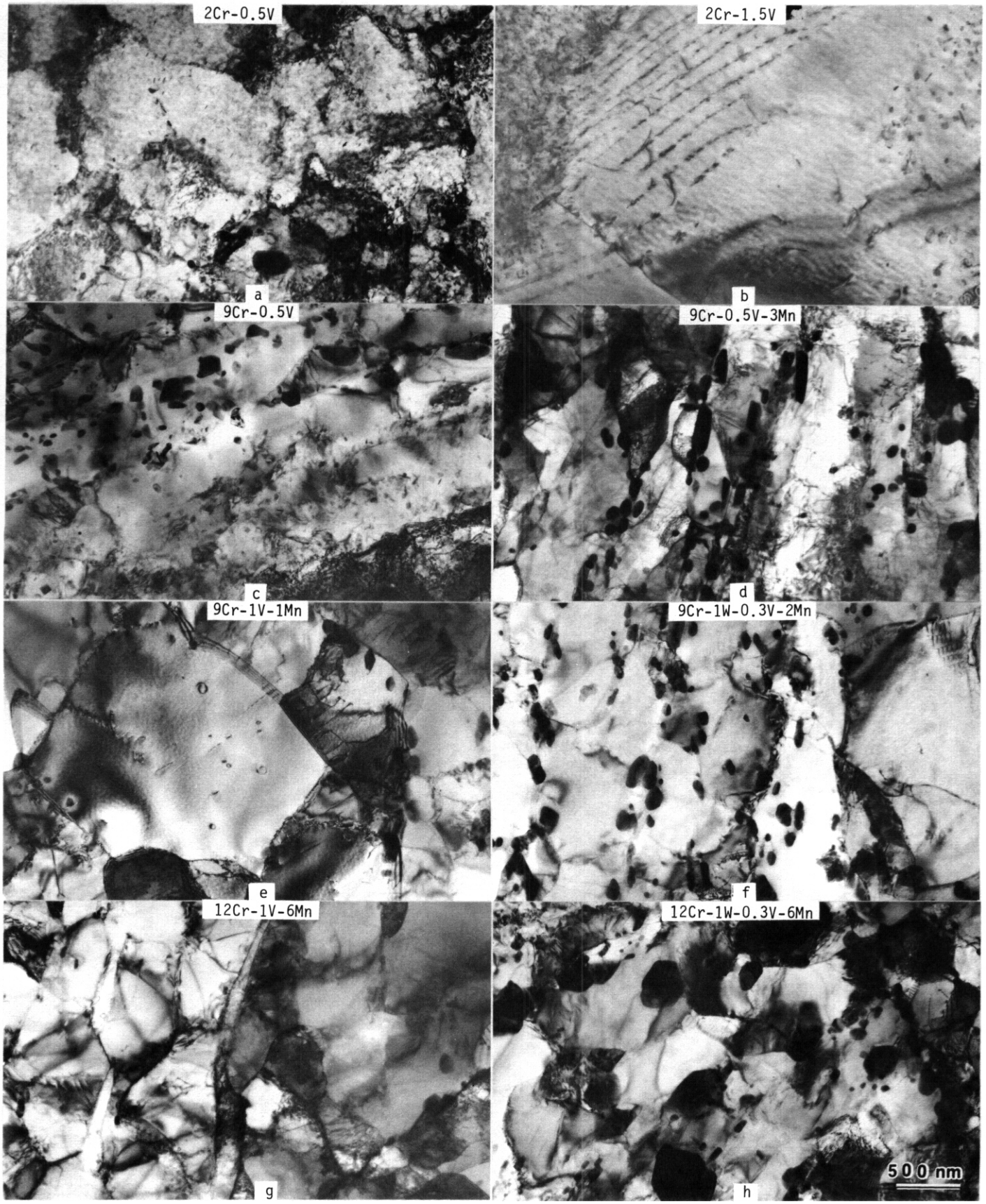

Fig. 7.3.7. Microstructures of the low activation ferritic alloys following irradiation at 520°C to 14.5 dpa.

undoubtably responsible for the reductions in strength found after irradiation at 585°C. The better strength properties found in alloy 9 can be traced to more limited subgrain growth and the formation of new small precipitate particles.

The results of compositional analysis of extracted precipitate particles from specimens irradiated at 520°C are given in Table 7.3.3. From Table 7.3.3, several conclusions can be drawn. Analysis of the bainitic alloys reveals that although the precipitates in alloy 3 were all V_4C_3, the majority of precipitates in alloy 1 were not. Therefore, the phase stability diagram for 700°C by Andrew et al, which is shown in Fig. 1 is not quite accurate for alloys held in-reactor for ∿3000 hrs at 520°C, the V_4C_3 phase field is shifted to higher vanadium content. Analysis of the martensitic alloys reveals comparable trends. For example, alloys 4, 5 and 6 contain some particles which are closer in composition to V_4C_3 or M_7C_3. Table 7.3.3 also provides an explanation for the higher strength observed in alloy 9 following irradiation at 520°C; an intermetallic phase rich in iron has formed and stabilized the microstructure.

Table 7.3.3. Metal compositions of extracted precipitated particles from specimens irradiated at 520°C to 14.5 dpa

Alloy	Metal Composition	Fe	Cr	Mn	V	W	#	Identification
1	2Cr-0.5V	3-4	16-18	--	74	--	2	V_4C_3
		41-56	41-52	--	5-9	--	10	M_7C_3?
		33-40	17-31	--	36-39	--	2	
3	2Cr-1.5V-0.3Mn	1-11	0-7	0-2	94-98	--	16	V_4C_3
4	9Cr-0.5V	35	59		6	--	1	$M_{23}C_6$
		1-68	2-8		25-32	--	2	
5	9Cr-1.3V-1Mn	19-31	57-74	0-3	2-16	--	12	$M_{23}C_6$
		10-22	24-25		54-66	--		V_4C_3?
6	9Cr-0.5V-2Mn	18-31	59-67	2-17	3-8	--	8	$M_{23}C$
		73-79	15-16	4	2-8	--	2	M_7C_3?
		57	38	2	4		1	
7	9Cr-0.3V-1W-2.5Mn	19-36	56-64	0-6	0-2	10-17	13	$M_{23}C_6$
8	12Cr-1V-6.5Mn	22-32	56-66	4-12	4-6	--	13	$M_{23}C_6$
9	12Cr-0.3V-1W-6.5Mn	19-29	56-67	2-4	0-2	11-13	4	$M_{23}C_6$
		53-60	19-27			9-13	10	Chi or Laves
9*		23-35	52-68	2-7	1-2	5-13	14	$M_{23}C_6$
		80-82	14-16	2-3	0-1	4	2	

*Irradiated at 420°C to 7.7 dpa.

7.3.4.5 Discussion

The results of this investigation demonstrate clearly that a low activation ferritic alloy should be possible if the tramp niobium content can be maintained below the acceptance limit of 3 ppm in commercial practice. The alloys in the present series have all been designed to eliminate other alloying elements which result in excessive long-term activity. In general, the alloys are weaker than presently available commercial alloy counterparts following irradiation at higher temperature. However, alloy 9 appears to be very promising because significant strength is retained even after irradiation at 585°C whereas no significant hardening is found following irradiation at 420°C.

These results also provide insight concerning optimum alloy design. For example, additions of vanadium for strength promote too much strengthening during irradiation at 420 C. It can be anticipated that the degree of hardening will be even greater at lower irradiation temperature and that ductility and ductile brittle transition temperature (DBTT) response will be very poor. In the 9Cr alloy range, the major concern is maintenance of high temperature strength. The present alloys are not yet optimized. Improvements could be made by increasing carbon, vanadium and tungsten alloying additions. However, such changes can be expected to degrade DBTT response. For the 12Cr alloy range, worthwhile improvements could be made to control prior austenitic grain size. Austenite grain growth is very rapid in alloy 9 and other strong carbide forming additions might be added. The manganese additions for austenite stabilization appear to be performing effectively without causing phase instability. However, it remains

to be demonstrated that the manganese additions have not degraded corrosion resistance. Finally, it is apparent that phase instability does occur in alloy 9 following irradiation at 520°C. Therefore, increasing the concentration of tungsten from 1 to 2 percent can be expected to cause more intermetallic precipitation which should degrade properties such as ductility and DBTT response. The extent of that degradation has yet to be determined.

7.3.5 Conclusions

Low activation ferritic alloys are feasible.

Fe-2-1/4C-V aloys are prone to carbide precipitation during irradiation at 420°C, which produces irradiation hardening.

Fe-2-1/4Cr-V and Fe-9Cr alloys are significantly weakened by irradiation at 585°C due to precipitate coarsening and dislocation recovery.

Fe-12Cr compositions appear to be the most interesting alloy class, showing negligible irradiation hardening at 420°C, and only moderate decrease in strength at 585°C.

7.3.6 References

1. R. W. Conn, et al., Report of the DOE Panel on Low Activation Material for Fusion Applications, UCLA/PPG-728, June 1983.

2. F. M. Mann, "Reduced Activation Calculations for the Starfire First Wall," Fusion Technology 6, (1984) p. 273.

3. G. J. Butterworth and O. N. Jarris, "Comparison of Transmutation and Activation Effects in Five Ferritic Alloys and AISI 316 Stainless Steel in a Fusion Neutron Spectrum," J. Nuc. Matl. 122 & 123, (1984), p. 982.

4. F. W. Wiffen and R. J. Santoro, "Control of Activation Levels to Simplify Waste Management of Fusion Reactor Ferritic Steel," DOE/ER-0045/11, (September 1983), p. 4.

5. R. L. Klueh and J. M. Vitek, "The Development of Ferritic Steels for Fast Induced-Radioactive Decay," DOE/ER-0045/12, (March 1984), p. 156.

6. S. W. K. Shaw and A. G. Quarrell, "The Formation of Carbides in Low-Carbon Chromium-Vanadium Steels at 700°C, JISI 185, (1957), p. 10.

7. K. W. Andrews, H. Hughes and D. J. Dyson, "Constitution Diagrams for Cr-Mo-V Steels," JISI, (1982), p. 337.

8. F. B. Pickering, Physical Metallurgy and the Design of Steels, [Applied Science Publishers Ltd, London, 19781, p. 166.

9. W. L. Bell, T. Lauritzen and S. Vaidyanathan, "Ferritics for Breeder Reactor In-Core Applications: A Survey of Alloys, Properties and Microstructures," Proceedings of Topical Conference on Ferritic Alloys for Use in Nuclear Energy Technologies, T. W. Davis and D. J. Michel, Eds., [The Metallurgical Society of AIME, Warrendale, PA, 19841, p. 113.

10. T. Lauritzen, W. L. Bell and S. Vaidyanathan, "Effects of Irradiation on the Mechanical Properties of Ferritic Alloys HT-9 and 2.25Cr-1Mo," ibid, p. 623.

11. J. M. Vitek and R. L. Klueh, "Variation of Postirradiation Strength Properties of Ferritic Steels with Irradiation Temperature," DOE/ER-0045/12, (March 1984), p. 110.

7.4 THE DEVELOPMENT OF FERRITIC STEELS FOR FAST INDUCED-RADIOACTIVITY DECAY

(R. L. Klueh and J. M. Vitek, Oak Ridge National Laboratory)

7.4.1 ADIP Tasks

ADIP Task I.A.5, Perform Fabrication Analysis, and I.C.1, Microstructural Stability.

7.4.2 Objectives

During the operation of a fusion reactor, the structural material of the first wall and blanket structure will become highly radioactive from activation by the high-energy fusion neutrons. A difficult radioactive waste problem will be involved in the disposal of this material after service. One way to minimize the disposal problem is the use of structural materials in which the induced radioactivity decays rather quickly to levels that allow for simplified disposal techniques. We are exploring the development of ferritic steels to meet this objective.

1.4.3 Summary

Tempering studies were conducted on eight heats of normalized chromium-tungsten steel that contained variations in the composition of chromium, tungsten, vanadium, and tantalum. Hardness measurements and optical metallographic observations were used to determine alloying effects on tempering resistance between 650 to 780°C. The results were compared to results for analogous chromium-molybdenum steels.

7.4.4 Progress and Status

7.4.4.1 Introduction

We have obtained eight heats of ferritic steel designed for fast induced-radioactivity decay (FIRD)[1] (the more rapid the decay of the induced radioactivity, the more easily are the reactor components disposed of after service). These FIRD steels have been patterned on the Cr-Mo steels that are of interest for fusion reactor applications — namely, 2 1/4 Cr-1 Mo, 9 Cr-1 MoVNb, and 12 Cr-1 MoVW steels. These Cr-Mo steels do not meet the FIRD requirements because of the presence of molybdenum in all three steels; the niobium in the 9 Cr-1 MoVNb steel and the nickel in the 12 Cr-1 MoVW steel are also above allowable levels.[1] As a replacement for molybdenum, tungsten was suggested;[3] tantalum was suggested as a possible replacement for niobium.[3]

Table 7.4.1 lists the nominal compositions of the major elements in the Cr-W steels being studied.[1] Alloy designations have been chosen to emphasize the major elements present in the steel. Similar designations are used for Cr-Mo steels. The compositions were chosen to develop information on the effect of chromium, tungsten, and vanadium on the properties of this class of steels. We attempted to vary the chromium from 2 1/4 to 12% and the tungsten from 0 to 2%. Where vanadium was added, 0.25% additions were made. An addition of 0.07% Ta was made to one heat of 9 Cr-2WV steel.

By varying the chemical composition and studying the effect of the various components on microstructural stability, strength, and fracture resistance in both the unirradiated and irradiated conditions, we hope to determine a best FIRD composition. Another objective is to obtain an understanding of the effect of variations in chromium, tungsten, and vanadium. Such information should prove useful not only for the FIRD steels, but should also help in understanding the Cr-Mo steels that are being investigated for fusion reactor applications.

Table 7.4.1. Chemical composition of fast induced-radioactivity decay (FIRD) ferritic steels

Alloy	Chemical composition[a,b] (wt %)						
	Cr	W	V	Ta	C	Mn	Si
2 1/4 CrV	2.36		0.25		0.11	0.40	0.17
2 1/4 Cr-1WV	2.30	0.93	0.25		0.10	0.34	0.13
2 1/4 Cr-2W	2.48	1.99	0.009		0.11	0.39	0.15
2 1/4 Cr-2WV	2.42	1.98	0.24		0.11	0.42	0.20
5 Cr-2WV	5.00	2.07	0.25		0.13	0.47	0.25
9 Cr-2WV	8.73	2.09	0.24		0.12	0.51	0.25
9 Cr-2 WVTa	8.72	2.09	0.23	0.075	0.10	0.43	0.23
12 Cr-2WV	11.49	2.12	0.23		0.10	0.46	0.24

[a] P = 0.014 to 0.016, S = 0.005 to 0.006, Ni ≤ 0.01, Mo ≤ 0.01, Nb < 0.01, Ti < 0.01, Co = 0.005 to 0.008, Cu = 0.02 to 0.03, Al = 0.02 to 0.03, B < 0.001.

[b] Balance iron.

7.4.4.2 Experimental Procedure

The eight heats of steel with compositions given in Table 7.4.1 were prepared by Combustion Engineering, Inc., Chattanooga, Tennessee. In addition to Cr, V, W, C, and Ta, which are considered of major importance in these steels and are given in Table 7.4.1, the concentrations of elements such as Mn, P, Si, S, etc.. were adjusted to levels typical of commercial practice. Detailed chemical compositions were previously published.[1]

All the steels were prepared as air-melted heats. which were then electroslag remelted (ESR) to obtain about 18 kg of usable material. The ESR ingot was hot rolled to 15.9- and 3.2-mm-thick plates. The 15.9-mm plate will be heat treated and used for making standard Charpy V-notch specimens to determine the impact behavior of these materials. Pieces of the 3.2-mm plate were further rolled into 0.25- and 0.76-mm sheet for transmission electron microscopy (TEM) and tensile specimen fabrication, respectively. Several TEM specimens from each heat were heat treated and shipped to HEDL for irradiation in the MOTA assembly in FFTF.

To determine the tempering characteristics of these new steels, a piece of each plate approximately 51 mm by 102 mm by 16 m was normalized. The 2 1/4 Cr-2W steel was annealed 1 h at 900°C and air cooled. All the other heats were annealed 1 h at 1050°C and air cooled. The Rockwell hardness of each heat was determined after this normalizing treatment. The normalized plates were sectioned into five approximately 19-mm by 51-mm by 16-mm specimens that were tempered for 2 h at different temperatures. Tempering temperatures were 600, 650, 700, 150, and 780°C. A piece of each specimen was sectioned for hardness determinations and metallography. Each of the shortened specimens was further tempered 8 h at the same temperature as it was ,tempered for 2 h. Hardness measurements were again made.

1.4.4.3 Results and Oiscussion

The steels were examined by optical microscopy after normalizing and after the 2-h tempering treatments. Microstructures varied according to the chemical composition. The 2 1/4 Cr alloys demonstrated the effect of the tungsten on hardenability. The 2 1/4 Cr alloy with 0.25% V (2 1/4 CrV) [Fig. 7.4.1(a)] and

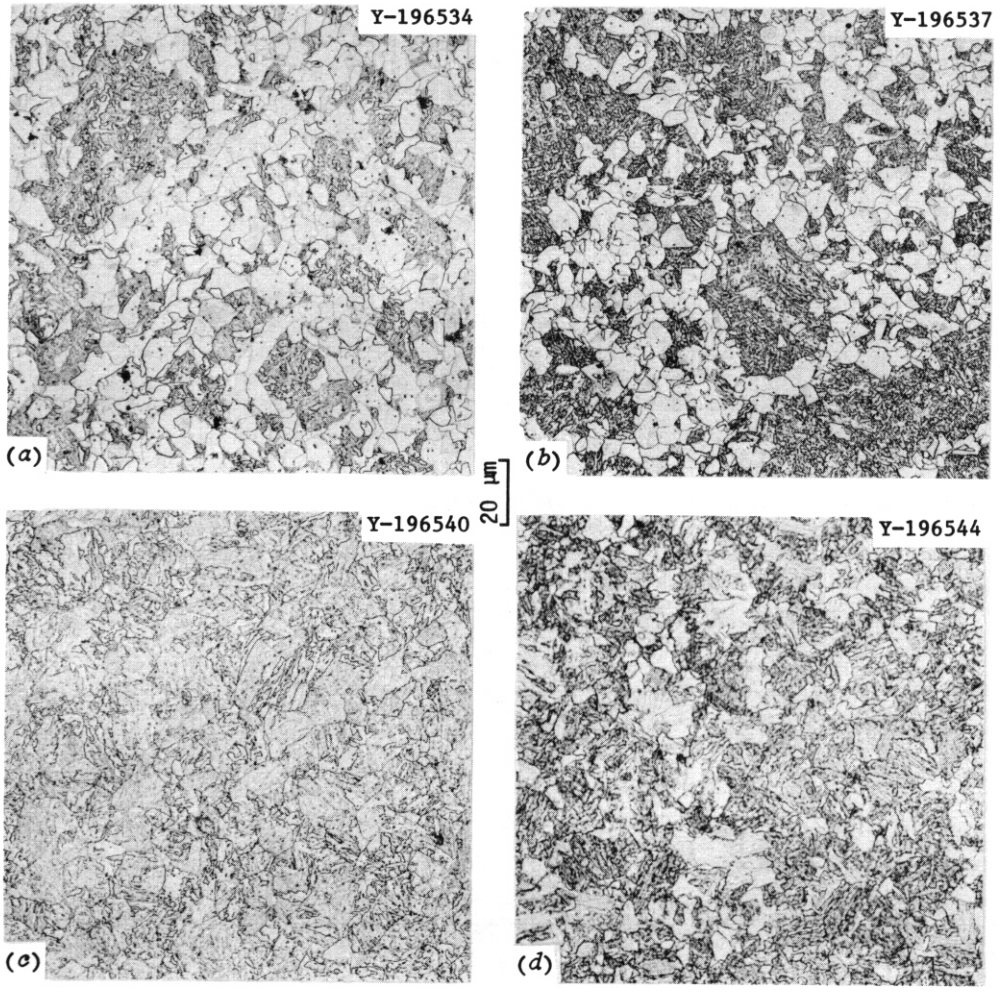

Fig. 1.4.1. Microstructures of normalized-and-tempered (a)2 1/4 CrV, (b) 2 1/4 Cr-1WV, (c) 2 1/4 Cr-2W, and (d) 2 1/4 Cr-2WV steels.

that with 1% W and 0.25% V (2 1/4 Cr-1WV) [Fig. 7.4.1(*b*)] had 30 to 35% polygonal ferrite, the remainder bainite. On the other hand, the 2 1/4 Cr-2W [Fig. 7.4.1(*c*)] and 2 1/4 Cr-2WV [Fig. 7.4.1(*d*)] steels contained much less polygonal ferrite. The 2 1/4 Cr-2W steel was almost entirely bainite (less than 1% ferrite); the 2 1/4 Cr-2WV steel contained 8 to 10% polygonal ferrite.

The appearance of ferrite in the 2 1/4 Cr-2WV steel was unexpected. A possible explanation is that the vanadium carbide present when the steel is austenitized does not completely dissolve. The lower concentration of dissolved carbon could then give a lower hardenability. This possibility had been considered prior to the heat treatment, and that is the reason the 1050°C austenitization temperature was used for the 2 1/4 Cr-2WV steel and only 900°C for the 2 1/4 Cr-2W steel. The 1050°C temperature was considered high enough to dissolve vanadium carbide.

The 5 Cr-2WV [Fig. 7.4.2(*a*)], 9 Cr-2WV [Fig. 7.4.2(*b*)], and 9 Cr-2WVTa [Fig. 7.4.2(*c*)] were 100% martensite. However, the 12 Cr-2WV steel [Fig. 7.4.2(*d*)] contained considerable amounts of delta-ferrite (approximately 26%). This alloy was patterned on the 12 Cr-1 MoVW steel that is being considered in the fusion reactor alloy development program, with tungsten substituted for the molybdenum. The appearance of the delta-ferrite indicates that insufficient amounts of austenite-stabilizing elements were present to form 100% austenite during the austenitization treatment. The 12 Cr-1 MoVW steel contains approximately 0.5% Ni and 0.2% C, both austenite-stabilizing elements, whereas the 12 Cr-2WV steel contains approximately 0.1% C and no nickel. Significant amounts of nickel will not be allowed in a FIRD steel,[2] and the carbon content was restricted to 0.1% to ensure good weldability.

As a substitute for nickel in FIRD steels, we have proposed the use of manganese.[3] According to the Schaeffler diagram,[4] an addition of 4 to 6% Mn would result in a nickel equivalent near that for 12 Cr-1 MoVW steel, which has been found to contain only small amounts of delta-ferrite, depending on the chemical composition (heats with essentially no delta-ferrite have been observed). To determine the effect of austenite-stabilizing additions, we have used the 12 Cr-2WV steel with 0.5% Mn as a base and melted and cast three alloys to which, respectively, 2.5% Mn, 5.5% Mn, and 0.1% C were added. These steels will be normalized and tempered, and metallographic observations and hardness measurements will be used to determine the effect of the manganese and carbon additions.

In addition to metallography, Rockwell hardness measurements were made on all heat-treated specimens. Figure 7.4.3 shows the hardness as a function of tempering temperature for the 2-h tempering treatment.

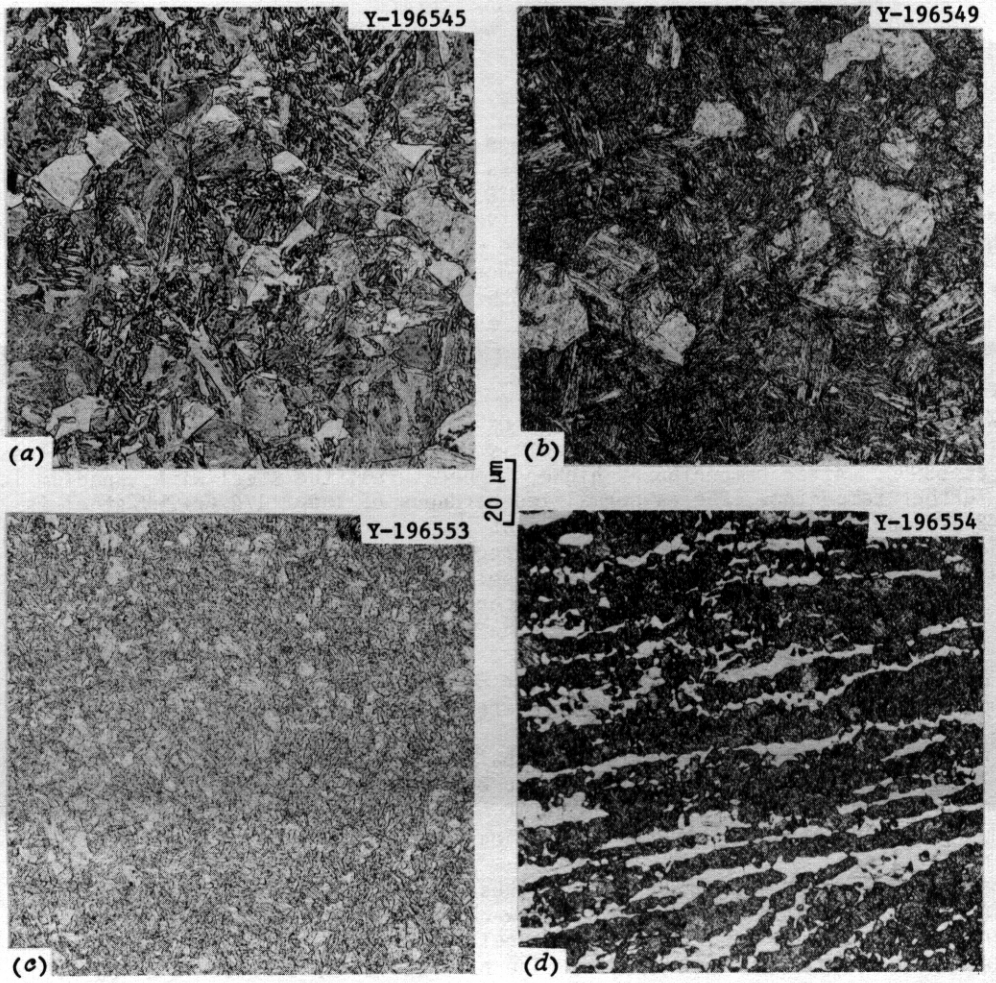

Fig. 7.4.2. Microstructures of normalized-and-tempered (*a*) 5 Cr-2WV, (*b*) 9 Cr-2WV, (*c*) 9 Cr-2WVTa, and (*d*) 12 Cr-2WV steels.

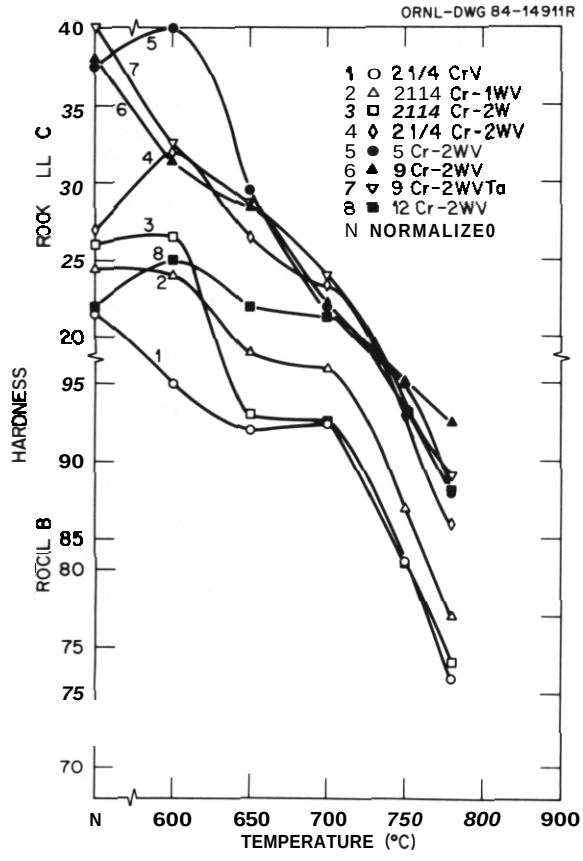

Fig. 7.4.3. Rockwell hardness plotted against tempering temperature for eight experimental steels. Steels were normalized (N) and pieces were tempered 2 h at 600. 650, 700, 750, and 780°C.

Also shown is the normalized hardness. Several of the heats displayed secondary hardening peaks after the initial 2-h heat treatment. Other heats may have developed such peaks during the 2-h temper at 650°C. All heats show a continuous decrease in hardness when tempered above 650°C.

An examination of the hardness results for the 2 1/4 Cr heats gives an indication of the effect of tungsten and vanadium. Although it is expected that vanadium carbide will play an important role in the strengthening of these steels, there is apparently a synergistic effect of tungsten and vanadium. The 2 1/4 CrV steel (without tungsten) is clearly the softest. On the other hand, the 2 1/4 Cr-2W steel (2% W but no vanadium) has a higher hardness after normalizing and after tempering at 650°C. but the hardness after tempering 2 h at 700°C approaches that of the 2 1/4 CrV steel. The greater hardness of the 2 114 Cr-2W steel for low tempering temperatures probably reflects the fact that this steel is entirely bainite, whereas the other steel contains significant amounts of polygonal ferrite.

The steels with 1 and 2% W and 0.25% V (2 1/4 Cr-1WV and 2 1/4 Cr-2WV) display increasing hardness with increasing tungsten content. The hardness of the 2 1/4 Cr-2W steel is harder than the 2 1/4 Cr-1WV steel as normalized and after tempering at 650°C. After tempering at higher temperatures, the steel with vanadium is harder and remains harder upon further tempering. The as-normalized hardness of the 2 1/4 Cr-2WV steel is similar to the hardness of the 2 1/4 Cr-2W steel despite the fact that it is not entirely bainite. The 2 1/4 Cr-2WV steel has the highest hardness of the 2 1/4 Cr steels, regardless of the tempering conditions. Tempering for 2 h at 650°C gives rise to a hardness peak for this steel, and for the highest tempering temperature, the hardness of this steel is similar to that of the high-chromium steels (Fig. 7.4.3).

The 5 Cr-2WV steel is interesting in that after 2 h at 650°C, the hardness approached the highest hardness achieved for these steels — similar to that for the as-normalized 9 Cr-2WVTa steel. The two 9 Cr steels show little difference, both having normalized hardnesses near R_C 40. after which the hardness decreases continuously with tempering temperature. In no case is there a large hardness difference for the two steels.

The 12 Cr-2WV steel contained approximately 26% delta-ferrite (balance martensite), and for that reason it would be expected to have a lower hardness than the steels made up entirely of martensite. This is the case in the normalized condition and after tempering at 650 and 700°C. However, the tempering resistance of the steel is such that when tempered at the highest temperatures the hardness approaches that of the 5 Cr and 9 Cr steels that contained no ferrite.

Because of the high hardenability of steel with 9 and 12% Cr, these steels are expected to transform completely from austenite to martensite when normalized. For the low-chromium steels, the lower hardenability makes an entirely martensitic or bainitic structure difficult to obtain. Furthermore, it is often difficult to differentiate between martensite and bainite. The hardness of martensite in a low-alloy

steel depends almost entirely on the carbon content, and for a steel with approximately 0.1% C, the R_C hardness of martensite is expected to be about 38 (ref. 5). This is very close to the hardness of the normalized 5% Cr steel (as well as the 9 Cr steels), indicating that the microstructure is primarily martensite. The acicular-appearing constituent in the 2 1/4 Cr steels (Fig. 7.4.1) is assumed to be bainite, which agrees with the normalized hardness. This is also expected from observations on 2 1/4 Cr-1 Mo steel, which should have a hardenability similar to the 2 1/4 Cr-2W steel. Extremely rapid cooling rates (e.g., a water quench of a thin section) are required to produce martensite.

In Fig. 7.4.4 the R_C and R_B values are plotted against the empirical Holloman-Jaffee tempering parameter, which attempts to account for the effect of both temperature and time. The parameter is defined as $T\ (20 + \log t)$, where T is the absolute temperature in Kelvin and t is tempering time in h. Hardnesses were determined for all the steels after tempering 2 h at the five tempering temperatures and after being further tempered 8 h at the same tempering temperature. The relative changes in hardness after a 10-h temper are similar to those observed in 2 h at the different tempering temperatures. After tempering to a parameter of $\sim 20 \times 10^3$, there was relatively little difference between the 2 1/4 Cr-2WV, the 5 Cr-2WV, the two 9 Cr steels, and the 12 Cr-2WV. For larger values of the parameter, the 2 1/4 Cr-2WV steel hardness decreases somewhat faster than that of the high-chromium steels.

No Cr-Mo steels were heat treated for comparison. However, some tempering data for 2 1/4 Cr-1 Mo steel obtained under similar circumstances[6] were available, and a tempering curve is shown in Fig. 7.4.4. It can be seen that 2 1/4 Cr-1 Mo steel appears to behave like the 2 1/4 Cr-2W steel at the higher tempering parameters. The 2 1/4 Cr-2WV steel has a somewhat greater tempering resistance than 2 1/4 Cr-1 Mo steel, probably because of the vanadium. The 2 1/4 Cr-1 Mo steel is used for elevated-temperature applications up to ~550°C.

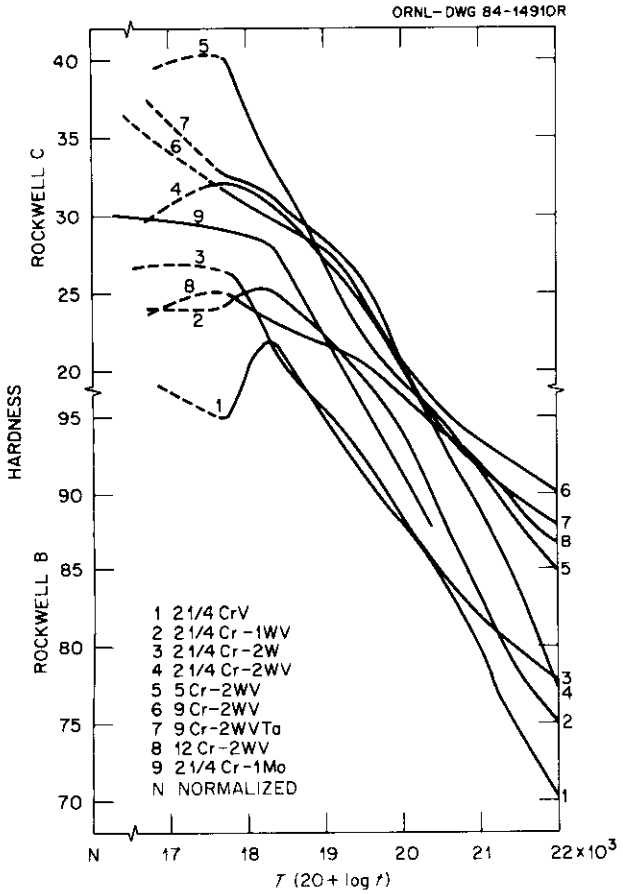

Fig. 7.4.4. Rockwell hardness plotted against the Holloman-Jaffee tempering parameter for eight experimental steels. Also shown is a curve for 2 1/4 Cr-1 Mo steel. The N denotes the hardness of the normalized, untempered steel.

Microhardness measurements were made on the metallography specimens of the steels tempered 2 h at each temperature and are plotted against tempering temperature in Fig. 7.4.5. As expected, the relative behavior is similar to that observed for Rockwell hardness measurements (Fig. 7.4.3).

The only tempering studies made on the 9 Cr-1 MoVNb and 12 Cr-1 MoVW steels were microhardness measurements on 0.76-mm-thick sheet. These steels were entirely martensite, and because martensite formation does not depend on cooling rate, a comparison can be made between the 9-Cr and 12-Cr Cr-Mo and Cr-W steels (Fig. 7.4.6). Both types of steel behaved similarly. The 12 Cr-2WV steel had a lower hardness at the lowest tempering parameter, but at long times it approached the values of the other steels. If the hardness values of the 2 1/4 Cr-2WV and 5Cr-2WV steels were plotted on this curve, they would also compare favorably.

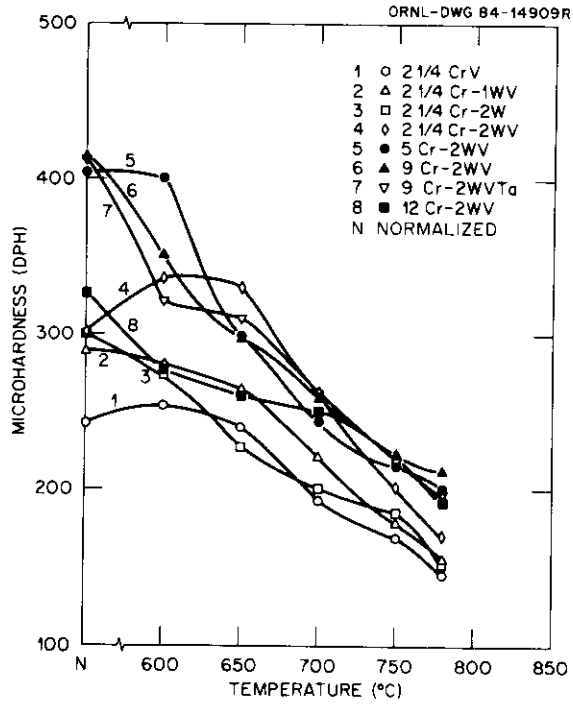

Fig. 7.4.5. Microhardness (DPH) plotted against the tempering temperature for eight experimental steels. Steels were normalized (N) and pieces were tempered 2 h at 600, 650, 700, 750, and 780°C.

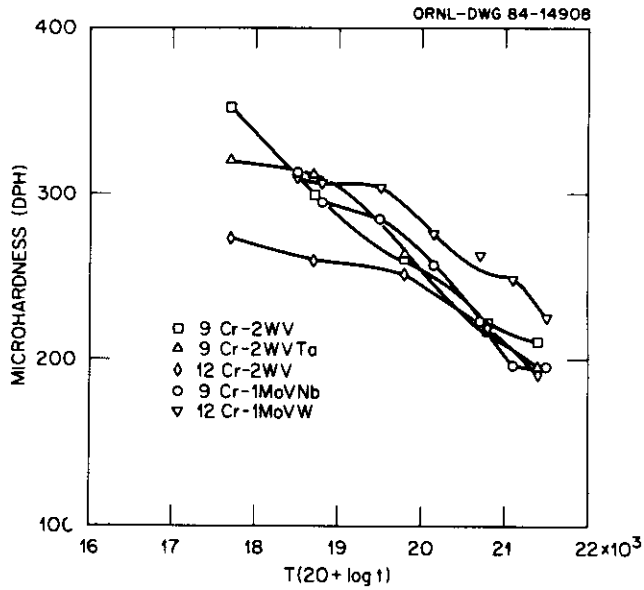

Fig. 7.4.6. Microhardness plotted against the Holloman-Jaffee tempering parameters for the 9 Cr-2WV, 9 Cr-2WVTa, 12 Cr-2W, 9 Cr-2 MoVNb, and 12 Cr-1 MoVW steels.

7.4.5 References

1. R. L. Klueh and J. M. Vitek, "The Development of Ferritic Steels for Fast Induced-Radioactivity Decay," pp. 156–57 in *ADIP Semiannu. Prog. Rep. March 31, 1984*, DOE/ER/0045/12, U.S. DOE, Office of Fusion Energy.

2. R. W. Conn et al., *Panel Report on Low Activation Materials for Fusion Applications*, UCLA Report PPG-728, University of California at Los Angeles, June 1983.

3. R. L. Klueh and E. E. Bloom, *Alloy Development for Fast Induced-Radioactivity Decay for Fusion Reactor Applications*, ORNL/TM-8944 (March 1984).

4. H. Schneider, "Investment Casting of High-Hot-Strength 12-Percent Chrome Steel," *Foundry Trade J.* 108, 563–64 (1960).

5. D. V. Doane, p. 369 in *Hardenability Concepts with Applications to Steel*, AIME, Warrendale, Pennsylvania, 1978.

6. R. L. Klueh, unpublished research.

7.5 RAPID SOLIDIFICATION OF CANDIDATE FERRITIC STEELS — J. Megusar, C. A. Craven, G. Kohse, J. Runkle+ O. K. Harling and N. J. Grant (Massachusetts Institute of Technology and Industrial Materials Technology*)

7.5.1 ADIP Task

The Department of Energy (DOE)/Office of Fusion Energy (OFE) has cited the need to investigate ferritic alloys under the ADIP program task, Ferritic Steels Development (Path E).

7.5.2 Objective

The objective of this work is to evaluate the potential of rapid solidification (RS) on the refinement of the microstructure and the potential for lowering irradiation-induced shifts in the ductile-to-brittle transition temperature (DBTT) in the Candidate Ferritic Steels.

7.5.3 Summary

HT-9 and 9Cr-1Mo steels were rapidly solidified by the liquid dynamic compaction (LDC) process and 2-1/4Cr-1Mo steel was prepared by the ultrasonic gas atomization (USGA) process. The consolidation was performed in the ferritic temperature range in order to minimize segregation. These alloys will be tested at ORNL using 1/3 CVN test specimens and the results will be compared with those for conventionally processed alloys.

7.5.4 Progress and Status

7.5.4.1 Introduction

Irradiation induced shifts in the ductile-to-brittle transition temperature and possible hydrogen embrittlement are currently considered major problems for the CTR application of ferritics. Improved ductility and lowering of the DBTT after irradiation are therefore major goals of our study to determine the potential of rapid solidification in the development of ferritic steels. Steel alloys HT-9, 9Cr-1Mo and 2-1/4Cr-1Mo, as candidate first wall ferritic materials, have been selected for this study.

Two different rapid solidification processing techniques have been used; namely, ultrasonic gas atomization and liquid dynamic compaction. A major aim of this research was to evaluate the feasibility of consolidating the rapidly solidified material in the ferritic temperature range. Processing in the ferritic (low temperature) state avoids coarsening of the austenitic grain structure and thereby minimizes interstitial element concentration and segregation on the austenitic grain boundaries, both of which should be beneficial to the observed DBTT. At the same time, the selected ferritic processing temperature appears to be adequate to permit production of a tempered martensite on cooling.

7.5.4.2 Experimental Procedure

Ultrasonic gas atomization[1] applies a Hartmann induced shock wave to produce a pulsed, high velocity gas jet to accomplish the atomization. Gas velocities, and therefore the velocity of the atomized liquid spheres, are generally less than about Mach 0.5 in conventional gas atomization processes, whereas they can exceed Mach 2 in ultrasonic gas atomization. USGA results in a finer and narrower powder size distribution, while achieving solidification rates up to 10^5 K sec^{-1}. This technique was used to atomize the 2-1/4Cr-1Mo steel.

Liquid dynamic compaction[2] was utilized to rapidly solidify the HT-9 and 9Cr-1Mo steels. In this technique, molten metal is atomized and delivered at relatively high velocity to achieve partially solidified fine droplets which are splat quenched initially against a high conductivity metallic substrate, and subsequently against the previously deposited layers of the quenched alloy. Solidification rates are as high as 10^3 K sec^{-1}, but secondary (solid state) cooling is relatively slower. Thicknesses of the order of the first wall thickness have been deposited in a one-step spray and collection operation directly from the melt. LDC was carried out while positioning a water cooled substrate at an appropriate distance below the gas atomization nozzle. The argon gas atomization pressure was 1.4 MPa and the melt superheat was about 100 K.

The preparation of the oxide dispersed 2-1/4Cr-1Mo steel and of pure iron has been initiated to develop a stable ferritic alloy for intermediate to high temperature service. The pure iron with OD strengthening would be low activation. The following steps describe the process[3]: (a) rapid solidification of the master alloy to prepare fine powders, plus selection of the size fraction smaller than about 50 μm; (b) attrition of the atomized powders to produce near micron thick flakes; and (c) ball milling of the flake metallic alloy with submicron oxide particles in the amounts of several volume percent in an inert atmosphere to obtain a uniform dispersion of the oxide phase.

7.5.4.3 Results and Discussion

2-1/4Cr-1Mo steel prepared by RS-PM

This steel grade was provided by Climax-Molybdenum Co. and had the following chemical composition (in wt%): 0.13 C, 0.48 Mn, 0.28 Si, 2.28 Cr, 1.02 Mo, 0.023 Al, 0.004 P, 0.0046 S, 148 ppm N. It was rapidly

solidified by the ultrasonic gas atomization technique. Powders finer than 53 μm were cold compacted, degassed by heating to approximately 700 K under vacuum, and extruded at 1023 K (in the ferritic temperature range) at an area reduction ratio of 10:1.

Figure 7.5.1 shows the microstructure of the as-solidified powders as observed in a scanning electron microscope. The structure is fully martensitic and the average grain size is 4 μm. The extrusion of powders at 1023 K resulted in a fully dense material, with a tempered martensite structure.

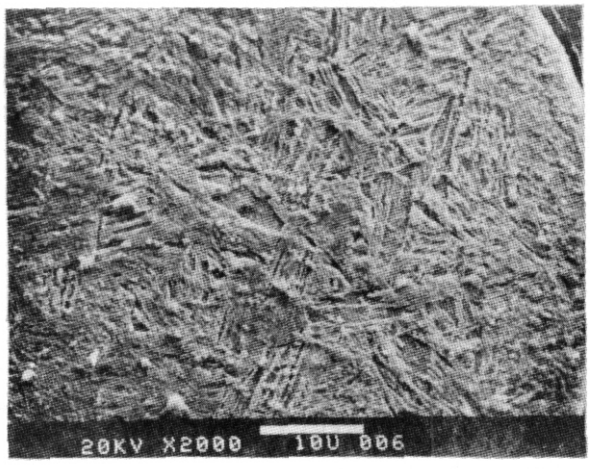

Fig. 7.5.1. SEM micrograph showing the microstructure of rapidly solidified powders of 2-1/4Cr-1Mo steel.

Microhardness measurements (Table 7.5.1) indicated a slight cold working effect during the high strain rate extrusion process. Importantly, the grain size remained unchanged after extrusion as well as after a standard austenitizing heat treatment (1173 K/ 1/2 h /AC).

Table 7.5.1. Vickers hardness and grain size of the extruded and heat treated RS-PM 2-1/4Cr-1Mo steel.[4]

Material Condition	Vickers Hardness 200 gm	Grain Size (Ferritic), μm
As-extruded (1023 K)	288	4
As-extruded + 973 K/1 h/AC	207	4
As-extruded + 1173 K/ 1/2 h/AC + 973 K/1 h/AC	239	5

The 2-1/4Cr-1Mo steel prepared by the RS-PM process was extremely resistant to grain coarsening. As shown in Table 7.5.2, the grain size can be kept below 10 μm after annealing at 1373 K. The morphological characteristics of the inhibited grain growth indicate strong pinning at prior particle boundaries. Similar observations have been made in other steel grades prepared by the RS-PM process.[5]

Table 7.5.2. Grain coarsening of the extruded RS-PM 2-1/4Cr-1Mo steel.[4]

Material Condition	Ferritic Grain Size, μm, after:		
	1273 K/1h	1373 K/1h	1453 K/1h
As-extruded (1023 K)	8	9	13

Room temperature tensile testing showed comparable strength and ductility values for the RS-PM extruded material and for the ingot material subjected to a standard heat treatment. However, examination of the fracture surfaces in a scanning electron microscope revealed isolated areas with poor particle bonding in the RS-PM product. Such an area is shown in Figure 6.5.2. This may be due to the following reasons: (a) the exposure of the powders to air prior to compaction, resulting in the formation of a thin oxide scale, and (b) the minimal reduction of area ratio of 10:1 during extrusion, which was not sufficient to break up the oxide films. To avoid powder bonding problems during low temperature extrusion, it is necessary to minimize any exposure to air, or to reduce the powders in dry hydrogen prior to cold compaction, or to increase the hot extrusion reduction ratio. In these first trials the powders were exposed to air prior to compaction; furthermore, we were limited to a maximum extrusion reduction of area ratio of 10:1 by the capacity of the available extrusion press.

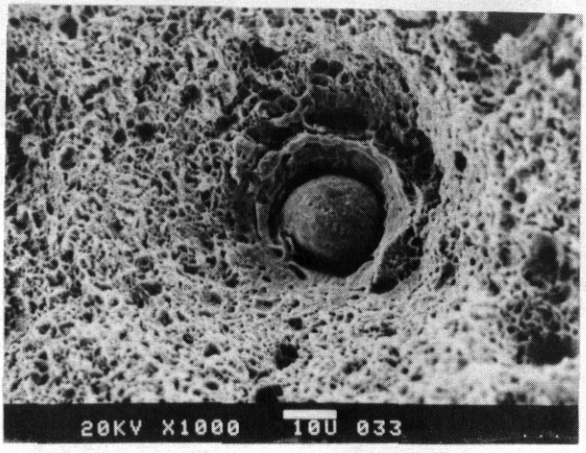

Fig. 7.5.2. Fracture surface (SEM) showing an isolated area with poor particle bonding in the extruded RS-PM 2-1/4Cr-1Mo steel.

As shown in Table 7.5.2, the 2-1/4Cr-1Mo steel prepared by the RS-PM technique is extremely resistant to coarsening; this makes it possible, if desired, to carry out the extrusion and/or austenitizing heat treatments at temperatures as high as 1373 K. Alternatively, higher extrusion ratios can readily be achieved with other extrusion facilities.

9Cr-1Mo and HT-9 steels prepared by liquid dynamic compaction

The LDC materials were approximately 95 percent dense. They were densified by hot isostatic pressing (HIP) (1040 K, 1 h, 207 MPa) and subsequently hot rolled at 1040 K to 25 and 50 percent reduction of thickness. The conditions of HIP and hot rolling were chosen in order to match the tempering conditions for these steel grades (1033 K/1 h/AC and 1053 K/2-1/2 h/AC for 9Cr-1Mo and HT-9, respectively) to optimize the mechanical properties. This would then, ideally, produce a fully dense material and at the same time result in a tempered martensitic structure. The results of consolidation are shown in Figures 7.5.3 and 7.5.4.

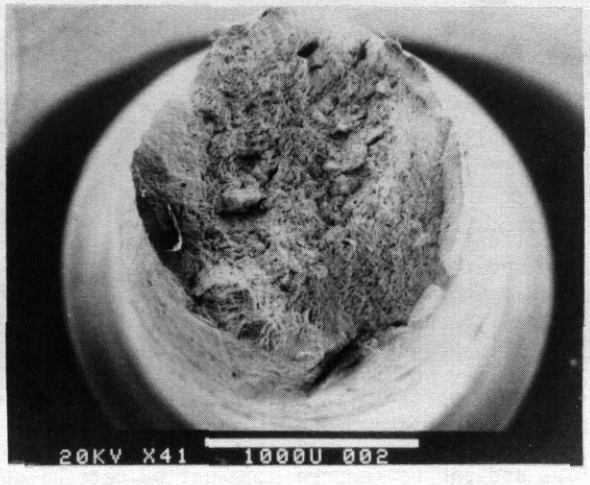

Fig. 7.5.3. Fracture surface (SEM) of HT-9 steel prepared by LDC process and densified by hot isostatic pressing (1040 K, 1 h, 207 MPa) and hot rolling at 1040 K to 25% reduction in thickness.

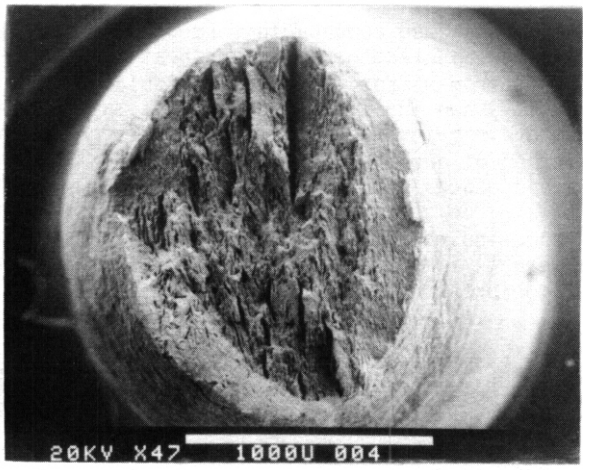

Fig. 7.5.4. Fracture surface (SEM) of HT-9 steel prepared by LDC process and densified by hot isostatic pressing (1040 K, 1 h, 207 MPa) and hot rolling at 1040 K to 50% reduction in thickness.

It appears from these trials that a practical consolidation process in the ferritic temperature range consists of hot isostatic pressing followed by 25 percent hot rolling (Fig. 7.5.3). When one exceeded 25 percent reduction of thickness during hot rolling, delamination problems were observed after 50 percent reduction of area, as shown in Fig. 7.5.4; however, the observed delaminations were not expected and their source will be studied.

The microstructure of hot rolled LOC 9Cr-1Mo alloy is shown in Fig. 7.5.5. It consists of a recovered structure, with a low dislocation density and with carbides precipitated on dislocations. The estimated carbide particle size is 10 nm. This microstructure is not appreciably different from that observed in melt spun ribbon after a 1 h tempering at 1033 K (see Fig. 7.5.6), despite the fact that the solidification rate may be several orders of magnitude higher after melt spinning as compared to that for the liquid dynamic compaction process.

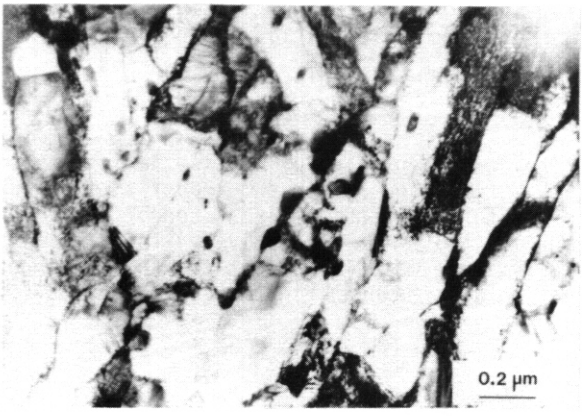

Fig. 7.5.5. TEM micrograph showing the microstructure of 9Cr-1Mo LDC steel hot rolled (50%) at 1033 K.[2]

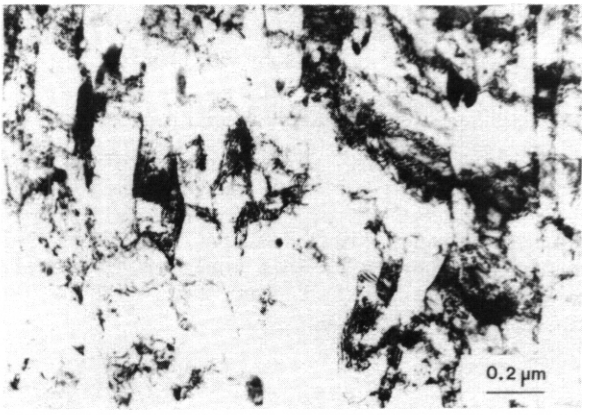

Fig. 7.5.6. TEM micrograph showing the microstructure of melt spun foil of 9Cr-1Mo steel annealed 1 h at 1033 K.[2]

The structure of the 9Cr-1Mo steel was fulled martensitic after spray deposition. On the other hand, the HT-9 alloy which was prepared under the same conditions showed a small fraction of the ferrite phase embedded in the martensitic matrix. This is shown in Figure 7.5.7. The size of the ferrite phase is approximately 5 - 10 μm and its lattice parameter, as determined by electron diffraction, is 0.285 nm. We attribute the presence of the ferritic phase to the higher Cr content in the HT-9 alloy. The structure was shown to be very stable and could not be redissolved during austenitizing treatments as high as 1323 K.

Figures 7.5.5 and 7.5.6 show an important feature which is a consequence of rapid solidification; namely, the refinement of second phase particles down to sizes of 0.1 μm and less. Such a fine size may render these particles less harmful as initiation sites in fracture processes. The grain size of the as-deposited material was 10 - 15 μm and can be reduced somewhat by careful control of the deposition parameters, i.e., distance between the atomization die and the water cooled substrate, the liquid metal superheat, the gas pressure and the thickness of the deposited material.

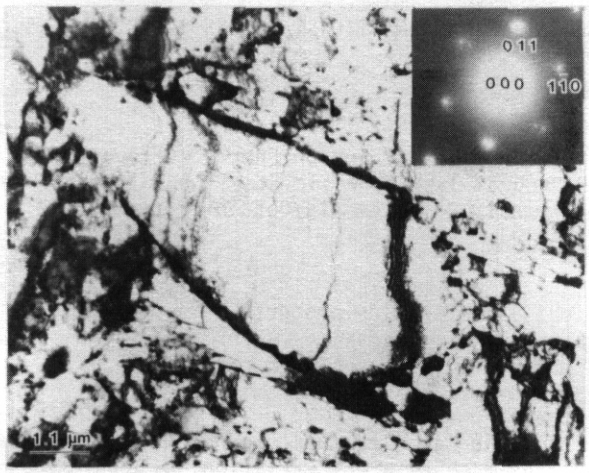

Fig. 7.5.7. TEM micrograph showing the ferrite phase (center of the micrograph) in HT-9 steel prepared by the LDC process.

Suppression of interstitial and substitutional segregation during liquid dynamic compaction and subsequent consolidation in the ferritic temperature range should be beneficial to the observed toughness and ductile-to-brittle transition temperature. These properties depend equally, however, on the morphology of the lath martensite, i.e., the lath spacing and the size of the martensite packets (dimension over which adjacent martensite laths have a common crystallographic orientation). As shown in Figures 7.5.3 and 7.5.4, the obtained lath spacing is ~ 0.1 - 0.2 μm and the martensite packet size (or its equivalent, the grain size) is about 10 μm in the spray deposited and tempered steel. Since these microstructural features appear to be inherent to the LDC process followed by the consolidation at a standard tempering temperature, we are studying different heat treatments which may allow further microstructural refinements. They include[6]: (a) tempering within the ($\alpha + \gamma$) field to precipitate islands of austenite along the lath boundaries of the initial martensite (these austenite islands refine the effective grain size by disturbing the alignment of the adjacent martensite lath); and (b) rapid thermal cycling treatments, which utilize successive thermal cycles to above the austenite reversion temperature to force the alloy through repeated martensitic transformations. It produces a martensitic structure with a small effective grain size.

Processing techniques which include liquid dynamic compaction, subsequent consolidation in the ferritic temperature range, and possible additional heat treatments appear to be suitable for the production of the first wall components. First wall design limits include thermal stresses and pressure stresses. A curved wall has been proposed to reduce the stresses in the coolant, and wall thicknesses of the order of 0.2 - 0.6 cm are being considered for design stress levels of 69 - 138 MPa. The first wall of a specified thickness and shape can be prepared directly from the melt. While a flat water cooled copper substrate was used in the present work, it can be replaced by a rotating tubular substrate to deposit tubular sections.

7.5.5 Future Work

Specimens of the 9Cr-1Mo and HT-9 alloys which were prepared by the LDC process and subsequently hot isostatically pressed and 25 percent hot rolled in the ferritic temperature range will be tested at ORNL using 1/3 CVN test specimens. The results will be compared with those for conventionally processed 9Cr-1Mo and HT-9 steels. Furthermore, different heat treatments which allow for further refinement of the martensite morphology will be evaluated; they include tempering within the ($\alpha + \gamma$) field and rapid thermal cycling. We have also initiated the production of OD dispersion strengthened 2-1/4Cr,1Mo and pure ferritic alloys. The OD iron would be low activation. Irradiation testing will be carried out on the optimized ferritic alloys.

7.5.6 References

1. V. Anand, A. J. Kaufman and N. J. Grant, "Rapid Solidification of a Modified 7075 Aluminum Alloy by Ultrasonic Gas Atomization," *Proc. 2nd Int. Conf. on RSP, March 23-26, 1980,* Reston, VA (Baton Rouge Clairtor's Publishing Division).

2. J. Megusar, E. Lavernia, P. Domalavage, O. K. Harling and N. J. Grant, "Structures and Properties of Rapidly Solidified 9Cr-1Mo Steel," *J. Nucl. Mater.* 122 & 123, 789-798 (1984).

3. A. I. Ibrahim, J. Megusar and N. J. Grant, "Mechanical Properties and Structure of Y_2O_3 Dispersion stabilized, Rapidly Solidified 316 Type Stainless Steel," pp. 239-249 in *ADIP Semiannu. Progr. Rep. Mar. 31, 1982,* DOE/ER-0045/8, U.S. DOE, Office of Fusion Energy.

4. C. A. Craven, B.Sc. Thesis, M.I.T., 1984.

5. G. B. Olson, M. Cohen and G. J. Yurek, "Structure-Property Relationships in RSP Steels," *Proc. 3rd Int. Conf. on RSP, Dec. 6-8, 1982,* Gaithersburg, MD (Baton Rouge Clairtor's Publishing Division).

6. H. J. Kim, Y. H. Kim and J. W. Morris, Jr., "Microstructure Refinement in Martensitic Fe-12Ni-0.25 Ti: Thermal Mechanisms of Grain and Packet Refinement," to be published.

7.6 POISSON'S RATIO MEASUREMENTS FOR MARTENSITIC STAINLESS STEELS - D. S. Gelles (Westinghouse Hanford Company)

7.6.1 ADIP Task

The Department of Energy (DOE) Office of Fusion Energy (OFE) has cited the need to investigate ferritic alloys under the ADIP Program Task Ferritic Steels Development (Path E). The task involved is akin to I.A.l Define Material Property Requirements/Obtain Property Data.

7.6.2 Objectives

The objective of this effort is to provide property data on candidate alloys for use in concept evaluation, design, safety analysis and performance/verification studies of various fusion energy systems.

7.6.3 Summary

Poisson's ratio measurements using an ultrasonic technique over the temperature range room temperature to 600°C are reported for HT-9. As much as a 0.1 variation is found as a result of specimen orientation. However, based on comparisons from the literature, it is concluded that such variations are common and are not due to orientation effects. Further measurements will be needed before a design equation for the MHFES can be generated.

7.6.4 Progress and Status

7.6.4.1 Introduction

As a part of an ongoing effort to provide physical property data for Path E alloys intended for inclusion in the Materials Handbook for Fusion Energy Systems,' measurements were performed on specimens of HT-9 in order to provide values for Poisson's Ratio (ν) as a function of temperature from room temperature to 600°C. Analysis of those results and for similar steels taken from the literature has now been completed. Based on that analysis, it is apparent that a design equation for Poisson's ratio with sufficiently small uncertainty to be meaningful cannot be made. Therefore, rather than define a design equation for Poisson's ratio for HT-9, the data base will be presented in this report in order to provide the available guidance to the fusion reactor design community.

7.6.4.2 Experimental Procedure

No published results for Poisson's ratio for HT-9 were available. Therefore, L. R. Bunnell of Battelle Pacific Northwest Laboratories, Richland, Washington was contracted to make measurements. Two specimens, both 0.3175 cm in diameter x 3.5 cm in length, were taken from the same bar of HT-9 heat 91354 and were given the same heat treatment, 1038°C/0.5 hourslcw cooled + 760°C/2.5 hours/air cooled. One specimen was of longitudinal orientation and the second was transverse orientation. The specimens were spotwelded to the end of a 0.159 in diameter wave guide, the other end of which was inserted into a high frequency transducer driven by a suitable pusher. This wave guide was a special one which works to generate both extensional and torsional waves. The elastic waves were partially reflected at the weld joint and fully reflected at the sample end, so that the received signal was a series of waves caused by repeated reflections in the sample. This signal was displayed on an oscilloscope, along with the output from a time-mark generator. A Polaroid camera was used to photograph both traces, and the distance between successive baseline intersections was measured with a caliper. The corresponding time was calculated by comparison with the distance for the 10 microsecond time-mark generator pulses. Transit time was calculated as follows:

$$\text{Transit time, seconds} = \text{Measured distance, inches} \times \frac{\text{10 microseconds}}{\text{Distance between peaks, inches}}$$

and

$$\text{Velocity} = \frac{\text{2 x sample length, inches}}{\text{Transit time, seconds}}$$

By inserting the wave guide and sample into a furnace, it was possible to measure the velocities as a function of temperature. The furnace was argon purged to retard sample oxidation. Temperatures were measured using a calibrated Type S thermocouples. Considering all measurement errors, the velocities were believed to be known to ±3% and temperatures to ±5°C. Poisson's ratio was calculated from velocity values, according to the relationship,

$$\nu = \frac{V_E^2}{2V_T^2} - 1$$

where V_E = extensional wave velocity

V_T = torsional wave velocity

As a result of concern regarding interpretation of the L. R. Bunnell data, assistance was requested and obtained from H. M. Ledbetter of the National Bureau of Standards, Boulder, Co. He provided a room temperature measurement of an HT-9 block specimen 1.4 cm x 1.4 cm x 1.7 cm which had been cut from the same bar of heat 91354 and had been given the same heat treatment. An ultrasonic pulse echo overlap technique at sequences between 5 and 12 MHz was used. The error was estimated to be one percent or less.

7.6.4.3 Results

The results of Poisson's ratio measurements on HT-9 rod specimens as a function of temperature are given in Table 7.6.1. Values range between 0.25 and 0.41 with the specimen of lonqitudinal orientation giving consistantly lower values. The unusually high value of 0.407 could possibly be incorrect but a check did not reveal the source of error.

The result of Poisson's ratio measurements on the HT-9 block specimen was intermediate in value, 0.283. This result along with modulus measurements, is given in Table 7.6.2.

Table 7.6.1. Results of Poisson's Ratio Measurements on HT-9 rod specimens, heat 91354 performed by L. R. Bunnell

Sample HT-9 # Longitudinal					
Temperature °C	25"	300"	400°	500"	600"
Extensional Velocity, in/sec	212,000	205,000	198,000	193,000	185,000
Torsional Velocity, in/sec	134,000	128,000	124,000	121,000	116,000
Poisson's Ratio, no units	.252	.283	.275	.272	.272
Sample HT-9 #2 Transverse					
Temoerature. °C	25"	300"	400°	500"	600"
Extensional 'Velocity, in/sec	212,000	205,000	203,000	196,000	188,000
Torsional Velocity, in/sec	129,000	125,000	121,000	119,000	114,000
Poisson's Ratio, no units	.350	.345	.407	.356	.360

Table 7.6.2. The result of Poisson's Ratio Measurements on an HT-9 block specimen, heat 91354 at room temperature performed by NUS

Mass density:	P (g/Cm^3)	7.779
Young's Modulus:	E (GPa)	2.182
Bulk Modulus:	B (GPa)	1.672
Shear Modulus:	G (GPa)	0.851
Poisson's ratio:	ν	0.783

7.6.4.4 Discussion

The literature contains several measurements of Poisson's ratio in martensitic stainless steels which are more divergent than those reported in Tables 7.6.1 and 7.6.2. ?he purpose of this section is to compare these results in order to emphasize the wide range of values which has been reported.

Figure 7.6.1 presents results of measurements of Poisson's ratio for a number of martensitic stainless steels.[2-5] The compositions for the various steels are given in Table 7.6.3. From Fiqure 7.6.1 it can be shown that Poisson's ratio measurements on martensitic steel vary from approximately 0.15 to 0.40 and that the extreme values were obtained by the same experimenter using the same technique on different steels. Different batches of the same steel, 9Cr-1Mo, measured by different techniques gave Poisson's ratio values which varied by as much as 0.10. Also, two identical specimens of 9Cr-1Mo as measured by Garofalo, gave values which varied by as much as 0.10. Similar variations were reported for pure iron although the variations only covered the range 0.23 to 0.42.' Therefore, variations between two specimens of HT-9 taken from the same bar stock and having different orientations may not be unusual.

However, it is not yet clear that differences between HT-9 rod specimens of different orientations are a result of specimen anisotropy. The major effect of orientation can be expected to be due to crystallographic texture developed during bar fabrication. However, if a texture were produced, the heat treatment process, which involves nucleation and growth both of austentic and ferrite, can be expected to destroy such texture. Some confirmation of this expectation is provided by the NRS result where it was found that, along the rod axis, the shear-wave velocity is polarization-direction independent. Also, the scale of the microstructure is very fine and appears isotopic. Therefore, it is anticipated that the larqe variations in results for the HT-9 rod specimens were not due to anisotrophy. More likely, they arise from difficulties in measuring shear wave velocities. The rod specimens were only 0.3175 cm in diameter and ultrasonic wave reflections from surfaces could well have affected shear wave measurements.

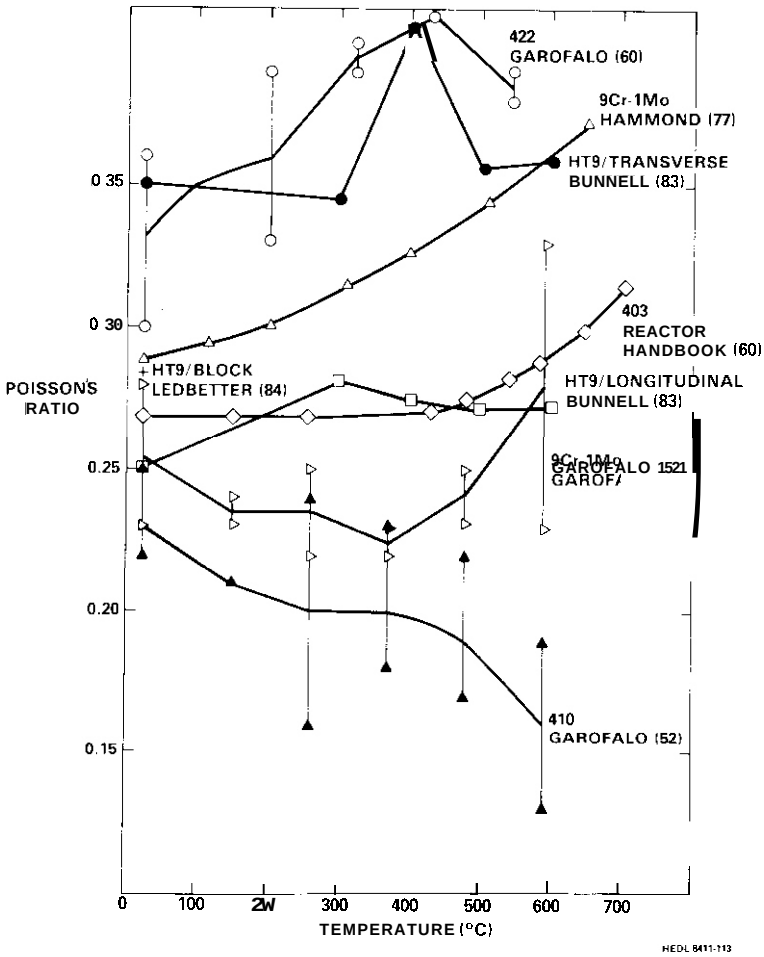

Fig. 7.6.1. Poisson's ratio measurements for martinsitic stainless steels.

Table 7.6.3. Compositions of the alloys for which Poisson's ratio measurements are available

Allay	Composition (W/o)										Reference
	Cr	C	Mo	Mn	Si	V	N	P	S	Ni	
AISI 422*	12.0	0.25	1.0	0.60	0.60	0.30	0.03	-		-	2
AISI 410	12.08	0.08	0.03	0.47	0.22		-	0.011	0.016	0.14	3
9Cr-1Mo	9.57	0.10	1.10	0.44	0.43	-	-	0.008	0.019	0.07	3
9Cr-1Mo*	9.0	<0.15	1.0	<0.45	<1.0			<0.03	<0.03		4
AISI 403	12.0	<0.15			<0.5						5
HT-9/91354	17.2	0.20	1.0	n.4	0.2	0.4	0.004	0.008	0.003	0.5	

*nominal composition

It *is* apparent that a need exists for further measurements of Poisson's ratio in martensitic stainless steels before a satisfactory design equation can he developed. Such an effort may well lend itself to a university project.

7.6.5 Conclusions

Poisson's ratio measurements are reported for HT-9 and comparison is made with similar martensitic stainless steels. The scatter in the reported data is sufficiently large hoth for HT-9 and for martensitic stainless steels so that a design equation for the MHFES cannot he prepared at this time with sufficiently small uncertainty limits to be meaningful.

7.6.6 Acknowledgements

We wish to thank Hassel M. Ledbetter and staff at the National Bureau of Standards, Boulder, Colorado for assistance with room temperature elastic modulus measurements on HT-9 and interpretation of results.

7.6.7 References

1. J. W. Oavis, "Materials Handbook for *Fusion* Energy Systems," DOE/ER-0045/12 (Period ending 3/31/84) p 2.
2. F. Garofalo, "Temperature Dependence of the Elastic Module of Several Stainless Steels," ASTM Proc V60 (1969) p 738.
3. F. Garofalo, P. R. Malenock and G. V. Smith, "The Influence of Temperature on the Elastic Constants of Some Commercial Steels," Symposium on Determination of Elastic Constants held June 25, 1952 in New York, NY, ASTM STP 129, p 10.
4. J. P. Hammond, ORNL, "Dynamic Elastic Constants of 9Cr-1Mo Steel," by J. P. Hammond and M. W. Moyer, (1977) private communication.
5. Reactor Handbook VI, 2nd edition, C. R. Tipton, Jr., editor, [Interscience Publishers, Inc., New York, 1960] p 580.
6. H. M. Ledbetter and R. P. Reed, J Phys Chem Ref. Data V2 (1973) p 608.

7.7 EFFECTS OF IRRADIATION ON THE FRACTURE TOUGHNESS OF HT-9 - F. H. Huang (Westinghouse Hanford Company)

7.7.1 ADIP Task

The Department of Energy/Office of Fusion Energy (DOE/OFE) has cited the need to investigate ferritic alloys under the ADIP program task Ferritic Steels Development (Path E).

7.7.2 objective

The objective of this work is to evaluate the effects of neutron irradiation on the fracture toughness of HT-9 irradiated to fluences of 2.7 x 10^{22} n/cm^2 and 5.5 x 10^{22} n/cm^2. The goal is to characterize the fracture behavior of fusion first wall ferritic materials.

7.7.3 *Summary*

Compact tension specimens of HT-9 irradiated at 390, 450 and 500°C were tested at 90, 205 and 450°C. Test results showed that both test and irradiation temperatures have insignificant effects on the fracture toughness of HT-9. However, the tearing modulus increases substantially with increasing irradiation temperature. In addition, the toughness of HT-9 at 205°C where a toughness trough was observed for unirradiated HT-9 remained unchanged after irradiation to a fluence of 5.5 x 10^{22} n/cm^2.

7.7.4 Introduction

Some of the fracture toughness specimens from the AD-2 experiment irradiated at 390°C were tested at 205°C and results reported! In this report specimens irradiated at various temperatures were tested at elevated temperatures. Specimens were irradiated to fluences of 2.7 x 10^{22} n/cm^2 and 5.5 x 10^{22} n/cm^2 (E > 0.1 MeV). Their grain sizes were varied by austenitizing and tempering treatments.

HT-9 has been seleted as a candidate material for component applications in both fusion and breeder reactors because of low swelling, acceptable corrosion resistance and high thermal stress resistance. However, it is known that the ductile-brittle transition temperature (DBTT) of HT-9 may be increased by irradiation, temper embrittlement and thermal aging with the possibility that the DBTT increases to be as high as the reactor operating temperature. Fracture toughness test were thus performed to investigate the effect of irradiation on the fracture behavior of the material.

As small specimens of HT-9 exhibits some plastic deformation prior to fracture, linear elastic fracture mechanics which assumes that the material behavior is linear elastic is not applicable for measuring the fracture toughness of the material. Elastic-plastic fracture mechanics has been developed to deal with the ductile fracture with extensive yielding. Results were therefore analyzed using the J-integral approach.

7.7.5 Progress and Status

7.7.5.1 Experimental Procedure

The configuration of the 2.54 mm thick circular compact tension specimens and the test procedures for in-cell fracture toughness using electropotential techniques were given in Reference 2. The irradiated specimens have two different grain sizes: ASTM 8-9 and ASTM 3-4.

Since the specimen is small, ASTM Standard E813 was adopted to measure the fracture toughness of the irradiated material. The specimen was first precracked using the electropotential techniques to monitor the precrack length. The final crack extensions measured from the heat tinted fracture surfaces of the specimens and the corresponding electropotential outputs were used to establish an empirical calibration curve. Continuous crack extensions were calculated from this calibration curve.

7.7.5.2 Results and Discussion

J-Aa curves were obtained from the value of J calculated from load versus displacement records and continuous crack extensions. The initial portion of J-Aa curve was fitted to the blunting line ($J=2\sigma_f \Delta a$) to determine the value of J_{IC}, critical fracture toughness. Results are given in Table 1 where the tearing modules (T), test and irradiation conditions are also listed.

The test temperature dependence of fracture properties of HT-9 irradiated at 390 and 500°C is shown in Figures 7.7.1 and 7.7.2. As can be seen from these figures, test temperature has little effect on the fracture behavior of the material under the irradiation conditions. During irradiation the material was subjected not only neutron flux but also thermal aging. The effects of irradiation temperature and fluence on the fracture behavior are shown in Figures 7.7.3 to 7.7.6. In these figures, results obtained from specimens of two different grain sizes are plotted. It is clear that the toughness with ASTM grain size of 8-9 is somewhat higher than that with an ASTM grain size of 3-4, although this is contrary to what was observed for the tearing modulus.

The mechanical properties of the chromium-molydenum series of steels are controlled by the microstructure which can be altered by the heat treatment used, certain testing or service conditions. During tempering and subsequent services, various precipitates are formed in HT-9. They can pin dislocations and stabilize the dislocation structure with the result of increasing the strength. However, the increase in

Table 7.7.1. Fracture toughness test results of irradiated HT-9

Irradiation Temp. (°C)	Test Temp. (°C)	Fluence (10^{22} n/cm^2)	J_{1c} (kJ/m^2)	Tearing Modulus	Grain Size (ASTM)
390	90	5.5	56.5	61	8-9
390	450	5.5	65.2	81	8-9
500	90	5.5	71.7	110	8-9
500	206	5.5	71.5	110	8-9
390	205	2.7	K6.9	61	8-9
450	205	2.7	60.6	113	8-9
500	205	2.3	54.8	142	3-4

strength due to precipitation may reduce the ductility and toughness of the material. The combined effects of thermal aging, radiation damaae and irradiation induced orecioitates on the strenoth and touahness are complicated, much remains to be explored.

In general, the fracture touqhness of HT-9 is not significantly deqraded after irradiation. At 205°C, test results showed that the value of J_{1c} somewhat increased as the fluence was increased from zero to 5.5 x 10^{22} n/cm^2. However, little is known beyond this level of fluence. The fracture toughness at higher doses can not be predicted based on the lower fluence data. As the fracture touahness of 20% cold worked Type 316 stainless steel[3] is degraded by a factor of two after irradiation to a fluence of 11 x 10^{22} nlcm^2, the high dose touqhness of HT-9 might be significantly reduced too.

7.7.6 Conclusions

The fracture toughness of HT-9 irradiated to a fluence of 5.5 x 10^{22} n/cm^2 is relatively independent of test temperature. At 205°C. the toughness increases slightly as the fluence increases from zero to 5.5 x 10^{22} n/cm^2. Irradiation temperature has a weak effect on the fracture toughness but a strong effect on the tearing modulus.

7.7.7 References

1. F. H. Huang, "Fracture Toughness of Irradiated HT-9," pp.104-109, in ADIP Semiannual Progress Report March 31, 1984, DOE/ER-0045/12, U.S. DOE, Office of Fusion Eneray.

2. F. H. Huang and D. S. Gelles, "Fracture Toughness of Irradiated HT-9 Weld Metal," pp. 125-130 in AOIP Semiannual Progress Report March 31, 1983, DOE/ER-0045/10, U.S. DOE, Office of Fusion Energy.

3. F. H. Huang, "The Fracture Characterization of Highly Irradiated Type 316 Stainless Steel," Intern. J. Fracture, 25, 181-193 (1984).

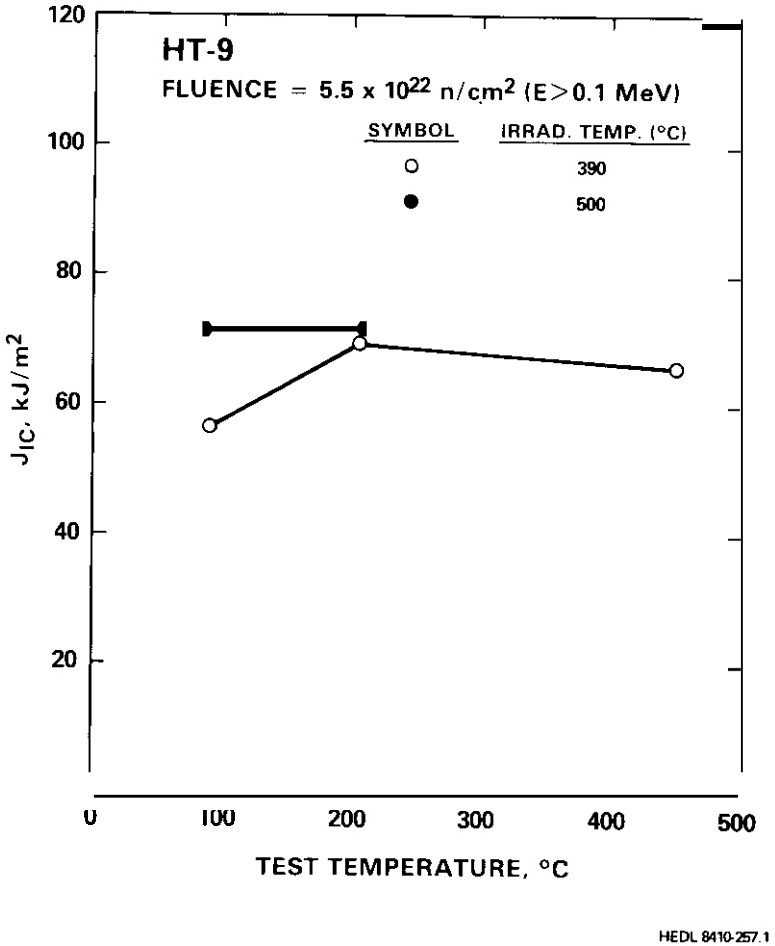

Fig. 7.7.1 Test temperature dependence of fracture toughness for irradiated HT-9.

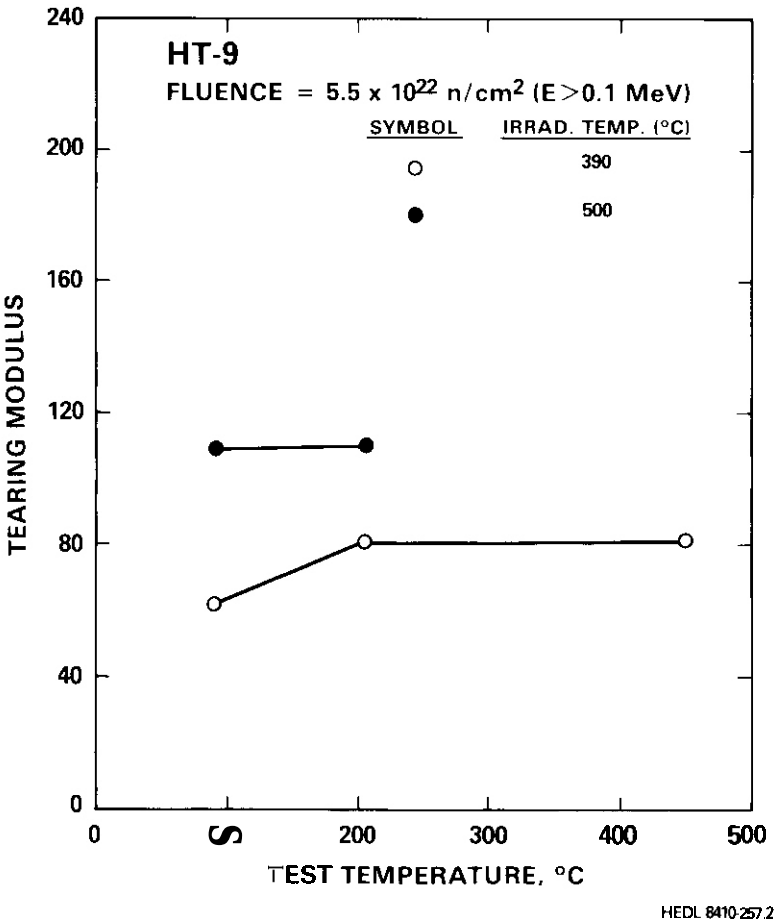

Fig. 7.7.2. Test temperature dependence of tearing modulus for irradiated HT-9.

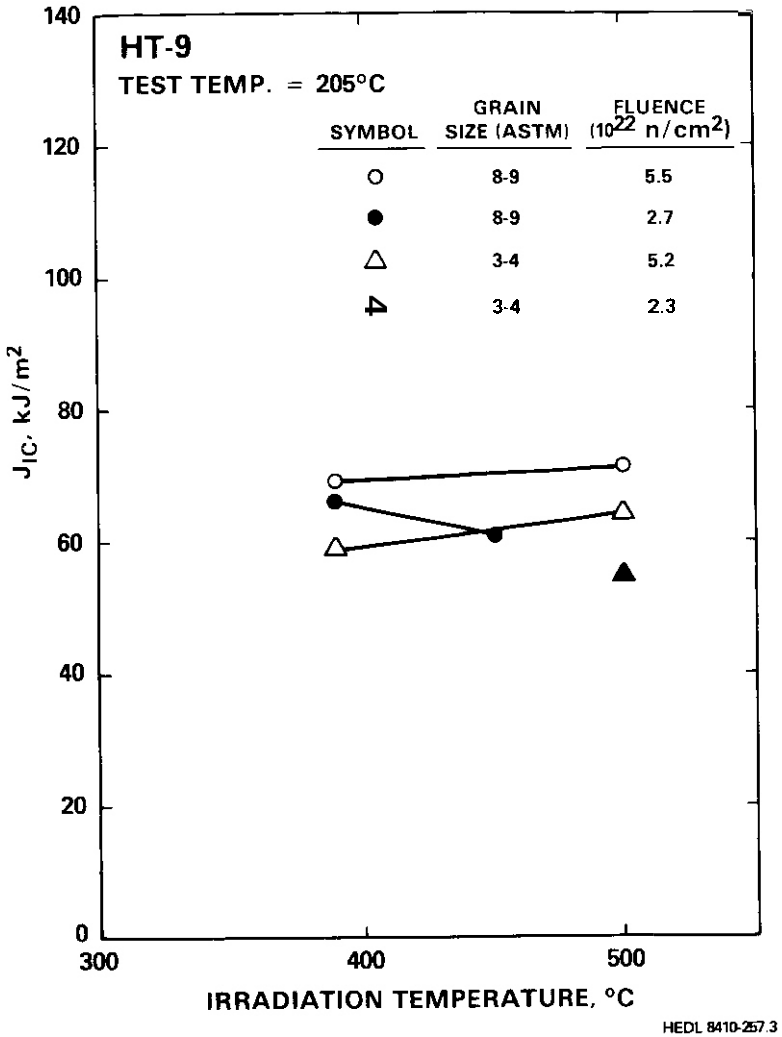

Fig. 7.7.3. Irradiation temperature dependence of fracture for irradiated HT-9.

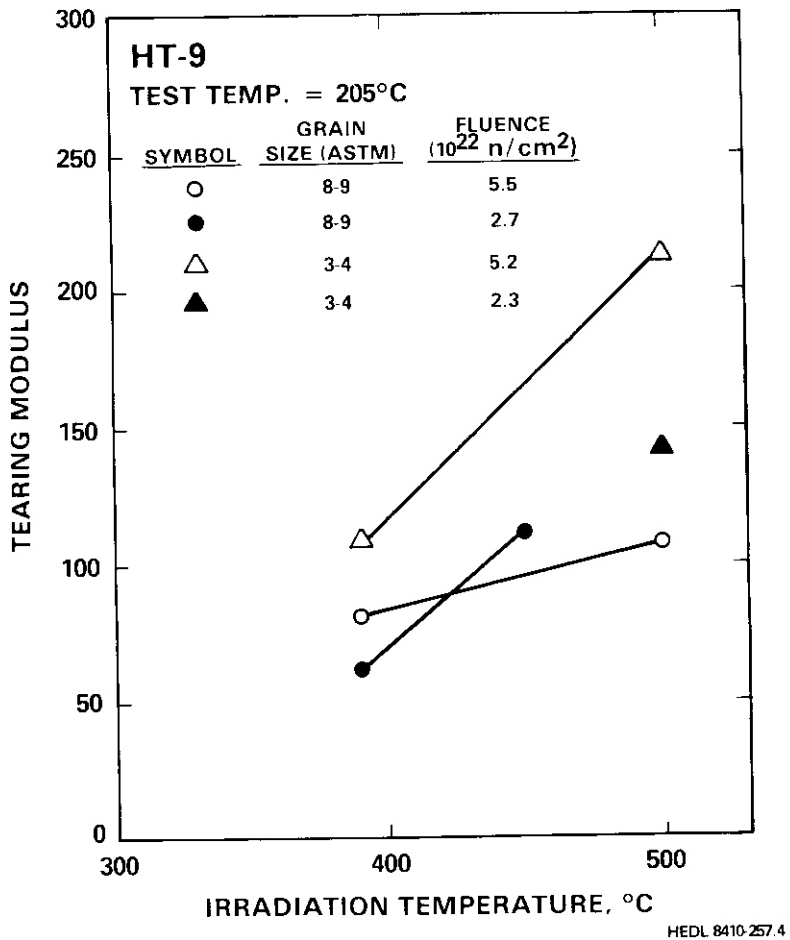

Fig. 7.7.4. Irradiation temperature dependence of tearing modulus for irradiated HT-9.

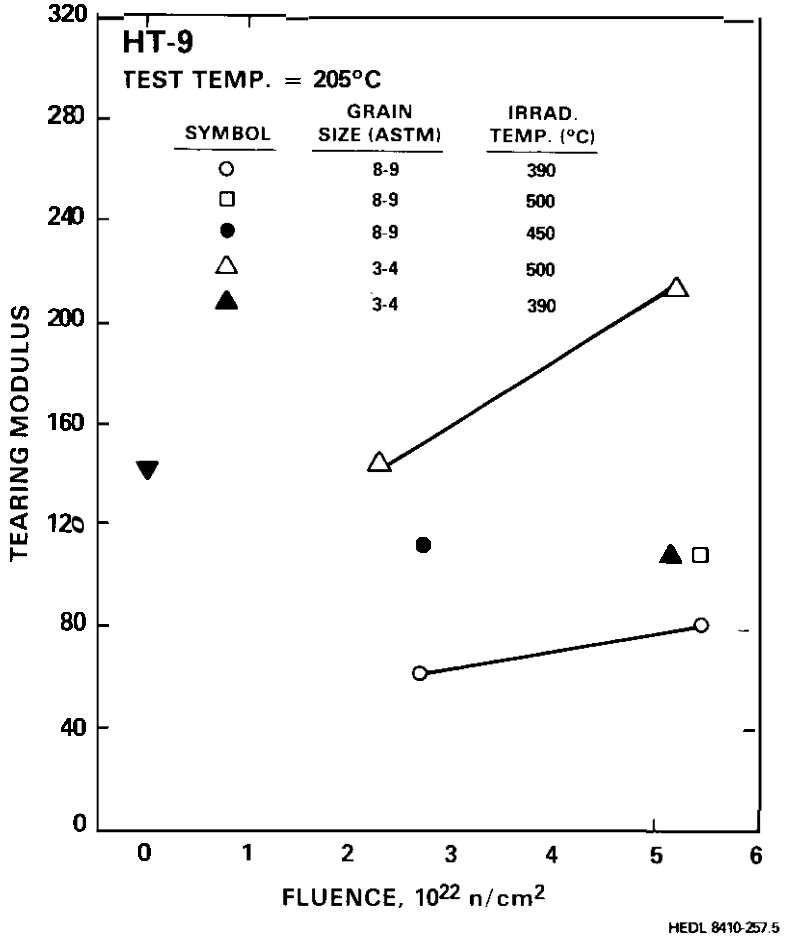

Fig. 7.7.5. of for HT 9 tested at 205°C.

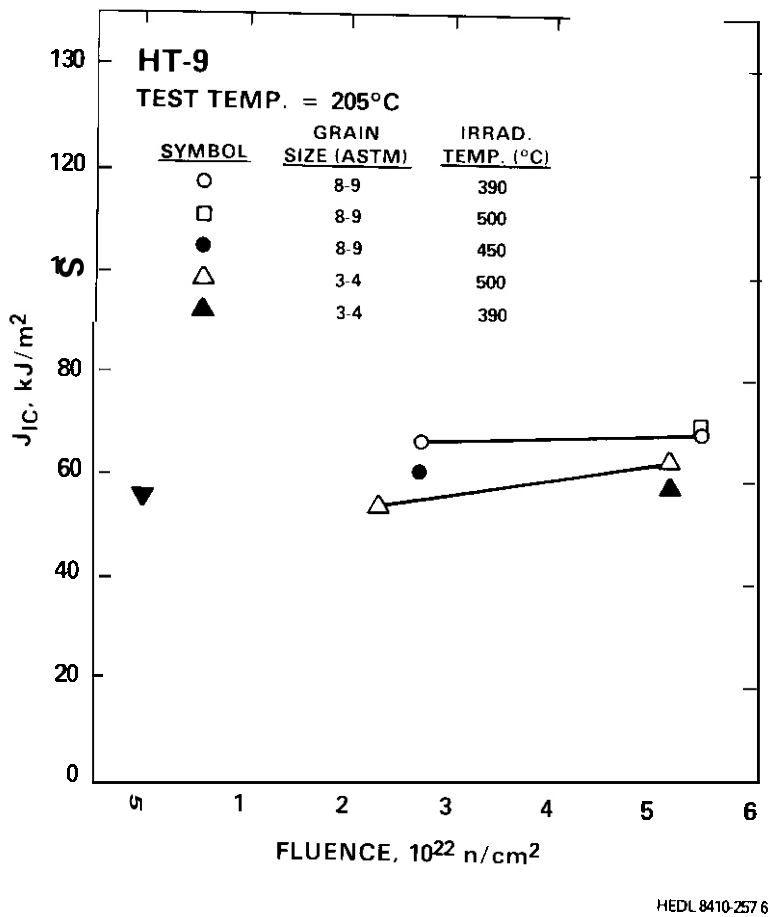

Fig. 7.7.6. of lus for HT 9 tested at 205°C.

7.8 MICROSTRUCTURAL EXAMINATION OF SEVERAL COMMERCIAL ALLOYS NEUTRON IRRADIATED TO 100 DPA - D. S. Gelles (Westinghouse Hanford Company)

7.8.1 ADIP Task

Task 1.C.2, Microstructures and Swelling in Austenitic Alloys, task 1.C.1 Microstructural Stability and related tasks based on the need of the Department of Energy/Office of Fusion Energy (DOE/OFE) to investigate ferritic alloys undo the ADIP program task Ferritic Steels Development (Path E).

7.8.2 Objective

The objective of this effort is to provide guidance on the applicability of austenitic and martensitic stainless steels for fusion reactor structural materials.

7.8.3 Summary

Microstructural examination of ferritic and austenitic commercial alloys neutron irradiated to ~100 dpa confirms that ferritic alloys are very low swelling but precipitate development can be very complex. Austenitic alloys can be very high swelling but no clearly defined microstructural differences could be found between two alloys of similar composition but very different swelling response or between alloys of very different composition but with similar swelling. Differences are ascribed to differences in the onset of swelling.

7.8.4 Progress and Status

7.8.4.1 Introduction

In a previous semiannual progress report, results were reported for density change measurements on a series of commercial alloys which had been irradiated with fast neutrons at temperatures from 400 to 650°C to fluences as high as 2.53 x 10^{23} n/cm² (E > 0.1 MeV) or ~125 dpa.[1] Because of the wide range of alloys included and the very high fluences obtained, these specimens offered a unique opportunity for further effort. The present report describes microstructural and precipitate composition analysis for several specimens selected from that experiment. The specimen matrix selected for examination consisted of two parts: 1) a series of three austenitic stainless steels chosen because they represented a wide range of swelling response with small variations in composition (AISI 330 versus Incoloy 800) and a wide range in composition with small variation in swelling (AISI 330 versus Incoloy 600), and 2) a series of ferritic/martensitic steels which had been previously examined at two lower fluences.[2,3] In order to limit the scope of this effort, only two irradiation temperature conditions were examined for each of the austenitic steels in order to provide insight into the swelling process and a maximum of two irradiation temperature conditions (in the swelling regime) were examined for each of the ferritic alloys in order to assess the effect of fluence on swelling. Precipitate extraction replicas of the ferritic alloys were also analyzed to provide information on phase stability and microchemical behavior.

7.8.4.2 Experimental Procedures

Details of the irradiation experiment have been documented previously.[1] The specimen matrix chosen for examination is given in Table 7.8.1. Specimen disks 0.3 mm thick were sliced from the 3.0 mm diameter rod specimens using a slow speed saw equipped with diamond impregnated blades. The disks were given a light electropolish and then ferritic alloy specimens were etched and a carbon extraction replica was taken from the etched specimen surface. The disks were then prepared for transmission electron microscopy. Microscopy was performed either on a 100CX JEOL STEM electron microscope operating at 100 keV or on a 1200EX JEOL STEM electron microscope operating at 120 keV. All procedures have been previously described.[1]

7.8.4.3 Results

The description of results will be subdivided inro rnree sections: transmission microscopy of ferritic alloys, microchemical analysis of ferritic alloys and transmission microscopy of austenitic alloys.

Ferritic alloy microstructures

The ferritic alloys were found to remain swelling resistant to neutron radiation at fluences up to 2.1 x 10^{23} n/cm². Five of the six alloys contained cavities, the exception being alloy H11, and only EM12 exhibited significant swelling. (The EM12 specimens had developed swelling as measured by density change of only 0.6 percent.[1]) Also, precipitate structures had stabilized in comparison with lower fluence examinations. In other words, precipitate structures had changed only as a result of coarsening; no new phases appeared to be present.

Examples of the microstructures of the comnercial ferritic alloys at low magnification are provided in Figure 7.8.1. Figure 7.8.1a shows H11 after irradiation at 425°C to 99 dpa. Several precipitate morphologies can be identified but no cavities were found. Figure 7.8.1b shows EM12 following irradiation at 425°C to 99 dpa.

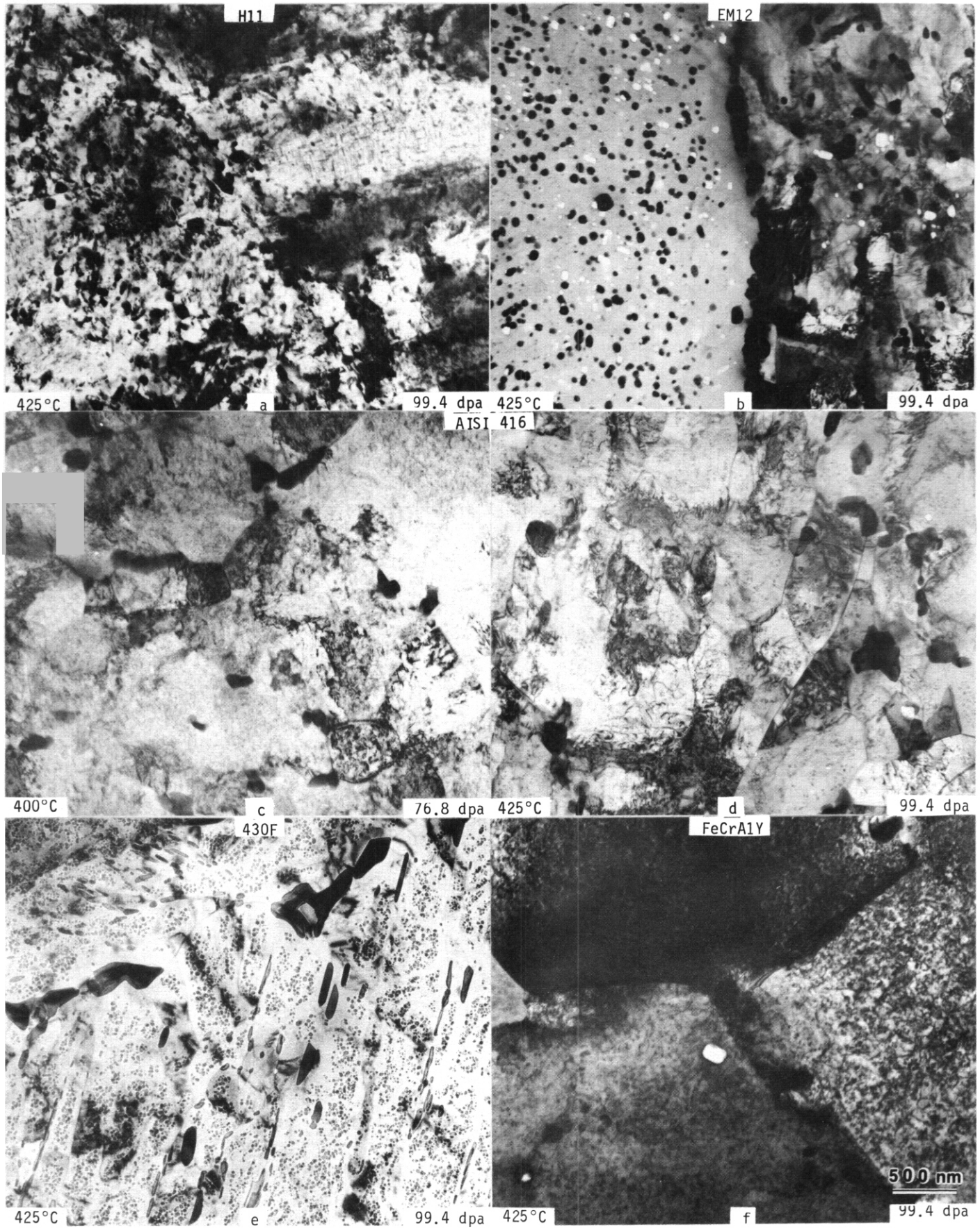

Fig. 7.8.1. Low magnification examples of microstructure in irradiated commercial ferritic alloys.

Table 7.8.1. Specimens from B116 of the AAI test selected for microstructural examination.

Identification	Alloy	Condition*	Irradiation Temperature °C	Irradiation Fluence X 10^{23} n/cm² (dpa)	Swelling %
93L7	H11	Q+T	425	2.07 (99.4)	0.14
98M7	EM12	N+T	400	1.60 (76.8)	0.57
98L7	EM12	N+T	425	2.07 (99.4)	0.56
64M7	AISI 416	F.C.	400	1.60 (76.8)	0.35
64L7	AISI 416	F.C.	425	2.07 (99.4)	0.25
91L7	430 F	ST	425	2.07 (99.4)	0.20
99L7	FeCrAlY	C	425	2.07 (99.4)	0.12
89L7	RA-330	ST	425	2.07 (103)	12.4
89G7	RA-330	ST		2.32 (116)	2.04
79L7	INC. 800	ST			41.1
79G7	INC. 800	ST			12.0
77L7	INC. 600	ST			12.7
77G7	INC. 600	ST			1.6

*Q+T: Quenched and tempered, N+T: normalized and tempered, F.C.: furnace cooled, ST: solution treated, C: consolidated at 1150°C. Details can be found in reference 1.

A ferritic region on the left is found to contain a fairly uniform distribution of voids and blocky precipitate particles. The region on the right is a tempered martensite region. The tempered martensite does contain voids but they are non-uniformly distributed. The grain boundary separating these regions is heavily decorated with precipitation and the adjacent region in the ferrite is somewhat denuded of precipitate and voids. In comparison with the lower fluence condition examined previously, voids are larger and more voids are present in tempered martensite regions. Figure 7.8.1c shows AISI 416 following irradiation at 400°C to 77 dpa. The structure can be characterized by a high density of uniformly distributed small particles, a moderate density of small voids and a low density of blocky carbide particles at grain boundaries. In comparison, AISI 416 following irradiation at 425°C to 99 dpa contains a lower density of larger voids and precipitate particles. The void swelling found in AISI 416 is considerably higher than was found at the lower fluences where very few voids were observed. Figure 7.8.1e shows 430°F following irradiation at 425 to 99 dpa. The structure consists of blocky carbide particles at grain boundaries and equiared γ' particles distributed fairly uniformly between subgrain boundaries. A few small cavities were found in the proximity of grain boundaries but the accumulated swelling was negligible. Figure 7.8.1f provides an example of FeCrAlY irradiated at 425°C to 99 dpa. The structure contains a high density of precipitate particles in the matrix, a well developed dislocation structure with loops and tangles and large blocky particles at grain boundaries.

Examples of the irradiated ferritic alloy structures at higher magnification are shown in Figure 7.8.2. Examples of the different precipitate morphologies in H11 following irradiation to 99 dpa at 425°C are shown in Figure 7.8.2a. Figure 7.8.2b provides an example of dislocation structure in a ferrite grain of EM12 following irradiation at 425°C to 99 dpa. Note that precipitate interfaces show arrays of misfit dislocations and that matrix dislocation tend to be connected to particles. Figure 7.8.2c shows dislocation loops and precipitates in AISI 416 after irradiation at 400°C to 77 dpa whereas the same alloy after irradiation at 425°C to 99 dpa contains a coarser structure, shown in Figure 7.8.2d. In comparison, alloy 430F contains more precipitate and a lower dislocation density as shown in Figure 7.8.2e. Figure 7.8.2f-g show the void dislocation and precipitate structure in FeCrAlY. The larger precipitate particles are expected to be Y O and the dislocation loop structure is characteristic of a <100> Burger vectors. The precipitate structure which formed in FeCrAlY is shown to be quite globular in appearance.

Ferritic alloy precipitate compositions

A tabulation of precipitate composition measurements are provided in Table 7.8.2. Only metal atom compositions are given. A tentative identification of each composition type is also given. From Table 7.8.2, it can be shown that precipitation in H11 appears to be predominantly carbide particles (this no doubt arises from the high carbon content of 0.42% in the alloy). The precipitates which form in EM12 are of different types depending on irradiation temperature. For example, following irradiation at 400°C molybdenum rich phases form. The molybdenum rich phase may be Laves but the vanadium rich phase has not bet been identified. However, following irradiation at 425°, the precipitates which form during irradiation include niobium-rich Laves. In AISI 416, following irradiation at 400°C, evidence for α' was found whereas following irradiation at 425°C a phase similar in composition to sigma was detected and evidence for G phase was found. In 430F, the predominate phase which forms during irradiation is α'. However, in FeCrAlY, α' is not the dominant phase; the dominant phase appears to be closer in composition to sigma. This could be the reason why the precipitate morphology is different. From these results, it is apparent that during irradiation

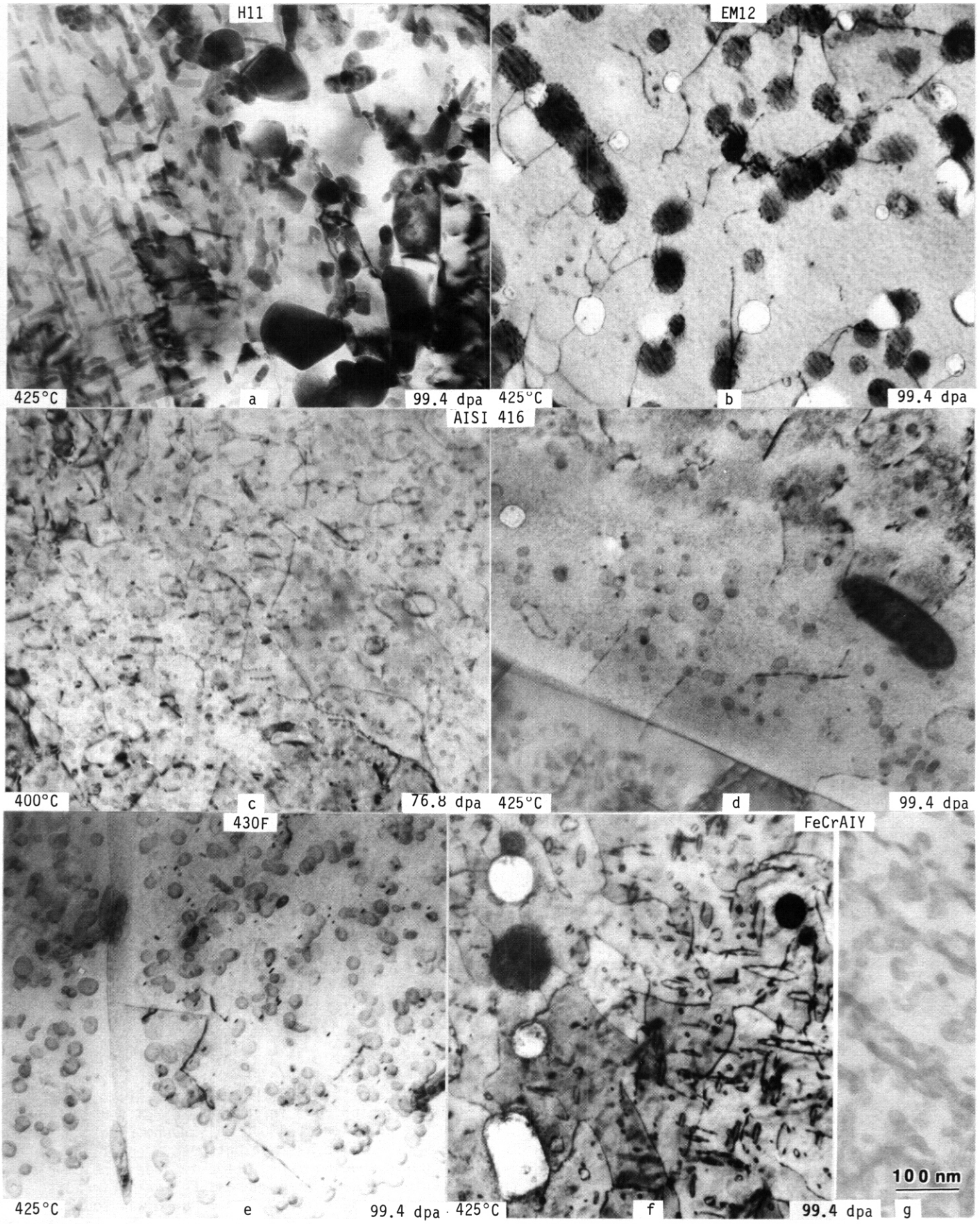

Fig. 7.8.2. Examples of microstructures in irradiated ferritic alloys at high magnification showing dislocation and precipitate structure.

Table 7.8.2. Compositions (in weight percent) of precipitate particles extracted from irradiated ferritic alloy specimens

Sample Identity	Alloy	Composition								No. Measured	Identification
		Fe	Cr	Mo	V	Si	Mn	Ni	Other		
93L7	H11	23-27	60-70	8-11	2-4	--	0-1	--		8	$M_{23}C_6$
	at 425°C	23-34	46-58	13-15	3-5	0-2	0-5	--		7	M_7C_3
		0-15	42-53	19-48	7-9	--	0-3	--		4	M_6C
98M7	EM12	9-29	60-77	0-6	8-15	0-2	--	--		13	$M_{23}C_6$
	at 400°C	0-4	4-5	16-29	60-79	0-3	--	--		2	?
		31-39	8-9	27-47	0-5	5-8	0-1	--		12	Laves ?
98L7	EM12	22-34	52-63	11-13	.5-1.3	.3-3	0-.8	0-5		12	$M_{23}C_6$
	at 425°C	52-68	23-37	3-13	0-.1	.6-2	0-4	0-3		16	chi
		5-34	11-20	--	0-.8	--	0-2	0-5	Nb:45 35	5	Laves
64M7	416	21-30	54-69	0-11	--	0-5	--	0-13		10	$M_{23}C_6$
	at 400°C	3-8	87-96	0-6	0-2	--	--			12	α'
64L7	416	23-29	57-77	0-6	--	0-5	--	0-6		9	$M_{23}C_6$
	at 425°C	31-54	46-53	--	--	0-11	0-4			3	sigma ?
		20	41	--	--	11	--	28		fine background	G ?
		26	40.5	--	--	12.5	1.6	19.2		1	G ?
91L7	430F	--	28-43	--	--	0.7	16-34	0-1.8	S:36-41	4	MnS
	at 425°C	12-24	65-78	--	--			0-10		7	$M_{23}C_6$
		3-17	82-96	0-.4	--	.2-7	--	0-1.7		22	α'
99L7	FeCrAlY	17-20	79-84	--	--	--	--	--	Al:0-1.7	4	α'
	at 425°C	51-77	18-40	--	--	--	--	--	Al:4-9	11	sigma ?
		0-4	2-5	--	--	--	--	--	Y:90-95	4	Y_2O_3
		12-26	6-24						Y:51-79	3	?
		38-48	39-50						Al:6-12	5	?

precipitate development in ferritic alloys is very complex. Carbides, intermetallic phases and phase separation are found but changes in irradiation temperature can promote very different precipitate phases.

Austenitic alloy microstructures

Microstructural examinations of Incoloy 800, AISI 330 and Incoloy 600 demonstrate that all three alloys swell, that Incoloy 800 swells more than the other two alloys because voids have grown larger and that AISI 330 and Incoloy 600 behave quite similarly despite large differences in composition. Examples of the void structures for each of these alloys following irradiation at 425°C to 103 dpa and at 540°C to 116 dpa are given in Figure 7.8.3. It should be noted that the micrographs of the lower irradiation temperature condition are at twice the magnification of the higher temperature conditions. The void structures in Incoloy 800 have grown largest and several examples of void coalescence can be seen. (Void coalescence tends to create voids with unusual elongated shapes.) Also, the largest voids tend to be associated with large precipitate particles.

These microstructures are shown at higher magnification in Figure 7.8.4. Figures 7.8.4a-b give examples of dislocation and gama prime precipitate structures in an Incoloy 800 specimen irradiated at 425°C to 103 dpa. In those micrographs, the specimen is much thinner than the mean void diameter so that holes exist where voids were once present. The dislocation structure consists of a fine tangle of dislocations and loops and the precipitate structure includes blocky gamma prime particles and a fine dispersion of MC carbide particles. Figures 7.8.4c-d show dislocation and precipitate structures in a specimen of AISI 300 irradiated at 540°C to 116 dpa. The scale of the dislocation structure is similar to that in Incoloy 800 irradiated at 425°C but the gama prime precipitates are much larger. The gama prime in AISI 330 is expected to be Ni_3Si whereas in Incoloy 600 and 800 it would include $Ni_3(Al,Ti)$. Figures 7.8.4e-f show dislocation and precipitate structures in a specimen of Incoloy 600 irradiated at 425°C. The dislocation structure contains more loops but the scale is similar.

7.8.5 Discussion

7.8.5.1 Swelling in Ferritics

The present results further demonstrate that ferritic alloys do swell. Voids were found in four of the five alloys examined. However, only EM12 showed significant swelling and even then it only amounted to 0.6 %. Therefore, this work confirms that comnercial ferritic alloys remain highly resistant to dimensional changes caused by swelling in fast neutron environments.

7.8.5.2 Precipitate Formation in Ferritics

The present results confirm that precipitate development can be quite complex in irradiated comercial ferritic alloys. A number of phases form including carbides, intermetallics and products of phase separation. Furthermore. the densitv of these Dhases can be auite high so as to affect dislocation mobility and misfit effects can promote disiocation interactions.

As a function of irradiation temperature not only is the distribution of precipitate particles altered but the number of phases can change. The consequence is that properties are generally degraded for low irradiation temperatures due to the number distribution and complexity of the phases formed. The degradation is more severe than for equivalent specimens which were not irradiated.

7.8.5.3 Swelling in Austenitics

Microstructural comparisons between Incoloy 800, AISI 330 and Incoloy 600 confirm density measurements which showed Incoloy 800 to be high swelling whereas AISI 330 and Incoloy 600 developed similar but lower levels of swelling. These similarities and differences are perhaps surprising. For example, all alloys contained gama prime and all large voids appeared coupled to precipitate particles. Yet two alloys with very similar compositions developed very different levels of swelling and two alloys with very different compositions developed very similar levels of swelling. These observations are compatible with the explanation put forward by Garner that swelling in austenitic alloys can be expected to show the same peak steady-state swelling rate and that material difference are solely as a result of differences in the time to reach steady state swelling.' The delay in the onset of swelling for AISI 330 can be attributed to silicon but the cause for similar behavior in Incoloy 600 is not yet understood.

7.8.6 Conclusions

Microstructural examinations have been performed on a series of commercial ferritic and austenitic alloys following irradiation in a fast reactor to doses on the order of 100 dpa. It is found that:

1) four of the five ferritic alloys developed cavities due to irradiation, but only in the case of EM-12 was the swelling significant and in that case, swelling was less than one percent.

2) ,precipitate development had occurred in all alloys examined. In the ferritic alloys, a wide variety of phases was found including intermetallic phases such as Laves, chi and sigma, carbide phases such as $M_{23}C_6$, M_7C_3 and M_6C and products of phase separation, a'. In austenitic alloys, gamma prime was identified in all alloys.

Fig. 7.8.3. Swelling in austenitic commercial alloys Incoloy 800, AISI 330 *and* Incoloy 600 following irradiation at 425 and 540°C to high dose.

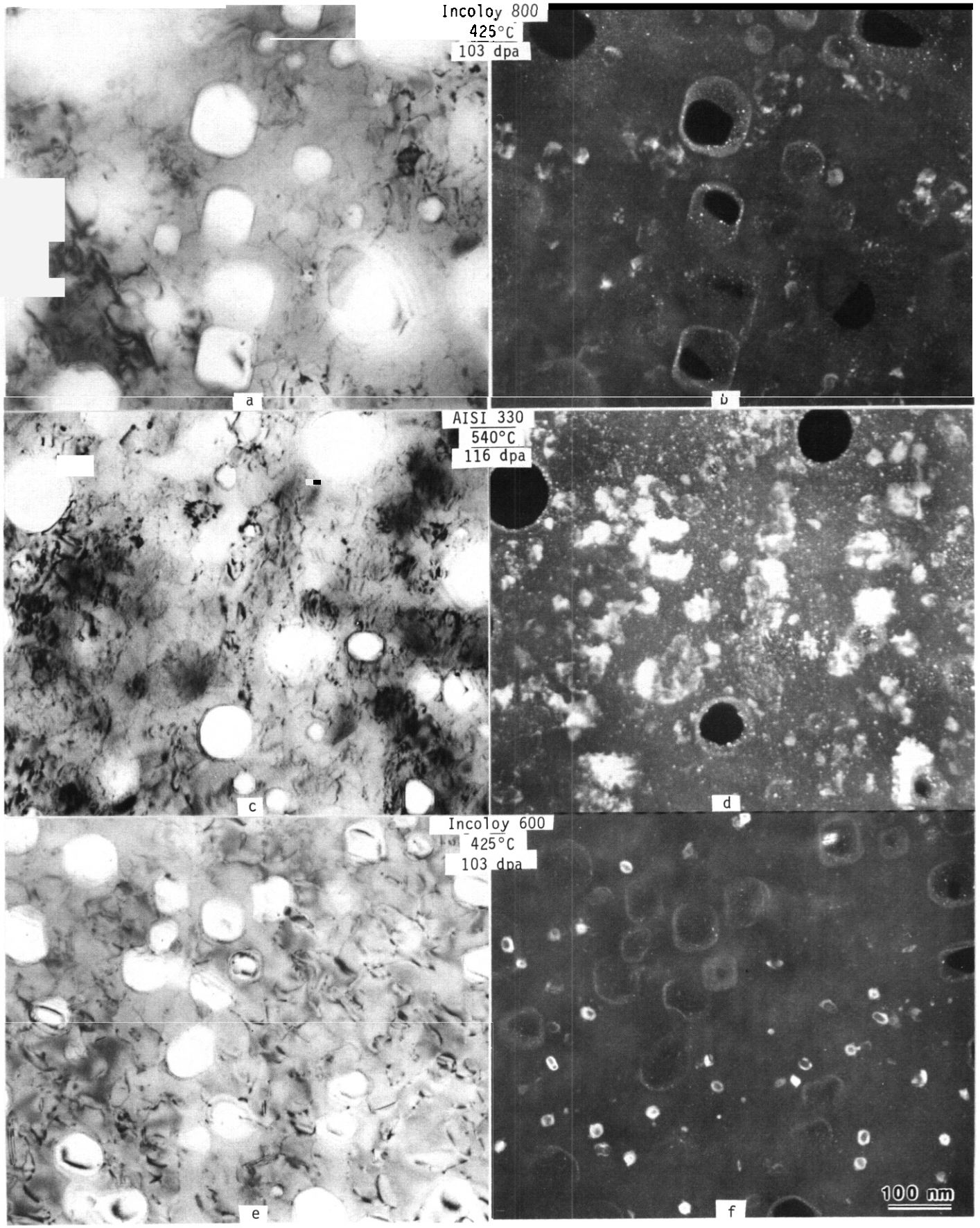

Fig. 7.8.4. Comparison of dislocation and precipitate structures in commercial austenitic alloys following irradiation.

3) Comparisons between austenitic alloys confirmed that large differences in swelling could occur as a result of small differences in composition whereas large differences in composition could produce only small differences in swelling. No straightforward microstructural explanations were found except that differences could be traced to differences in the onset of steady state swelling.

7.8.7 References

1. D. S. Gelles and J. S. Pintler, "Swelling in Several Commercial Alloys Irradiated to Very High Neutron Fluence," DOE/ER-0045/11 (1983) p.75.
2. D. S. Gelles, "Microstructural Examination of a Series of Commercial Ferritic alloys Irradiated to Very High Fluence," DOE/ER-0045/5 (1980) p.187
3. D. S. Gelles, "Microstructural Examination of a Series of Commercial Ferritic Alloys Irradiated to Moderate Fluence," DOE/ER-0045/6 (1981) p.157.
4. D. S. Gelles and L. E. Thomas "Microstructural Examination of HT-9 and 9Cr-1Mo Contained in the AD-2 Experiment," DOE/ER-0045/8 (1982) p.343.
5. F. A. Garner and H. R. Brager, "Swelling of Austenitic Fe-Ni-Cr Ternary Alloys During Fast Neutron Irradiation," in the proceedings of the Twelfth International ASTM Symposium on Effects of Radiation on Materials, ASTM STP 870 (1984).

8.1 RESPONSE OF SELECTED HIGH STRENGTH HIGH CONDUCTIVITY COPPER ALLOYS TO SIMULATED FUSION IRRADIATION AND TEMPERATURE CONDITIONS - J. A. Spitznaqel (Westinghouse R&D Center and University of Pittsburgh), and J. W. Davis (McDonnell Douglas Company)

8.1.1 ADIP Task

ADIP Tasks are not defined for copper alloys in the 1978 program plan. The tasks involved are similar to Task Number 1.C.2, Microstructures and Swellinq in Austenitic Alloys and Task Number 1.C.1, Microstructural Stability.

8.1.2 Objective

The objective of this work is to scope the irradiation response of three classes of high strength, high conductivity copper alloys and to provide guidance for alloy development for fusion reactor structural components.

8.1.3 Summary

Microstructural changes are reported for a solid solution cold work strengthened alloy (AMZIRC), a precipitation strengthened alloy (Beryllium Copper) and a dispersion hardened alloy (Ai-60) after dual ion irradiation at fluences to ~5 dpa at 450°C and 500°C. The Amzirc and A1-60 alloys are from the same heats being examined by LANL in a EBR-II neutron irradiation program. Void swelling at a level of ~1-5% per dpa is observed in selected areas of the Amzirc alloy that have experienced texture dependent recovery by dislocation annihilation and rearrangement. Coarsening of the G.P. zones and accelerated precipitate growth are observed in the INESCO supplied beryllium copper alloy. The mechanically alloyed Al-60 is stable and the misfit strains at the interfaces between the Al_2O_3 particles and the Cu matrix are retained. These results are used to extend a proposed test matrix and to suggest (oreliminary) alloy modifications for future neutron irradiation experiments.

8.1.4 Progress and Status

8.1.4.1 Introduction

The Electric Power Research Institute of Palo Alto, CA has funded a program entitled Evaluation of Irradiated Metal Samples for Use in Fusion Components under contract RP-1597-1 with McDonnell Douglas Astronautics Company. Westinghouse R&D Center and the University of Pittsburgh have been participants in that program under Contract Y4E034R entitled Radiation Response of Copper. The first phase of the planned effort has been completed. In order to disseminate the results of this work to the fusion materials community in timely fashion, a brief summary covering the highlights is being included in the Alloy Development for Irradiation Performance Progress Report.

Copper is of interest to fusion for a number of reasons. The two leading applications, however, are as high heat flux components and as first walls in high wall loading devices. Both of these applications require materials that have high thermal conductivity. In this study, dual ion irradiation techniques are being used to simulate the combined effects of temperature, atomic displacements and helium production in the fusion environment. The emphasis is on scoping the general radiation response of three types of copper alloys: a solid solution and mechanically worked alloy (Cu-0.15 wt% Zr), a precipitation strengthened alloy (Cu-0.4 wt% Be-1.9 wt% Ni), and a dispersion strenqthened alloy (Cu-0.6 wt% Al as Al_2O_3 oarticles).

8.1.4.2 Experimental Procedures

Table 8.1.1 summarizes the Copper Development Association designation, commercial supplier, and fusion materials community source of each material used in these experiments.

Table 8.1.1 Alloy Desiqnation and Source

Alloy	CDA No.	Commercial Supplier	Trade Name	Source of Material
Cu-0.15 wt% Zr	C15000	Amax Copoer Inc.	Amzirc	LANL
Cu-0.4 wt% Be -1.9 wt% Ni	C17510	Brushwellman	Brush Be-Cu Alloy 3	INESCO Heat No. 23764
Cu-0.6 wt% Al (Al_2O_3)	C15760	Glidden Metals	Glidcop Grade A1-60	LANL

Unirradiated samples of Amzirc and Al-60 alloys were obtained from Dr. Frank Clinard of Los Alamos National Laboratory. These specific heats have been included in an EBR-II neutron irradiation study as part of the LANL Magnetic Fusion Energy Program. The beryllium-copper alloy was supplied by Dr. R. Daniel Stevenson of INESCO and had been studied as part of the materiais activities for compact reactor development.

Chemical analysis of each heat as suoolied by the commercial vendors and check analysis by Westinqhouse andlor Los Alamos National Laboratory is given in Table 8.1.2 Check chemistry measurements entailed neutron activation analysis at LANL (coordinated by Dr. Ronald J. Livak of LANL) and dispersive energy X-ray techniques at Westinghouse. Both Westinghouse and LANL measurements show a smaller than nominal aluminum concentration in the Ai-60 alloy. The oxygen concentrations for the Amzirc and beryllium-copper alloys as determined by neutron activation analysis at LANL are considerably higher than the nominal levels (3 ppm - 10 ppm) usually quoted for OFHC copper melting practice. They are, however, lower than the levels encountered in electrolytic refining (>200 ppm) and are being checked again by the commercial suppliers.

Table 8.1.2 Chemical Analysis of Copper Alloys as Supplied by the Vendors (in ppm by weight unless otherwise noted)

Element	Amzirc	Beryl1ium Copper *	Al-60 *
Zr	0.15/0.25* wt%	<10	<10
Fe	22/10*	100/60*	60*
S	12/25*	10*	15*
Ag	12/20*	20*	20*
Ni	5	--	--
Sb	5	<40*	<40*
AS	3	--	--
Sc	2	--	--
Te	1	<10*	<10*
Pb	5	30/10*	<10*
Sn	1/40*	50/10*	30*
Bi	1	--	< 4*
Mn	0.5	--	< 4*
P	12*	5*	6*
O	100*	160*	0.49%
Cr	4*	50/10*	10*
Al	20*	100/20*	0.60/0.45* wt%
Be	<1*	0.40/0.36* wt%	<1*
Mg	4*	40*	<1*
Ni	<4*	1.90/1.86* wt%	10*
co	--	100/10*	<10*
Si	--	100/10*	<10*
Zn	--	100/40*	<40*

*Check analysis by Westinghouse or Los Alamos National Laboratory

Table 8.1.3 Heat Treatments and Product Form Prior to Irradiation

Alloy	Heat Treatment	Product Form
Amzirc	Solution treated 900°C-1/2h/quenched + cold rolled 90% + aged 425°C-lh	Sheet (0.022" thick)
Beryllium - Copper	Solution treated 954°C-1/2h/water quenched + cold rolled 37% + aqed 482°C-3h in formiq gas	Sheet (0.019" thick)
Al-60	Powder mixture placed in OFHC copper tube and hot extruded to 3/8" diameter	3/8" diameter rod with 0.012" thick OFHC copper outer sheath

Heat treatments and product form prior to irradiation are summarized in Table 8.1.3. High strength and high conductivity in the zirconium-copper alloys are achieved by first placing the zirconium in solution. A combination of a high degree of cold work and texture hardening results in nominal room temperature yield strengths ~50-60 ksi. Stabilization of the cold worked structure and an increase in electrical and thermal conductivity is achieved by an aging treatment that precipitates Cu_5Zr phase as very fine particles on the dislocations.[1] The aging process also results in a modest (~15%) increase in the yield strength at a piven level of cold work and retention of the room temperature strength at temperatures up to ~450°C. The nominal values of electrical conductivity range from ~90% IACS (Internationally Agreed-Upon Copper Standard for OFHC Cu) at room temperature to ~30% IACS at 500°C for the alloy given the heat treatment specified in Table 8.1.3

Beryllium-copper is a classic precipitation hardening system and simple binary alloys have been studied extensively, The addition of nickel further decreases the solubility of Be in Cu (from ~1.0 wt% Be to ~0.08 wt% Be at 500°C) and may also retard discontinuous (cellular) precioitation of the ordered CuBe phase at grain boundaries.[3] The combination of high strength and high conductivity is achieved by: placing the Be and Ni in solid solution; cold working to harden the alloy, form to final net shape and accelerate aging kinetics; and aging to produce G.P. zones (Guinier-Preston) and an ordered bcc Cu-Be phase (γ') with the CsCl-type structure. Room temperature yield strengths on the order of 118 ksi and electrical conductivities of ~48% IACS have been measured by INESCO for the conditions given in Table 8.1.3. Elongation can be quite low for these alloys (e.g. 5.9% at 150°C as measuredfor this heat) and grain boundary effects under irradiation are likely to be very important.

The manufacturing process for the dispersion hardened Al-60 alloy involves melting a dilute solid solution alloy of aluminum in copper and atomizing the melt into powder by a high pressure gas such as nitrogen. The resulting powder is blended with an oxidant (mainly Cu_2O) in an amount sufficient to oxidize all the aluminum in the alloy. The mixture is heated to ~870°C for 1 hour to convert the aluminum into fine Al_2O_3 particles embedded in a high purity copper matrix. Any excess oxygen remaining in the powder after complete oxidation of the aluminum is removed by heating the powder in dissociated ammonia atmosphere. Rod stock is produced by canning the powder in copper tubing and hot extruding to final size. High strength and electrical conductivity are imparted by dispersion hardening resulting from the hard Al_2O_3 particles and high purity Cu matrix respectively. Nominal room temperature yield strength and electrical conductivity for the Al-60 alloy in the condition indicated in Table 8.1.3 are 65 ksi and 78% IACS, respectively.

Specimen Preparation

Specimens were preoared from the Amzirc and beryllium-copper sheets by coring 0.95 cm diameter discs. Slow speed abrasive cutting with a hollow cylindrical brass cutting tool in a slurry containing diamond abrasive oroduced flat discs with minimal distortion. A diamond wire saw was used to wafer 0.5 mm thick, 0.95 cm diameter slices from the Al-60 alloy. A seven stage lapping and polishing process developed by the Westinghouse R&D Center Optical Shop for laser mirrors was used to reduce the discs to 0.3 mm thickness. One of the 0.95 cm diameter faces was given a final polish usinq Linde B powder in a solution of 4 parts distilled water to 1 part hydrogen peroxide (30% solution) to produce an oxidation resistant surface with a maximum 200 nm thick debris layer. The 0.95 cm diameter discs served both as irradiation and thermal control specimens since only a central 3 mm diameter area was irradiated by the coimpinging ion beams.

Oxygen is purported to play a significant role in the swelling of OFHC copper.[4] It can be shown from residual gas analysis and kinetic theory that the vacuum ambient in the accelerator system (10^{-8} Torr) corresponds to the impingement of a monolayer of oxygen (principally as H_2O molecules) every ~70 sec. It was not known whether these impinging water molecules would react with the copper alloys from recoil assisted and/or thermal diffusion processes at irradiation temperatures up to 500°C. Consequently a significant part of this Phase 1 study has been directed toward answering this question. Two approaches were used to address the issue. First, duplicate specimens of each alloy were prepared for irradiation and one set was processed usinq procedures for putting oxygen diffusion barriers on contacts for semiconductor devices. The conditions used to sputter deposit tungsten or coat the copper discs with silicon nitride by means of a low temperature chemical vapor deposition process are given in Table 8.1.4. Comparison of irradiated microstructures from coated and uncoated specimens provided one measure of the effect of the vacuum ambient. A second parallel approach was also taken; namely, direct measurement of changes in oxygen content by secondary ion mass spectrometry (SIMS).

Table 8.1.4 Deposition Conditions for Oxygen Diffusion Barrier Coatings

Coating	Method	Conditions	Thickness	Thickness Measurement
Tungsten	AC Sputtering	100 Å/Min Substrate Temperature ~300°C	2500 Å	Inficon (Quartz Oscillator)
Silicon Nitride	CVD	Flow Rates: N_2 - 73 sccm NH_2 - 97 sccm	3000 Å	Color Chart Comparison (Silicon Crystal Monitor)

Table 8.1.4 (continued)

Coating	Method	Conditions	Thickness	Thickness Measurement
		SiH_4 - 5 sccm Frequency 12 kHZ Power 5 watts Time 20 min. Substrate Temperature <150°C		

Unirradiated (control), and irradiated (both coated and uncoated) specimens were submitted to Charles Evans and Associates of San Mateo, CA for SIMS analysis.

A second issue addressed in this Phase 1 study was the possible back-diffusion of the deposited heavy ion used to create atomic displacement damage (28 MeV Si^{+6}). Althounh range-energy calculations (modified E-DE?-1 code) show that tie heavy ion comes to rest ∿2 μm downrange from the region of observation, and the rms thermal diffusion distance ai 500°C for the highly soluble ion is only ∿500 Å for the time-temperature conditions of the bombardment,[5] radiation enhanced solute segregation could not be ruled out Aoriori. Thus, SIMS analysis was also used to profile the heavy ion distribution after irradiation. In addition, duplicate specimens were prepared as prethinned TEM discs, similar to those used in HVEM irradiation studies. The heavy ion beam was allowed to pass completely through these samples. TEM comparisons of full thickness and pre-thinned specimens irradiated under comparable conditions provided a second means of evaluating possible deoosited ion effects. Table 8.1.5 summarizes the irradiation condition to be discussed.

Table 8.1.5 Dual-Ion Irradiation Conditions

Material	Condition	Temperature	DPA @ Xm	APPM He @ 3.5 μm	Run Duration (hrs)
Beryllium Copper	As-polished	500°C	25	216	7.25 h
Beryl1ium Copper	Tungsten Barrier Layer	500°C	27	186	7.25 h
Beryllium Copper	As polished	425°C	28	190	7.25 h
Amzirc	Silicon Nitride Barrier Layer	500°C	22	200	7.25 h
Amzirc	As polished	425°C	24	219	7.25 h
Al-60	As polished	500°C	25	194	7.25 h
Al-60	As polished	425°C	25	200	7.25 h

Nominal dpa rate of 1 X 10^{-4} dpa/s over helium implanted region
Temperature variation ±2°C

The copper alloys were irradiated at the High Energy Ion Beam Studies Facility at the University of Pittsburgh. The experimental conditions were similar to those employed in previous studies on ferrous alloys in the DOE-OFE Magnetic Fusion Energy Program.[6] Helium and heavy ion damage are introduced simultaneously through the use of two accelerators. The helium beam (≤ 2 meV) passes through an energy degrading wheel composed of aluminum foils of predetermined thickness. This results in a helium doping profile that very losely matches the deposited damage energy profile over a depth of ∿1 μm to 3.5 μm in the copper alloys.' The range of the heavy ions used in this phase of the work (28 meV Si^{+6}) is 4.51 μm and the peak damage depth, Xm, is 4.35 μm. All data reported here were taken from the helium dooed region where the atomic displacement profile is reasonably flat and SIMS analysis shows no back diffusion of the deposited heavy ion. Precision sectioning of the irradiated specimens to a desired depth was accomplished using a Veeco ion milling machine. Specimens were individually masked with Mo washers during milling. A DEKTAK II stylus profilometer was used to measure the step height and hence the amount of material removed with an accuracy of ∿±10%. The irradiated specimens were back-thinned for TEM examination using a solution of 250 ml phosphoric acid, 500 ml deionized water, 250 ml ethanol, 50 ml propanol and 5 gm urea. Excellent polishing conditions were obtained at room temperature with a Fischione jet polisher using a low to moderate jetting speed, 12-15 volts (dc) and an anode current of 60-70 ma. Cross-section

TEM specimens to permit full range imaging were also prepared using procedures described by Knoll.[8] Specimens were examined using Phillips EM400 and EM301 microscopes.

8.1.4.3 Results and Discussion

Optical micrographs of the three alloys in the unirradiated condition are shown in Figure 8.1.1. The samples were etched in a solution consisting of 630 ml deionized H_2O, 225 ml HCl and 45 grams ($Fe(NO_3)$ at room temperature for ~30 seconds. Similar structures were revealed by ion beam etching the polished discs.

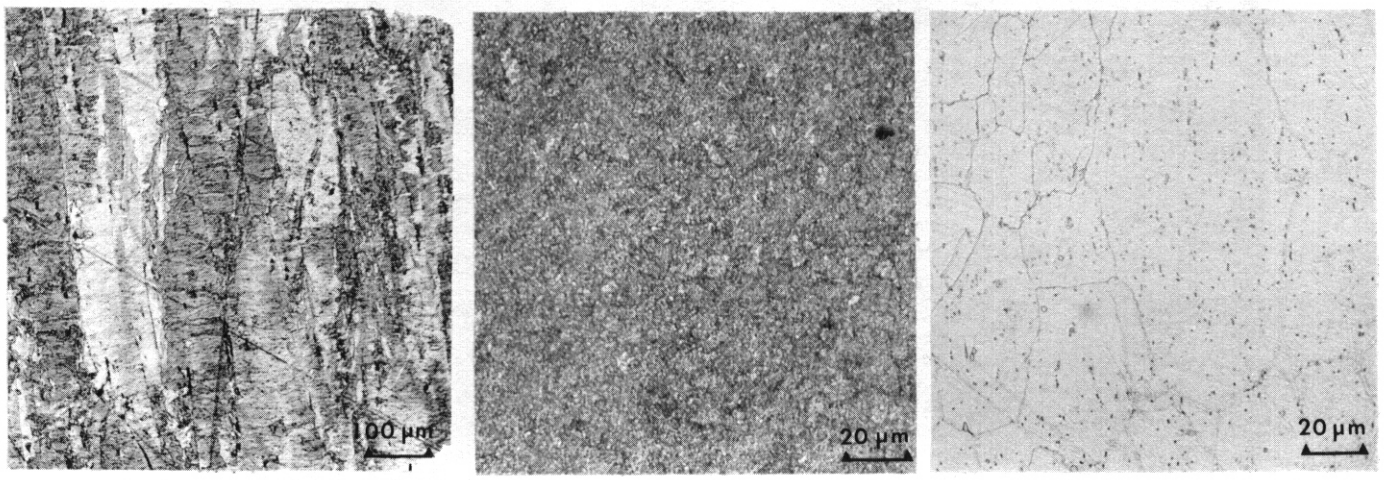

a) b) c)

Figure 8.1.1 Optical Micrographs of Unirradiated Alloys a) Amzirc, b) Al-60 and c) Beryllium-Copper

A pronounced banding is observed in the Amzirc. Electron microprobe traces across the bands show no compositional variations. The structure is due to grain orientation dependent (inhomogeneous) deformation during cold rolling and as, will be shown, leads to inhomoaeneous irradiation response in the alloys. The Al-60 alloy exhibits very fine grain size (less than ASTM 10). Ion beam etching and stylus profilometer traces across an etched face of the Al-60 alloy indicate that in some regions the Al_2O_3 particles surround areas 2 µm to 5 µm in extent that contain few particles in their interior. The effect is most clearly seen in profilometer traces of ion beam etched surfaces due to the very different sputtering rates for copper and alumina. The beryllium-copper alloy has a grain size of ~25 µm to 50 µm (ASTM #7). A low number density (~$10^6/cm^2$) of second phase particles are observed both within these grains and at the grain boundaries. Dispersive energy X-ray analysis shows them to be predominantly nickel.

TEM micrographs of the unirradiated microstructures are shown in Figures 8.1.2-8.1.4. The presence of deformation bands bend contours, and subgrains in the Amzirc reflect the high degree of cold work in the alloy. The Cu_5Zr phase is present as very fine precipitates visible as black spots in bright field images at much higher magnifications. The precipitate particles appear to be associated with the dislocations although high resolution imaging is extremely difficult in this highly strained alloy. The beryllium-copper alloy contains a very high density (~7 X 10^{17} cm^{-3}) of small disc or plate-like precipitates that produce <100> streaks or relrods in selected area diffraction patterns. This is similar to the effects of G.P. zone formation on [100] planes observed in more concentrated binary Cu-Be alloys.[9] Additional distortion of the diffraction spots in <011> directions are also observed. Similar results in the binary alloys have been attributed to anisotropic elastic distortions around the G.P. zones resulting from lower values of elastic moduli in the cube directions.[10] In general, it is not possible to obtain accurate measurements of precipitate thickness or elastic strain from measurements of relrod length, and we have concentrated at present on observing the presence or absence of the streaking in thermal control and irradiated specimens. Stability of the G.P. zones adjacent to grain boundaries has also been carefully studied since both thermal and irradiation effects on grain boundary motion may be exoected to enhance discontinuous precipitation at the boundaries. For the Al-60 alloy in the as hot extruded condition, dislocation tangles surround the visible particles of the dispersoid phase (Al_2O_3). Thus no simple Ashby-Brown strain contrast is associated with these highly misfitting particles. Elastic misfit strain effects, however, are evident at the particle matrix interfaces. We have looked for evidence of relaxation of these strains and helium bubble/void nucleation at these interfaces in this first phase of the scoping study.

Figure 8.1.2 Microstructure of Unirradiated Amzirc Alloy at Low Magnification, Deformation Bands, Subgrains and Bend Contours are Visible.

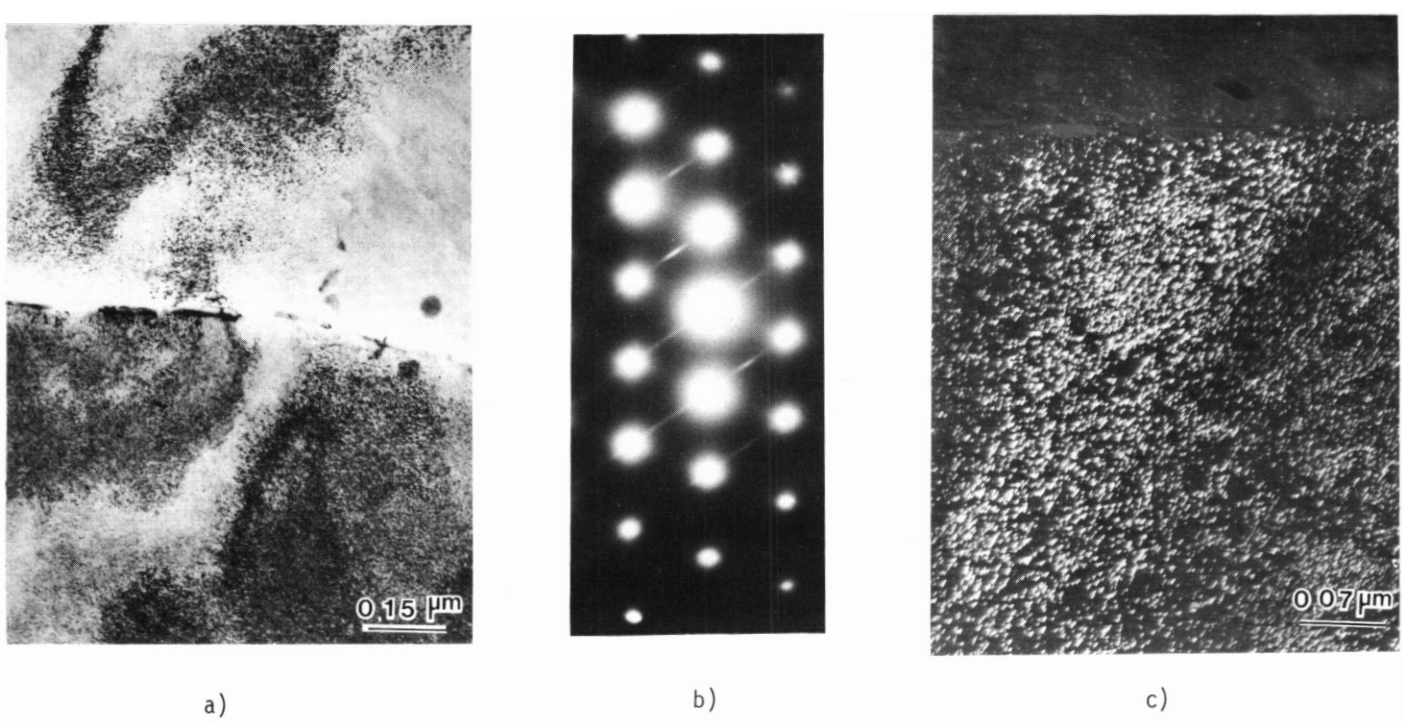

Figure 8.1.3 Microstructure of Unirradiated Cu-0.4 wt% @e-1.9 wt% Ni Alloy a) Bright-field, b) Selected Area Diffraction Pattern from Lower Grain of Alloy a) Showing <001> Relrods Resulting from thin Disc or Plate-like Precipitates on <001> Planes; <011> Zone Axis, c) Dark Field Image of Precipitates using <001> Relrod

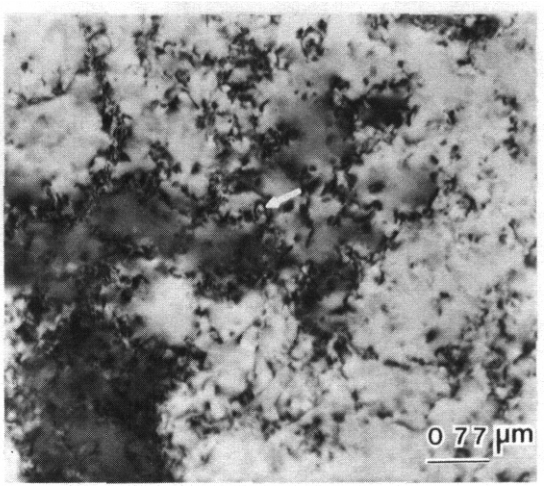

Figure 8.1.4 Microstructure of Unirradiated Al-60 Alloy. Dislocation Tangles Surround Visible Al_2O_3 Particles (arrow)

Effects of Irradiation

Details of the SIMS analysis of the alloys following dual ion irradiation at 425°C and 500°C have been presented at the Phase 1 program review at EPRI and will not be discussed in detail in this report. However, since a prime goal of this Phase 1 effort was to evaluate oossible oxygen pickup and redistribution of the deposited heavy ion, the principal conclusions are restated here: 1) within the sensitivity of the technique (~10 ppm) no measurable changes in oxygen concentration occur relative to unirradiated control specimens over a depth of 20 µm from the ion bombarded surface for either uncoated or diffusion barrier coated thermal controls or dual ion irradiated specimens **2)** a nickel concentration gradient extending approximately 1 µm from the tungsten coated surfaces of thermal control and irradiated specimens results from the high solubility of nickel in tungsten 3) the silicon concentration profile is symmetrical around the peak value which occurs at a depth corresponding to the calculated projected range. The peak width at half maximum is approximately a factor of two larger than the calculated rms range straggle. This broadening of the concentration profile is within a factor of two for that expected from thermal diffusion alone. From these SIMS measurements it was decided that no oxygen diffusion barriers are required for scoping the response of these alloys to atomic displacement damage and helium doping. The barriers, in fact, may be harmful; introducing solute concentration gradients. No significant radiation enhanced seqreaation or back diffusion of the heavy ions occurs under these irradiation conditions. Additional evidence ***for*** the lack of ***a*** complicating effect by the heavy ion is the similarity in irradiated microstructures of normal and pre-thinned specimens.

Amzirc

The Cu-0.15 wt% Zr alloy exhibits the lowest thermal and irradiation stability of the three alloys studied. Figures 8.1.5 to8.1.7 are representative of the principal effects resulting from irradiation and/or thermal exposure. At 425°C the cold-worked microstructure is stable over the 7.25h exposure as indicated by sharp selected area diffraction patterns and little evidence of dislocation rearrangements. Dislocation densities range from $\sim 10^9 cm^{-2}$ in the cell interiors to $>10^{12} cm^{-2}$ in the cell walls. Irradiation to very low fluences at 1×10^{-4} dpa $\cdot s^{-1}$, however, induces the formation of low angle polygonal boundaries and splitting of the diffraction spots. The effect occurs preferentially in grains with <110> surface normals and the majority of grains with other orientations retain the unirradiated cold worked microstructure. It is unlikely that the crystallographic nature of the microstructural instability results from orientation dependent atomic displacement effects, because the specimens were bombarded at ~45° with respect to their polished surface. As is the case with many copper alloys the predominant texture component in the rolled sheet is of the [110] <112> brass type.[1] While texture-hardening is often desirable it may, in fact, lead to instabilities under irradiation as evidenced here. No definitive explanation for the enhanced dislocation climb and glide in grains with <110> surface normals can be offered at this time. These

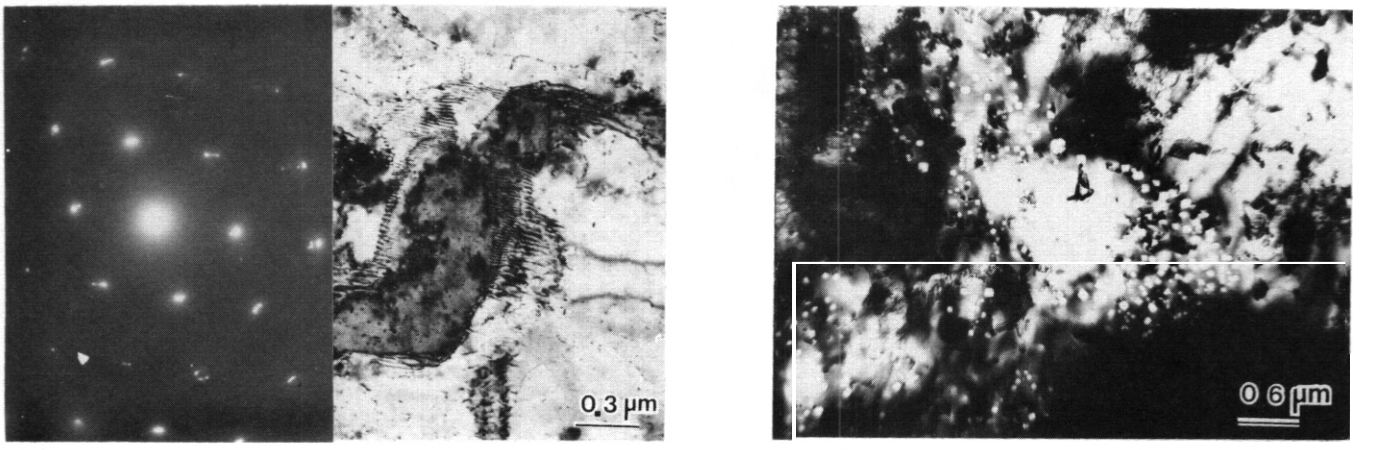

Figure 8.1.5. Polygonization and Dislocation Annihilation in Grains with <110> Surface Normals (a) is Followed by Void Formation at the Boundaries of the Recovered Regions (b) in Amzirc Irradiated at 425°C to 1.5 dpa and 46 appm Helium.

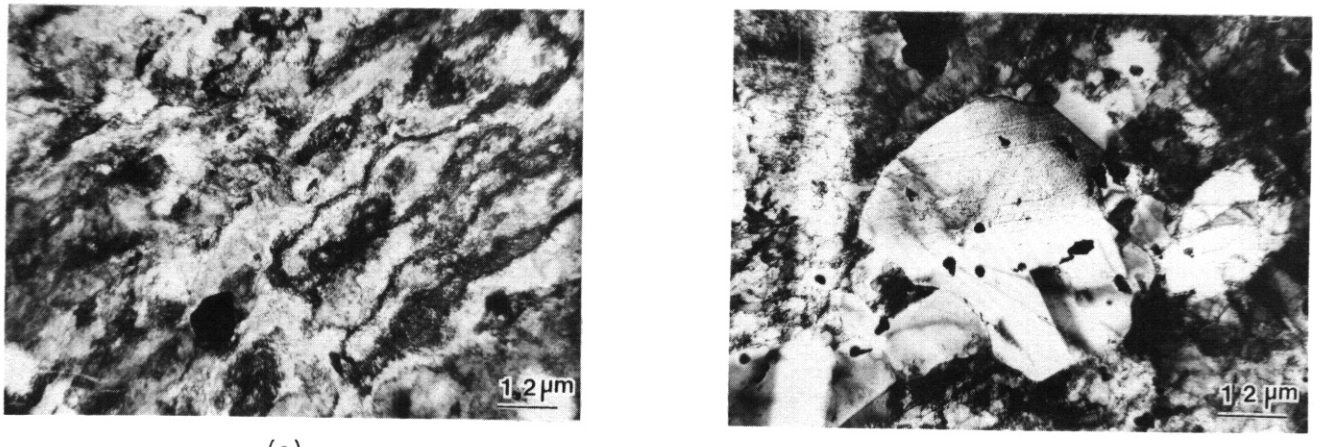

Figure 8.1.6. Thermal Control Specimens of Amzirc Aged for 7.25h at 500°C Show Extensive Regions with Stable Cold Worked Microstructure (a) and Widely Spaced Grains Exhibiting Twinning, Reduction in Dislocation Density and/or Recrystallization (b).

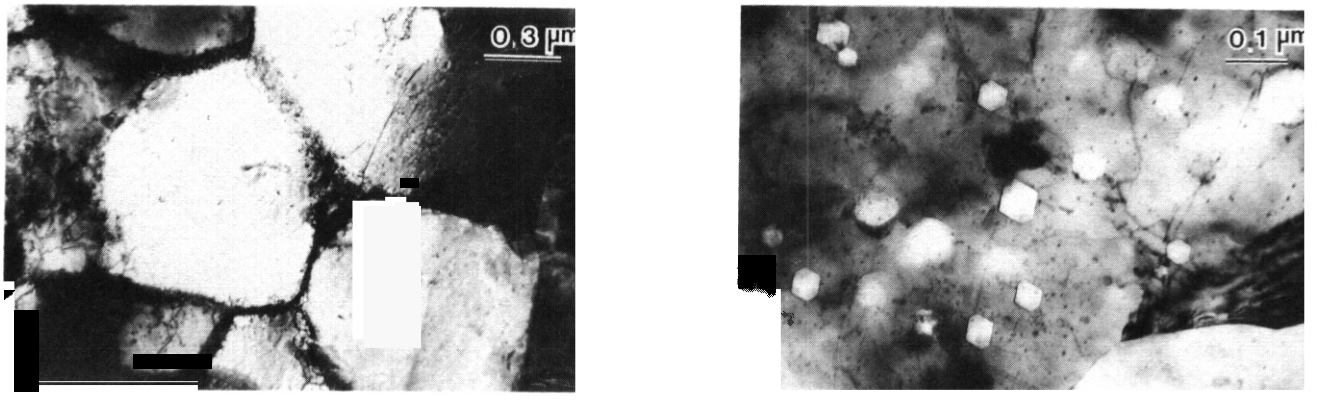

Figure 8.1.7. Dual Ion Irradiation of Amzirc at 500°C to Fluences of 5 dpa and Helium Concentration ~150 appm Accelerates Recovery in Grains with <110> or <112> Surface Normals and Results in a Swelling Rate of ~1% to 5% per dpa in the Recovered/Recrystallized Regions.

recovery processes may depend on subtle differences in deformation substructure, pinning by Cu_5Zr precipitates or elastic anisotropy effects in the alloy and require further study. Whatever their origin the rearrangement of the dislocations into low angle boundaries and reduction of the dislocation density by annihilation or boundary movement leads to pronounced swelling in the altered grains. The voids are often concentrated at the boundaries of the recovered regions suggesting the possible sweeping of helium atoms to form bubbles that exceed the critical cavity size at the boundaries. It is difficult to obtain accurate TEM measurements of swelling in such a microstructure, but it is estimated that the local swelling rate corresponds to ∿1% to 5% per dpa for fluences up to 5 dpa. The alloy is inherently less stable under thermal aging at 500°C. Formation of annealing twins and recrystallization in small regions separated by a few hundred microns of cold worked microstructure are observed. The principal effects of irradiation to ∿5 dpa with simultaneous helium doping to ∿150 appm are the formation of polygonized regions followed by dislocation annihilation and low angle boundary motion resulting in void formation at the boundary of the recovered grains. Dislocation climb and glide were again most evident in grains with <110> surface normals at 500°C although a number of grains with <112> normals also exhibited appreciable reduction in the dislocation density and some void formation. Swelling values in the recovered <110> regions are estimated to be 1% to 5% per dpa and are lower in grains with <112> directions perpendicular to the surface. The swelling values appear to be consistent with preliminary density measurements on specimens of Amzirc from the same heat irradiated in EBR II to fluences of 2 and 10 dpa at a reported irradiation temperature of 387°C.[12] Radiation-enhanced recovery and partial recrystallization but no swelling have been reported recently for an Amzirc alloy under 14 MeV copper ion irradiation at these temperatures without simultaneous helium doping.[13] Cross rolling of sheet and use of other product forms may mitigate these orientation dependent recovery processes which undoubtedly degrade the strength and possibly embrittle the alloy.

Beryllium-Copper

Results of dual ion irradiation of the Cu-0.4 wt% Be-1.9 wt% Ni alloy at 425°C and 500°C to fluences equivalent to ∿1 MW - y/m^2 are shown in Figures 8.1.8 to 8.1.11. Thermal aging at 425°C for times commensurate with the irradiation produced no discernible changes in precipitate structure or morphology either within the matrix or at the grain boundaries. Some bunching of the <100> streaks in the diffraction pattern around 2/3 (200) reciprocal lattice positions on electron diffraction patterns occurs. It has been postulated that such effects in binary Cu-Be alloys represent growth of the G.P. zones to a maximum size and formation of a second metastable phase.[9]

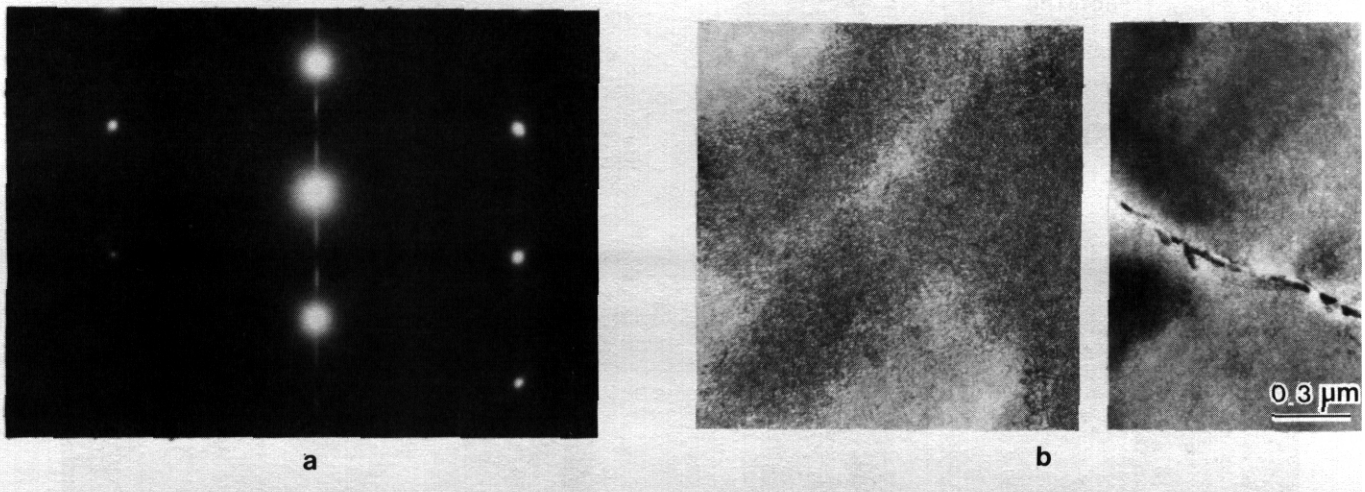

Figure 8.1.8 Selected Area Diffraction Pattern Near [013] Zone Axis of Matrix Showing <100> relrods (a) and Bright Field Image $\bar{g}$ = [131] of G.P. Zones and γ'-Phase Particles in Grain Boundary in Beryllium Copper Alloy after Thermal Aging at 425°C for 7.25h.

Irradiation to 0.6 dpa and 19 appm He at 425°C produces no additional microstructural changes. At 1.4 dpa and 43 appm helium the <100> relrods are still evident but distortion of the <110> reciprocal lattice spots is reduced indicating, perhaps, a lessening of coherency strain effects. This is further suggested by the increased ease of imaging dislocations in the microstructure. At 5 dpa and ∿150 appm helium only faint <100> streaks remain and the intergranular precipitates have coarsened. A low density of voids heterogeneously distributed has been observed in regions where the precipitate coarsening is most severe. The principal effect of irradiation thus appears to be to accelerate the coarsening of the G.P. zones at 425°C. At 500°C, which is above the aging temperature used for processing the alloy (482°C), thermal aging for 7.25h results in appreciable coarsening of the G.P. zones. Discrete diffraction spots associated with a bcc (γ) phase are also visible in some regions of the foil. Irradiation appears to accelerate the

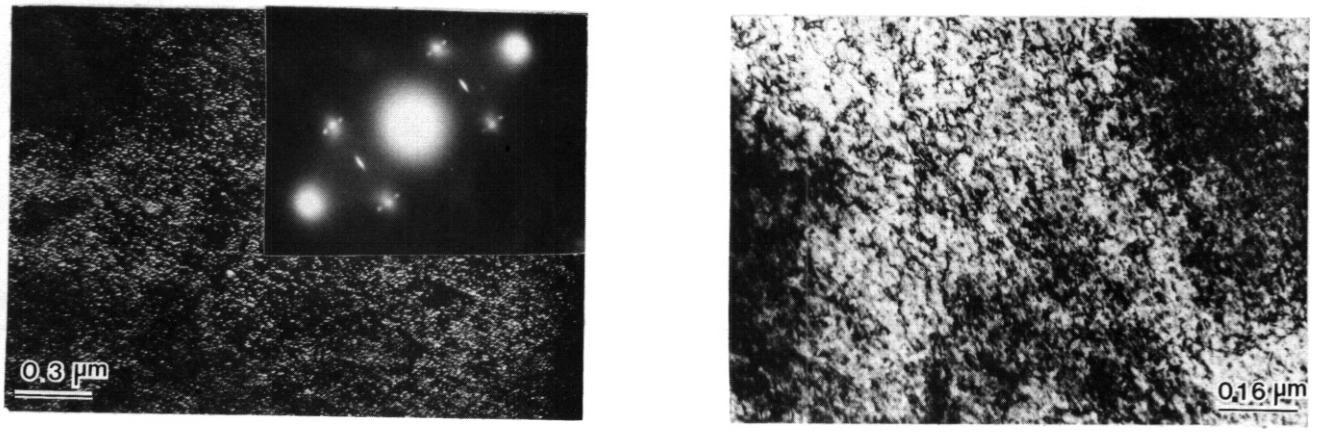

(a) (b)

Figure 8.1.9 Beryllium Copper Alloy after Irradiation to 1.4 doa and 43 appm He a) SAD Pattern Showing <100> Relrods from G.P. Zones and Associated Dark Field Image b) Two Beam Dynamical Briqht Field Image, Z = [112]; g = [11$\bar{1}$] of Dislocation Structure.

coarsening of the intergranular orecipitates, but no evidence for enhanced cellular precioitation at grain boundaries has been found. Voids are not observed at 500°C at fluences up to ~5 dpa. The microstructural effects suggest that a loss in strength and increase in electrical conductivity should result from the combination of elevated temperature aging an irradiation. This is consistent with recent measurements on a similar alloy irradiated in FFTF at 450°C. Q4

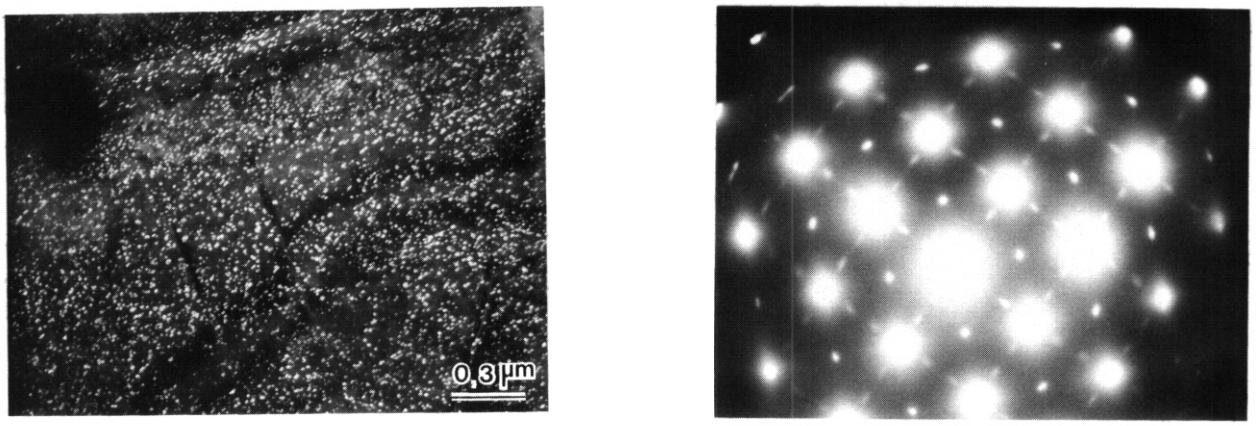

(a) (b)

Figure 8.1.10. Beryllium topper Alloy Aaed at 500°C for 7.25h a) Dark Field Image of Coarsened Intergranular Precipitate Structure and b) Associated Bunching of Streaks Around 2/3 [200] Positions in SAD Pattern.

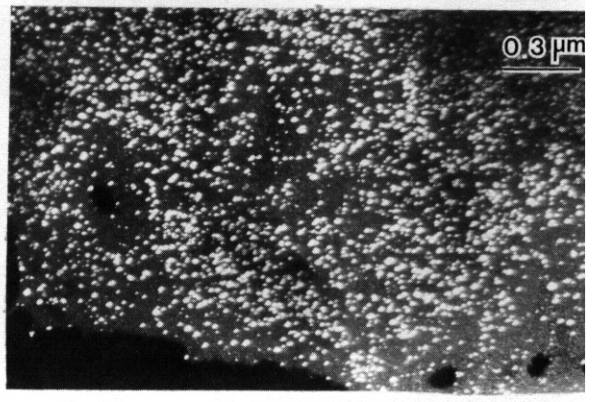

Finure 8.1.11. Dark Field Image of Intergranular Precipitates Obtained from <100> Streak in Diffraction Pattern of Beryllium Copper Alloy after Irradiation at 500°C to 5 dpa and 150 appm Helium.

Al-60

The dispersion hardened Cu - 0.6 wt% Al (Al_2O_3) material has exhibited the greatest microstructural stability of the three alloys exposed to these irradiation conditions, Figure 8.1.12 and 8.1.13. In a few regions with low number densities of alumina particles, some irradiation-induced dislocation rearrangement and reduction in dislocation density is observed. However, even in these regions, no bubbles or voids are visible at fluences up to ∿5 dpa and helium levels of ∿150 appm at 425°C or 500°C. Over most of the regions examined, particle/matrix interfacial strains and dislocation structure visible in weak beam dark field images near the angular shaped Al_2O_3 particles are retained after irradiation and/or thermal aging. This suggests that a high density of point defect recombination and helium trapping sites exists in the alloy in the hot extruded condition.

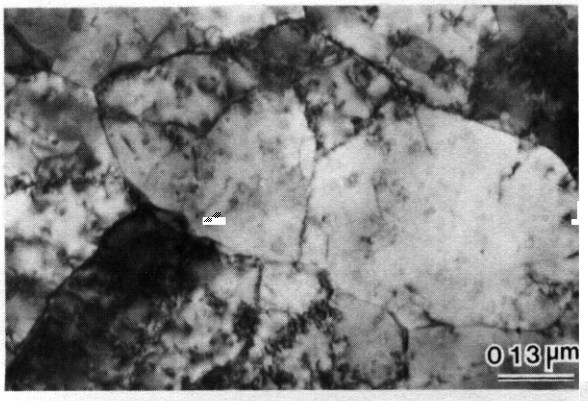

Figure 8.1.12. Low Magnification Micrograph of Al-60 Alloy after Irradiation to ∿5 dpa and 150 appm He at 500°C.

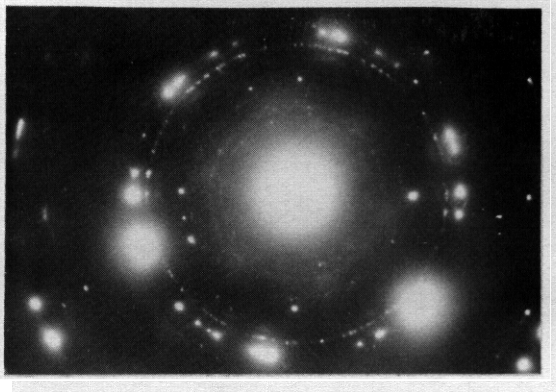

(a)

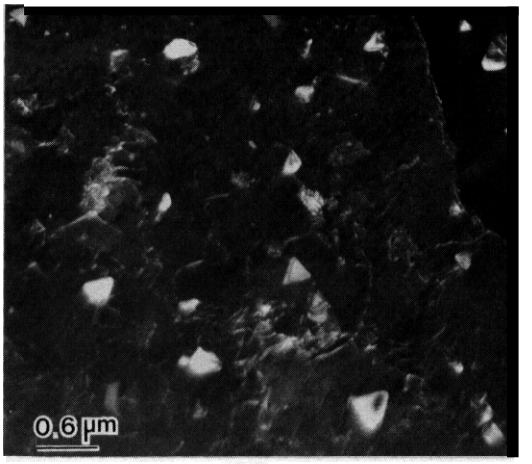

(b)

Figure 8.1.3. a) Selected Area Diffraction Pattern Showing Matrix Spots from Cu and Rings From Angular $A1_2O_3$ Particles and b) Associated Dark Field Image of Particles Including a Weak g = [222] Cu Matrix Reflection in Al-60 Alloy after Irradiation to ∿5 dpa and 150 appm He at 500°C.

8.1.5 Future Work

As a result of the inhomogeneities observed in the thermal aging and irradiation response of the Amzirc alloy, efforts are being concentrated on the beryllium copper and Al-60 materials. Specimens of those alloys have been subjected to dual ion irradiation at 300°C and 350°C to oeak damage levels of 100 dpa. Data obtained from the flat portion of the damage curve will cover the fluence range of 10 dpa to 20 dpa and helium levels of 300 apom to 600 appm. Examination is in orogress. Irradiation at still lower temperatures and hiqher fluences is planned for late January 1985.

8.1.6 References

1. M. Y-W. Lou and N. J. Grant, MET. Trans. A, 15A, 1491-1493 (1984).

2. N. F. Mott and H. Jones, "The Theory of the Properties of Metals and Alloys" Dover Publications Inc. New York (1958).

3. K. B. Alexander, D. A. Steigerwald and D. E. Laughlin, "Effect of Continuous Precipitation Kinetics on Discontinuous Precipitation in Cu-Be and Al-Ag Alloys", in "Solid-Solid Phase Transformations" Ed. H. I. Aaronson, D. E. Laughlin, R. F. Sekerka and C. M. Wayman, TMS-AIME, p. 945-949 (1982).

4. W. M. Stacey, et. al. Critical Issues, Volume I, USA Fed-Intor/82-1, Appendix VII.A Materials Data Base Assessment, Section A.2.2, Properties of Copoer Alloys, p. 404 (1982).

5. F. N. Rhines, and R. F. Mehl, Trans. AIME 128 185-220 (1938).

6. J. A. Soitznagel, W. J. Choyke, J. Lauer, 8. O. Hall, J. N. McGruer, J. R. Townsend and R. B. Irwin, J. Nucl. Mater. 117, 198-207 (1983).

7. J. N. McGruer, D. S. Croft, R. B. Irwin, J. A. Rabel, J. H. Sheehan, W. J. Choyke and N. J. Doyle, Proc. Fourth Int. Conf. on Ion Imolantation Equipment and Techniques, Berchtesgaden Germany September (1982).

8. R. W. Knoll, "Effects of Heavy-Ion Irradiation on the Phase Stability of Several Coooer-Base Alloys" Ph.D. Thesis, University of Wisconsin-Madison (1981).

9. R. J. Rioja and D. E. Laughlin, Acta Met. 28, 1301-1313 (1980).

10. L. E. Tanner, Phil. Mag. 14, 111-130 (1966).

11. R. R. Hart, B. C. Wonsiewicz and G. Y. Chin. Met. Trans. 1, 3163-3171 (1970).

12. R. J. Livak and F. W. Clinard, "High Dose Neutron Radiation Damage Study of Coooer Alloys for the CRFPR First Wall" Los Alamos National Laboratory FY1984 Energy Systems ISRD Annual Report (1984).

13. S. J. Zinkle, G. L. Kulcinski and R. A. Dodd. "Microstructure of High-Strength, High Conductivitv Copper Alloys Irradiated at Low Temperatures; pp. 149-153 in DAFS Quarterly Progress Report, August 1984, DOE/ER-0045/18, U.S. DOE, Office of Fusion Energy.

14. H. R. Brager, H. L. Heinisch, and F. A. Garner, Effects of Neutron Irradiation at 450°C and 16 dpa on the Properties of Various Commercial Copper Alloys" Proc. Int. Conf. on Fusion Reactor Materials, Tokyo, Japan, December 3-5, 1984, and HEDL-SA-3174 (1984).

8.2 EFFECTS OF NEUTRON IRRADIATION AT 450°C AND 16 dpa ON THE PROPERTIES OF VARIOUS COMMERCIAL COPPER ALLOYS - H. R. Brager, H. L. Heinisch, and F. A. Garner (Hanford Engineering Development Laboratory)

8.2.1 AOIP Tasks

Not included in current ADIP Task Structure.

8.2.2 Objective

The object of this effort is to provide data on the radiation-induced response of high conductivity alloys.

8.2.3. Summary

High-purity copper and eight copper alloys were irradiated to ~16 dpa at ~450°C in the MOTA experiment in FFTF. These alloys were also examined after aging at 400°C for 1000 hours. The radiation-induced changes in the electrical conductivity, tensile properties and density were measured and compared to those of the aged materials. The changes in conductivity can be either positive or negative depending on the alloy. Changes in tensile properties of most, but not all, of the alloys seem to be primarily dependent on thermal effects rather than the effect of atomic disolacements. Radiation at 450°C induced chanaes in density varying from 0.66% densification to 16.6% swelling. The latter occurred in Cu-0.1% Ag and implies a swelling rate of at least 1%/dpa.

8.2.4 Progress and Status

8.2.4.1 Introduction

Copper alloys have been proposed for service in fusion reactors, not only for magnets but also for components which must withstand high levels of heat flux.[1] While many irradiation experiments have been conducted on copper and copper alloys,[2] there is very little data at high neutron exposure levels. In order to provide such data, a series of representative commercial copper alloys is now being irradiated in the Materials Open Test Assembly (MOTA) in the Fast Flux Test Facility (FFTF), located in Richland, WA. The first of four discharges of this experiment has occurred for specimens irradiated to 2.5 x 10^{22} n/cm² (E > 0.1 MeV). This corresponds to ~16 dpa in pure copper. Only data for one temperature, ~450°C, is currently available.

8.2.4.2 Experimental Details

The alloys listed in Table 8.2.1 were irradiated in the form of miniature tensile specimens and standard microscopy disks, both of which were punched from the same sheet. While the discs are used only for microscopy, the tensile specimens provide data on changes in density, electrical conductivity and tensile properties, all measured at room temperature. Identical tensile specimens were also subjected to thermal aging at 400, 500, 600 and 700°C for 1000 hours and others are being aged to 10,000 and 30,000 hours. Those specimens aged at 400°C for 1000 hours have been examined in order to partially separate the effects of temperature and irradiation.

The specimens were irradiated in 4 mm diameter helium-filled sub-capsules and were tightly packed with copper specimens separated with aluminum foil spacers. The aluminum minimizes self-welding of copper specimens. The copper specimens span four classes: pure metal, and solution-strengthened, precipitation-hardened and dispersion-strengthened alloys. A nickel-beryllium alloy and AISI 316 were also included, the latter as a reference material.

8.2.4.3 Results

Tables 8.2.1 and 8.2.2 contain the measured changes in density, electrical conductivity and tensile Properties, all measured at room temperature. A wide range of density changes was observed. The Cu-Be and Ni-Be alloys densified as did the reference AISI 316. Of the remaining alloys, the lowest swelling (0.13%) occurred in the dispersion-strengthed Cu-0.25 Al_2O_3 alloy. Relatively large swellings were observed in annealed zone-refined copper (6.5% $\Delta V/V_o$), CuAgP (7.9%) and Cu-0.1 Ag (16.6%). The latter represents a swelling rate of at least 1%/dpa.

The electrical conductivity measurements were all determined relative to that obtained for the unirradiated zone-refined copper specimen, which was assumed to have an International Annealed Copper Standard (IACS) value of 101%. The pre- and post-irradiation conductivities were determined on the same specimen using a four point resistivity technique.

The radiation-induced changes in conductivity varied strongly among the alloys but appear to exhibit some correlation with the conductivity of the unirradiated material, as shown in Figure 8.2.1. Alloys which contained beryllium increased in conductivity while those that did not contain beryllium decreased. The largest reduction occurred in the Cu-0.1 Ag alloy, which also had the highest swelling.

With respect to thermally or radiation-induced changes in mechanical properties, the alloys developed three separate classes of behavior, as shown in Fig. 8.2.2. In the first group (zone-refined copper and solution-strengthened low-solute alloys CuAg and CuAgP) the yield strengths after irradiation were relatively small and essentially identical to those produced by aginq, indicating that the high test temperature is the controlling factor in the response of the alloy.

In the second group, two of the precipitation-hardened copper alloys containing beryllium lost a larger fraction of their strength upon aging and exhibited a measurable but moderate further decrease due to irradiation. Finally, in the third group [CuBeNi(AT), CuAl25 and MZC], aging had little effect and the major decrease was attributable to the irradiation. The chanqes induced in uniform elongation by both aging and irradiation are not so easily characterized. However, the largest reduction in uniform elongation of aged or irradiated specimens occured in alloys which swelled the most.

8.2.5 Discussion

In addition to microstructural changes induced by thermal aging and irradiation, transmutation also occurs. In the FFTF spectrum it was calculated that 0.1 wt.% nickel would be produced by transmutation in pure copper and that less than 0.01 wt.% metallic elements would be produced from various solute elements in the other alloys. Helium is produced at this dpa level in pure copper, CuBeNi and CuBe alloys at levels of about 2, 5 and 20 appm, respectively. These transmutant levels are not expected to significantly influence the room temperature properties measured in this study.

These are two particularly significant aspects of the results of this study. First, all but three of the copper alloys responded more to the irradiation temperature than to the displacement of atoms. Second, it is believed that copper alloys exhibit the propensity to swell at rates of at least ~1%/dpa, as indicated by the copper-0.1% silver alloy. Thus copper behaves in a similar manner to that of pure nickel, simple Fe-Ni-Cr ternary alloys and commercial austenitic stainless steels.[3] The lower swelling of zone-refined copper is thought to be a reflection of the tendency of pure metals to saturate in swelling. Makin has shown that the addition of 1% silver to copper shortens the transient regime of swelling in electron-irradiated copper and also suppresses the tendency of copper to saturate in swelling at 250°C.[4] In the CuAgP alloy there is three times as much Ag as in the CuAg alloy, but the swelling of 7.9% is lower. The decrease in swelling is probably due to the presence of phosphorus rather than the increase in silver. Phosphorus is known to strongly extend the transient regime of swelling in Fe-Cr-Ni alloys[3] and may serve the same role in copper.

The data in Table 8.2.1 show that beryllium is an effective suppressor of swelling in copper, particularly at the 2% level. Makin also showed in his electron irradiation studies that the addition of 1% beryllium at 250°C resulted in a total suppression of swelling to 100 dpa.[4] One clue to beryllium's effectiveness in suppressing swelling lies in the large densification observed in the Cu-2% Be alloy. Such changes in density are usually associated with segregation and/or formation of ordered phases, particularly when substantial solute-solvent misfit is involved. Indeed, beryllium has a large negative misfit of -26% and forms CuBe precipitates in Cu-1.35 at % Be during ion irradiation in the range of 300-700°K.[5/6] Beryllium additions were also shown to strongly enhance diffusion in copper during irradiation.[6] Both ordering and solute-enhancement of diffusion rates are thought to influence swelling.

The most interesting swelling response in the MOTA experiment was that of Cu-0.25 Al_2O_3. Alumina additions should be inert at this temperature and yet the swelling was reduced from the 6.5% level of pure copper to only 0.13%.

It is anticipated that the changes in yield strength and conductivity arise partially from the swelling but are related primarily to the changes in matrix solute level, dislocation microstructure and precipitate distribution and identitv. For those alloys with acceptably low swelling, the optimum alloy for a given application will be chosen on the basis of its strenuth'and its electrical or thermal conductivity. Fig. 8.2.3 presents a comparative compilation of the pre-irradiation and post-irradiation strength and electrical conductivity data for the copper alloys discussed in this paper.

8.2.6 Conclusions

Copper alloys may swell at rates approaching ~1%/dpa during neutron irradiation at 450°C. Zone-refined copper, however, appears to be swelling at a somewhat lower average rate, perhaps due to saturation. Addition of various alloying or hardening elements can delay or suppress swelling. Irradiation also induces changes in tensile properties and electrical conductivity that vary widely among the alloys and depend on their starting condition. In many of the copper alloys studied, the changes observed during irradiation at 450°C seem to be related primarily to the irradiation temperature rather than to the direct effect of the irradiation itself.

Table 8.2.1. Swelling of various commercial copper alloys, Ni-1.9Be and AISI 316 in MOTA at ~450°C and 2.5 x 10^{22} n/cm^2 (E > 0.2 MeV)

	Alloy Composition	Condition	% Swelling
Cu (MARZ)	Cu (99.999%)	Annealed	6.5
CuAg	Cu-0.1 Ag	20% CW	16.6
CuAgP	Cu-0.3 Ag-0.06 P-.08 Mg	20% CW	7.9
CuNiBe (1/2 HT)+	Cu-1.8 Ni-0.3 Be	20% CW & Aged (3 hr at 480°C)	1.70
CuNiBe (AT)'	Cu-1.8 Ni-0.3 Be	Annealed & Aged (3 hr at 480°C)	0.29
CuBe (1/2 HT)	Cu-2.0 Be	20% CW & Aged (2 hr at 320°C)	-0.18
CuBe (AT)	Cu-2.0 Be	Annealed & Aged (2 hr at 320°C)	***-0.66***
MZC	Cu-0.9 Cr-0.1 Zr-0.05 Mg	*90%* CW, Aged 1/2 hr at 470°C	1.03
Cu-A125	Cu-0.25 Al_2O_3	20% CW	0.13
NiBe	Ni-1.9 Be	Annealed *R* Aged 1 1/2 hr at 500°C	-0.37
AISI 316 (heat CN-13)*	Fe-18 Cr-13 Ni-2.5 MO-0.5 Si	Annealed	-0.20

*Included as a standard reference material.
+1/2 HT and AT are industry designations for half-hard and tempered, and annealed and tempered, respectively.

8.2.7 Future Work

Microscopy examination will proceed on these alloys.

8.2.8 References

1. F. W. Wiffen and R. E. Gold, Eds., "Copper and Copper Alloys for Fusion Reactor Applications," Proceedings CONF-830466, Washington, D.C., April 1983.
2. S. J. Zinkle and R. W. Knoll, "A Literature Survey of Radiation Damage Data for Copper and Copper Alloys," University of Wisconsin - Madison Report, UWFDM-578, June 1984.
3. F. A. Garner, J. Nucl. Mater., 122 & 123 (1984), pp. 459-471.
4. M. J. Makin in Voids Formed by Irradiation of Reactor Materials, S. F. Pugh, Ed., British Nuclear Energy Soc. (1971) 269.
5. R. Koch, R. P. Wahi, and H. Wollenberger, J. Nucl. Mater., 103 & 104 (1981) 1211.
6. M. P. Macht, V. Naundorf, R. P. Wahi, and H. Wollenberger, J. Nucl. Mater., 122 & 123 (1984) 698.

Table 8.2.2. Pmperties of various copper alloys

	Electrical Conductivity (% IACS)		Yield Strength (MPa)			Uniform Elongation (%)		
	Unirradiated	Irradiated**	Unirradiated	Aged*	Irradiated**	Unirradiated	Aged*	Irradiated*+
Copper (99.999%) Zone-Refined	101	86	**58**	58	**43**	**28**	26	14
Solution-Strengthened								
CuAg	**97**	77	**254**	78	57	2.2	**34**	11
CuAgP	**96**	**80**	**408**	115	**109**	**2.1**	**24**	**9.8**
Dispersion-Strengthened								
CuAl25	84	73	**483**	476	396	**1.8**	5.5	**5.9**
Precipitate-Strengthened								
MZC (HT)	83	77	**450**	**401**	767	**2.5**	6.2	8.7
CuBeNi (1/2 HT)	74	84	563	308	211	3.2	8.9	12
CuBeNi (AT)	61	71	561	566	451	**3.4**	1.3	**0.9**
CuBe (1/2 HT)	18	29	647	403	351	**7.7**	15	11

*Aged 1000 hours @ 400°C.
**Irradiated at ~450°C to ~ 16 dpa 2.5 x 10^{22} n/cm^2 (E > 0.1 MeV) in the MOTA of the FFTF.

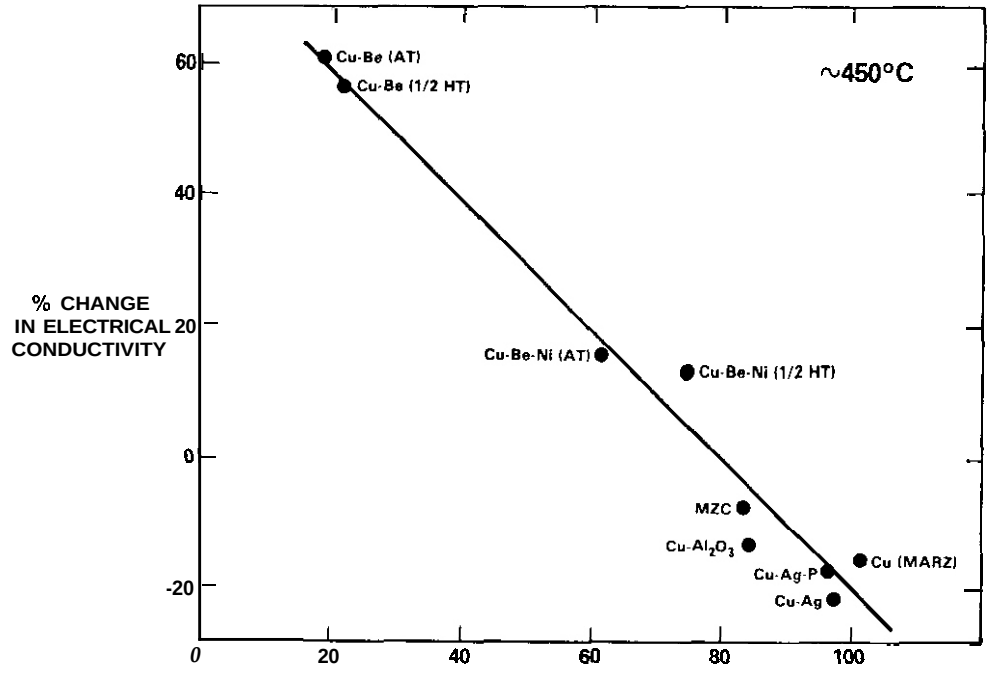

Fig. 8.2.1. Conductivity changes observed in various copper alloys after irradiation at approximately 450°C in MOTA-FFTF to 16 dpa.

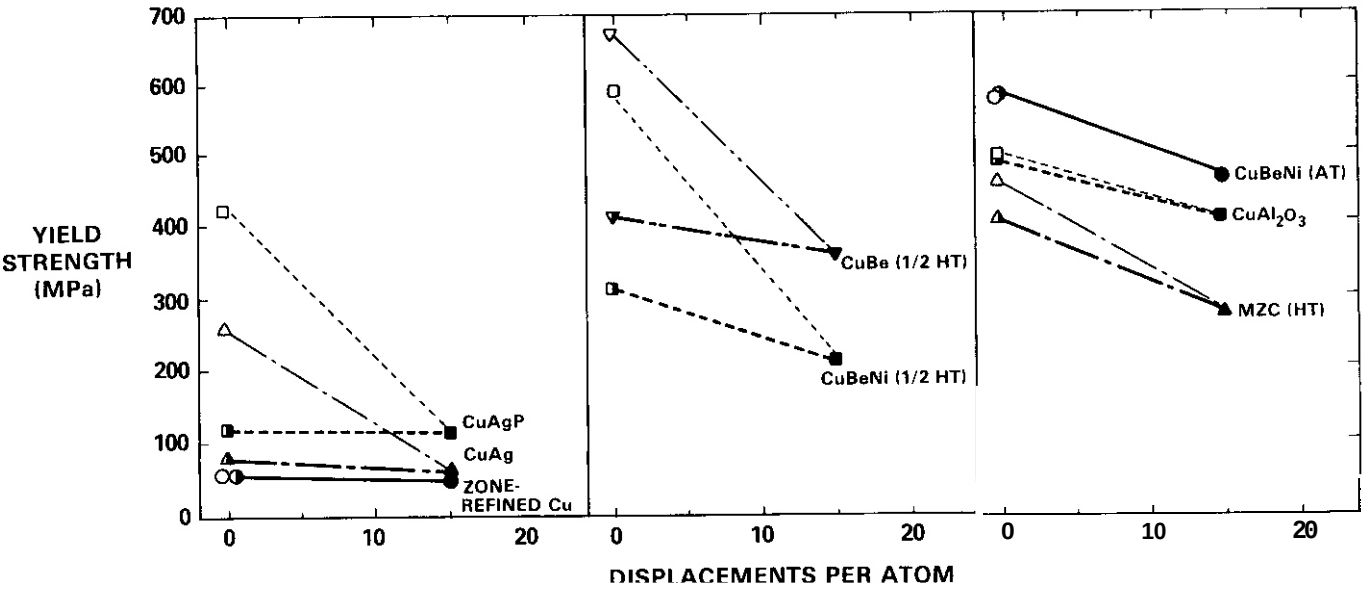

Fig. 8.2.2. Effects of aging or neutron irradiation on the yield strength of copper alloys. Open symbols denote as-prepared condition, half-filled symbols the aged condition (400°C for 1000 hr) and solid symbols refer to the irradiated condition (16 dpa at ~450°C).

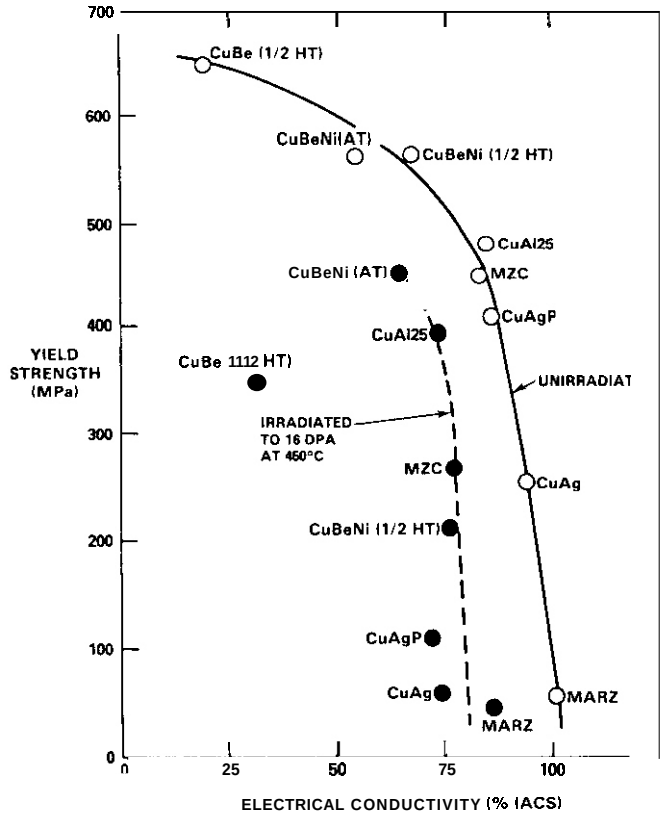

Fig. 8.2.3. Shift in strength and electrical conductivity of copper alloys due to irradiation to ~16 dpa at ~450°C. The trend lines shown in this figure do not imply an identical shift for each alloy.

9. MATERIALS COMPATIBILITY AND HYDROGEN PERMEATION STUDIES

9.1 CORROSION OF LOW ACTIVATION AUSTENITIC ALLOYS AND STANDARD Fe-12 Cr-1 MoVW STEEL IN THERMALLY CONVECTIVE LITHIUM — P. F. Tortorelli and J. H. DeVan (Oak Ridge National Laboratory)

9.1.1 ADIP Task

ADIP Task I.A.3, Perform Chemical and Metallurgical Compatibility Analyses.

9.1.2 Objective

The purpose of this task is to determine the corrosion resistance of candidate first-wall materials to slowly flowing lithium in the presence of a temperature gradient. Corrosion and deposition rates are measured as functions of time, temperature, additions to the lithium, and flow conditions. These measurements are combined with chemical and metallographic examinations of specimen surfaces to establish the mechanisms and rate-controlling processes for dissolution and deposition reactions.

9.1.3 Summary

Manganese-containing steels (15-30 wt %) experienced substantial corrosion when exposed to thermally convective lithium at 500°C with the 30 wt % Mn steels showing unacceptably high corrosion losses. The mass transfer of 12 Cr-1 MoVW steel at 600°C in lithium was significantly less than that of type 316 stainless steel exposed under similar conditions.

9.1.4 Progress and Status

Because of their lower activation during neutron irradiation, manganese-containing austenitic stainless steels are currently being investigated as part of the fusion alloy development effort. Consequently, an initial, qualitative assessment of the resistance of such steels to corrosion by molten lithium has been conducted using specimens provided by Hanford Engineering Development Laboratory. The compositions of these specimens are given in Table 9.1.1. The only prior work with manganese steels in liquid lithium was reported by Rued1 et al.,[1-3] who showed that, as with nickel in the 300 series of stainless steel, manganese is preferentially leached from the alloy surface such that a phase transformation from austenite to ferrite occurs in the manganese-depleted zone.

Table 9.1.1. Compositions of Fe-Mn-Cr and Fe-Ni-Cr steels exposed to thermally convective lithium between 500 and 480°C

Alloy	Composition (wt %)						
	Mn	Cr	Ni	C	N	Si	Fe
18-18+	18	18	0.5	0.1	0.4	0.6	bal
AMCR	17	10	0.7	0.2	0.06	0.6	bal
R88	15	15	0.5	0.3	0.30	0.4	bal
Y75	30	2	0.5	0.1	0.15	0.4	bal
R77	30	2	0.5	0.6	0.15	0.4	bal
R80	30	10	0.5	0.50	0.10	0.4	bal
CN13	1.7	17	14.0	0.05		0.6	bal
316 SS	2	17	10	0.05		0.4	bal

Our experiments with the low activation alloys have been conducted using a thermal convection loop with removable specimens (of a type described previously[4]). The loop was constructed of type 316 stainless steel which, because of prior operation with lithium and associated preferential leaching of nickel and chromium, was known to have a considerably higher iron concentration at hot leg surfaces than found in the starting material. The specimens of interest were exposed to lithium in a region of the loop near the top of the hot leg. Because of the non-isothermal nature of the loop, the temperatures of these specimens varied from 500°C [maximum loop temperature (T_{max})] to 480°C. However, this temperature difference was small relative to the temperature differential (ΔT) of the loop (150°C). Coupons of type 316 stainless steel were included with the seven alloys listed in Table 9.1.1 and also at the standard specimen positions around the remainder of the loop. All specimens were exposed for a total of 3340 h during which time they were thrice removed for intermediate and final weighings.

The weight change results for the type 316 and manganese-containing steels are compared in Fig. 9.1.1. Of the higher manganese alloys (R80, R88, X75, AMCR, R77, 18-18+), those containing 30 wt % Mn suffered very large weight losses, while the alloys containing between 15 and 18 wt % Mn showed relatively small net weight changes. Given an exposure temperature of 500°C, the present results, while qualitative in nature, indicate unacceptably-high corrosion rates for 30 wt % Mn alloys in thermally convective lithium. Furthermore, the lower manganese alloys experienced significant corrosion despite the low net weight changes shown in Fig. 9.1.1: scanning electron microscopy and associated energy' dispersive x-ray analysis revealed a complex overall corrosion process that resulted in the depletion of manganese and surface enrichment in chromium (see Figs. 9.1.2 and 9.1.3). As shown in Fig. 9.1.2, nodular deposits were observed on all the exposed surfaces. While the size and density of such nodules varied among the specimens, these features were found, in all cases, to be greatly enriched in chromium relative to the underlying matrix (see, for example, Fig. 9.1.4). In addition, closer examination of the surface underlying the deposits showed it to be roughened, porous (in some cases), and depleted in manganese to below 2 to 3 wt %. It is thus apparent that the lower manganese alloys (18-18+, AMCR, RRR) also suffered significant dissolution but that the associated weight losses were offset by weight gains due to the deposition of chromium onto the specimen surfaces. This, therefore, resulted in the relatively small net weight changes that were measured. On the

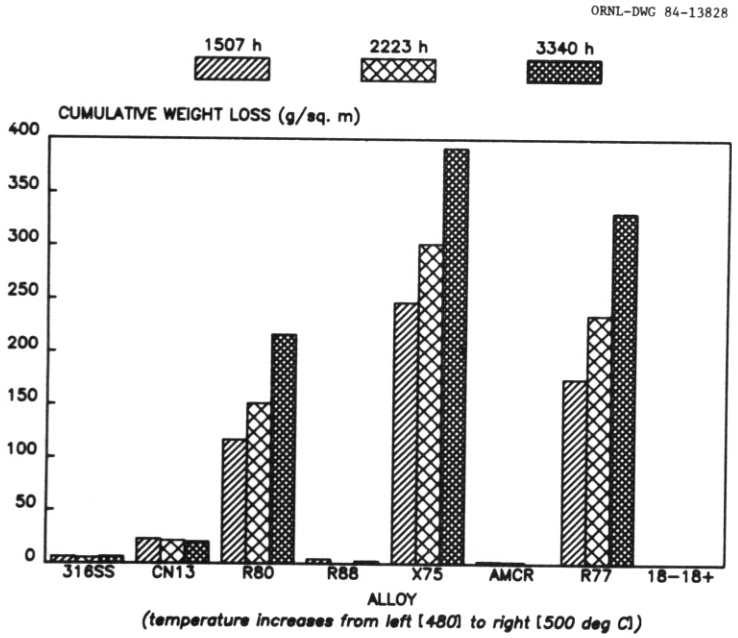

Fig. 9.1.1. Net weight loss for various alloys exposed to thermally convective lithium. Low net weight losses are indicative of competing dissolution and deposition reactions.

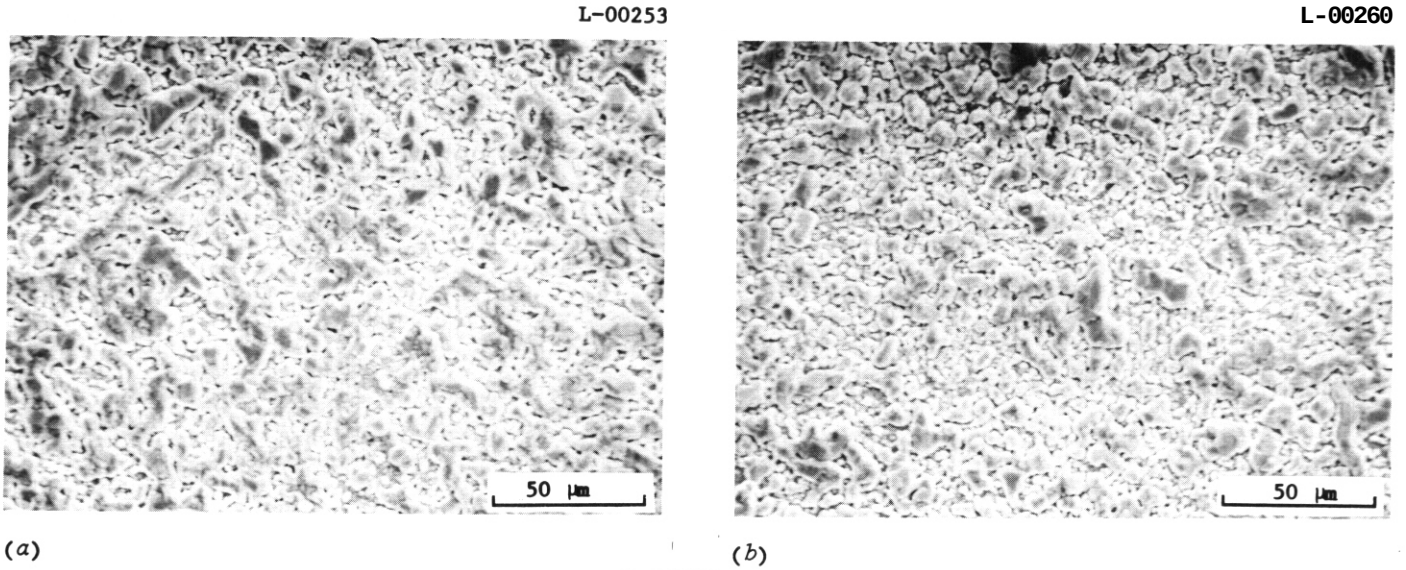

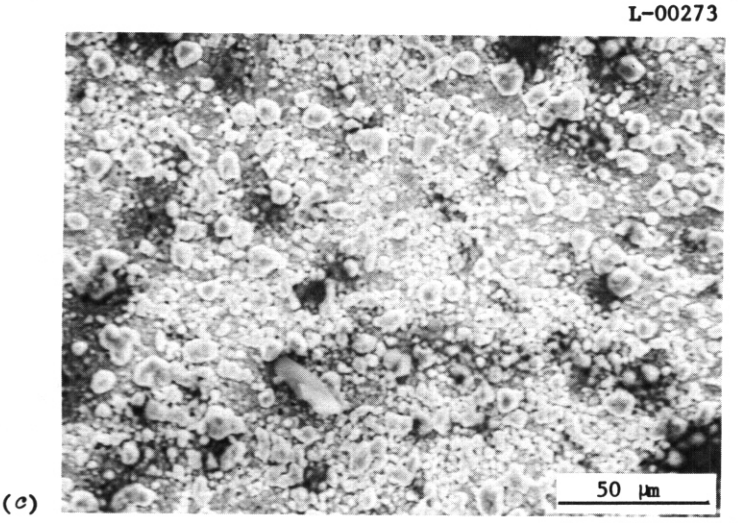

Fig. 9.1.2. Scanning electron micrographs of manganese steels exposed to thermally convective lithium for 3340 h, *(a)* 18-18+, 500°C, *(b)* AMCR, 495°C, *(c)* R88, 490°C.

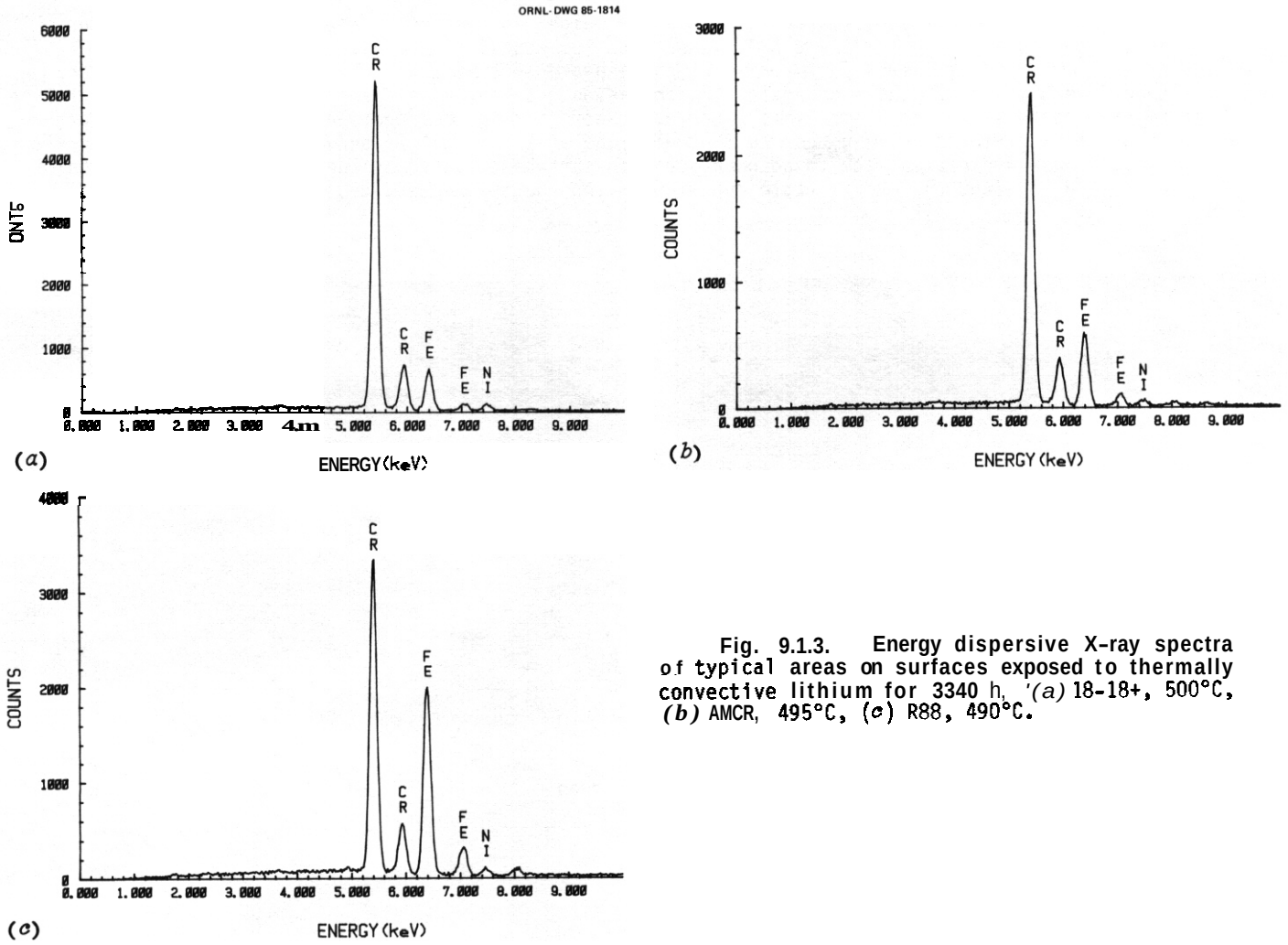

Fig. 9.1.3. Energy dispersive X-ray spectra of typical areas on surfaces exposed to thermally convective lithium for 3340 h, *(a)* 18-18+, 500°C, *(b)* AMCR, 495°C, *(c)* R88, 490°C.

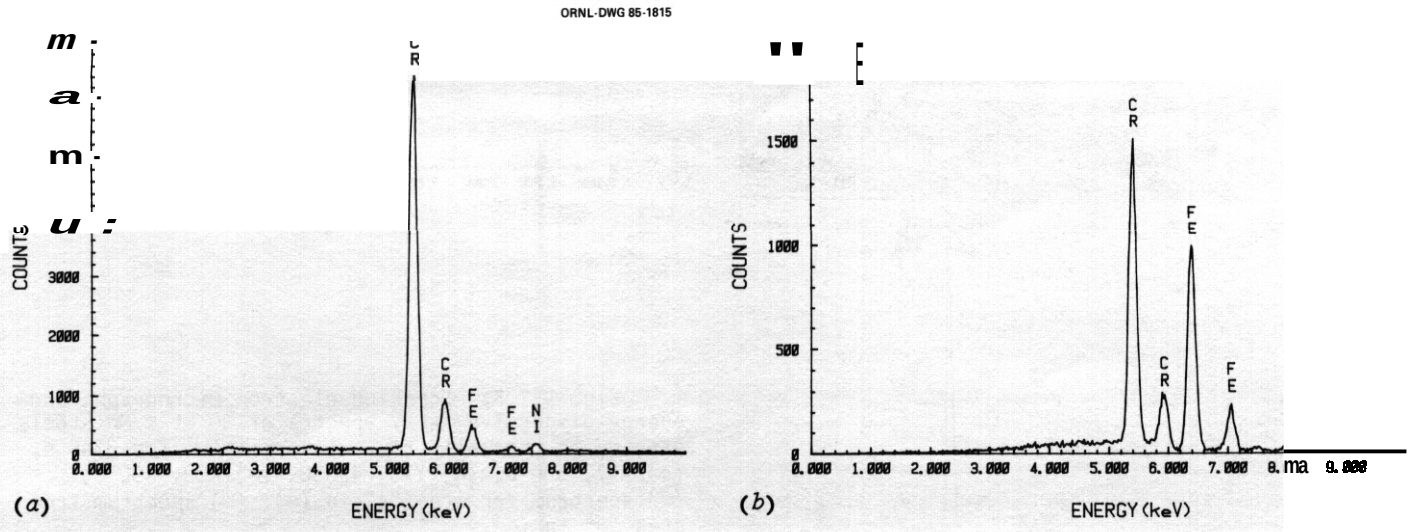

Fig. 9.1.4. Typical energy dispersive X-ray spectra of nodule *(a)* and matrix *(b)* for 18-18+, AMCR, and R88 exposed to thermally convective lithium for 3340 h at 490–500°C; spectra shown are from 18-18+ specimen surface.

other hand, the 30 wt % Mn alloys suffered large overall weight losses due to their higher starting concentrations of manganese and, for X75 and R77, fewer chromium deposits (see Fig. 9.1.5).

The general surface enrichment in chromium of the exposed specimens and the distinct chromium-rich deposits that formed indicate that substantial concentration gradient mass transfer occurred in the hot zone in which these specimens were located. This chromium transfer among the specimens in the hot leg occurred in association with transport of manganese to the cold zone of the loop. As shown in Fig. 9.1.6, discrete deposits of manganese and nickel were found on a specimen surface situated at the lowest temperature point of the loop's cold leg (350°C). Very little chromium or iron deposition was detected in these colder regions.

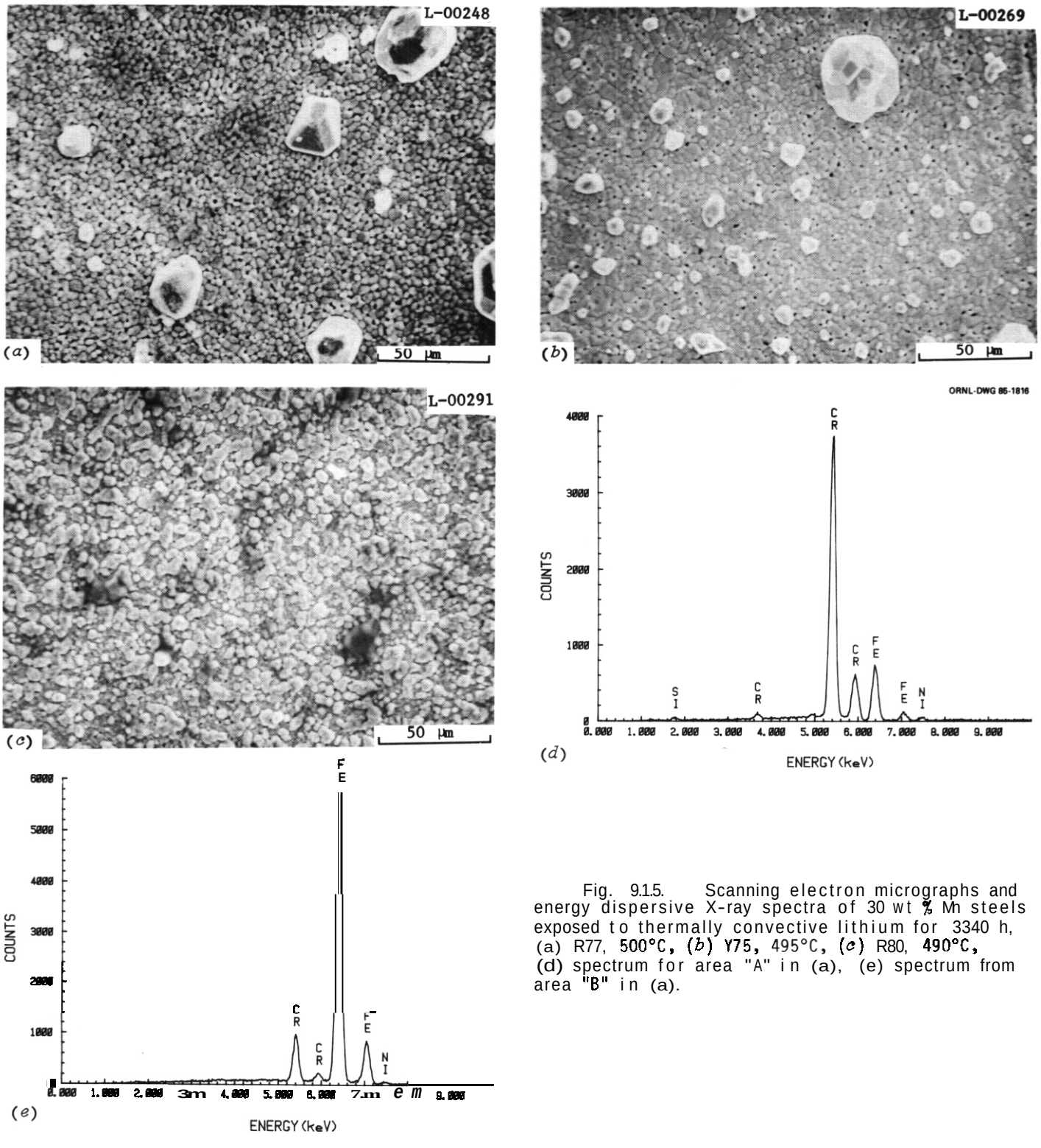

Fig. 9.1.5. Scanning electron micrographs and energy dispersive X-ray spectra of 30 wt % Mn steels exposed to thermally convective lithium for 3340 h, (a) R77, 500°C, (b) Y75, 495°C, (c) R80, 490°C, (d) spectrum for area "A" in (a), (e) spectrum from area "B" in (a).

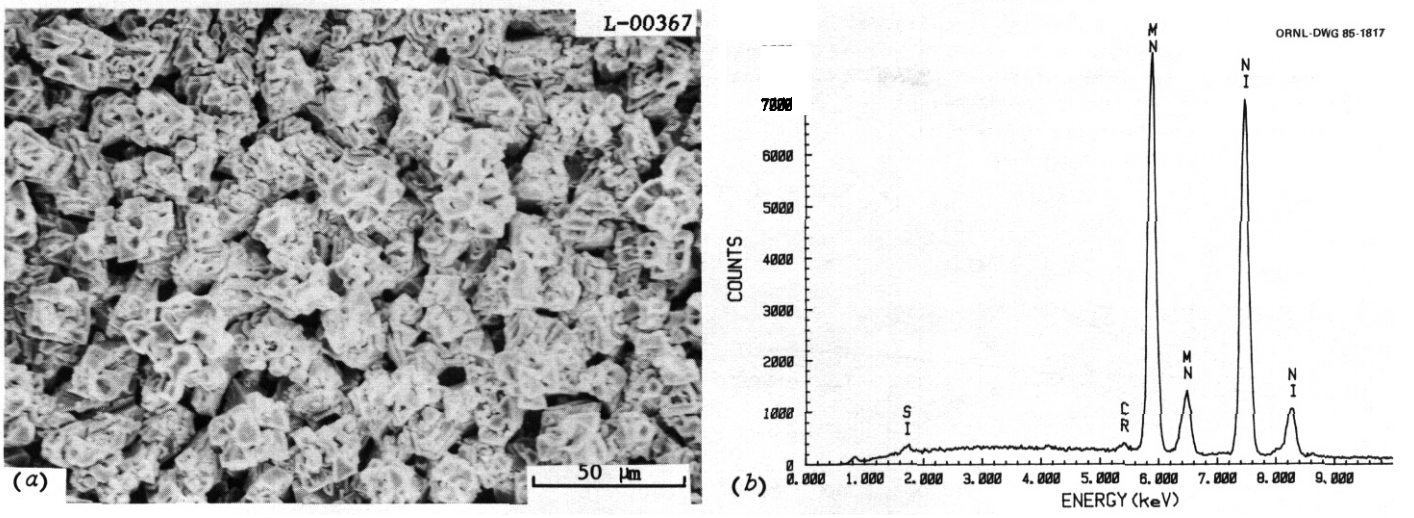

Fig. 9.1.6. (a) Scanning electron micrograph of deposits on a type 316 stainless steel coupon located in the cold leg (350°C) of a lithium loop operated with Mn steel specimens in the hot leg for 3340 h. Maximum loop temperature was 500°C. (*b*) Typical energy dispersive X-ray spectrum from deposits such as shown in (*a*).

The hot leg dissolution/deposition reactions involving chromium may be exacerbated by the relatively high nitrogen concentrations of the manganese steels (see Table 9.1.1) and the possibility for Cr-N and Li-Cr-N reactions at the steel surfaces.[5,6] Indeed, experimental observations have shown that higher levels of nitrogen in lithium and/or in steel can increase corrosion.[1,6-8] Furthermore, in the present case, it was qualitatively observed that a higher starting N/Cr concentration ratio led to decreased Cr/Fe ratios (i.e., increased dissolution of chromium) in the underlying matrix. Consequently, a significant amount of chromium can be expected to be dissolved from, and reacted with, the surfaces in the loop's hot zone depending on various localized concentration gradients. On the other hand, nitrogen-related reactions appear much less important in the case of manganese (or nickel) such that the deposition of this element is controlled by the thermal gradient in the lithium system.

The complexity of the overall corrosion process prohibits a comprehensive explanation of all the observations described above. While the present results show that 30 wt % Mn alloys are not acceptable for lithium service at 500°C, they are less definitive in the case of the alloys containing 15 to 18 wt % Mn due to the competing effects of chromium deposition and manganese dissolution. However, the scanning electron microscopy and energy dispersive x-ray analysis of the exposed surfaces do reveal that such alloys are subject to rather extensive dissolution when exposed to thermally convective lithium at 500°C and, consequently, are not particularly corrosion resistant. These results are consistent with earlier work in static lithium,[1-3] which showed that manganese-containing alloys suffered preferential dissolution and that the high nitrogen concentrations of these steels would accelerate corrosion in lithium.

In the preceding progress report,[9] we reported that the initfal weight change results from a loop experiment in which 12 Cr-1 Mo VW steel was exposed to thermally convective lithium circulating between 600 and 450°C showed substantial changes in the mass transfer profile when compared with data from a lower temperature loop experiment with this alloy. Thermal gradient mass transfer appeared to become the dominant corrosion mechanism at the higher temperatures, while (C,N) reactions were thought to be more important at the lower temperatures.[10] Longer-term results at the higher loop operating temperatures continue to support this conclusion. Weight loss data for the 12 Cr-1 MoVW steel at 600°C over a test period of 5960 h are shown in Fig. 9.1.7 and reveal a dissolution rate of 3.0 mg/m^2·h determined on the basis of linear dissolution kinetics. Data for HT-9 at a maximum loop temperature of 500°C, also shown in Fig. 9.1.7, show a higher initial corrosion rate followed by a much lower "steady state" ratio. As shown in Fig. 9.1.8, the dissolution rate of 12 Cr-1 MoVW steel at 600°C is significantly less than that of type 316 stainless steel exposed in a lithium-type 316 stainless steel loop under similar conditions.

While the present and preceding 12 Cr-1 MOVW steel loop results have shown that thermal gradient mass transfer becomes dominant at the higher temperature (600°C), surface analysis of a corner clipped from a specimen exposed at 600°C revealed that one or more other corrosion reactions are still occurring at this temperature. Specifically, preliminary scanning electron microscopy and energy dispersive x-ray analysis showed the presence of chromium-rich nodules on the surface of a 12 Cr-1 MoVW steel that suffered net dissolution. Such a finding, if confirmed by ongoing analyses of other exposed surfaces, would indicate that interstitial reactions with chromium are probably influencing the overall corrosion behavior in lithium even at the higher temperatures. These reactions may very well be similar (although less in magnitude) to those discussed above in relation to chromium transfer in the hot zone of the lithium loop containing the manganese steel specimens.

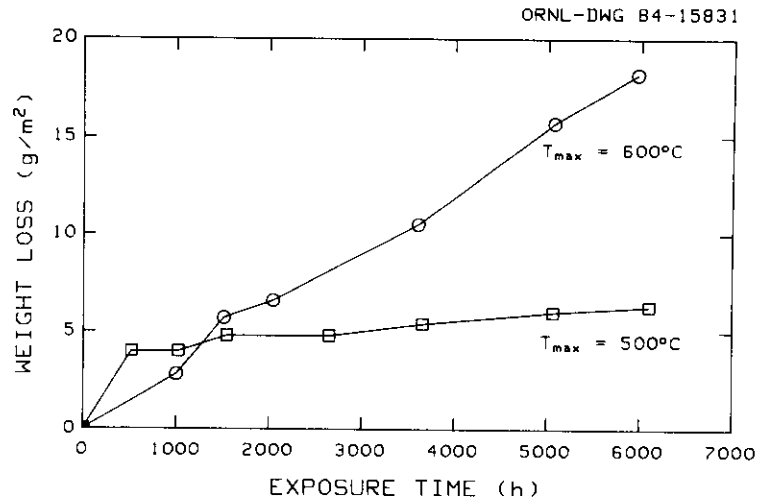

Fig. 9.1.7. Weight loss versus exposure time for 12 Cr-1 MoVW steel in thermally convective lithium.

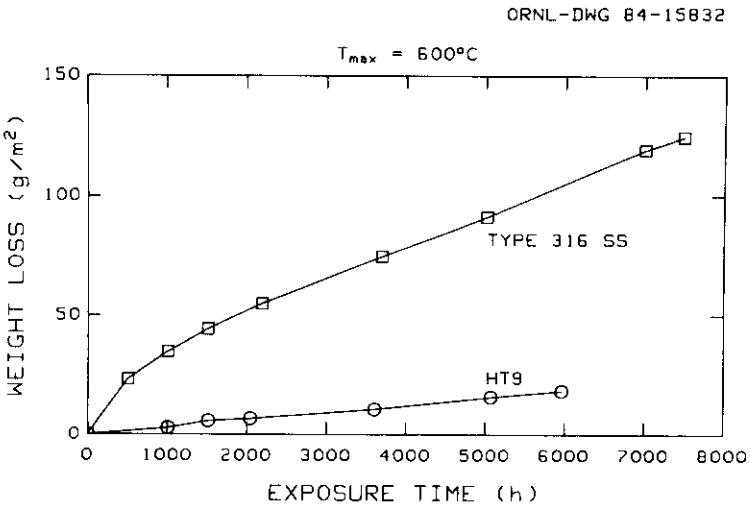

Fig. 9.1.8. Weight loss versus exposure time for 12 Cr-1 MoVW steel and type 316 stainless steel exposed to thermally convective lithium at 600°C.

9.1.5 Conclusions

1. Manganese-containing steels suffered significant corrosion when exposed to thermally convective lithium circulating between 500 and 350°C. In particular, the 30 wt % Mn steels exhibited very severe corrosion. Thermal gradient mass transport of manganese and hot leg reactions with chromium were observed.
2. The small net weight changes of the 15 to 18 wt % Mn steels exposed to lithium resulted from competing processes of manganese dissolution and chromium deposition.
3. Thermal gradient mass transfer is the dominant corrosion process for 12 Cr-1 MoVW steel exposed to thermally convective lithium circulating between 600 and 450°C. However, there is some evidence that chromium reactions also occur under these conditions. The dissolution rate of 12 Cr-1 MoVW steel in this lithium at 600°C was significantly less than that measured for type 316 stainless steel measured under similar conditions.

9.1.6 References

1. E. Ruedl, V. Coen, T. Sasaki, and H. Kolbe, "Intergranular Lithium Penetration of Low-Ni, Cr-Mn Austenitic Stainless Steel," *J. Nucl. Mater.* 110 (1982) 28–36.
2. E. Ruedl and T. Sasaki, "Effect of Lithium on Grain Boundary Precipitation in a Cr-Mn Austenitic Steel," *J. Nucl. Mater.* 116 (1983) 112–122.
3. E. Ruedl, V. Coen, T. Sasaki, and H. Kolbe, "Phase Stability and Corrosion of Cr-Mn Austenitic Steels Exposed to Pure Lithium," *J. Nucl. Mater.* 122&123 (1984) 1247–51.

4. J. H OeVan and J. R. DiStefano, "Thermal-Convection Loop Tests of Type 316 Stainless Steel in Lithium," pp. 200–208 in *ADIP Quart. Prog. Rep. Mar. 31, 1982,* DOE/ET-0058/1, U.S. DOE, Office of Fusion Energy.

5. W. F. Calaway, "The Reaction of Chromium with Lithium Nitride in Liquid Lithium," pp. 18-8–18-26 in *Proc. Second Int.* Conf. *on Liq. Metal Technot. in Energy Production,* U.S. DOE, CONF-800401-P2, 1980.

6. M. G Barker et al., "The Interaction of Chromium with Nitrogen Dissolved in Liquid Lithium," *J. Nucl. Mater.* 114, 143–49 (1983).

7. O. L. Olson, G. N Reser, and O. K. Matlock, "Liquid Lithium Corrosion Rate Expressions for Type 304L Stainless Steel," corrosion *(Houston)* 36 (1980) 140–44.

8. P. F. Tortorelli, J. H DeVan, and J. E. Selle, "Effects of Nitrogen and Nitrogen Getters in Lithium on the Corrosion of Type 316 Stainless Steel," *NACE Corrosion/79,* preprint 115, March 1979.

9. P. F. Tortorelli and J. H DeVan, "Corrosion of Type 316 Stainless Steel, Path A PCA, and 12 Cr-1 MoVW Steel in Thermally Convective Lithium" *ADIP Semiannual* Prog. *Rep. Mar. 31, 1984,* DOE/ER0045/12, U.S. DOE, Office of Fusion Energy.

10. P. F. Tortorelli and J. H DeVan, "Corrosion of an Fe-12 Cr-1 MoVW Steel in Thermally Convective Lithium," pp. 215–221 in *Proc. Topical* Conf. *a Ferritic Alloys* for *Use in Nuclear Energy Technologies,* AIME, 1984.

9.2 CORROSION OF TYPE 316 STAINLESS STEEL AND 12 Cr-1 MOVW STEEL IN FLOWING Pb17 at. % Li — P. F. Tortorelli and J. H DeVan (Oak Ridge National Laboratory)

9.2.1 ADIP Task

ADIP Task I.A.3, Perform Chemical and Metallurgical Compatibility Analyses.

9.2.2 Objective

The purpose of this task is to determine the corrosion resistance of candidate first-wall materials to slowly flowing Pb17 at. % Li in the presence of a temperature gradient. Dissolution and deposition rates are measured as functions of time, temperature, and additions to the lead-lithium. These measurements are combined with chemical and metallographic examinations of specimen surfaces to establish the mechanisms and rate-controlling processes for the dissolution and deposition reactions.

9.2.3 Summary

Type 316 stainless steel and 12 Cr-1 MoVW steel were exposed to Pb—17 at. % Li for about 2000 h at 500°C. Type 316 stainless steel was severely corroded with deep penetration of the alloy by lead-lithium. The 12 Cr-1 MOVW steel did not suffer penetration and corroded uniformly.

9.2.4 Progress and Status

During the current reporting period, a thermal convection loop (TCL) study of type 316 stainless steel in Pb17 at. ■Li was continued while a TCL experiment with 12 Cr-1 MoVW steel in this liquid metal was started. Both loops were of a type described previously;' the loop design allowed corrosion coupons to be withdrawn and inserted without interrupting the lead-lithium flow. The loop used for investigating the corrosion of type 316 stainless steel coupons was fabricated of the same alloy but had previously circulated lithium for over 10,000 h. The interior surface of its hot leg was therefore depleted in nickel. While the presence of the resultant ferritic surface may affect dissolution of the fresh austenitic loop coupons, this effect has been measured for lithium, was found to be not large, and was taken into account when we compared the present dissolution data with prior results for type 316 stainless steel in lithium by using only data typical of such loop conditions. The TCL in which the 12 Cr-1 MoVW steel specimens were exposed to Pb—17 at. ■Li was made from 9 Cr-1 Mo steel and was new at the start of the present study. Both the type 316 stainless steel and 12 Cr-1 Mo steel loops circulated Pb—17 at. % Li at a maximum temperature of 500°C and had temperature differentials of 100 and 150°C, respectively. The details of the procedure for the preparation of the lead-lithium were given previously.[2]

In the preceding progress report,[3] results from metallographic examination and energy dispersive x-ray analysis of type 316 stainless steel exposed to thermally convective Pb—17 at. % Li were found to be consistent with a stripping of the corrosion layer during the rinsing of specimens in lithium to remove the residual lead-lithium from the exposed coupons. Recently, a type 316 stainless steel specimen was continuously exposed at 500°C in the TCL for 2015 h and then polished and examined in cross-section without undergoing the rinsing procedure in lithium. The resulting micrographs revealed the presence of an extended corrosion layer, approximately 80 μm in depth (see for example, Fig. 9.2.1). On the other hand, as previously reported,[3] such a corrosion layer is not observed when the specimen is first cleaned in lithium to remove the residual lead. Electron microprobe analysis of this corrosion layer showed it to be composed of stainless steel that was severely penetrated by lead (and presumably lithium) — see Figs. 9.2.2 and 9.2.3. When such a specimen is rinsed in molten lithium, the lithium removed both the residual lead on the surface (clearly seen in Fig. 9.2.2) and also the lead that has penetrated the steel. Because of the severity of the penetration, most of the steel component of the layer is also removed. The present observation of lead penetration (as shown in Figs. 9.2.1—9.2.3) is quite similar to the previous findings of other investigators studying the corrosion of austenitic stainless steel by lead-lithium.[4,5]

In a similar manner to the procedure used for the type 316 stainless steel specimen shown in Figs. 9.2.1—9.2.3, a coupon of 12 Cr-1 MoVW steel was exposed to thermally convective Pb17 at. ■Li for 2000 h at 500°C in the 9 Cr-1 Mo steel loop and then metallographically examined without any removal of the adhering lead. In contrast to the austenitic stainless steel, the resulting polished cross-section showed no evidence of any internal penetration or localized corrosion (Fig. 9.2.4). Such a result is therefore qualitatively similar to the behavior observed in pure lithium systems, where a porous corrosion layer forms on exposed type 316 stainless steel but not on ferritic steels, which undergo fairly uniform corrosion. The preferential dissolution of nickel, in both lithium and lead-lithium systems, obviously plays an important role in the formation of internal corrosion layers, albeit such zones are more severely attacked for the case of lead-lithium systems under otherwise comparable conditions.

9.2.5 Conclusions

1. Type 316 stainless steel was severely corroded after exposure for 2015 h at 500°C in a thermal convection loop of type 316 stainless steel that circulated Pb—17 at. % Li. The exposure resulted in the formation of a thick corrosion layer which contained a significant amount of lead-lithium.

Y-200325

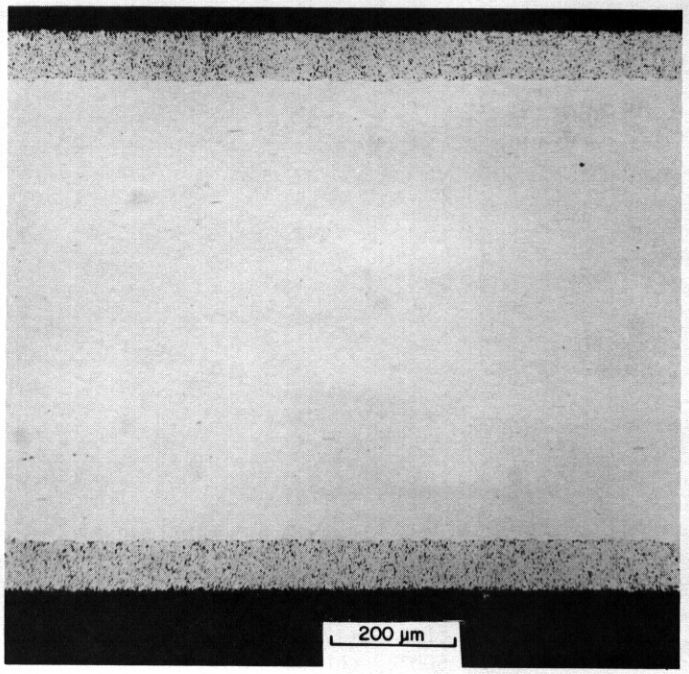

Y-200327

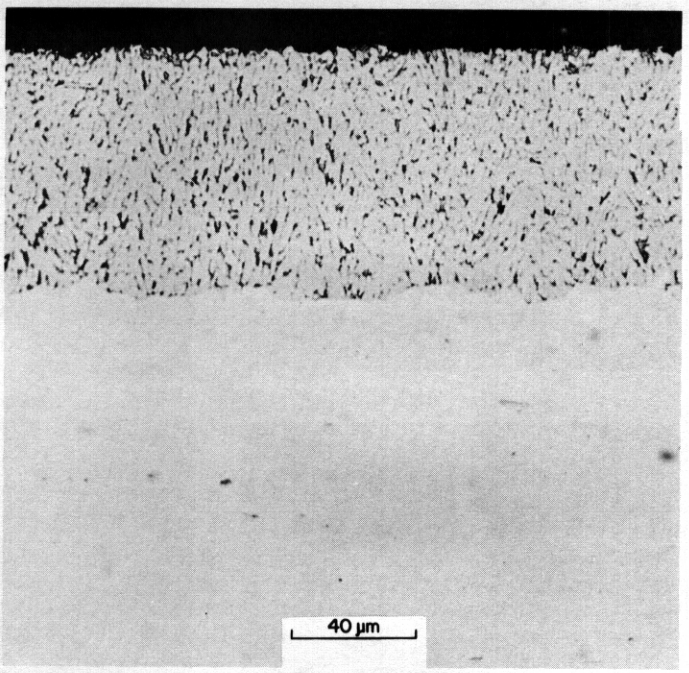

Fig. 9.2.1. Polished cross-section of type 316 stainless steel exposed to thermally convective Pb–17 at. % Li for 2015 h at 500°C; no specimen cleaning prior to examination.

ORNL-PHOTO 7878-84

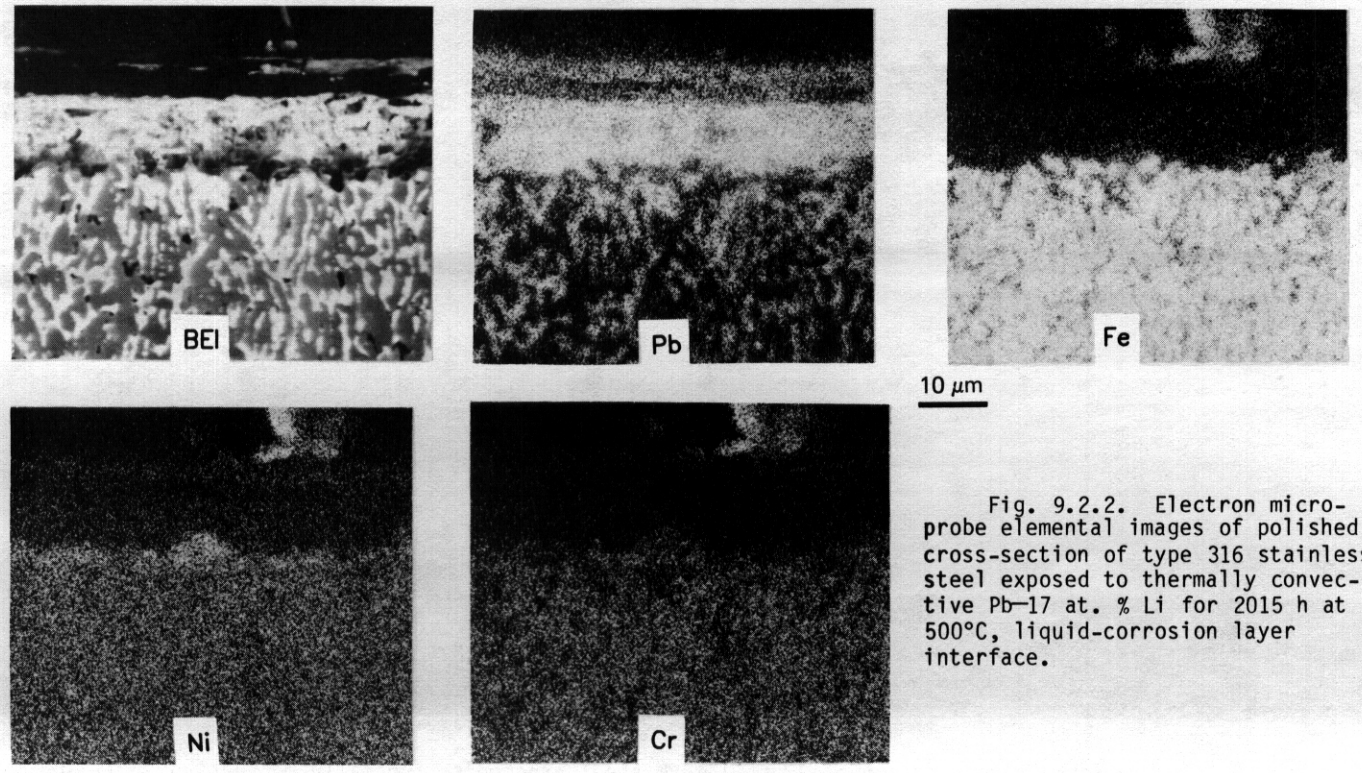

Fig. 9.2.2. Electron microprobe elemental images of polished cross-section of type 316 stainless steel exposed to thermally convective Pb–17 at. % Li for 2015 h at 500°C, liquid-corrosion layer interface.

ORNL-PHOTO 7879-84

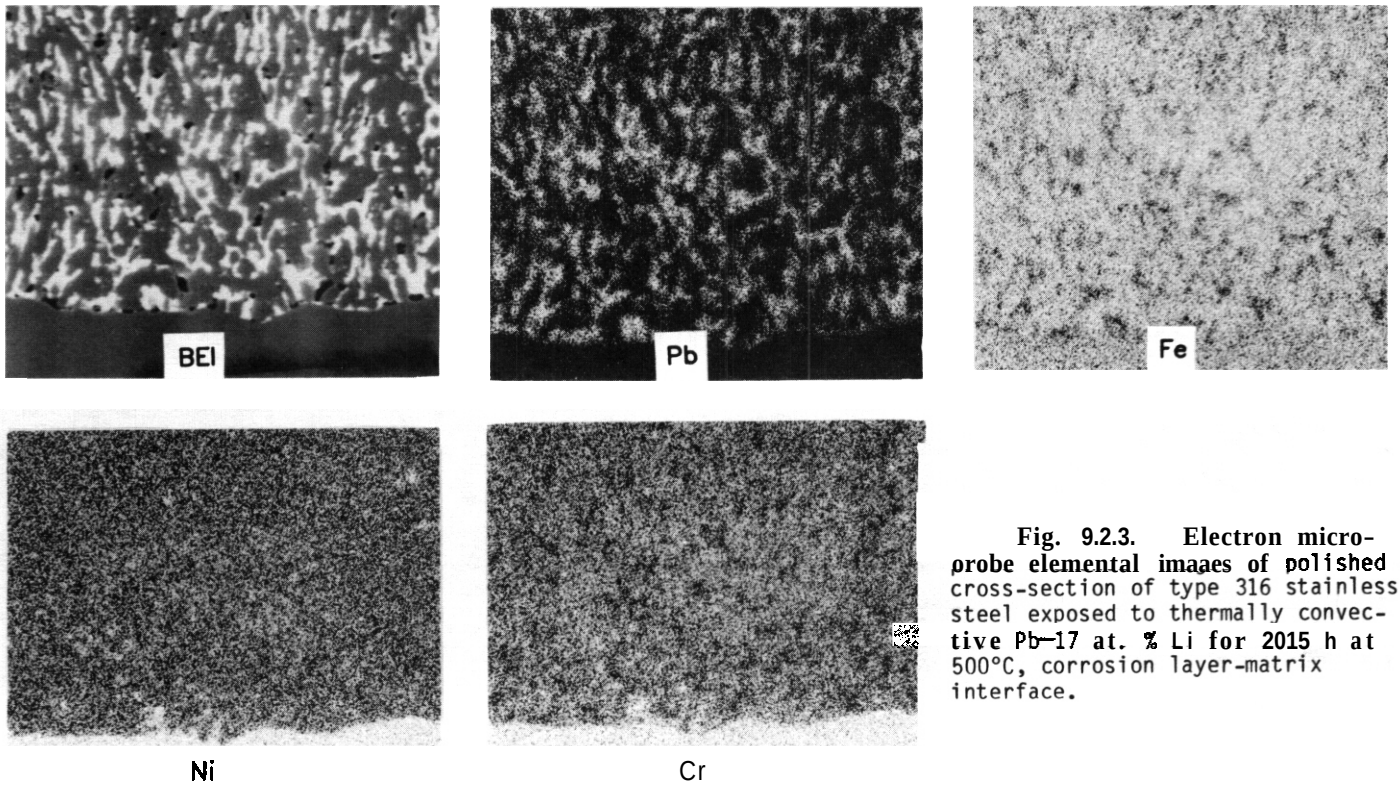

Fig. 9.2.3. Electron microprobe elemental imaaes of polished cross-section of type 316 stainless steel exposed to thermally convective Pb–17 at. % Li for 2015 h at 500°C, corrosion layer-matrix interface.

Y-200328

Y-200330

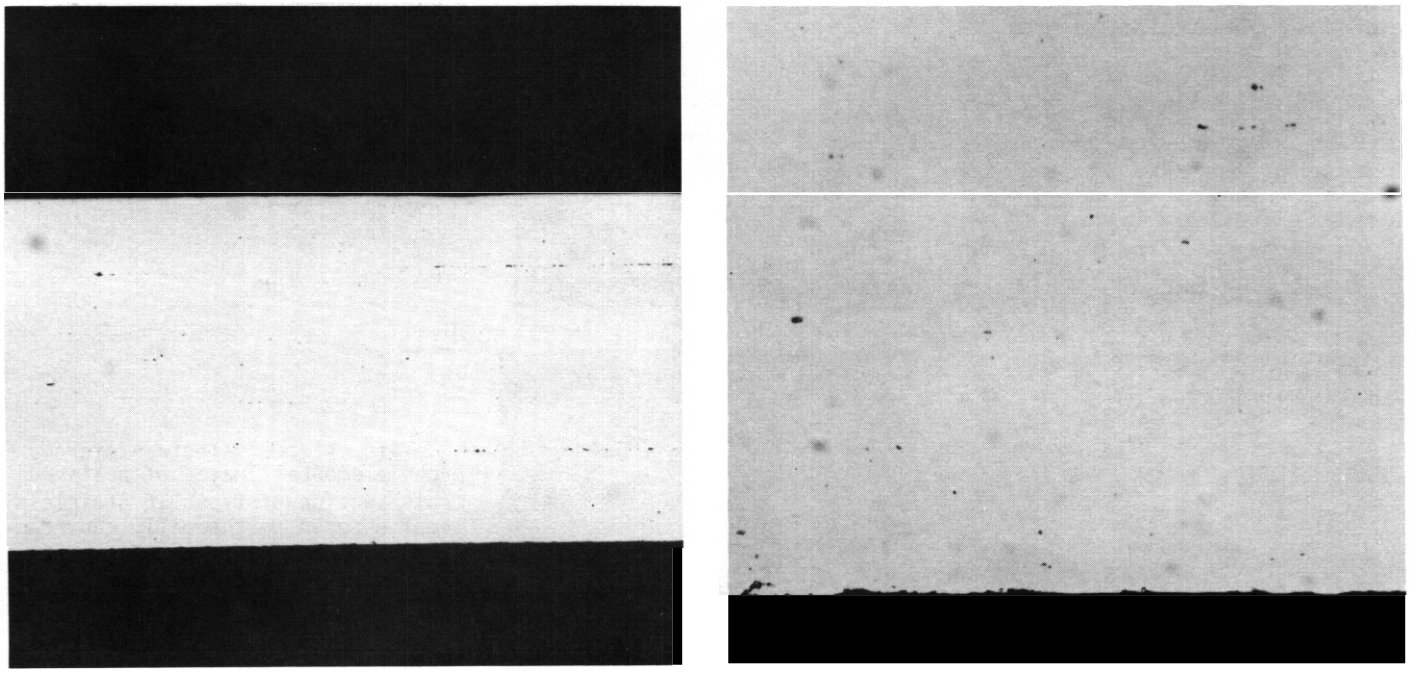

Fig. 9.2.4. **Polished cross-section of** 12 Cr-1 MoVW **steel exposed to thermally convective** Pb–17 at. % Li **for 2000** h **at** 500°C; no **specimen cleaning prior to examination.**

2. 12 Cr-1 MoVW steel, after exposure to Pb–17 at. % Li for 2000 h at 500°C in a 9 Cr-1 MoVW steel loop, corroded relatively uniformly without any significant penetration by the lead-lithium.

9.2.6 References

1. J. H. DeVan and J. R. DiStefano, "Thermal-Convection Loop Tests of Type 316 Stainless Steel in Lithium," pp. 200–208 in *ADIP Quart. Prog. Rep. Mar. 31, 1978,* DOE/ET-0058/1, U.S. DOE, Office of Fusion Energy.

2. P. F. Tortorelli and J. H. DeVan, "Corrosion of Type 316 Stainless Steel in Flowing Pb–17 at. % Li," pp. 203204 in *ADIP Semiannu. Prog. Rep. Sept. 30, 1983,* DOE/ER-0045/11, U.S. DOE, Office of Fusion Energy.

3. P. F. Tortorelli and J. H. DeVan, "Corrosion of Type 316 Stainless Steel in Flowing Pb17 at. % Li," pp. 190–92 in *ADIP Semiannu. Prog. Rep. Mar. 31, 1984*, DOE/ER-0045/12, U.S. DOE, Office of Fusion Energy.

4. O. K. Chopra and D. L. Smith, "Corrosion of Ferrous Alloys in Eutectic Lead-Lithium Environment," *J. Nucl. Mater.* 122&123 (1984) 1219–24.

5. P. Fauvet, G. Santarini, and G. Sannier, CEA, Fontenay-aux-Roses, France, to be published.

9.3 ENVIRONMENTAL EFFECTS ON PROPERTIES OF STRUCTURAL ALLOYS IN FLOWING LITHIUM - O. K. Chopra and D. L. Smith (Argonne National Laboratory)

9.3.1 ADIP Task

ADIP Task I.A.3, Perform Chemical and Metallurgical Compatibility Analyses.

9.3.2 Objective

The objective of this program is to investigate the influence of a flowing lithium environment on the corrosion behavior and mechanical properties of structural alloys under conditions of interest for fusion reactors. Corrosion rates are determined by measuring the weight change and depth of internal corrosive penetration as a function of time and temperature. These measurements, coupled with metallographic evaluation of the alloy surface, are used to establish the mechanism and rate-controlling process for the corrosion reactions. Initial effort on mechanical properties is focused on fatigue and tensile tests in a flowing lithium environment of controlled purity.

9.3.3 Summary

Data on the surface composition of Type 316 stainless steel exposed to lithium under various conditions of time, temperature, and nitrogen content in lithium are presented. The results indicate that the depletion of chromium from the steel depends on the exposure conditions. The depletion of nickel is rapid and independent of temperature and lithium purity.

9.3.4 Progress and Status

The effects of a flowing lithium environment on the corrosion behavior of austenitic and ferritic steels are being investigated. The corrosion tests are conducted in a test facility consisting of a forced-circulation lithium loop and an MTS closed-loop servohydraulic fatigue machine for performing mechanical tests in the liquid lithium environment. A schematic diagram of the facility is shown in Fig. 9.3.1. The liquid lithium system, which is constructed of Type 304 stainless steel, consists of a primary loop with three test vessels and a secondary cold-trap purification loop. Hot gettering is also used for controlling the interstitial elements in lithium. A magnetic trap (not shown in the figure) is located upstream from the flowmeter and pump sections of the cold-trap loop. The quantity of lithium in the loop is ~20 liters and lithium is recirculated at ~1 liter/min in the primary loop. Filtered lithium samples are periodically obtained for analyses of nitrogen and carbon in lithium. The hydrogen concentration in lithium is determined by equilibrating yttrium samples in lithium and using the reported data on the distribution of hydrogen between lithium and yttrium.'

Flat corrosion coupons ~70 x 10 x 0.3 mm in size are exposed to flowing lithium and the corrosion behavior is evaluated from measurements of weight loss and depth of internal penetration for specimens exposed for different times. Tests are conducted in the test vessel andlor specimen exposure vessel. During the corrosion tests, the concentrations of carbon and hydrogen in lithium were ~10 and 120 wppm, respectively, and the nitrogen content was maintained at <100 wppm.

The corrosion data for Type 316 stainless steel, PCA, HT-9, and Fe-9Cr-1Mo steel in flowing lithium at 755 and 700 K have been reported earlier.[2-4] The results indicate that the weight losses of ferritic HT-9 and Fe-9Cr-1Mo steel follow a linear law with time and yield a constant dissolution rate. For both ferritic steels, the dissolution rates at 700 K are a factor of ~2 lower than those at 755 K. The dissolution rates for austenitic PCA and Type 316 stainless steel reach a steady-state value after an initial ~1500-h period of high rates. The steady-state dissolution rates for Type 316 stainless steel are an order of magnitude greater than for ferritic steels and the rates for PCA are a factor of 2 to 4 greater than for Type 316 stainless steel. The dissolution rates for both austenitic steels at 755 and 700 K are anomalous, i.e., slightly higher at 700 K than at 755 K. After exposure to lithium, the austenitic steels develop a porous ferrite layer owing to depletion of nickel and to some extent chromium from the steel. The concentration of nickel decreases abruptly across the ferrite-austenite boundary. Measurements of internal penetration indicate that the thickness of the ferrite layer formed on Type 316 stainless steel follows a power-law relationship with time. The ferritic steels show little or no internal corrosion.

The anomalous results for dissolution rates of Type 316 stainless steel at 755 and 700 K indicate that different corrosion mechanisms may dominate the dissolution behavior in different temperature regimes. Limited data show that a small increase in the concentration of nitrogen in lithium increases the weight losses of both austenitic and ferritic steels by a factor of 2 to 4.[3] Nitrogen can react with alloy elements and lithium to form stable ternary nitrides, such as Li_9CrN_5 and Li_3FeN_2, and thus accelerate the dissolution process of ferrous alloys.[5] During the current reporting period, energy dispersive x-ray analyses (EDAX) were performed to determine the differences in surface composition of Type 316 stainless steel specimens exposed to lithium at different temperatures and lithium purity conditions. The

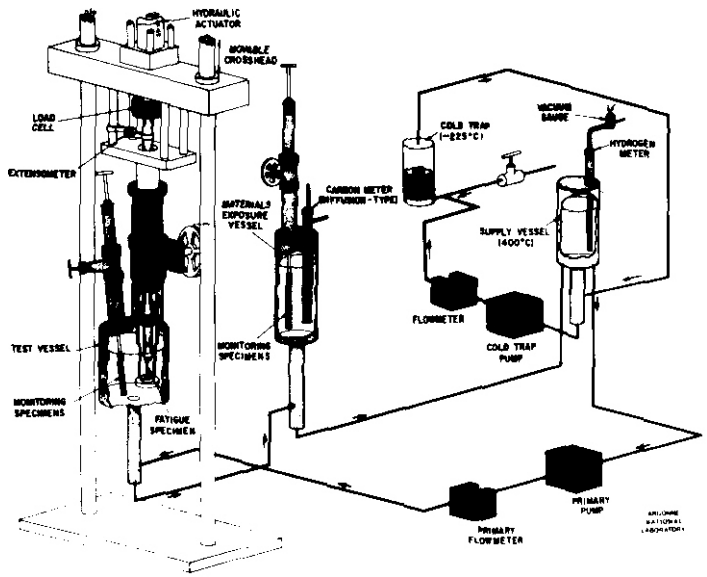

Fig. 9.3.1. Schematic of liquid lithium loop and facility for performing mechanical tests in the lithium environment.

concentration of Cr, Fe, and Ni was measured for specimens exposed during different test runs. The time and temperature of exposure and the loop operating conditions for the test runs are given in Table 9.3.1. The weight loss, internal penetration (i.e., thickness of ferrite scale), and surface composition of lithium exposed specimens are given in Table 9.3.2.

The results show that irrespective of the time and temperature of exposure, the Ni concentration in both annealed and cold-worked Type 316 stainless steel is <1.2%. However, the depletion of Cr from the steel depends on time, temperature, and nitrogen content in lithium. Data for test runs 1 and 4 indicate that the concentration of Cr decreases with an increase in exposure time, e.g., -13% after 1295 h and -9.8% after 5521 h. Specimens exposed at 755 K in lithium containing ~250 wppm nitrogen (run 2) show greater depletion of Cr than those exposed to lithium with <100 wppm nitrogen. During test run 4, the concentration of Cr is lower in specimens exposed at 700 K than in specimens exposed at 755 K. Annealed and cold-worked Type 316 stainless steel specimens exposed at 700 K for 1100 h (run 3) show little or no loss of Cr. In fact, these specimens show large deposits of Cr on the surface.

The differences in the Cr content are reflected in the surface features of the lithium-exposed specimens. Micrographs of the surface of 20% CW Type 316 stainless steel exposed for 5521 h at 755 K and 5739 h at 700 K are shown in Fig. 9.3.2. Both specimens show a pebbled or dimpled appearance and contain some surface cavities or porosity. However, the specimen exposed at 700 K exhibits greater porosity than that exposed at 755 K. Type 316 stainless steel exposed to high-nitrogen lithium (run 2) also shows large porosity (Fig. 9.3.3). These results indicate that the porosity in the ferrite layer is associated with the depletion of Cr from the steel. Specimens with greater porosity and depletion of Cr also show larger weight loss and internal penetration.

Corrosion data from the lithium thermal convection loop (TCL) at different maximum temperatures indicate that the depletion of Cr from Type 316 stainless steel decreases with a decrease in temperature.[6] For example, after a 3000-h exposure to lithium, the Cr concentration ratios for lithium-exposed vs unexposed steel are 0.42 at 923 K, 0.58 at 873 K, 0.65 at 823 K, and 0.91 at 773 K. A similar effect of temperature on Cr depletion was observed for Type 316 stainless steel specimens exposed at different temperatures in a lithium TCL operated for 7488 h at a maximum temperature of 873 K.[7] The concentration of Cr increased from 2.8% for specimens exposed at the maximum temperature of 873 K to 6.8% for specimens exposed downstream at 813 K. These results are different from those observed in the present study, viz., the depletion of Cr is higher at 700 K than at 755 K. The corrosion data at 700 K during run 4 and at 155 K during run 2 were obtained in the specimen-exposure vessel of the lithium loop and the lithium flow was from the test vessel to the specimen-exposure vessel. The differences in loop geometry, surface area of the structural material, or downstream effects may influence the dissolution and mass transfer behavior for ferrous alloys. Additional data over a wide range of loop temperature and system parameters are required to establish the influence of these parameters on the dissolution behavior of austenitic steels in lithium.

9.3.5 Conclusions

Data on the surface composition of Type 316 stainless steel exposed to flowing lithium under different time, temperature, and lithium purity conditions indicate that irrespective of the exposure conditions, all specimens show significant depletion of nickel. The concentration of nickel in both annealed and cold-worked Type 316 stainless steel is <1.2%. The depletion of chromium from the steel depends on time,

TABLE 9.3.1. Lithium loop operating conditions for various corrosion tests

Test Run	Loop Temperatures (K)				N Content in Lithium	Test Duration (h)	
	Test Vessel	Spec. Exp. Vessel	Supply Vessel	Cold Trap		Test Vessel	Spec. Exp. Vessel
1	755	755	705	485	<50	1295	3000
2	755/700[a]	755	680	503[b]	-250	-	1997
3	700	755	680	503	-100	1100	-
4	755	700	683	485	<100	5521	6501

[a]Test vessel temperature changed from 755 to 700 K after 1540 h.
[b]No flow through cold trap after 890 h due to plugging. Plugged sections replaced and flow started after an additional 480 h.

TABLE 9.3.2. Weight loss, depth of internal penetration, and surface compositions of Type 316 stainless steel exposed to flowing lithium[a]

Test Run	Time (h)	Temp. (K)	Weight Loss (g/m^2)	Penetration (μm)	Surface Composition (%)		
					Cr	Fe	Ni
			Annealed Type 316 SS				
1	1295	755	6.7	13	12.2	81.6	1.2
2	1997[b]	755	21.0	25	6.2	90.9	1.1
4	5521	755	31.8	37	9.7	84.0	0.7
3	1100[c]	700	17.2	21	18.7	77.1	1.8
4	5739	700	42.2	38	8.1	86.6	0.8
4	5739	700	41.5	37	8.3	88.4	0.9
			20% CW Type 316 SS				
	1295	755	23.8	24	13.9	78.0	0.6
	1997[b]	755	46.5	47	5.6	88.1	0.6
	5521	755	35.0	40	10.0	85.6	0.7
	1100	700	24.9	25	14.3	82.6	1.3
	5739	700	47.9	42	8.6	86.8	0.9
4	5739	700	51.6	40	8.8	88.3	1.0
4	6501	700	52.9	46	7.3	87.9	0.8

[a]During test runs 1, 3, and 4, the concentration of nitrogen in lithium was <100 wppm.
[b]Concentration of nitrogen in lithium -250 wppm. No flow through cold trap for -480 h.
[c]Large deposits of chromium observed on the specimen. The surface composition represents regions away from these deposits.

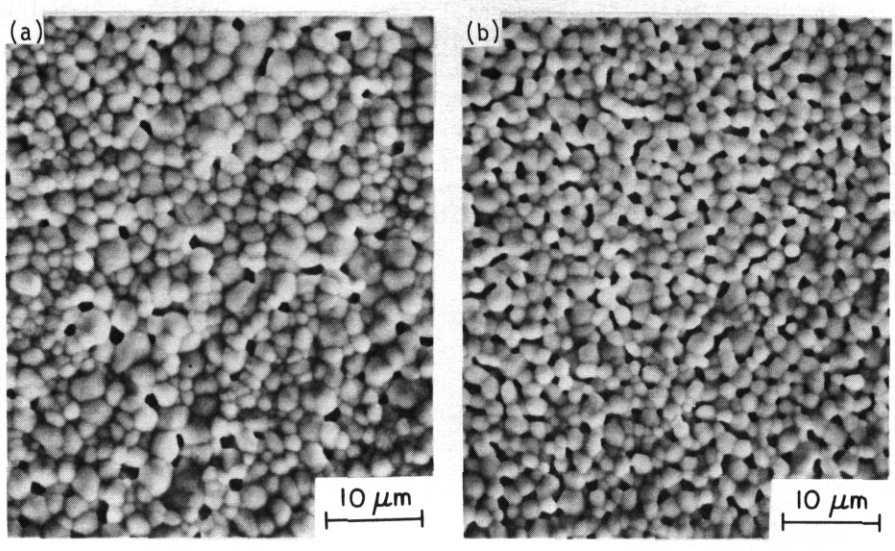

Fig. 9.3.2. Micrographs of the surface of 20% cold-worked Type 316 stainless steel exposed to flowing lithium (a) for 5521 h at 755 K and (b) for 5739 h at 700 K.

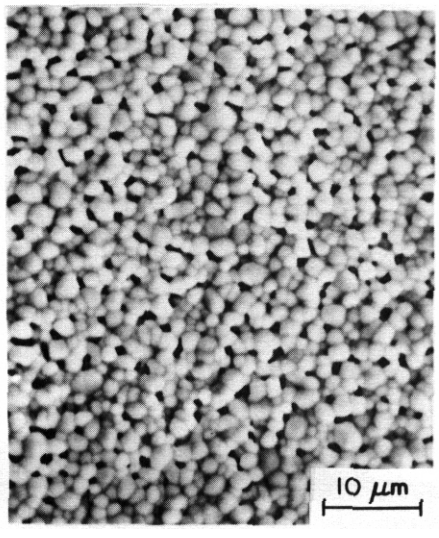

Fig. 9.3.3. Micrograph of 20% cold-worked Type 316 stainless steel exposed for 1997 h at 755 K to flowing lithium containing ~250 wppm nitrogen.

temperature, and nitrogen content in lithium. Chromium depletion increases with exposure time and is higher for specimens exposed at 700 K than for those exposed at 755 K. An increase in the nitrogen content in lithium also increases the depletion of chromium from the steel. Specimens that show greater depletion of chromium also exhibit large porosity in the ferrite layer that form on the specimen surface. The large surface porosity may account for the large weight losses and high dissolution rates observed for these specimens.

9.3.6 References

1. D. L. Smith, R. H. Lee, and R. M. Yonco, pp. 2.72-2.80 in Proc. Intl. Conf. on Liquid Metal Technology in Energy Production, CONF-800401-P1, U. S. DOE, 1980.

2. O. K. Chopra and O. L. Smith. "Environmental Effects on Properties of Structural Alloys." pp. 304-313 in Alloy Development for Irradiation Performance: Semiannual Progress Report for Period Ending September 30, 1982, DOE/ER-0045/9, Oak Ridge National Laboratory, Oak Ridge, Tenn., February 1983.

3. O. K. Chopra and D. L. Smith, "Environmental Effects on Properties of Structural Alloys," pp. 195-200 in Alloy Development for Irradiation Performance: Semiannual Progress Report for Period Ending March 31, 1983, DOE/ER-0045/10, Oak Ridge National Laboratory, Oak Ridge, Tenn., October 1983.

4. O. K. Chopra and D. L. Smith, "Environmental Effects on Properties of Structural Alloys in Flowing Lithium," pp. 176-182 in Alloy Development for Irradiation Performance: Semiannual Progress Report for Period Ending March 31, 1984, DOE/ER-0045/12, Oak Ridge National Laboratory, Oak Ridge, Tenn., July 1984.
5. M. G. Barker, P. Hubberstey, A. T. Dadd, and S. A. Frankham, J. Nucl. Mater. 114, 143-149 (1983).
6. P. F. Tortorelli, J. H. DeVan, and J. E. Selle, pp. 13.44-13.54 in Second Intl. Conf. on Liquid Metal Technology in Energy Production, CONF-800401-P2, U. S. DOE, 1980.
7. P. F. Tortorelli and J. H. DeVan, "Effects of a Flowing Lithium Environment on the Surface Morphology and Composition of Austenitic Stainless Steel," to be published in Microstructural Science.

9.4 COMPATIBILITY OF Li_2O IN A FLOWING HELIUM ENVIRONMENT - O. K. Chopra and D. L. Smith (Argonne National Laboratory)

9.4.1 ADIP Task

ADIP Task I.A.3, Perform Chemical and Metallurgical Compatibility Analyses.

9.4.2 Objective

The objective of this task is to evaluate the compatibility of solid breeder materials with structural alloys in a flowing helium environment. The interactions between breeder material, alloys, and gas are investigated as a function of temperature, time, and environmental parameters (e.g., different H_2O and H_2 contents in helium). Reaction rates are determined by measuring the weight change of the breeder material and the alloys as well as the thickness of the reaction scales on the alloys. These measurements, coupled with metallographic evaluation of the alloy surfaces, are used to establish the mechanisms and rate-controlling processes for the corrosion reactions.

9.4.3 Summary

Sintered Li_2O pellets exposed to flowing helium containing 1 ppm each of H_2O and H_2 show weight losses at 550 and 650°C and a weight gain at 450°C. The rates of weight loss are ~3 orders of magnitude greater than those predicted from equilibrium reaction kinetics.

9.4.4 Progress and Status

Data on the corrosive interactions between structural alloys and Li_2O pellets at 550°C in a flowing helium environment containing 1 ppm H_2 and 1 or 93 ppm H_2O indicate that the Li_2O pellets lose weight after exposure. The loss of weight for Li_2O follows a linear law with time and the rate of weight loss is 12.2 and 3.8%/yr in helium with 93 and 1 ppm H_2O, respectively.[1] The corrosion behavior of austenitic Type 316 stainless steel is similar to that of ferritic HT-9 or Fe-9Cr-1Mo steel. All alloy specimens develop a dense iron-rich outer scale and a porous chromium-rich subscale.[1,2] The scale on Type 316 stainless steel also consists of a thin manganese-rich surface layer and an inner band rich in nickel. The results also show that the depth of internal penetration for alloy specimens exposed in helium containing 1 ppm each of H_2O and H_2 reaches a constant value after ~500 h. The reaction rates in helium containing 93 ppm H_2O are greater than in helium with 1 ppm H_2O. The duration of the compatibility test with high moisture content was 2000 h, and the internal penetration for all alloys increased with time. However, the results suggest that the depth of penetration may reach a constant value after longer times.

The weight loss for Li_2O pellets results from two separate interactions, namely gas-pellet and alloy-pellet interactions. Consequently, compatibility tests were conducted with Li_2O pellets, without the alloy specimens, at 450, 550, and 650°C, in flowing helium containing 1 ppm each of H_2O and H_2 to determine the weight loss due to gas-pellet interactions. Three Li_2O pellets, ~12-mm in diameter by ~2.4-mm thick, were mounted in a specimen holder such that the surface of the pellets was exposed to the flowing gas environment. The specimen holder with the Li_2O pellets is shown in Fig. 9.4.1. Details of the compatibility test facility have been described elsewhere.[2] During the test, the flow rate of the gas mixture was 0.45 mL/s, which corresponds to a velocity of ~1.6 mm/s. Prior to the test in the flowing gas mixture, the Li_2O pellets were baked at the test temperature under dynamic vacuum for ~7 h. The weight change of the pellets was measured after several exposure times.

The weight losses of the Li_2O pellets at 450, 550, and 650°C are shown as a function of time in Fig. 9.4.2. At all temperatures, the pellets lost weight after baking under dynamic vacuum. The weight loss increased with an increase in test temperature, e.g., ~0.8, 1.4, and 2.5 mg/cm^2 at 450, 550, and 650°C, respectively. When exposed to the flowing gas mixture, the pellets gained weight at 450°C and lost weight at 550 and 650°C. For all temperatures, the change in weight increases linearly with time. The rate of weight change is given in Fig. 9.4.2.

The equilibrium partial pressures of various gas species for reactions between Li_2O pellets and helium gas containing 1 ppm each of H_2O and H_2 are given in Table 9.4.1. The partial pressure of O_2 in the gas environment is set by reaction (1) between H_2O and H_2. Under these conditions, LiOH (solid at 450°C and liquid at 550 and 650°C) would not be stable, since at each temperature, the partial pressure of H_2O for reaction (3) is significantly higher than that in the gas environment. Consequently, any residual LiOH in the Li_2O pellets would dissociate into $Li_2O(s)$ and H_2O.

Table 9.4.1 also indicates that reaction (4) will be favored at all temperatures, e.g., the partial pressure for Li(g) for reaction (4) is higher than that in the gas environment. Thus, $Li_2O(s)$ in contact with the stainless steel holder would react to form ternary metal oxide, $LiCrO_2$. Thermodynamic data[4] also indicate that the partial pressure of O_2 in the gas environment is higher than that required for the formation of Li_5FeO_4.

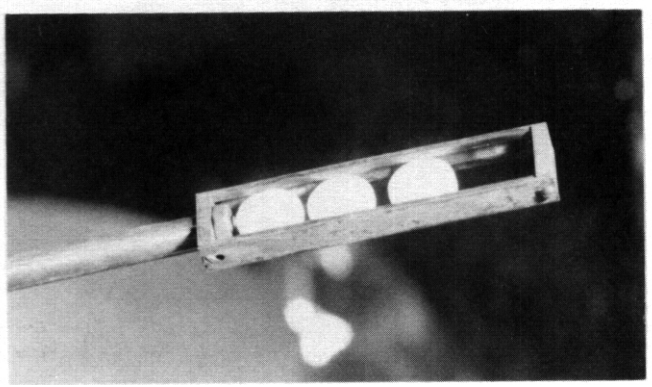

Fig. 9.4.1. Specimen holder with Li_2O pellets.

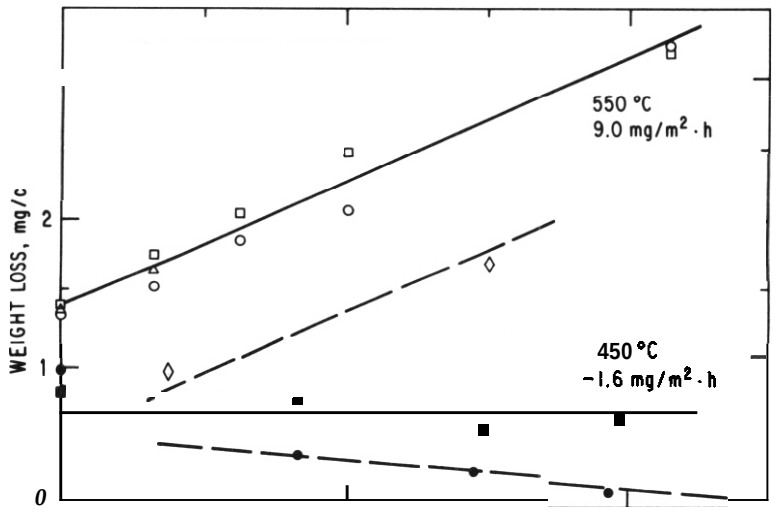

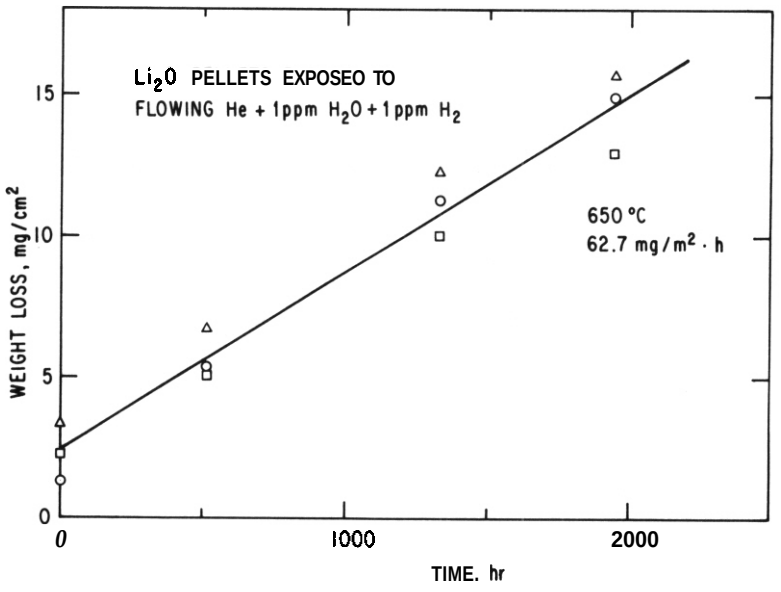

Fig. 9.4.2. Weight loss of Li_2O pellets exposed at 450, 550, and 650°C in flowing helium containing 1 ppm each of H_2O and H_2. Each symbol type represents weight loss for a single pellet after various times.

Table 9.4.1. Partial pressures of various gas species for reaction between Li_2O pellets and helium gas containing 1 ppm each of H_2O and H_2

	Equilibrium Partial Pressure,[a] log P (atm)		
	450°C	550°C	650°C
(1)	$H_2(g) + \frac{1}{2}O_2(g) \rightleftarrows H_2O(g)$		
P_{O_2}	-30.00	-25.68	-22.28
(2)	$Li_2O(s) \rightleftarrows 2\ Li(g) + \frac{1}{2}O_2(g)$		
P_{Li}	-16.86	-13.81	-11.65
(3)	$Li_2O(s) + H_2O(g) \rightleftarrows 2\ LiOH(s, \ell)$[b]		
P_{H_2O}	-2.23 (-2.84)	-1.48 (-2.08)	-1.00 (-1.501
P_{O_2}	-22.46	-16.64	-12.29
(4)	$Cr + 2\ Li_2O(s) \rightleftarrows LiCrO_2 + 3\ Li(g)$[c]		
P_{Li}	-10.81	**-8.68**	-7.00
(5)	$Li_2O(s) + H_2O(g) \rightleftarrows 2\ LiOH(g)$[d]		
P_{LiOH}	-10.29 (-10.37)	-8.81 (-8.92)	-7.66 (-7.79)

[a] Partial pressures calculated with thermodynamic data from JANAF tables.
[b] LiOH(s) below 472°C and LiOH(ℓ) above 472°C. Values within parentheses calculated with data from Ref. 3.
[c] Partial pressures calculated with data from Ref. 4.
[d] Values within parentheses calculated with data from Ref. 5.

The partial pressure of LiOH(g) in the environment is established by reaction (5). The weight loss of Li_2O pellets due to the formation of LiOH(g) can be determined from

$$\Delta W\ (g/h) = P_{LiOH}\left(\frac{V}{RT}\right)\left(\frac{M}{2}\right),$$

where V is the volume of the carrier gas (in m^3/h) at room temperature T and M is the molecular weight of Li_2O. The calculated values for the rate of wight loss at 450, 550, and 650°C are 1.6 x 10^{-4}, 4.8 x 10^{-3}, and 6.8 x 10^{-2} $mg/m^2 \cdot h$, respectively. The values at 550 and 650°C are ~3 orders of magnitude lower than those observed experimentally.

Reaction (4) can also contribute to the wight loss of Li_2O pellets. Data for compatibiltty tests between structural alloys and Li_2O indicate that the depth of internal penetration reaches a constant value of ~15 μm after ~500 h. The reaction stops when the partial pressure of Li(g) in the oxide scale increases to the equilibrium value. Furthermore, the area of contact between Li_2O pellets and the stainless steel holder was minimal la line contact). Consequently, the weight loss due to the formation of ternary oxides, i.e., reaction (4), is expected to be negligible. Results at 450°C also support this behavior, viz., although reaction (4) should occur at 450°C. the pellets in fact gain weight. The increase in weight at 450°C may be attributed to absorption of moisture from the environment.

Dissociation of residual LiOH can also lead to loss in weight of the Li_2O pellets. Data on the thermal decom osition of LiOH at temperatures between 270 and 460°C indicate that the reaction rates are relatively high.' Since LiOH is unstable at the test temperatures, baking the pellets under dynamic vacuum should decompose all the LiOH present in the pellets. Otherwise, Li_2O exposed to the gas environment at 450°C should also have lost weight. Furthermore, one sample of Li_2O exposed to a flowing gas environment at 550°C, without prior baking (shown as diamond symbols in Fig. 9.4.2), showed significant weight loss after the initial exposure. Yet the subsequent rate of weight loss is comparable to that observed for the samples that were baked before exposure to the gas environment. These results indicate that decomposition of residual LiOH cannot account for the large weight losses that were observed experimentally for Li_2O.

9.4.5 Conclusions

The Li_2O pellets exposed to flowing helium containing 1 ppm each of H_2O and H_2 showed weight losses of 9.0 and 62.7 $mg/m^2 \cdot h$ at 550 and 650°C, respectively. The pellets gained weight at 450°C. The rate of weight gain was 1.6 $mg/m^2 \cdot h$. The weight losses at 550 and 650°C are ~3 orders of magnitude greater than those predicted from equilibrium reaction kinetics. However, data indicate that the high rates of weight loss cannot be attributed to interactions with the stainless steel holder or decomposition of residual LiOH in the Li_2O pellets.

9.4.6 References

1. O. K. Choora and D. L. Smith, "Compatibility Studies of Structural Alloys with Solid Breeder Materials," pp. 205-208 in Alloy Development for Irradiation Performance: Semiannual Progress Report for Period Ending September 30, 1983, DOE/ER-0045/11, Oak Ridge National Laboratory, Oak Ridge, Tenn., March 1984.

2. O. K. Choora, T. Kurasawa. and D. L. Smith, "Comoatibility of Ferritic Steels with Sintered Li_2O Pellets in a Flowing Helium Environment," pp. 209-214 in Proc. Topical Conf. on Ferritic Alloys for Use in Nuclear Energy Technologies, eds. J. W. Davis and D. J. Michel, AIME, New York, 1984.

3. M. Tetenbaum and C. E. Johnson, "Partial Pressures of H_2O Above the Diphase $Li_2O(s)$-LiOH(s,ℓ) System," to be published in J. Nucl. Mater.

4. R. J. Pulham, W. R. Watson, and J. S. Collinson, "Chemical Compatibility between Lithium Oxide and Transition Metals," J. Nucl. Mater. 1226123, 1243-1246 (1984).

5. M. Tetenbaum and C. E. Johnson, "Vaporization Behavior of Lithium Oxide: Effect of Water Vapor in Helium Carrier Gas," to be published in J. Nucl. Mater.

6. H. Kudo, "The Rates of Thermal Decomposition of LiOH(s), LiOD(s), and LiOT(s)," J. Nucl. Mater. **87**, 185-188 (1979).

9.5 ENVIRONMENTAL EFFECTS ON THE PROPERTIES OF VANADIUM-BASE ALLOYS — D. R. Diercks and D. L. Smith (Argonne National Laboratory)

9.5.1 AOIP Task

ADIP Task I.A.3, Perform Chemical and Metallurgical Compatibility Analyses

9.5.2 Objective

The objective of this task is to experimentally evaluate the corrosion behavior of selected vanadium-base alloys in a number of aqueous, liquid metal, and gaseous environments. The results of these investigations will be used in the selection of appropriate vanadium-base alloys for structural applications in fusion reactors.

9.5.3 Summary

Exposures of V-15Cr-5Ti, V-20Ti, and VANSTAR-7 specimens for 2000 h to pressurized flowing water containing 4 ppm dissolved O_2 at 288°C have been completed. Both the V-20Ti and VANSTAR-7 alloys formed nonadherent and nonprotective corrosion products, and both alloys exhibited relatively high corrosion rates. The V-15Cr-5Ti alloy formed a thin adherent film, and its corrosion rate was more than two orders of magnitude lower. Further results obtained in a scanning Auger microprobe study of sulfur segregation in vanadium-base alloys indicate that the extent of intergranular segregation varies markedly with different heats of material.

9.5.4 Progress and Status

9.5.4.1 Aqueous Corrosion Behavior of Vanadium-Base Alloys

A pressurized-water refreshed autoclave system has been designed and constructed for the purpose of conducting controlled corrosion testing of selected vanadium-base alloys, as described in the previous semiannual report.[1] Three different vanadium-base alloys were chosen for testing, namely V-15Cr-5Ti, V-20Ti, and VANSTAR-7. Samples of all three alloys were obtained from the Fusion Power Program (FPP) Materials Inventory in the form of 0.76-mm (0.030-in.)-thick sheet and 6.35-mm (0.250-in.)-diameter rods. The latter will be used for subsequent CERT (constant-extension-rate) stress-corrosion cracking testing. In addition, V-15Cr-5Ti and V-20Ti material was obtained in the form of 1.52-mm (0.060-in.)-thick sheet from the old ANL LMFBR Inventory.

The sheet material from both inventories was sheared into weight-change specimens approximately 7.1 cm (2.8 in.) long and 1 cm (0.4 in.) wide as well as "penetration coupons" approximately 2 cm (0.8 in.) long and 1 cm (0.4 in.) wide. These penetration coupons were to be removed periodically during the course of the exposures and examined destructively to determine the depth of corrosive penetration into the base metal and the general microstructural features of the corrosion process. All of the specimens were lightly grit blasted and cleaned with acetone and ethanol before being suspended from a stainless steel rack and placed in the autoclave. Two weight-change and two penetration specimens of each alloy and heat of material were exposed in the first corrosion test. The specimens were originally suspended from the rack with 0.25-mm (0.010-in.)-diameter vanadium wire, but this wire underwent excessive wastage during the course of the tests and was replaced with platinum wire. The test specimens were carefully positioned on the rack to avoid physical contact between adjacent specimens.

The first corrosion test was conducted with high-purity distilled inlet water (conductivity ~0.1 μS/cm) containing approximately 7 to 8 ppm dissolved oxygen. The solution in the autoclave was maintained at a temperature of 288°C (550°F) and a pressure of 8.3 MPa (1200 psi), and the flow rate through the system was about 11 cm^3/min. Under these conditions, the dissolved oxygen content in the exit stream from the autoclave was determined to be about 4 ppm. This oxygen content is considered to be representative of that in the specimen chamber, and the first test is described here as having been conducted in water containing 4 ppm dissolved oxygen.

The first corrosion test was interrupted after exposure times of 192, 496, 1000, and 2000 h to weigh the weight-change specimens, and, after 496 and 1000 h, to remove penetration coupons. The weight-change specimens were cleaned upon each removal before weighing by immersion in ethanol and light wiping with a soft cloth in order to remove any loose corrosion scale. Weights were determined to six significant figures with a Mettler mechanical microbalance.

The observed weight changes for the alloys and heats tested are summarized in Table 9.5.1 and plotted in Figs. 9.5.1 and 9.5.2. In all cases the test specimens lost weight, but dramatically larger weight losses were observed for the V-20Ti and VANSTAR-7 alloys than for the two heats of V-15Cr-5Ti. The weight losses for V-20Ti and VANSTAR-7 appear to be approximately linear with time out to 1000 h (Fig. 9.5.1), but the 2000-h data points indicate weight losses that are greater than would be extrapolated from this

Table 9.5.1. Observed weight losses for vanadium-base alloys from Fusion Power Program (FPP) Materials Inventory and ANL LMFBR Inventory exposed to water containing 4 ppm dissolved oxygen at 288°C and 8.3 MPa pressure

Alloy	Source	Weight Loss/Unit Area (mg/cm^2) after Indicated Exposure Time			
		792 h	496 h	1000 h	2000 h
V-15Cr-5Ti	FPP	0.113	0.189	0.287	0.590
	FPP	0.111	0.181	0.280	0.535
	LMFBR	0.111	0.198	0.325	0.709
	LMFBR	0.095	0.182	0.313	0.639
V-20Ti	FPP	5.85	14.33	38.04	97.33
	FPP	5.89	13.98	37.69	95.56
	LMFBR	5.05	14.63	33.52	112.27
	LMFBR	5.76	16.17	35.26	112.68
VANSTAR-7	FPP	4.32	11.45	24.58	63.76
	FPP	4.14	10.91	24.11	63.73

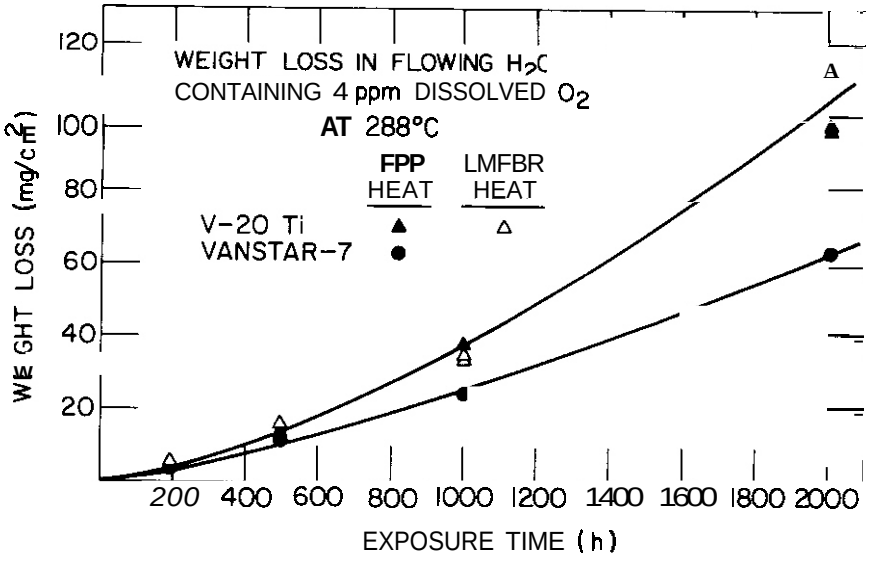

Fig. 9.5.1. Observed weight losses for V-20Ti and VANSTAR-7 exposed to water containing 4 ppm dissolved oxygen at 288°C.

initially linear behavior. The reasons for this behavior are not clear. Best-fit equations representing all of the data of Fig. 9.5.1 for each of the two alloys were obtained as follows:

$$\text{V-20Ti:}\quad W = 1.519 \times 10^{-3}\, t^{1.465},$$

$$\text{VANSTAR-7:}\quad W = 3.030 \times 10^{-3}\, t^{1.309},$$

where W is weight change in mg/cm^2. These equations are plotted as the solid curves in Fig. 9.5.1. The inclusion of the 2000-h data points in the best-fit equations causes the rate-law exponents in both equations to exceed unity, and no physical significance is attached to this unexpected behavior.

A similar best-fit equation representing the V-15Cr-5Ti weight loss data is plotted in Fig. 9.5.2, namely:

$$\text{V-15Cr-5Ti:}\quad W = 6.190 \times 10^{-4}\, t^{0.9075}.$$

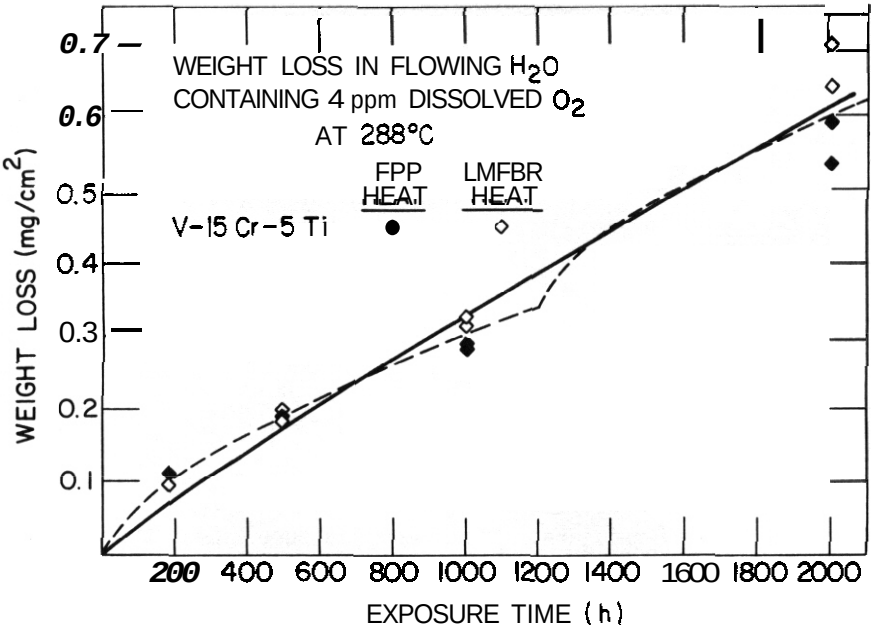

Fig. 9.5.2. Observed weight losses for V-15Cr-5Ti exposed to water containing 4 ppm dissolved oxygen at 288°C. The solid curve represents a power-law best fit to all of the data, and the dashed curve represents a best fit to the data out to 1000 h. which is extrapolated by assuming a reestablishment of the initial corrosion kinetics after 1200 h.

However, the data out to 1000 h suggest a more nearly parabolic behavior than that indicated by the above fit to all the data. For this reason, a second best-fit equation was determined for the V-15Cr-5Ti data out to 1000 h, as follows:

$$\text{V-15Cr-5Ti (to 1000 h):}\quad W = 3.371 \times 10^{-3}\, t^{0.6502}.$$

This equation is plotted as the dashed curve in Fig. 9.5.2. This dashed curve is arbitrarily terminated at 1200 h, which is taken to be the starting point for a second curve of the same functional form. If, in fact, the dashed curve gives an accurate representation of the rather limited data, it suggests that this alloy exhibited approximately parabolic corrosion kinetics during the first part of the exposure, followed by the loss of protection at the surface and the onset of another parabolic regime. In contrast, the steadily increasinq corrosion rates for the other two alloys (Fig. 9.5.1) rather clearly Indicate the absence of any protective surface oxide formation.

Figure 95 .3 shows the visual appearance of each of the five specimen types upon removal from the autoclave system after 2000 h total exposure time. The nature of the corrosion products formed on the specimen surfaces was found to be in general agreement with the observed corrosion kinetics. The V-20Ti specimens from both heats of mterial were covered with a heavy grayish-green granular corrosion product that rubbed off readily in handling and appeared to offer little or no protection to the underlying base metal. The surfaces of the VANSTAR-7 specimens were covered with a similarly heavy gray layer that readily spalled off as flakes., exposino an underlvina dark gray-to-black porous nonadherent layer. Again, the corrosion product appeared to offer little protection lO the underlying base metal. Figure 9.5.1 shows that both of these alloys underwent relatively rapid corrosion during the test. Furthermore, both alloys showed increasing rates with time; this observation indicated that no protective surface oxide formation was taking place.

On the other hand, the corrosion product formed on the surface of the V-15Cr-5Ti specimens was a relatively thin, dense, and apparently adherent film. This alloy showed a much lower corrosion rate (Fig. 9.5.2), and there is some Ouggestion of an approximately parabolic initial behavior. One may speculate that some corrosion layer spallation occurred with increased thickness sometime after the first 1000 h of exposure, thereby leading to a somewhat increased subsequent corrosion rate.

Attempts were made to identify the nature of the corrosion products formed on the various specimens after both 1000 and 2000 h of exposure. by use of x-ray diffraction powder pattern techniques. Corrosion product samples were carefully scraped from the surfaces of the penetration samples after 1000 h and the

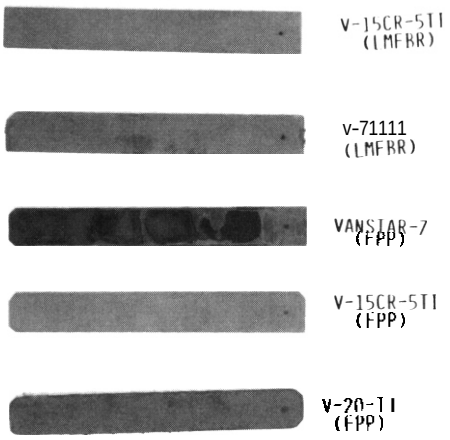

Fig. 9.5.3. Visual appearance of the vanadium alloy specimens after 2000-h exposure to water containing 4 ppm dissolved oxygen at 288°C.

weight-change samples after 2000 h of exposure. After both exposure times, the V-20Ti corrosion product was clearly identified as rutile (TiO_2), with no other phases detected.

The corrosion product formed after 1000 h on the VANSTAR-7 specimens produced a very diffuse and poorly defined diffraction pattern that could not be indexed. Somewhat sharper diffraction lines were produced by the corrosion product formed on this alloy after 2000 h, but again the pattern could not be satisfactorily indexed. An identifiable VO_2 phase was found in the 1000-h corrosion product from the V-15Cr-5Ti specimens. along with one or more unidentifiable phases. No further phase identification was possible in the diffraction patterns obtained from the V-15Cr-5Ti specimens exposed for 2000 h. Quantitative analyses of the corrosion products by means of energy dispersive x-ray analysis techniques are presently under way in an attempt to better define their chemical nature.

Preliminary metallographic examinations of the exposed specimens indicate that the observed weight losses were due to relatively uniform wastage of the specimens, and there was little or no apparent penetration into the base metal ahead of the water/metal interface. Thus, little information could be obtained from the penetration coupons removed periodically during the test. Assuming uniform corrosion and an approximate density of 6.16 g/cm3 for each of the three alloys, wastage rates on a linearly extrapolated annual basis were calculated from the observed 2000-h weight loss data of Table 9.5.1. These calculated wastage rates are about 0.7 mm/yr for the V-20Ti alloy, 0.5 mm/yr for VANSTAR-7, and 0.005 mm/yr for V-15Cr-5Ti. By comparison, a maximum corrosion wastage rate of 0.005 mm/yr for a fusion reactor first wall has been suggested. Preparations are presently under way to expose these same alloys and heats of material to water containing lower dissolved oxygen levels more prototypic of anticipated service conditions.

9.5.4.2 Segregation of sulfur in Vanadium-Base Alloys

The previous report' described results obtained on the intergranular segregation of sulfur in unirradiated V-15Cr-5Ti material (heat H5V-207, R1301) from the ORR-MFE-2 experiment provided by Westinghouse. Specimens from that material fractured in situ in the scanning Auger microprobe (SAM) at liquid nitrogen temperature were observed to fracture largely intergranularly with relatively little ductility. The transgranular cleavage fracture regions showed no unusual chemistry variations, but the intergranular regions were found to have sulfur contents estimated to be greater than 10 wt %. A chemical analysis of the specimen material performed at ANL indicated that the bulk sulfur content was less than 0.02 wt %. These results are similar to observations made by Westinghouse on this heat of material, except that they obtained only transgranular cleavage fracture and observed high sulfur levels on these transgranular fracture surfaces.

During the past six months, we have conducted follow-up SAM examinations of the fracture surfaces of the V-20Ti, VANSTAR-7, and V-15Cr-5Ti alloys from the FPP heats and the V-20Ti and V-15Cr-5Ti alloys from the ANL LMFBR heats. The three FPP alloys, when fractured in situ in the-as-received condition at liquid nitrogen temperature, all failed transgranularly in a relatively ductile fashion. No sulfur was detected at any of several locations examined in the V-20Ti and V-15Cr-5Ti specimens; this observation indicated that the sulfur levels were below a few tenths of 1 wt %, the detection limit of the instrument. Of the five regions examined on the VANSTAR-7 fracture surface, however, sulfur was seen at three sites. At one of these locations, both sulfur and phosphorus were present at levels of the order of 1 to 2 wt % (Fig. 9.5.4).

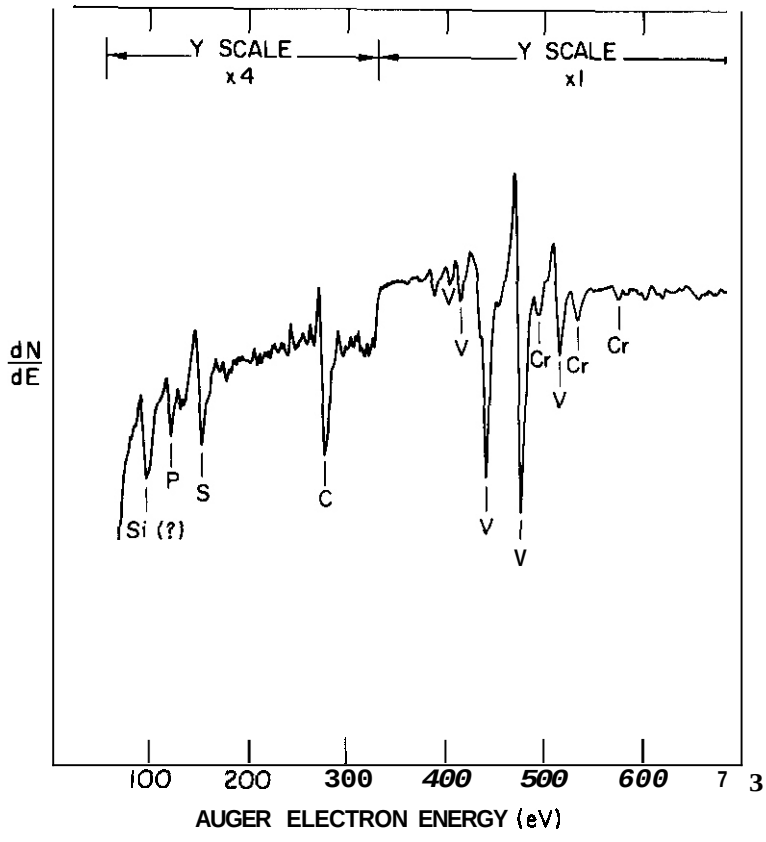

Fig. 9.5.4. SAM analysis obtained from a VANSTAR-7 fracture surface region where sulfur, phosphorus, and possibly silicon were detected.

Specimens of the three above alloys were then annealed for 1 h at 850°C (1562°F) in vacuum before being fractured in situ in the SAM. The purpose of this anneal was to encourage the intergranular segregation of any sulfur that might be present in the alloys. The V-20Ti and VANSTAR-7 specimens again fractured in a ductile transgranular fashion, but the V-15Cr-5Ti specimen appeared to fail predominantly by brittle transgranular cleavage. No traces of sulfur could be detected at any of three locations analyzed on the V-15Cr-5Ti fracture surface, but isolated possible indications of phosphorus and chlorine were noted. No unusual chemistry variations were seen at any of seven locations examined on the VANSTAR-7 specimen. However, a fairly prominent sulfur peak was seen at one fracture area on the annealed V-20Ti specimen, and less prominent peaks were seen at two other locations.

Finally, V-20Ti and V-15Cr-5Ti specimens from the ANL LMFBR heat of material were annealed for 1 h at 850°C in vacuum and fractured in situ in the SAM. The V-20Ti specimen failed transgranularly in a ductile fashion, and the fracture surface of the V-15Cr-5Ti specimen appeared to consist largely of transgranular cleavage. Five locations were examined on the fracture surface of the V-20Ti specimen and seven on the V-15Cr-5Ti, and only slight possible traces of either sulfur or phosphorus could be detected.

The conclusions to be drawn from this investigation of sulfur segregation in various vanadium-base alloys and heats of material are not yet entirely clear. The Westinghouse V-15Cr-5Ti alloy exhibited a highly brittle intergranular fracture behavior, and a pronounced intergranular segregation of sulfur appeared to be associated with this behavior. On the other hand, none of the FPP or ANL alloys could be induced to fracture in a brittle intergranular manner, and, with a few exceptions, no substantial segregation of sulfur to the fracture surfaces was observed. It should also be noted that the grain sizes of both the FPP and ANL alloys were substantially smaller than that of the Westinghouse V-15Cr-5Ti alloy. Samples of all of the alloys examined here have been submitted for high-sensitivity analyses of bulk sulfur contents in order to determine to what extent the tendency toward intergranular sulfur segregation and embrittlement is related to bulk sulfur chemistry.

9.5.5 References

1. O. R. Oiercks and D. L. Smith. "Environmental Effects on the Prooerties of Vanadium-Base Alloys," pp. 75-19 in Alloy Development for Irradiation Performance: Semiannual Progress Report for Period Ending March 31, 1984, DOE/ER-0045/12, Oak Ridge National Laboratory, Oak Ridge, Tenn., July 1984.

9.6 STRESS CORROSION CRACKING OF PCA — INITIAL CONSIDERATIONS AND CHARACTERIZATION OF GRAIN BOUNDARY PRECIPITATION — P. F. Tortorelli (Oak Ridge National Laboratory)

9.6.1 ADIP Task

ADIP Task I.A.3, Perform Chemical and Metallurgical Compatibility Analyses.

9.6.2 Objective—

The purpose of this task is to determine the susceptibility of ADIP developmental alloys to stress corrosion cracking in aqueous environments applicable to water-cooled fusion reactors. The resistance of these alloys to stress corrosion cracking is being assessed relative to that of commercial alloys for which a large body of data exists. In this way, the effects of compositional modifications on cracking susceptibility can be discerned.

9.6.3 *Summary*

According to a thermodynamic model of intergranular stress corrosion cracking, PCA is predicted to have about the same cracking susceptibility as type 316 stainless steel. However, microstructural manipulation of the PCA alloy may allow improvement in the resistance to sensitization and, therefore, to intergranular stress corrosion cracking.

9.6.4 Progress and Status

The feasibility of water cooling a fusion reactor obviously depends on the resistance of ADIP developmental alloys to corrosion in aqueous environments. Consequently, a study of the aqueous compatibility of the path A prime candidate alloy (PCA) was initiated. PCA is composed of

Element	Content (wt %)	Element	Content (wt %)	Element	Content (wt %)
Ni	15.9	Mn	1.9	Al	0.05
Cr	14.0	Si	0.4	C	0.05
Mo	1.9	Ti	0.3	N	<0.01
Fe	65.0				

It mainly differs from type 316 stainless steel in its higher nickel and lower chromium and carbon content and a minor titanium addition. It is thus interesting to examine how these compositional differences between PCA and type 316 stainless steel may affect the respective aqueous corrosion reactions of these alloys.

In addressing the corrosion resistance of austenitic stainless steels in aqueous environments, the phenomenon of stress corrosion cracking is of primary importance. While the general corrosion resistance of such alloys in relatively pure water is quite good, austenitic stainless steels can undergo transgranular or intergranular cracking in chloride-containing environments and intergranular stress corrosion cracking (IGSCC) of sensitized material in sulfur oxyanion-containing solutions (<100°C) and in oxygenated water at temperatures up to about 300°C (see, for example, ref. 1). Since these two latter environments are particularly pertinent to water-cooled reactor conditions, the sensitization and IGSCC of susceptible austenitic alloys are of concern for such applications. It was therefore deemed important to study the sensitization behavior of PCA relative to a typical austenitic stainless steel as the first stage of this stress corrosion cracking investigation.

Sensitization in steels is the process whereby carbide formation at grain boundaries results in the uptake of chromium from the surrounding matrix such that a zone depleted in chromium forms near the grain boundaries. Such behavior typically occurs after exposure of solution annealed austenitic alloys at 600 to 800°C after several hours or longer (depending on the temperature). In austenitic steels containing iron, chromium, and nickel, the resulting grain boundary carbide is normally assumed to be of a $M_{23}C_6$ type with chromium being the main metal constituent. The resulting chromium-depleted zone around the grain boundaries in sensitized material is less corrosion resistant because of the reduced concentration of this element and therefore provides a susceptible Dath for attack (and cracking) under the appropriate environmental and stress conditions. Therefore, delaying the onset of sensitization in austenitic alloys, by microstructural or compositional manipulation, could improve their IGSCC resistance considerably.

One way to increase the resistance of an Fe-Ni-Cr alloy to sensitization is by changing the activity of chromium in equilibrium with the carbide through composition modification such that the "effective" chromium concentration of the alloy is increased. In this regard, Fullman' has developed a thermodynamic model of the effects of compositional variations on the susceptibility of austenitic alloys to sensitization, and, therefore, IGSCC. Using grain boundary carbides of the $M_{23}C_6$ type, Fullman derived "chromium equivalency parameters" for various alloying elements such that the "effective" chromium content, Cr^e, of an alloy could be expressed as

$$Cr^e = Cr + \alpha Ni + \beta Mo + \gamma Mn + \delta C + \ldots \quad (1)$$

where

Cr, Ni, . . . = elemental concentrations in alloy and
α, β, ... = chromium equivalency parameters.

A positive chromium equivalency parameter (CEP) was defined as the percent chromium reduction permitted for a 1% addition of the subject element such that equivalent IGSCC susceptibility (i.e., equivalent chromium activity) is maintained. A negative CEP (such as for carbon) indicates the percent chromium addition needed to retain equivalence. It is therefore relatively2 straightforward to qualitatively compare alloys of different compositions using the results of Fullman. In such a comparison, the alloy with the higher Cr^e will be less susceptible to sensitization and, presumably, IGSCC if all other factors are the same.

In order to estimate the susceptibility of PCA to sensitization relative to other, standard austenitic steels, an equation of the form of (1) was used to calculate Cr^e for the different compositions. For most alloying elements of interest, Fullman[2] reported a range for the CEP due to variations in the thermodynamic data used in the model. For purposes of the present comparison, the following equation was used:

$$Cr^e \text{ (wt \%)} = Cr - 0.2\ Ni + 1.4\ Mo + 0.15\ Mn + 1.0\ Ti - 100\ C \qquad (2)$$

where the elemental concentrations are in wt %. Note the large negative value of the CEP for carbon; this reflects the crucial influence of carbon levels on sensitization. The CEP of 1.4 for molybdenum was chosen because it fell well within the range of Fullman's values and has also been experimentally confirmed.[3]

Using Eq. (2), values of Cr^e were calculated for PCA and several standard austenitic stainless steels. The results of these calculations for PCA and type 316 and 316L stainless steel are shown in Table 9.6.1 and indicate that PCA has about the same general susceptibility to sensitization as the standard grade of type 316 stainless steel. Note, however, that this prediction is based on a model that does not account for microstructural modifications that may change kinetic factors and/or cause different carbides to form. Such manipulations, which are used with PCA to control irradiation response,[4] may result in an alloy that is more resistant to IGSCC than Fullman's model would predict.

Table 9.6.1. Effective chromium concentrations of selective austenitic alloys[a]

Alloy	Concentration (wt %)	
	Actual	Effective
PCA	14	9.1
316[b]	17	9.9
316L[c]	17	14.9

[a] Based on model of Fullman. R. L. Fullman, "A Thermodynamic Model of the Effects of Composition on the Susceptibility of Austenitic Stainless Steels to Interaranular Stress Corrosion Cracking," *Acta Metall.* 30 (1982) 1407–15.

[b] Composition used in calculation: 17 Cr-1 Ni-2 Mo-2 Mn-0.08 C (wt %).

[c] Composition used in calculation: same as for 316 except for a carbon concentration of 0.03 wt %.

An oxalic acid etch test (ASTM-262-A) was used as a first step in experimentally evaluating the relative stress corrosion cracking susceptibilities of PCA and typical types of austenitic stainless steel. Since the oxalic acid solution preferentially attacks the chromium-rich carbides, this technique is sensitive to the presence of such carbides at the grain boundaries and therefore qualitatively reveals, by optical microscopy, whether carbide precipitation has occurred. It does not, however, indicate the existence of chromium-depleted zones that may accompany the formation of the grain boundary carbides. The test is therefore not a direct indicator of IGSCC, but, if the technique does not show grain boundary precipitation, sensitization has not occurred. (It reveals a necessary but not sufficient condition for IGSCC.) Preliminary results from a series of such tests showed attack of the grain boundaries of solution annealed type 316 stainless steel subjected to a sensitizing heat treatment (SHT) of 675°C for 2 h and also of the grain boundaries of annealed PCA-A1 and PCA-B2 in both the non-SHT and SHT conditions. Furthermore, only type 304L stainless steel (CEP = 14.3) did not have etched grain boundaries after the SHT and subsequent exposure to the oxalic acid solution.

The observation of attacked grain boundary carbides for the PCA-82 specimen that did not undergo the SHT is not surprising considering its thermomechanical processing history (see Fig. 9.6.1): the prior aging steps can account for the carbide precipitation without the necessity of the SHT. However, such precipitation is not necessarily expected for PCA-A1 in the absence of the SHT (see Fig. 9.6.1), and, indeed, in one case, attack of the grain boundaries of "unsensitized" PCA-A1 was not observed. The conflicting results may indicate the inadequacy of the oxalic acid etch technique for detecting the relevant grain boundary precipitation in, at least, the A1 version of PCA despite the consistency of the observations with expected behavior in the cases of the other alloy specimens. Subsequent experiments, based on a modified Strauss test (ASTM-A262-E), will allow determination of whether the observed carbide formation in the PCA specimens does indeed lead to chromium-depleted zones adjacent to the grain boundaries and therefore causes IGSCC.

9.6.5 Conclusions

1. Based on thermodynamic composition considerations, path A PCA has about the same IGSCC susceptibility as the regular grade of type 316 stainless steel.
2. Microstructural manipulation of the PCA alloy may allow improved resistance to intergranular stress corrosion.

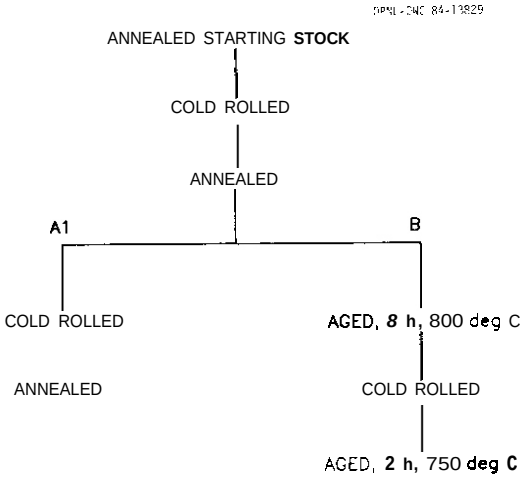

Fig. 9.6.1. Simplified flow chart for thermomechanical processing of PCA. Annealing was at >1100°C for 15 to 30 min.

9.6.6 References

1. F. P. Ford, "Stress Corrosion Cracking of Iron-Base Alloys in Aqueous Environments," Chap. 7 in *Embrittlement of Engineering Alloys*, C. L. Briant and S. K. Banerji (eds.), Academic Press, 1983.

2. R. L. Fullman, "A Thermodynamic Model of the Effects of Composition on the Susceptibility of Austenitic Stainless Steels to Intergranular Stress Corrosion Cracking," *Acta Metall.* 30 (1982) 1407–15.

3. C. L. Briant, R. A. Mulford, and E. L. Hall, "Sensitization of Austenitic Stainless Steels, I. Controlled Purity Alloys," Corrosion *(Houston)* 38 (1982) 468–77.

4. P. J. Maziasz and D. N. Braski, "Microstructural Design of PCA Austenitic Stainless Steel for Improved Resistance to Helium Embrittlement under HFIR Irradiation," *J. Nucl. Mater.* 122&123 (1984) *305–10.*

10. STATUS OF IRRADIATION EXPERIMENTS AND MATERIALS INVENTORY

10.1 FUSION PROGRAM RESEARCH MATERIALS INVENTORY — T. K. Roche, F. W. Wiffen (Oak Ridge National Laboratory), J. W. Davis (McDonnell Douglas Company), and T. A. Lechtenberg (GA Technologies)

10.1.1 ADIP Tasks

ADIP Task I.D.1, Materials Stockpile for Magnetic Fusion Energy Programs.

10.1.2 Objective

Oak Ridge National Laboratory maintains a central inventory of research materials to provide a common supply of materials for the Fusion Reactor Materials program. This will minimize unintended material variations and provide for economy in procurement and for centralized record keeping. Initially this inventory is to focus on materials related to first-wall and structural applications and related research, but various special purpose materials may be added in the future.

The use of materials from this inventory that is coordinated with or otherwise related technically to the Fusion Reactor Materials program of the Department of Energy is encouraged.

10.1.3 Materials Requests and Release

Materials requests shall be directed to the Fusion Program Research Materials Inventory at ORNL (Attention: F. W. Wiffen). Materials will be released directly if (a) the material is to be used for programs funded by the Office of Fusion Energy, with goals consistent with the approved Materials Program Plans of the Materials and Radiation Effects Branch and (b) the requested amount of material is available without compromising other intended uses.

Materials requests that do not satisfy both (a) and (b) will be discussed with the staff of the Reactor Technologies Branch, Office of Fusion Energy, for agreement on action.

10.1.4 Records

Chemistry and materials preparation records are maintained for all inventory materials. All materials supplied to program users will be accompanied by summary characterization information.

10.1.5 Summary of Current Inventory and Material Movement During Period April 1, 1984, through September 30, 1984

A condensed, qualitative description of the content of materials in the Fusion Program Research Materials Inventory is given in Table 10.1.1. This table indicates the nominal diameter of rod or thickness of sheet for product forms of each alloy and also indicates by weight the amount of each alloy in larger sizes available for fabrication to produce other product forms as needed by the program. There was no material added to or distributed from the inventory during this reporting period.

Alloy compositions and more detail on the alloys and their procurement and/or fabrication are given in this and earlier ADIP progress reports.

Table 10.1.1 Summary status of materials available in the fusion program research materials inventory

Alloy	Product form			
	Ingot or bar[a] weight (kg)	Rod diameter (mm)	Sheet thickness (mm)	Thin-wall tubing wall thickness (mm)
		Path A alloys		
Type 316 SS	900	16 and 7.2	13 and 7.9	0.75
Path A PCA[b]	490	12	13	0.25
USSR Cr-Mn steel[c]		10.5	7.6	
NONMAGNE 30[d]		18.5	10	
		Path B alloys		
PE-16		16 and 7.1	13 and 1.6	
B-1				
B-2				
B-3	180			
B-4	180			
B-6	180			

Table 10.1.1 (Continued)

Alloy	Product form			
	Ingot or bar[a] weight (kg)	Rod diameter (mm)	Sheet thickness (mm)	Thin-wall tubing wall thickness (mm)
Path C alloys				
Ti-64			2.5 and 0.76	
Ti-6242s		63	6.3, 3.2, and 0.76	
Ti-5621s			2.5 and 0.76	
Ti-38644			0.76 and 0.25	
Nb—1% Zr		6.3	2.5, 1.5, and 0.76	
Nb—5% Mo—1% Zr		6.3	2.5, 1.5, and 0.76	
V—20% Ti		6.3	2.5, 1.5, and 0.76	
V—15% Cr—5% Ti		6.3	2.5, 1.5, and 0.76	
VANSTAR-7		6.3	2.5, 1.5, and 0.76	
Path D alloy				
LRO-37[e]			3.3, 1.6, and 0.8	
Path E alloys				
HT9 (AOD fusion heat)[f]	3400		28.5, 15.8, 9.5, and 3.1	
HT9 (AOD/ESR fusion heat)	7000	25, 50, and 75	28.5, 15.8, 9.5, and 3.1	
HT9			4.5 and 18	
HT9 + 1%Ni			4.5 and 18	
HT9 + 2% Ni			4.5 and 18	
HT9 + 2% Ni + Cr adjusted			4.5 and 18	
T-9 modified[g]			4.5 and 18	
T-9 modified + 2% Ni			4.5 and 18	
T-9 modified + 2% Ni + Cr adjusted			4.5 and 18	
2 1/4 Cr-1 Mo			[h]	

[a] Greater than 25 mm, minimum dimension.

[b] Prime candidate alloy.

[c] Rod and sheet of a USSR stainless steel supplied under the U.S.-USSR Fusion Reactor Materials Exchange Program.

[d] NONMAGNE 30 is an austenitic steel with base composition Fe—14% Mn—2% Ni—2% Cr. It was supplied to the inventory by the Japanese Atomic Energy Research Institute.

[e] LRO-37 is the ordered alloy $(Fe,Ni)_3(V,Ti)$ with composition Fe—39.4% Ni—22.4% V—0.43% Ti.

[f] Alloy 12 Cr-1 MoVW, with composition equivalent to Sandvik alloy HT9.

[g] T-9 modified is the alloy 9 Cr-1 MoVNb.

[h] Material is thick-wall pipe, rerolled as necessary to produce sheet or rod.

10.2 IRRADIATION EXPERIMENT STATUS AND SCHEDULE — M. L. Grossbeck (Oak Ridge National Laboratory)

A large number of planned, in-progress, and completed reactor irradiation experiments support the ADIP program. Table 10.2.1 summarizes the parameters that describe completed experiments. Experiments that have been removed from the reactor recently; that are now undergoing irradiation', or that are planned for future irradiation are shown in the schedule barcharts of Table 10.2.2.

Experiments were under way during the reporting period in the Oak Ridge Research Reactor (ORR) and the High Flux Isotope Reactor (HFIR), which are mixed-spectrum reactors, and in the Fast Flux Test Facility (FFTF), which is a fast reactor.

A totbl of five capsules began irradiation in the HFIR. One, HFIR-CTR-50, was the first HFIR capsule designed for 100 dpa. This is the first of several experiments to explore the response of ferritic alloys to high levels of displacement damage and helium generation. Two of the HFIR capsules were part of the collaborative program between the United States and Japan. A total of six such capsules are now being irradiated in the HFIR. One capsule, HFIR-CTR-52, was removed from the HFIR. This is another joint irradiation experiment; it is being conducted by the European Community, the United States, and Japan. The capsule contains fatigue specimens of type 316 stainless steel from the European Community.

Table 10.2.1. Descriptive parameters for completed ADIP program fission reactor irradiation experiments

Experiment	Major objective	Alloy	Temperature (°C)	Displacement damage (dpa)	Helium (at. ppm)	Duration (months)	Date completed
			Experiments in ORR				
ORR-MFE-1	Scope the effects of composition and microstructure on tensile, fatigue, and irradiation creep	Paths A, B, C	250–600	2	<10	4	6/78
ORR-MFE-2	Scope the effects of composition and microstructure on tensile, fatigue, and irradiation creep	Paths A, B, C	300–600	6	<60	15	*4/80*
ORR-MFE-5	In-reactor fatigue crack growth	Path A	325–460	1	<10	2	*2/81*
			Experiments in EBR-II				
Subassembly X-264	Effect of preinjected helium on microstructure, tensile properties, and irradiation creep	316, PE-16, V–20% Ti. V–15% Cr–5% Ti. Nb–1% Zr	500–825	8	2–200	4	1/77
AA-X Subassembly X-287	Effect of preinjected helium on microstructure, tensile properties. and irradiation creep	316, PE-16, V–20% Ti, V–15% Cr–5% Ti, Nb–1% Zr	400–700	20	2–200	23	12/78
Subassembly X-2170	Stress relaxation	Titanium alloys	450	2		1	1/78
Pins 8285, 8286, and 8284	Swelling, fatigue crack growth, and tensile properties	Titanium alloys	370–550	25		14	9/79
			Experiments in HFIR				
HFIR-CTR-3	Swelling and tensile properties	PE-16, Inconel 600	300–700	4.3–9	350–1800	3	2/75
HFIR-CTR-4	Swelling and tensile properties	PE-16	300-700	2.2–4.5	100–350	2	3/77
HFIR-CTR-5	Swelling and tensile properties	PE-16, Inconel 600	300–700	4.3–9	350-1800	3	4/75
HFIR-CTR-6	Swelling and tensile properties	PE-16, Inconel 600	300–700	4.3–9	350–1800	3	4/75
HFIR-CTR-7	Swelling and tensile properties	PE-16	300-700	9–18	1250–3000	7	8/77
HFIA-CTR-8	Swelling and tensile properties	PE-16	300–700	9–18	1250–3000	7	8/77
HFIR-CTR-9	Swelling and tensile properties	316, 316 + Ti	280–680	10–16	400–1000	6	5/77

Table 10.2.1. (continued)

Experiment	Major objective	Alloy	Temperature (°C)	Displacement damage (dpa)	Helium (at. ppm)	Duration (months)	Date completed
HFIR-CTR-10	Swelling and tensile properties	316, 316 + Ti	280–680	10–16	400–1000	6	5/77
HFIR-CTR-11	Swelling and tensile properties	316, 316 + Ti	280–680	10–16	400-1000	6	5/77
HFIR-CTR-12	Swelling and tensile properties	316, 316 + Ti	280–680	7-10	200–500	4	2/77
NFIR-CTR-13	Swelling and tensile properties	316, 316 + Ti	280–680	7–10	200–500	4	2/77
HFIR-CTR-14	Fatigue	316	430	9–15	400-1000	7	12/77
HFIR-CTR-15	Fatigue	316	550	6-9	200–400	4	10/78
HFIR-CTR-16	Weld characterization, swelling, and tensile properties	316, PE-16, Inconel 600	55	6-9	150–2700	4	8/77
HFIR-CTR-17	Weld characterization	316	280–620	7-13	180–460	5.5	10/77
HFIR-CTR-18	Swelling and tensile properties	316, PE-16	280–700	17-27	1600–5600	12	6/78
HFIR-CTR-19	Weld characterization	316	280–620	7-10	200–500	4	12/77
HFIR-CTR-20	Fatigue	316	430	6-9	200–400	4	1/78
HFIR-CTR-21	Fatigue	316	550	9–15	400–1000	7	7/78
HFIR-CTR-22	Fatigue	316	430	6–9	200–400	4	3/78
HFIR-CTR-23	Fatigue	PE-16	430	6–9	370-1000	3.5	2/79
HFIR-CTR-24	Temperature calibration and tensile properties	316	300–620	2.2	30	1	12/78
HFIR-CTR-26	Swelling and tensile properties	316	284–620	30	1900	10	4/80
HFIR-CTR-27	Swelling and tensile properties	316	284–620	56	3500	18	1/81
HFIR-CTR-28	Swelling and tensile properties	316	370–560	30	1900	10	12/80
HFIR-CTR-29	Swelling and tensile properties	316	370–560	56	3500	18	8/81
HFIR-CTR-30	Swelling, microstructure, and ductility	Paths A, B, C, D, E	300–600	40	~15,000	14	11/8/81
HFIR-CTR-31	Swelling, microstructure, and ductility	Paths A, B, C, D, E	300–600	20	≤7500	8	5/28/81
HFIR-CTR-32	Swelling, microstructure, and ductility	Paths A, B, C, D, E	300–600	10	≤3000	4	12/81
HFIR-CTR-33	Swelling, tensile properties, weld characterization	Paths A and C	55	10	≤510	4	10/80
HFIR-CTR-34	Charpy	Path E	300, 400	10	0–75	4	5/82
HFIR-CTR-35	Charpy	Path E	300, 400	10	0–75	4	5/82
HFIR-CTR-39	Swelling and tensile	Path E	300–500	12	0–90	5	10/82
HFIR-CTR-40	Swelling and tensile	Path E	300–500	12	0–90	5	12/82
HFIR-CTR-41	Swelling and tensile	Path E	300–500	12	0-90	5	1/83
HFIR-MFE-RB1	Swelling, microstructure, crack growth, fracture toughness, Charpy, tensile, and fatigue	Path E	55	10	90	8	7/82
HFIR-MFE-RB2	Swelling, microstructure, crack growth, fracture toughness, Charpy, tensile, and fatigue	Path E	55	20	200	17	7/83
HFIR-MFE-T1	Swelling, tensile fatigue	Path E	55	30	≤300	12	8/10/82
HFIR-MFE-T2	Swelling, tensile fatigue	Path E	55	9	≤75	3	5/3/81
HFIR-MFE-T3	Impact properties	Path E	55	10	≤85	4	12/24/81

Table 10.2.2. Objectives and schedule for current and planned ADIP program reactor irradiation experiments

Experiment designation	Major objective
A. Oak Ridge Research Reactor	
ORR-MFE-4	Effect of irradiation on tensile, fatigue, and irradiation creep of path A PCA (Prime Candidate Alloy) and path B base research alloys. Spectral tailoring to maintain correct He/dpa ratio. Irradiation on continuing basis. 330–600°C (1)
ORR-MFE-6J	Swelling, tensile, irradiation creep fatigue, crack growth, and microstructure of Path A alloys. 60 and 200°C. Evaluated at 10 to 15 dpa intervals. Employs spectral tailoring to achieve fusion He:dpa value.
ORR-MFE-7J	Similar to ORR-MFE-6J but 300 and 400°C.
B. Experimental Breeder Reactor (EBR-II)	
Experiment plan depends on alloy availability. EBR-II space not yet identified.	Effect of irradiation on swelling, tensile, fatigue, and crack growth properties of V and Nb scoping alloys. 370, 450, 550, and 650°C. Position in reactor not finalized, therefore no fluence estimate. (3)

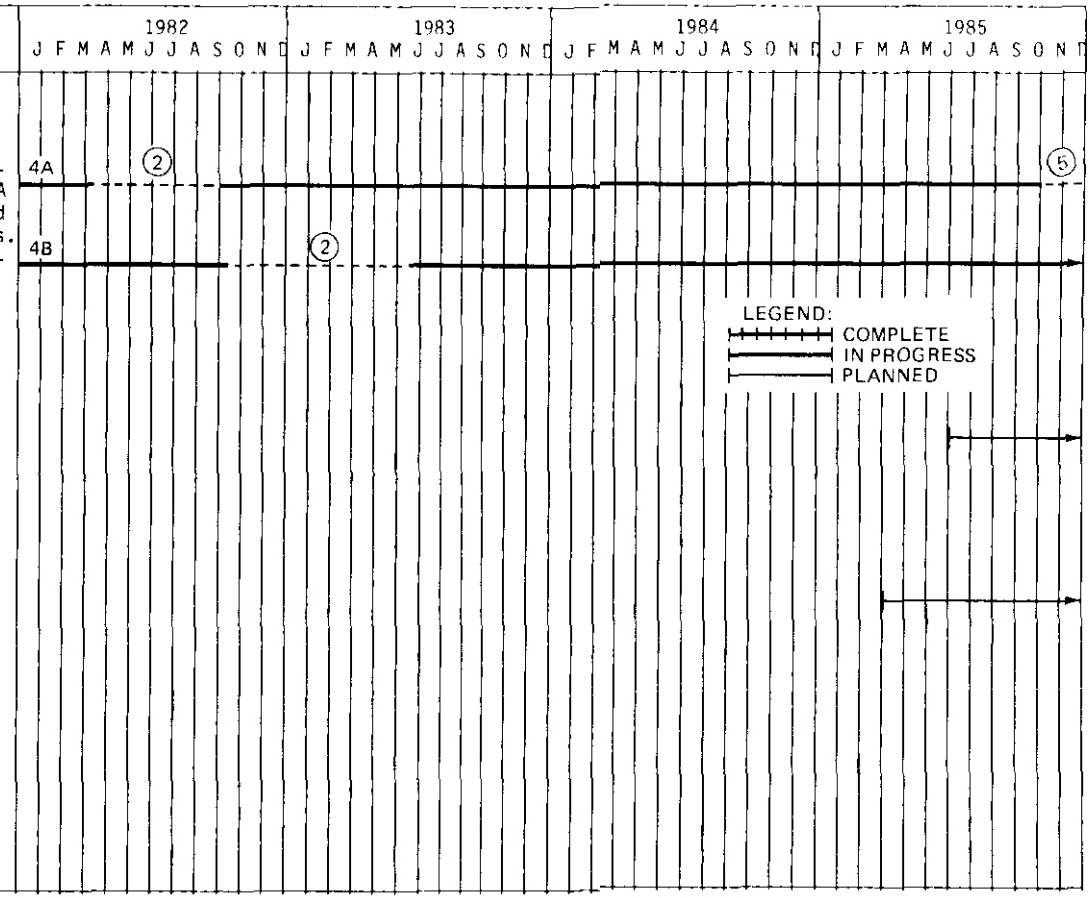

(1) MFE-4A operates at 330 and 400°C. MFE-4B will operate at 500 and 600°C.

(2) Removed from reactor for reencapsulation.

(3) Delayed for undetermined period.

(4) Interim examination. Experiment out of reactor. Reencapsulated in subassembly X-344B.

(5) Remove from reactor for 15 dpa specimen discharge.

(6) Remove for specimen discharge.

(7) HFIR shut down for reflector replacement.

(8) The HFIR-JP experiment series is a joint program shared by the U.S. and Japan Fusion Reactor Materials activities.

Table 10.2.2. (continued)

Experiment designation	Major objective
AD-2 (6 pins in separate subassemblies of row 4)	To supplement present EBR-II data on ferritic alloys with data on crack growth, fatigue, and fatigue toughness. Temperature 390, 450, 500, and 550°C. 15 and 30 dpa.
C. *Fast Flux Test Facility (FFTF)*	
FFTF MOTA Fusion Experiment	Microstructural and mechanical properties of Path A, C, and E alloys.
D. *High Flux Isotope Reactor (HFIR)*	
HFIR-CTR-36	Fatigue properties of path A alloys. 30 dpa, 2000 ppm He.
HFIR-CTR-42	Swelling, tensile properties of path A alloys. 20 dpa, 1100 ppm He, 300 to 600°C.
HFIR-CTR-43	Swelling, tensile properties of path A alloys. 20 dpa, 1100 ppm He, 300 to 600°C.
HFIR-CTR-44	Swelling, tensile properties of path A alloys. 10 dpa, 500 ppm He, 250 to 400°C. Joint experiment of U.S., European Community, and Japan.
HFIR-CTR-45	Similar to HFIR-CTR-44
HFIR-CTR-46	Impact properties of path E alloys. 10 dpa, 5 ppm He, 300 and 400°C.

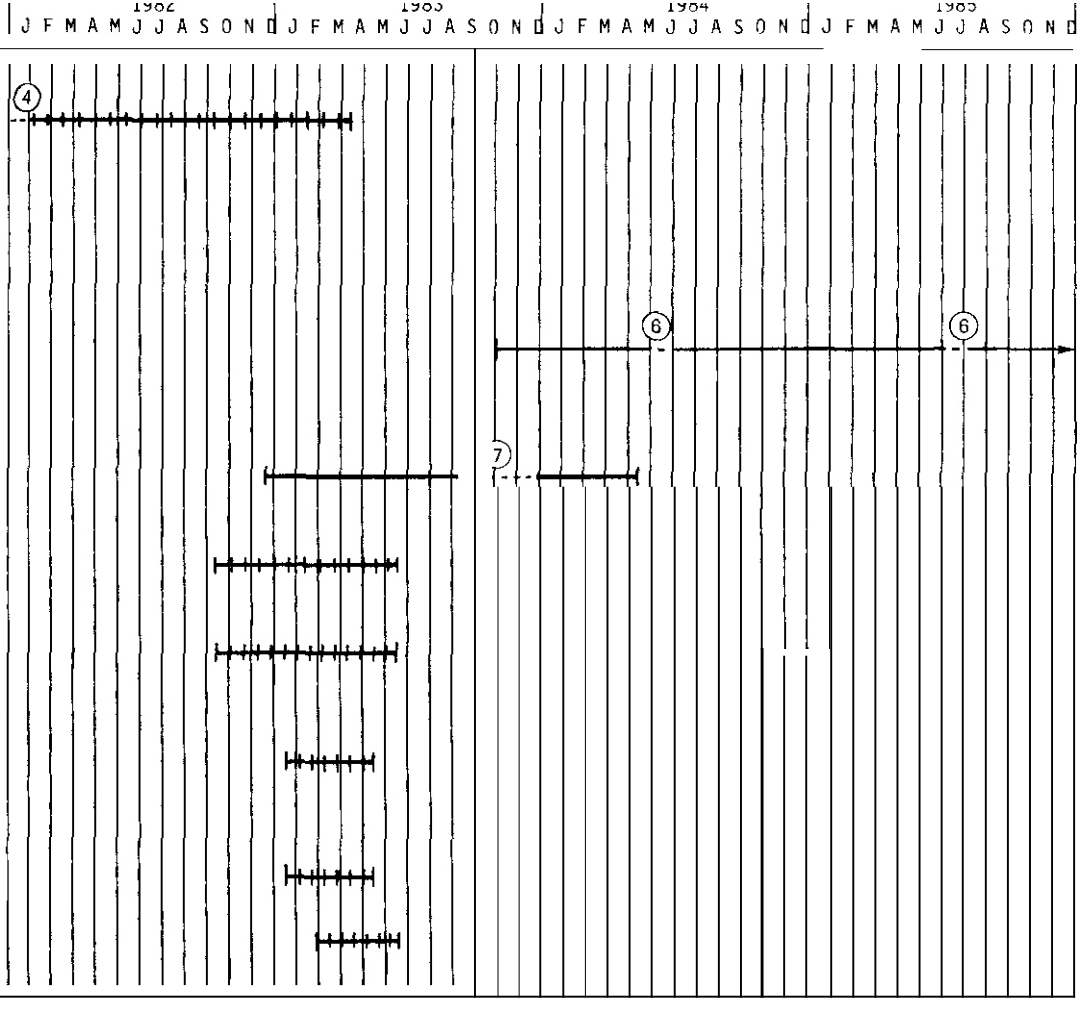

Table 10.2.2. (continued)

Experiment designation	Major objective	1983 J F M A M J J A S O N D	1984 J F M A M J J A S O N D	1985 J F M A M J J A S O N D	1986 J F M A M J J A S O N D
HFIR-CTR-47	Impact properties of path E alloys. 40 dpa, 400 ppm He 300 and 400°C.				
HFIR-CTR-48	Similar to HFIR-CTR-47.				
HFIR-CTR-49	Tensile properties and microstructure of path E alloys. 50 dpa, 70 to 500 ppm He, 300 to 500°C.				
HFIR-CTR-50	Tensile, swelling, microstructure of path E alloys, 100 dpa, 150 to 1000 ppm He 400, 600°C.				
HFIR-CTR-51	Swelling, tensile properties of low-activation alloys. 20 dpa, 300–600°C				
HFIR-CTR-52	Fatigue properties of 316 SS 10 dpa, 500 ppm He 430°C. Joint experiment with European community and Japan.				
HFIR-CTR-53	Impact properties of path E alloys. 10 dpa 75 ppm He, 200, 300°C, one-third size Charpy.				
HFIR-CTR-54	Similar to HFIR-CTR-53				
HFIR-CTR-55	Tensile swelling, microstructure of path E alloys. 50 dpa, 400 ppm He, 400, 600°C.				
HFIR-CTR-56	Tensile, swelling microstructure of path E alloys. 100 dpa, 150–1000 ppm He, 400, 600°C.				

Table 10.2.2. (continued)

Experiment designation	Major objective
HFIR-JP-1⑧	Swelling, tensile and fatigue properties, and microstructure of path A alloys. 300–600°C, 30 dpa, 2000 ppm He.
HFIR-JP-2	Similar to HFIR-JP-1 but to 50 dpa, 3500 ppm He.
HFIR-JP-3	Similar to HFIR-JP-1.
HFIR-JP-4	Swelling, tensile properties, and microstructure of path A alloys. 55°C, 50 dpa, 2000 ppm He.
HFIR-JP-5	Similar to HFIR-JP-2.
HFIR-JP-6	Similar to HFIR-JP-1.
HFIR-JP-7	Similar to HFIR-JP-1.
HFIR-JP-8	Similar to HFIR-JP-2.

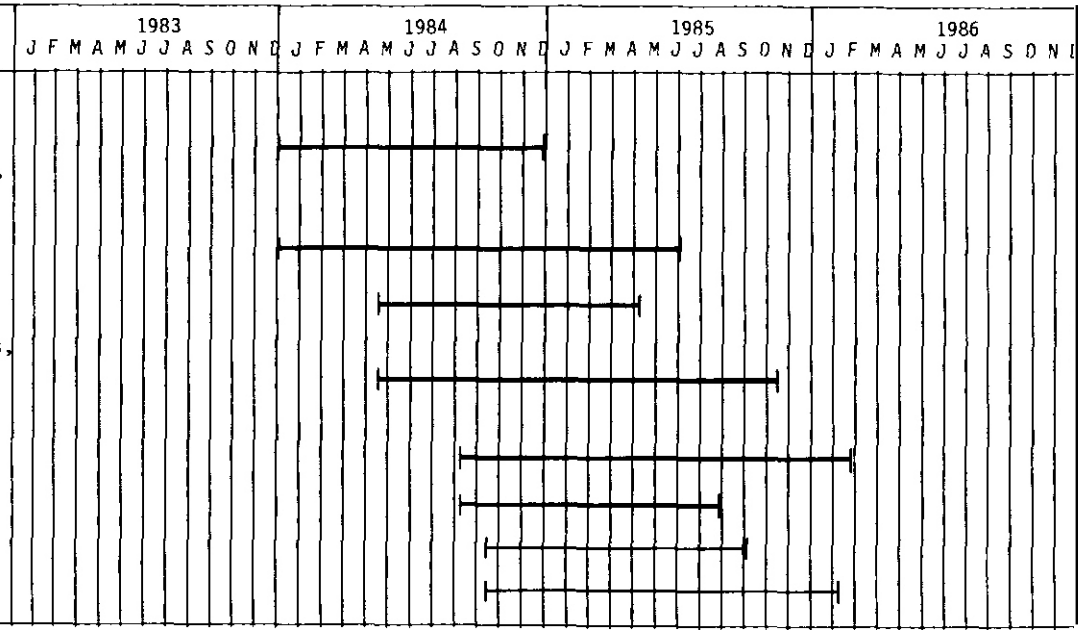

DOE/ER-0045/13
Distribution
Category
UC-20, 20c

DISTRIBUTION

1–5. Argonne National Laboratory, 9700 South Cass Avenue, Argonne, IL 60439

L. Greenwood
V. Maroni
R. F. Mattas
D. L. Smith
H. Wiedersich

6. Auburn University, Department of Mechanical Engineering, Auburn, AL 36849

B. A. Chin

7. Battelle-Pacific Northwest Laboratory, P.O. Box 999, Richland, WA 99352

J. L. Brimhall

8. Rrookhaven National Laboratory, Upton, NY 11973

C. L. Snead, Jr.

9. Carnegie-Mellon University, Pittsburgh, PA 15213

J. C. Williams

10. Colorado School of Mines, Golden, CO 80401

G. R. Edwards

11–194. Department of Energy, Technical Information Center, Office of Information Services, P.O. Box 62, Oak Ridge, TN 37830

For distribution as shown in TID-4500 Distribution Categoory, UC-20 (Magnetic Fusion Energy), and UC-20c (Reactor Materials)

195–201. Department of Energy, Office of Fusion Energy, Washington, DC 20545

M. M. Cohen
G. M. Haas
T. C. Reuther, Jr. (5 copies)

202. Oepartment of Energy, Oak Ridge Operations Office, P.O. Box E, Oak Ridge, TN 37830

Office of Assistant Manager for Energy Research and nevelopment

203. Energy Technology Engineering Center, P.O. Box 1449, Canoga Park, CA 91304

ETEC Library

204–205. GA Technologies, Inc., P.O. Box 81608, San Diego, CA 97138

T. A Lechtenberg
D. I. Roberts

206–208. Lawrence Livermore National Laboratory, P.O. Box 808, Livermore, CA 94550

E.N.C. nalder
M. Guinan
C. M. Logan

209. Massachusetts Institute of Technology, 138 Albany Street, Cambridge, MA 02139

O. K. Harling

210. Massachusetts Institute of Technology, 77 Massachusetts Ave., Cambridge, MA 02139

N. J. Grant

211. McDonnell Douglas Astronautics Company, East, P.O. Box 516, St. Louis, MO 63166
J. W. Davis

212. National Materials Advisory Board, 2101 Constitution Ave., Washington, DC 20418
K. M. Zwilsky

213214. Naval Research Laboratory, Washington, DC 20375
Superintendent, Materials Science and Technology Division
J. A. Sprague

215–245. Oak Ridge National Laboratory, P.O. Box X, Oak Ridge, TN 37831
Central Research Library (2 copies)
Document Reference Section
Laboratory Records Department (2 copies)
Laboratory Records Department, RC
ORNL Patent Section
E. E. Bloom
D. N. Braski
W. R. Corwin
J. H. DeVan
I. T. Dudley
M. L. Grossbeck
R. L. Klueh
R. A Lillie
C. T. Liu
K. C. Liu
L. K. Mansur
P. J. Maziasz
C. J. McHargue
T. K. Roche
A. F. Rowcliffe (2 copies)
M. J. Saltmarsh
J. L. Scott
P. T. Thornton (3 copies)
P. F. Tortorelli
J. M Vitek
F. W. Wiffen

246. Princeton University, Plasma Physics Laboratory, P.O. Box 451, Princeton, NJ 08544
P. Bonanos

247–248. Rensselaer Polytechnic Institute, Troy, NY 12181
D. Steiner
N. Stoloff

245–250. Sandia National Laboratories, Livermore Division 8316, Livermore, CA 94550
W. Bauer
J. C. Lippold

251–252. Sandia National Laboratories, P.O. Box 5800, Albuquerque, WM 87185
M. J. Davis
W. B. Gauster

253. Science Applications, Inc., 1200 Prospect, La Jolla, CA 92037
H. Gurol

254–256. University of California, Department of Chemical, Nuclear, and Thermal Engineering, Los Angeles, CA 90024

M. A. Abdou
R. W. Conn
N. M. Ghoniem

257. University of California, Santa Barbara, CA 93106

G. R. Odette

258. University of Missouri, Department of Mechanical and Aerospace Engineering, Columbia, MO 65211

M. Jolles

259. University of Virginia, Department of Materials Science, Charlottesville, VA 22901

W. A. Jesser

260. University of Wisconsin, 1500 Johnson Drive, Madison, WI 53706

W. G. Wolfer

261. Westinghouse Electric Company, Advanced Energy Systems Division, P.O. Box 10864, Pittsburgh, PA 15236

W. A. Boltax

262–269. Westinghouse Hanford Company, P.O. Box 1970, Richland, WA 99352

H. R. Brager
D. G. Doran
A. M. Ermi
F. A. Garner
D. S. Gelles
E. C. Opperman
R. W. Powell
J. L. Straalsund